

Engineered Porous Carbon Adsorbents for Radionuclide Remediation: A Study of Chemical and Physical Factors



Stella Jane Foster

Submitted in accordance with the requirements for the degree of

Doctor of Philosophy

University of Leeds

School of Process and Chemical Engineering

March 2023

The candidate confirms that the work submitted is her own and that appropriate credit has been given where reference has been made to the work of others.

This copy has been supplied on the understanding that it is copyright material and that no quotation from the thesis may be published without proper acknowledgement

The right of Stella Foster to be identified as Author of this work has been asserted by Stella Foster in accordance with the Copyright, Designs and Patents Act 1988

Acknowledgements

First, I would like to express my gratitude to my academic supervisors Profs Bhoopesh Mishra, Bruce Hanson and Dr Andy Ross. Their expertise, insight, encouragement and enthusiasm were pivotal to this work. The same sentiments are extended to Dr Robert Menzel with whom, had global circumstances not necessitated a change of plan, I feel certain I would have generated some exciting results.

I wish to express my admiration and respect to my closest colleagues, Flora Brocza and Dr Innes Deans and Dr Luke Higgins for the collaborative team working ethic which not only stimulated my scientific curiosity but also provided continual support and friendship. The nuclear engineering group also provided me with a vital space for collaboration and support for which I am very grateful. Dr Alastair Baker in particular provided unparalleled mentorship and support and continues to set an example for how to nurture colleagues. I remain proud of the work we achieved around the participation of women in STEM. Dr Lois Tovey, whom I assisted on the A-CINCH project, also deserves a large thank you for support, advice and allowing me tap into her extensive knowledge of the nuclear industry. There is large circle of wider collaborators who I wish to thank. At the School of Process and Chemical Engineering, my thanks go out to the technical team. Dr Adrian Cunliffe, Karine Alves Thorne, Chris Bulman, Ben Douglas, Edward Woodhouse and Simon Lloyd for invaluable technical advice, untiring assistance and their willingness to experiment with technical equipment and accommodate unconventional requests. Dr Nicole Hondow for access to her image analysis hardware. Drs Nitya Ramanan, Shashi Marathe and their colleagues at Diamond Light Source for help and advice as well as running my experiments when the pandemic restrictions prevented me from doing so myself. Likewise, Dr Mahalingam Balasubramanian at the Advanced Photon Source, Argonne.

My family have been a constant source of support throughout, as have the many friends I have made while living in Leeds, who provided an excellent contrast and distraction, when needed, to the demands of a PhD. My thanks to Jet Thomas for understanding and support, and to Deb Evans, without which this would never have even begun.

Abstract

Accidental release of radioactive material to the environment poses a widespread threat to health of the biosphere, including to humans through contamination of food or water sources, or through inhalation of airborne radioactive particles. The development of targeted, functionalised adsorbents and remediation materials which have the versatility to work effectively in varying groundwater conditions, often containing high quantities of dissolved matter, is necessary. Biopolymers are such a class of materials which are well suited to remediation and immobilisation of contaminants such as radionuclides from groundwater and soil. Not only do they possess promising physicochemical characteristics such as extensive hierarchical porosity, surface functionality and recalcitrance, they are inherently compatible with environmental systems. They can be further functionalised or activated, or incorporated into monolithic composites with specific, engineered functionality and morphology for enhanced uptake and removal of radionuclides. Despite this promise, they are poorly understood at a mechanistic level, in part, due to their amorphous nature which makes analysis of molecular scale processes difficult. Therefore consistent bulk behaviour is more difficult to predict. Understanding the underpinning physical and chemical features of biopolymers and their composites is a crucial step to both further optimisation and deployment of such a material in a remediation setting. Several functionalised biopolymers and monolithic composites were created for strontium uptake and immobilisation. Both the physical and chemical factors governing uptake behaviour were examined. The binding mechanism of strontium was examined using X-ray absorption spectroscopy and paired with bulk strontium uptake isotherm data. High and rapid uptake capacities were achieved to functionalised biochar with even higher uptake achieved to novel biochar-alginate hydrogel composites. EXAFS fitting results indicated biochars and hydrogels alike exhibit an inner sphere binding mechanism to engineered biopolymer adsorbents, indicating strong binding to the adsorbent. Pores, specifically macro pores play a crucial role in mass transport of radionuclides to/from active adsorption sites. They can also prevent pore blocking or fouling during adsorption. The pore architecture of a range of functionalised biochars was investigated quantitatively using X-ray tomography, revealing the pore tuning effect of several common activators on the macro pore space. Each choice of biochar-activator combination yields distinct pore architecture, which can be selected in response to varying application or conditions.

Abbreviations

BET	Brunauer–Emmett–Teller
ALPS	Advanced liquid processing system
CaOx	Calcium oxalate
CMC	carboxymethylcellulose
DOM	Dissolved organic matter
EDX	Electron dispersive X-ray spectroscopy
EXAFS	Extended X-ray Absorption Fine Structure
HEC	Hydroxymethylcellulose
HFO	Hydrous ferric oxide
HTT	Highest treatment temperature
IUPAC	International Union of Pure and Applied Chemistry
MEE	Multi-electron excitation
MnOx	Manganese oxide(s)
N	Coordination number
nZVI	Nano-zero valent iron
OMC	Ordered mesoporous carbon
PDM	Pore diffusion model
Q_e	Equilibrium uptake capacity (mg g^{-1})
Q_m	Maximal uptake capacity, derived via the Langmuir isotherm model (mg g^{-1})
RT	Room temperature
SEM	Scanning electron microscopy
SSA	Specific surface area ($\text{m}^2 \text{g}^{-1}$)
STEM	Scanning Transmission Electron microscopy
TEM	Transmission electron microscopy
XANES	X-ray Absorption Near-Edge Spectroscopy
XAS	X-ray Absorption Spectroscopy

XEDS

Energy Dispersive X-ray spectroscopy

ZVI

Zero valent iron

Table of Contents

Acknowledgements.....	iii
Abstract	iv
Abbreviations.....	v
Table of Contents	vii
List of Figures	xi
List of Tables	xviii
Chapter 1 Introduction	1
1.1 Context and motivation.....	1
1.1.1 Future planning and strategy.....	2
1.1.2 Wider Energy and De-carbonisation context	2
1.1.3 Biopolymer based adsorbent materials	3
1.2 Research questions.....	4
Chapter 2 Literature Review	6
2.1 Structure of literature review.....	6
2.2 Background	6
2.2.1 Selected properties of common radionuclides	7
2.2.2 Adsorption and ion-exchange.....	10
2.2.3 Absorbent classes.....	11
2.3 The binding mechanism of strontium to adsorbents.....	22
2.3.1 Binding in Biochar	23
2.3.2 Alginate and alginate-biochar composites	24
2.3.3 Strontium EXAFS literature	25
2.3.4 Knowledge gaps.....	30
2.4 The physical and morphological features of biopolymers.....	31
2.4.1 Pore structure	32
2.4.2 Porosity in biopolymers	38
2.4.3 Pore space tunability via activation	40
2.4.4 Pore space measurement techniques	45
2.4.5 Knowledge Gaps.....	49
2.5 Iron-biopolymer composites	51
2.5.1 Overview of iron-bearing minerals	51
2.5.2 Iron-biopolymer composites	55
2.5.3 Uranium uptake.....	60

2.5.4	Strontium uptake	71
2.5.5	Cesium uptake	76
2.5.6	Other radionuclides	81
2.5.7	Future perspectives.....	81
Chapter 3 Analytical Theory		82
3.1	Adsorption Isotherms	82
3.1.1	Isotherm models.....	82
3.1.2	Langmuir	82
3.1.3	Freundlich equation.....	82
3.2	X-ray techniques	84
3.2.1	X-Ray Absorption Spectroscopy.....	84
3.2.2	X-ray Computed Tomography (XCT).....	87
Chapter 4 Materials and Methods.....		92
4.1	Introduction	92
4.2	Biopolymer composites synthesis.....	93
4.2.1	Biochar.....	93
4.2.2	Biochar activation and functionalisation protocols	93
4.2.3	Hydrogel preparation.....	95
4.3	Physical characterisation.....	95
4.3.1	Elemental Analysis.....	95
4.3.2	Fourier Transform Infrared Spectroscopy (FTIR).....	96
4.4	Strontium uptake experiments	96
4.4.1	SEM-EDX.....	96
4.4.2	Preliminary comparison of strontium uptake for several functionalised/activated biochars.....	96
4.4.3	Kinetic investigation of biochar and activated biochar	96
4.4.4	Strontium uptake isotherms.....	97
4.4.5	Atomic Absorption Spectrophotometry (AAS).....	97
4.4.6	Inductively-Coupled Plasma Mass Spectrometry (ICP-MS).....	98
4.5	X-ray Absorption Spectroscopy	98
4.5.1	Strontium EXAFS.....	98
4.5.2	Manganese XANES	99
4.6	X-ray Computed Tomography (XCT)	100
4.6.1	Initial investigation.....	100
4.6.2	Expanded Sample Set.....	100

Chapter 5 Chemical characterisation: composition and functional groups	103
5.1 Elemental Analysis	103
5.1.1 Biochars and activated biochars.....	103
5.1.2 Nitric acid activation	105
5.1.3 Zinc (II) chloride activation	105
5.1.4 Potassium permanganate activation.....	105
5.1.5 Van Krevelan diagram.....	106
5.1.6 Hydrogel composites.....	109
5.2 Fourier Transform Infra-Red Spectroscopy.....	111
5.2.1 Feedstock effects	114
5.2.2 Activation	116
5.3 Conclusions.....	116
Chapter 6 Strontium uptake – Biopolymer composites	117
6.1 HNO ₃ activated adsorbents	117
6.1.1 Biochar - uptake isotherms.....	117
6.1.2 Hydrogel composites - uptake isotherms.....	118
6.1.3 Decontamination Factor	122
6.1.4 Extended strontium uptake isotherm data series	123
6.2 MnO _x activated adsorbents	129
6.2.1 Isotherm modelling.....	129
6.2.2 Decontamination Factor	131
6.2.3 Discussion – MnO _x activated adsorbents.....	131
6.3 Conclusions.....	132
Chapter 7 X-ray Absorption Spectroscopy: binding mechanism of strontium to biopolymer adsorbents	133
7.1 Introduction	133
7.1.1 Standards spectral analyses	134
7.2 Biopolymer composite adsorbents spectral analyses	135
7.2.1 Results.....	136
7.2.2 Discussion.....	150
7.3 MnO _x activated hydrogel composites	158
7.3.1 Manganese oxide identification	161
7.4 Conclusions.....	162
Chapter 8 Pore space analysis of biochar X-ray μ-tomography	164
8.1 Method Development	164

8.1.1	Method 1: Low-pass contrast enhancement and the Savu pipeline	166
8.1.2	Method 2: Machine learning segmentation	170
8.1.3	Thresholding	172
8.2	Alternative methods	173
8.3	Results: initial investigation with spent coffee ground biochar	175
8.3.1	Qualitative data initial set	175
8.3.2	Activation	176
8.3.3	Quantitative analysis	177
8.3.4	Discussion.....	178
8.4	Results: expanded Sample Set	180
8.4.1	Qualitative analysis	180
8.4.2	Quantitative analysis	189
8.5	Discussion.....	204
8.6	Conclusions.....	208
Chapter 9 Concluding Remarks.....		209
9.1	Binding mechanism of strontium to biopolymer composites.....	209
9.1.1	Bulk uptake experiments	209
9.1.2	X-ray spectroscopic studies	210
9.1.3	Implications and possible application areas.....	210
9.1.4	Future work	211
9.1.5	Limitations.....	212
9.2	Physical morphology and pore space analysis of biochar.....	212
9.2.1	Future work	213
9.2.2	Implications and possible application areas.....	213
9.2.3	Limitations.....	213
Appendices		217
	Bibliography.....	228

List of Figures

Figure 1.1 The various impacts of radioactive environmental contamination, adapted from <i>Management of large volumes of waste arising in a nuclear or radiological emergency (IAEA-TECDOC-1826)</i> IAEA, 2017 . 1	
Figure 2.1 Water tanks containing radioactively contaminated water across the Fukushima Daiichi site. Adapted from https://www.science.org/content/article/japan-plans-release-fukushima-s-contaminated-water-ocean (accessed June 2022)..... 9	
Figure 2.2 Outer sphere complexation (left) and inner sphere complexation (right) of a strontium ion to a surface 10	
Figure 2.3 The structure of a zeolite and principle of its ion-exchange capacity 12	
Figure 2.4 Relationship between feedstock type, pyrolysis regime and resulting physicochemical characteristics of biochar 13	
Figure 2.5 The calcium alginate biopolymer..... 14	
Figure 2.6 The structure of chitosan 15	
Figure 2.7 Nitric acid mesomeric forms..... 18	
Figure 2.8 Common Manganese oxide structures. Adapted from Qiao & Swihart 2017..... 20	
Figure 2.9 Ionotropic gelation of an alginate hydrogel composite (top) and the egg-box model of the gelation cross-linking process (below) 21	
Figure 2.10 SEM image on a cross-sectioned alginate hydrogel monolith bead doped with hexacyanoferrate. Adapted from Vipin et al. 2014.... 22	
Figure 2.11 Selected ionic radii values of group I and II metals for visual comparison. Adapted from Shannon 1975..... 22	
Figure 2.12 A typical set Sr EXAFS spectra of Sr adsorbed on Goethite, dominated by first shell oxygen backscattering signal. Adapted from Nie et al. 2017..... 25	
Figure 2.13 The calcium oxalate monomer 28	
Figure 2.14 Schematic representation of hierarchical porosity - how pores of all sizes contribute to overall performance of a porous material 31	
Figure 2.15 Number of entries returned for the term "hierarchical porosity" using the Scopus search tool (www.scopus.com) 2000 - 2022 (accessed 28/11/2022) 32	
Figure 2.16 Schematic representation of pores and pore features 33	
Figure 2.17 Schematic representation of a pore running between two parallel planes. This also visually represents the definition of a definition of tortuosity defined in equation 2 35	
Figure 2.18 Schematic representation of the proposed hierarchical pore space classification system, with proposed definitions below. Adapted from Schwieger et al. 2016 37	

Figure 2.19 Caguiat et al. 2018 tested the capacitance of wood-based biochar in different orientation, finding significant differences in performance	38
Figure 2.20 A schematic representation of various models of capillary flow in (a) closed rectangular, (b) open rectangular, (c) open U-shaped, and (d) open V-shaped microchannels. Adapted from Kolliopoulos et al. 2021	40
Figure 2.21 FESEM of a cross-sectioned alginate-nZVI composite monolith. Adapted from Huang et al. 2016	44
Figure 2.22 Scale of pore size ranges spanning five orders of magnitude, showing the working ranges of the most common pore space measurement techniques	45
Figure 2.23 A 2D XCT image of Jones et al.'s cotton hull biochar in false colour (dark regions indicate pore space).	47
Figure 2.24 Orthogonal XCT reconstruction of Jeffrey et al.'s straw biochar. The field of view represents 4.9 mm ³ . Adapted from Jeffrey et al. 2015	48
Figure 2.25 An example of the manual thresholding (right) from reconstructed XCT image slice (left) by Quin et al. 2014 on biochar-treated soil. Adapted from Quin et al. 2014	49
Figure 2.26 Core-shell model of zero valent iron nano-particles.....	52
Figure 2.27 adapted from Ling et al. 2018 showing the different distribution of uranium adsorbed to zvi and hematite. HAADF and element mapping (Fe, O, U and Fe+O+U from left to right) showing zvi at 1 hr (a-e), zvi at 24 hr (f-j) and hematite at 24 hr (k-o)	53
Figure 2.28 Example of the Molecular Structure of Prussian blue (Akira Takahashi, 2018)	54
Figure 2.29 Summary of biopolymer-iron composites examined for radionuclide immobilisation. Classified by radionuclide (left), iron phase (middle) and by biopolymer type (right). Colour groupings refer to radionuclide	56
Figure 2.30 L3-edge uranium XANES data from Li et al. 2019 showing the slow reduction of U(VI) to U(IV)	66
Figure 2.31 SEM Cross-sectional image of a HCF-alginate hydrogel. Adapted from Vipin et al. 2014.....	77
Figure 2.32 Synthesis of HCF-alginate hydrogels via an in-situ HCF synthesis (A) versus incorporation of HCF powder (B). Adapted from Mihara et al	78
Figure 3.1 Excitation of a core electron from the K (n = 1) shell (left) and a schematic representation of photoelectron backscattering due to neighbouring atoms (right)	84

Figure 3.2 Example plot of X-ray absorption coefficient plotted with incident X-ray energy, showing the Sr K-absorption edge at 16105 keV and EXAFS or fine structure oscillations at higher energy for a strontium oxalate standard	85
Figure 3.3 Schematic of the principle steps of the parallel beam X-ray computed tomography	87
Figure 3.4 As the sample (left, plan view) is rotated through 180° and exposed to X-rays, a sonogram (right) is generated from the attenuated signal. This represents the sequential X-ray signals at all projections or orientations between 0-180°	89
Figure 3.5 Examples of reconstructed 2D images	91
Figure 4.1 Feedstocks selected for comparison in tomographic pore space analysis	92
Figure 4.2 Photographic image of biochar sample SCG350 mounted to a pin and magnetic contact for tomographic image acquisition	100
Figure 5.1 Van Krevelan diagram for biochars derived from Oak wood, spent coffee and rice husk, and their activated analogues	106
Figure 5.2 FTIR spectra for oak biochar (Oak BC), activated oak biochar (A-Oak BC), oak hydrogel composite (Oak HG) and activated oak hydrogel composite (A-Oak HG) as well as calcium alginate (ALG)	112
Figure 5.3 FTIR spectra for rice husk biochar (RH BC), activated rice husk biochar (A-RH BC), rice husk hydrogel composite (RH HG) and activated rice husk hydrogel composite (A-RH HG) as well as calcium alginate (ALG)	113
Figure 6.1 Uptake isotherm data for rice husk (RH) and oak wood (OK) biochars, both unactivated and HNO ₃ activated. Error bars in x and y represent one SD; each data point was taken in triplicate.....	117
Figure 6.2 Strontium isotherm uptake data for rice husk (RH) hydrogels (left) and biochars (right). Data are plotted across identical axis for clarity. Error bars in x and y represent one SD; each data point was taken in triplicate	119
Figure 6.3 Strontium isotherm uptake data for oak wood (OAK) hydrogels (left) and biochars (right). Data are plotted across two identical axis for clarity. Error bars in x and y represent one SD; each data point was taken in triplicate.....	121
Figure 6.4 Extended strontium uptake isotherms for rice husk and oak wood activated hydrogel composites. Error bars in x and y represent one SD; each data point was taken in triplicate	123
Figure 6.5 Isotherm data series for activated RH and activated OAK hydrogel composites, showing the variation in uptake performance at increasing strontium concentration.	128

Figure 6.6 Strontium uptake isotherms for Manganese activated biochar and manganese activated hydrogel composites (left) with the initial data points (right) plotted on a smaller scale. Error bars in x and y represent one SD; each data point was taken in triplicate.....	129
Figure 7.1 Normalised strontium K-edge EXAFS data for four standards: A) K-edge position, B) EXAFS data in k-space, C) the real part of the Fourier transform and D) the magnitude of the Fourier transform. Standards are labelled to the right of D).....	134
Figure 7.2 EXAFS spectrum for strontium oxalate standard (A) and the real part of the Fourier transform (B). Plots include individual paths for oxygen and carbon shell fits (offset for clarity) as well as overall fit. Fitting range = 2.5-11.5 Å ⁻¹ , dk = 1, fitting range is 1.25-3.5 Å.	135
Figure 7.3 Normalised strontium K-edge data of representative samples, showing both activated and unactivated hydrogels (left), and biochar and alginate control samples (right). All samples displayed	140
Figure 7.4 Normalised k-space data of representative samples, showing both activated (A-) and unactivated hydrogels (left), and biochar and alginate control samples (right)	140
Figure 7.5 The real part of the Fourier transform for three representative biochar adsorbents and calcium alginate, including fits and individual paths (offset for clarity). Data are enumerated in Table 6-1	141
Figure 7.6 The real part of the Fourier transform for four representative hydrogel adsorbents including fits and individual paths (offset for clarity). Data are enumerated in Table 6-1	141
Figure 7.7 Magnitude of the Fourier transform for four representative hydrogel adsorbents including fits and individual paths (offset for clarity)	142
Figure 7.8 Magnitude of the Fourier transform for three representative biochar adsorbents and calcium alginate, including fits and individual paths (offset for clarity)	142
Figure 7.9 Schematic representation of a partial sphere of hydration around a strontium atom, displaying interatomic distance to the second sphere of hydration.....	150
Figure 7.10 Typical Sr-C interatomic distances from crystallographic data for common organic strontium compounds. Carbon is shown in grey and oxygen in dark red. Note: dashed lines represent electrostatic Sr-O attraction not Sr-C distances.....	154
Figure 7.11 A representation of the likely binding environments of strontium in biochar and hydrogel composites, showing (left) a range of possible binding modes in biochar components: bi-dentate, mono-dentate and retention of a partial hydration sphere. (right), strontium in the “egg-box” binding model of divalent cations to alginate.....	155

Figure 7.12 Coordination number of absorbing Sr ²⁺ atom derived from EXAFS fitting arranged by activation and adsorbent type (top), and biochar feedstock type as well as initial strontium concentration (bottom)	155
Figure 7.13 Interatomic distances from absorbing Sr ²⁺ atom derived from EXAFS fitting organised by adsorbent type and activation (top), initial strontium concentration and biochar feedstock (bottom)	157
Figure 7.14 Example fit of a MnOx activated hydrogel composites. Magnitude of the Fourier transform (A) and the real part of the Fourier transform (B) including fits and individual paths (offset for clarity)	159
Figure 7.15 Two distinct binding environments are proposed for MnOx biochar and hydrogel composites: an inorganic-type MnOx binding at defect sites (left) and an organic-type binding to alginate or biochar phases within the composite	161
Figure 7.16 Manganese K-edge XANES of MnOx hydrogels with several manganese standards	162
Figure 8.1 A reconstructed tomographic image of biochar pore space without contrast enhancement (left) with its greyscale histogram (right)	164
Figure 8.2 The difference in image produced via phase contrast (left) and absorption contrast (right) for an oakwood biochar courtesy of Dr Luke Higgins. Note images are of the same sample but are not identical slice numbers	165
Figure 8.3 Schematic representation of default tomographic reconstruction steps (top) as well as the two modified methods used for contrast enhancement of biochar images	166
Figure 8.4 The difference in contrast before (left) and after (centre) applying the phase enhancement contrast ($\delta/\beta = 120$). The greyscale histogram (right) is displayed for the enhanced image	168
Figure 8.5 Ring artefact removal using two different ring removal processes, the Raven filter (left) and ccpi ring artefact remover (right) in the Savu pipeline	169
Figure 8.6 An image of biochar processed via the Paganin filter (left) and the same image with a thresholding mask applied (right) with greyscale histogram overlaid	169
Figure 8.7 Process overview of the Ilastik machine learning object classification method	171
Figure 8.8 Example of three phase training on a rice husk biochar in Ilastik (top) with each of the three green, blue and red layers (let to right) extracted below	172
Figure 8.9 The Feret diameter is a measure along the longest axis of a pore or space	173

Figure 8.10 Selected 2D (top) and 3D (bottom) reconstructions of initial data set using spent coffee ground biochar. 3D images are shown in a false colour heat map to depict the extensive internal structure. 3D images are not scaled due to angled orientations.	175
Figure 8.11 Image slices no. 1382 &1649 of unactivated biochar sample volume showing larger voids present within the internal structure. The widest void diameter (max Feret diameter) are indicated and annotated	177
Figure 8.12 Macro pore volume for spent coffee ground as well as a control biochar and ZnCl ₂ activated biochar. Measured from a 0.4 mm ³ sample volume and a pixel size of 0.325 μm.....	178
Figure 8.13 Pore circularity (top) and Feret diameter (bottom) distributions for all pores detected for unactivated biochar and ZnCl ₂ activated biochar	179
Figure 8.14 3D reconstructions of all samples. Field of view = 0.2 mm ³ , scale bar not included due to angled orientations	182
Figure 8.15 Representative 2D tomographic images of the internal macro pore structure for several activated biochars with corresponding unactivated biochar control samples and precursor biomass samples for oak wood, spent coffee grounds and rice husk feedstock precursors	183
Figure 8.16 Apparent filling of pores in KMnO ₄ activated OAK by an unknown phase.....	184
Figure 8.17 Orthogonal views of oak wood biochars: unactivated control biochar (a, e, i), HNO ₃ activated (b, f, j), ZnCl ₂ activated (c, g, k) and KMnO ₄ activated (d, h, l) in the XY, XZ and YZ planes respectively..	185
Figure 8.18 Orthogonal views of spent coffee ground biochars: unactivated control biochar (a, e, i), HNO ₃ activated (b, f, j), ZnCl ₂ activated (c, g, k) and KMnO ₄ activated (d, h, l) in the XY, XZ and YZ planes respectively	187
Figure 8.19 Orthogonal views of Rice husk biochars: unactivated control biochar (a, e, i), HNO ₃ activated (b, f, j), ZnCl ₂ activated (c, g, k) and KMnO ₄ activated (d, h, l) in the XY, XZ and YZ planes respectively..	188
Figure 8.20 Macro pore volume of oak wood biochars and the biomass precursor. Representative XCT images of each material are displayed above for comparative purposes.....	189
Figure 8.21 Macro pore volume of spent coffee ground biochars and the biomass precursor. Representative XCT images of each material are displayed above for comparative purposes.....	191
Figure 8.22 Macro pore volume of rice husk biochars and the biomass precursor. Representative XCT images of each material are displayed above for comparative purposes.....	192
Figure 8.23 Percent macro pore volume for biochars, activated biochars and precursor feedstocks.	194

Figure 8.24 Feret diameter distributions for all biochar samples for the range 0 – 200 μm . Axes are common for all. Note that an artificial cut-off in the bar chart has been defined at 200 μm for comparison of smaller pores. The curve represents a normal distribution of the untruncated data set and thus represents the distribution of pore sizes across the entire range of detection.	195
Figure 8.25 Pore circularity distributions for all biochar samples where 1 indicates a perfect circle and approaching 0 indicates low circularity (x-axis). Oak wood biochar (top), spent coffee ground biochar (middle) and rice husk biochar (bottom). The curve represents a normal distribution of the untruncated data set.	196
Figure 8.26 Directional tortuosity of oak wood (top) and spent coffee grounds (bottom) biochar pore space and their activated analogues	199
Figure 8.27 SEM-EDX spectroscopy of KMnO_4 activated oak wood biochar site 1. Top panel showing backscattering electron SEM image at 15 keV & x1000 magnification (top left) and 2D elemental maps for calcium, manganese and oxygen. Bottom panel shows a line spectrum through the formation showing elemental composition	202
Figure 8.28 SEM-EDX spectroscopy of KMnO_4 activated oak wood biochar site 2, showing backscattering electron (BSE) SEM image at 15 keV & x1000 magnification (top left) and 2D elemental maps for calcium, manganese and oxygen	203
Figure B.1 Evidence of formation of a film or coating on Oak wood hydrogel	220

List of Tables

Table 2-1 Typical decay routes of common radio isotopes of strontium and cesium	8
Table 2-2 IUPAC pore size classifications	33
Table 2-3 A summary of zero valent iron – biopolymer composites studied for uranium uptake (1/2).....	63
Table 2-4 Summary of selected iron oxide biopolymer composite materials examined for uranium uptake (1/3)	68
Table 2-5 Summary of iron-biopolymer composites studied in strontium uptake experiments	75
Table 4-1 Sample matrix displaying samples for expanded sample set	102
Table 5-1 Percent weight content of biochars, activated biochars and their feedstocks. Uncertainty is one standard deviation	104
Table 5-2 Hydrogel composite beads weight percent chemical composition, with uncertainty is expressed as one SD	110
Table 6-1 Strontium uptake isotherm parameters for biochar and hydrogel composite adsorbents.....	120
Table 6-2 Decontamination factors of all HNO ₃ activated biochars and hydrogels at initial strontium concentration of 5 mgL ⁻¹	122
Table 6-3 Isotherm modelling parameters using extended data series for activated hydrogel composites derived from both rice husk and oak wood biochars.....	124
Table 6-4 Decontamination factor at an initial strontium concentration of 5 ppm for the extended activated hydrogel data sets	125
Table 6-5 Summary of relative uptake behaviour - rice husk and oak wood biochar - as a function of initial strontium concentration	126
Table 6-6 Isotherm modelling parameters for manganese adsorbent materials.....	130
Table 6-7 Decontamination factors for manganese adsorbents	131
Table 7-1 EXAFS fitting parameters for hydrogel beads, biochar and alginate samples. Both Oak wood (Oak) and rice husk (RH) biochar was used. Table continued overleaf (1/3)	145
Table 7-2 Comparison of R-factor values for a range of fit types. In the majority of cases, a Sr-O Sr-C fit yields the lowest R-factor values, suggesting these fits most accurately follow experimental data. Sr-O Sr-Cl fits also yield low R-factor values in several cases. Thus, coordination number values are also reported for this fit 1/2.	148
Table 7-3 Simultaneous EXAFS fitting parameters for MnOx biochar and hydrogel samples at initial strontium concentrations of 50 and 250 mg L ⁻¹	160

Table 8-1 Quantitative pore space data for spent coffee ground biochar - control unactivated and ZnCl ₂ activated	179
Table 8-2 Macro pore dimension values for oak wood, spent coffee ground and rice husk biochars	197
Table 8-3 Summary of tuneable hierarchical pore space differences observed using XCT and literature BET micro pore analysis data	207
Table A-1 Selected compositional data for common three feedstock types, expressed in percent dry weight	217
Table A-2 Selected literature values for BET surface area of activated biochars versus unactivated control biochars	218

Chapter 1 Introduction

1.1 Context and motivation

Since the dawn of the nuclear industry over 70 years ago, fission-derived technology has made significant contributions to improvements in the standard of living, healthcare and scientific knowledge, through energy generation, medical and industrial applications. However, safely isolating and disposing of radioactive waste materials generated during fission remains a formidable technical challenge, one that is yet to be fully met. Indeed, it is arguably one of the defining issues of the modern era¹. Accidental release has resulted in groundwater, soil, ocean and atmospheric contamination at sufficiently elevated levels to pose a widespread and serious threat to life, both acute and chronic. Some radionuclides such as radio strontium or cesium are isoelectronic with bio-essential minerals and thus preferentially taken up into the food chain, where they are capable of exerting considerable damage to life. The impacts to life, as identified by the International Atomic Energy Agency (IAEA), are in fact multi-fold² as illustrated in Figure 1-1. Releases of radioactive material to the environment have occurred through historic weapons testing, improper disposal of waste, accidental release due to leaks from aging storage facilities or following large scale accidents such as that at the Fukushima Daiichi power plant in 2011³. The duration that such materials will remain hazardous is

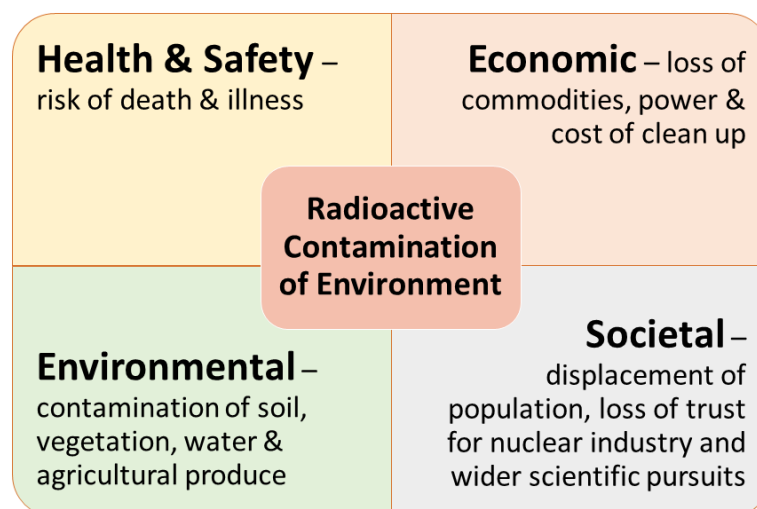


Figure 1-1 The various impacts of radioactive environmental contamination, adapted from *Management of large volumes of waste arising in a nuclear or radiological emergency (IAEA-TECDOC-1826)* IAEA, 2017

considerable, posing challenges for future generations. Current technology for removal of radionuclides from waste liquor released environmental systems typically utilise inorganic ion-exchange materials e.g. the natural zeolite clinoptilolite⁴ or synthetic zeolites. While these materials have proved efficient in certain conditions, they possess limitations that can dramatically reduce their efficacy, particularly in cases of environmental contamination. Fouling or blocking of pore channels can be an serious issue for ion-exchange zeolites in contact with groundwater rich in dissolved organic and inorganic matter. Thus, there is a need for remediation materials which can withstand such conditions.

1.1.1 Future planning and strategy

The IAEA detail the importance of pre-planning for future release events:

*[E]fforts for preparedness made in advance of an emergency will help facilitate recovery... Protection strategy and recovery actions will likely include use of **decontamination technologies** for agricultural, industrial, residential, and natural areas*

- IAEA, Adaptive Strategies for Waste Management p28, Management of large volumes of waste arising in a nuclear or radiological emergency (IAEA-TECDOC-1826), 2017² (bold added by this author)

Research and development of materials capable of meeting the needs of such protection strategies is vital in anticipation of future accidents⁵. This underscores the persisting deficiencies in current remediation technology that are yet to be addressed. Since accidental release can (and has) occurred in a wide range of global environmental contexts, development of versatile remediation materials which are tolerant to varying environmental conditions is also an important factor to be considered. Reducing the volume of radioactive waste is another key strategic point identified by the IAEA, the British Department for Energy and Climate Change (BEIS)⁶ and elsewhere^{2,7-9}. The UK's current fleet of advanced gas cooled (AGR) reactors are due to shut down from 2023. Future waste arisings from their decommissioning, as well as other activities exceed 4 million m³, a 3000 % increase on existing UK waste stocks¹⁰.

1.1.2 Wider Energy and De-carbonisation context

Co-incident with the issue of safely containing radiological waste is the pressing need to decarbonise energy, transport and production activity which drives life threatening climate change. This is especially the case in energy generation. The IPCC reports that the earth has already surpassed a temperature rise of 1 °C with attendant changes to terrestrial habitats and loss of biodiversity.

Acidification of the oceans will threaten ocean ecosystems and the melting of polar ice will cause rising sea levels which puts millions of households at risk, since 1/3 of the total human population live at or near to sea level¹¹. This means that current petroleum and oil consumption is unsustainable, creating demand for alternative sources for energy generation and necessitating the search for alternative feedstocks for a range of specialised materials that hitherto have been produced from petroleum-based feedstocks, such as plastics or sorption-optimised materials like activated carbons, used in gas and liquid phase contaminant immobilisation.

1.1.3 Biopolymer based adsorbent materials

Biopolymers are derived from biosynthetic processes e.g. photosynthesis. They are a broad and highly versatile class of materials (cellulose, chitosan, alginate etc.) that possess a number of advantageous properties for immobilisation of contaminants, including (but not limited to ionic radioactive species such as strontium, cesium or uranyl. Thermal processing of biopolymers via pyrolysis creates biochar, a stable and porous material with large surface areas.

Biopolymers are sustainable, compatible with environmental systems, economic and a large step towards carbon-negative materials. Traditionally dismissed as too amorphous or disordered for high-tech uses, developments in targeted modification and tuning methods mean that the performance and reliability of biopolymer materials are beginning to challenge more traditional and more expensive methods and materials. Attendant to this, newer analysis methods are capable of interrogating amorphous materials such as biopolymers on a mechanistic level.

1.2 Research questions

The treatment of groundwater and soil for removal of radionuclides is an active area of research. The nuclear power industry is growing, at a time when we must also find permanent disposal solutions to the waste materials of previous generations. It is therefore imperative that we continue to develop improved waste management and remediation methods to protect against future accidents. Remediation of contaminants is not only about protecting the biosphere but also for maintaining vital public confidence in science. This is especially true in the nuclear industry, which has suffered disproportionately from public relations issues. There are wider implications and a great deal of crossover with remediation of heavy metals too. Environmental contamination of heavy metals is a ballooning area of research and the demand for adsorbent technology is considerable.

The same drivers for the renewed interest in nuclear power, namely the rapid decarbonisation of anthropogenic activities, are also driving demand for novel sustainable and low carbon technologies in materials science. In fact, biopolymers are of increasing interest in several domains including catalysis, electrochemical and energy storage applications due to their economic, versatile and carbon-negative origins, as well as favourable surface chemistry, ease of activation and tunability and hierarchical porosity.

Partly due to their amorphous nature, biopolymers have historically been challenging to characterise and analyse, in terms of both mechanistic chemical interaction and physical morphology. Full understanding of the behaviour of such materials is vital for both optimisation and deployment as a technology.

Therefore, this work sets out to further understand the physical and chemical nature of biopolymers, with a view to increasing their efficacy and technology readiness level with a primary focus on adsorptive removal of radionuclides, and a secondary focus on wider implications of the underlying physicochemical characteristics. The following key questions are addressed:

1. What is the nature of the binding mechanism of radionuclides such as strontium, to biopolymers such as biochar and alginate?
2. How can limitations inherent to biopolymers be overcome or optimised using chemical engineering techniques such as functionalisation, activation or composite formation?
3. How can the hierarchical porosity of biopolymers be fully described and how variable can it be?

4. Can the hierarchical pore space be tuned or modified in a targeted way, and what pore space profile is optimal from an adsorptive removal point of view?

In order to appropriately address these research questions, and since biopolymers as a class encompass such a wide range of materials, I have chosen to focus on a small number of biopolymer types identified as particularly promising for certain key radionuclides. Namely, strontium, cesium and uranium. By reviewing relevant literature and applying a few key techniques, I have attempted to answer these questions. X-ray techniques are central to this thesis, with X-ray absorption spectroscopy (XAS) used to examine binding and chemical speciation, and X-ray computed tomography (XCT) used to examine hierarchical pore spaces. Synchrotron X-ray facilities play a crucial role in such data acquisition, while supporting methods such as uptake experiments also contribute to the results. As such, this work encompasses a number of facets: from reviewing relevant literature, thermal and chemical processing techniques, engineering rationally designed composite adsorbent materials, X-ray spectroscopy and microscopy, data analysis and image analysis with machine learning.

This work will begin with a comprehensive overview of relevant literature, including the state of the art for both chemical and physical modification and tuning of biopolymers. A summary of relevant analysis techniques is provided, including strengths and limitations with a particular focus on synchrotron X-ray techniques. This should provide sufficient background and context in which to understand the results, relevance and implications of subsequent data chapters, as well as the rigour in which this work has been completed.

Chapter 2 Literature Review

2.1 Structure of literature review

In order to address the research questions in Section 1.2, a review of relevant literature is organised into three sections. First, an introductory section covers background information about radionuclides, adsorption and remediation, and the suitability of biopolymers as adsorbents. This includes a review of the functionalisation and activation strategies used upon biopolymers, particularly those relevant to the subsequent sections. Building upon this, two thematic sections follow which provide a more in-depth analysis of 1. The binding mechanism of strontium to adsorbents (Section 2.3) and 2. The physical and morphological features of biopolymers relevant to adsorption (Section 2.4). The binding of strontium to biopolymers and manganese oxide-biopolymer composites is discussed in-depth, corresponding with data presented in Chapter 5 and Chapter 7. However consideration is also given to the binding of other common radionuclides in the Section 2.2. Finally, Section 2.5 discusses radionuclide binding to iron-biopolymer composites. No data is presented which corresponds with this section; it sits as a separate literature review section, relevant to the overall theme of this thesis but not directly related to the data chapters. Since this section forms the basis of a critical literature review publication, it is included in order to reflect the breadth of knowledge and work in this project. However, it is not directly relevant to data presented in subsequent chapters.

2.2 Background

Contamination of the biosphere with radioactive material poses a risk to life owing to their release of α , β , γ -rays. Mining activities¹², historic weapons testing¹³, accidents¹⁴ and degradation of storage facilities and waste management sites¹⁵ have released a great deal of radioactive materials to the environment since the birth of fission technology in the 1940s. Following the 2011 Fukushima Daiichi incident, a several further on-site leaks have occurred, including a 2013 incident during which a concentrated mix of ⁹⁰Sr, ¹³⁷Cs, ¹³⁴Cs, ⁵⁴Mn, ⁶⁰Co, ¹²⁵Sb and ³H accidentally leaked to the soil surrounding storage tanks¹⁴. Radioactive liquor is known to have leaked from many storage sites including storage ponds at the UK's Sellafield site¹⁶ and the USA's Hanford site¹⁵, where a series of leaks from aging storage tanks soil and groundwater has released an estimated 3800 m³ of mixed radioactive waste to the biosphere¹⁷. In fact over half of all US nuclear waste processing sites exhibit

significant soil contamination¹⁸. It is projected that energy generation through nuclear fission will increase in the coming decades¹⁹ due to increasing costs of fossil fuels, decarbonisation and air pollution improvement efforts. With this comes greater volumes of future waste arisings and attendant risk for further accidental release to the environment. The International Atomic Energy Agency (IAEA) has argued for the importance of advance planning in this regard, to continue to develop remediation technologies in the event of future accidental release². Radionuclides can directly cause a large number of serious health problems such as birth defects, cancer, neurological problems and infertility when inhaled or ingested^{20,21}.

2.2.1 Selected properties of common radionuclides

2.2.1.1 Uranium

As the fuel for most nuclear fission reactors, uranium is one of the most commonly studied radionuclides in remediation and immobilisation. Mining activities^{22,23}, release from accidents, at fuel processing and weapons testing sites² as well as depleted uranium (DU) used in munitions are all sources of exposure. In common with all transuranic elements such as americium and plutonium, uranium is extremely chemotoxic and is linked to developmental problems^{24,25}, cancers²⁶ as well as damage to tissues and organs including the brain, skin, liver, kidneys, reproductive organs and bones. It typically takes the form of a uranyl poly cation UO_2^{2+} as U(VI) in environmental systems. All three of its naturally occurring isotopes (^{234}U , ^{235}U and ^{238}U) are weakly radioactive and usually emit α -particles. The presence of uranium in aquifers is of increasing concern. In environmental systems, it forms highly soluble and strong complexes with carbonates, hydroxides and nitrates, as well as less soluble phosphates.

2.2.1.2 Strontium

The fission product yield of ^{90}Sr from thermal neutron fission of ^{235}U (as in most nuclear power plants) is 5.7 %. It is therefore abundant in spent fuel, other fission-derived wastes and following nuclear weapons detonations. Two isotopes, ^{90}Sr and ^{89}Sr are of particular concern, as summarized in Table 2-1. Owing to its chemical similarity to calcium, it is readily incorporated into milk or bones where it has an estimated biological half-life of 18 years²⁷. It causes functional changes in bone marrow stromal cells, even at low levels²⁸, capable of ionising surrounding organic matter and causing somatic changes. It is known to cause bone cancers and leukaemia²⁸. As a highly soluble, oxyphilic di-

cation (Sr^{2+}), its most common route of exposure is ingestion of contaminated food or water. Its mobility and fate in environmental systems depends heavily on the prevailing conditions: pH, soil physical and chemical characteristics and the concentration of other species in ground water or seawater²⁹. Radio strontium is routinely detected at virtually all major releases of radioactivity, and in large quantities. Early estimates at the Fukushima Daiichi site (in 2013) indicate 0.1-1 TBq of ^{90}Sr was released to the airborne environment³⁰.

Table 2-1 Typical decay routes of common radio isotopes of strontium and cesium

Radioisotope decay route	Half life	Energy of decay (MeV) and mode
$^{90}\text{Sr} \rightarrow ^{90}\text{Y} + \beta^-$	29 yr.	0.55
$^{89}\text{Sr} \rightarrow ^{89}\text{Y} + \beta^-$	51 d	1.5
$^{85}\text{Sr} \rightarrow ^{85}\text{Rb} + e^+ + \gamma$	65 d	0.51
$^{134}\text{Cs} \rightarrow ^{134}\text{Ba} + \beta^- + \gamma$	2.07 yr.	0.70
$^{135}\text{Cs} \rightarrow ^{135}\text{Ba} + \beta^-$	2.3×10^6 yr.	0.27
$^{137}\text{Cs} \rightarrow ^{137}\text{Ba} + \beta^- + \gamma$	30.2 yr.	0.51 β^- 0.66 γ

Release is ongoing and difficult to pinpoint. Studies show that radio strontium was continuing to leak to seawater from the damaged reactors in large quantities more than two years after the accident, with an estimated 9.6 ± 6.1 GBq ^{90}Sr released per day in May 2013³¹. A later leakage of highly contaminated wastewater from storage tank area H4 lead to an estimated 45 TBq ^{90}Sr released to groundwater^{14,32}. Numerous waste water tanks populate the site (). After the Chernobyl incident an estimated total 10 PBq is thought to have been released³³ over a vast area of Europe³⁴. As of 2022, some 36 years after the accident, levels of radio strontium near the Ivankiv district south of the exclusion zone exceed Ukrainian safety limits in almost half of 116 grain samples and three-quarters of wood samples, with no evidence of a reduction

levels over time³⁵. Exposure via eating contaminated crops or by burning wood remains a very real possibility. As a result of historical fission weapons detonations and related activities, radio strontium is present in groundwater at > 50 % of the United States Department of Energy sites (Hanford WA, Savannah River GA, Idaho National Laboratory ID and Oak Ridge National Laboratory TN)^{21,36}. Some of these sites exceed safe ⁹⁰Sr concentrations in groundwater by as much as five orders of magnitude³⁷.



Figure 2.1 Water tanks containing radioactively contaminated water across the Fukushima Daiichi site. Adapted from <https://www.science.org/content/article/japan-plans-release-fukushima-s-contaminated-water-ocean> (accessed June 2022)

2.2.1.3 Cesium

Along with strontium, cesium is also considered a dangerous fission product. A number of cesium radioisotopes are generated during fission, the most important of which are ¹³⁴Cs, ¹³⁵Cs and ¹³⁷Cs (Table 2-1). Known to be among the more volatile of radionuclides, it tends to disperse rapidly following a contamination event in atmospheric, oceanic and terrestrial systems³⁸, which increases the risk of exposure markedly. It readily enters food chains and is of particular concern in agriculture, where permaculture activities and the grazing of large areas of grassland tends to bio accumulate radio cesium within plants and animals intended for human consumption. Radio cesium (Cs⁺) is isoelectronic with potassium (K⁺) and sodium (Na⁺), thus tends to disperse throughout soft tissues of the body such as the thyroid gland, where it can rapidly cause serious damage. It is implicated in immune deficiencies, thyroid and pancreatic cancers, neurological disorder as well as congenital and foetal deformations and it is thought to particularly affect children³⁹. Cesium, although less oxyphilic than strontium, readily forms a wide variety of oxides and is

termed as a “soft” Lewis acid. This describes its tendency to form compounds with larger, more polarisable Lewis bases such as sulphide. Release of radio cesium to the atmosphere after the Fukushima Daiichi accident is estimated at 10-37 PBq⁴⁰, with 90-900 TBq released to the oceans⁴¹.

2.2.2 Adsorption and ion-exchange

Adsorption is a mass transfer process in which a target solute, in this a case radionuclide, is transferred from solution phase to a solid surface where it is immobilised. This process is facilitated by favourable electrostatic interaction between surface functional groups and the ion in question. This interaction governs the strength and reversibility of the binding interaction.

Ion-exchange is a substitution process of ions in solution with those complexed in a solid phase. The molar ratios (assuming equal charge) of exchanging ions are thought to be equal.

In most “real world” systems, pure adsorption or pure ion-exchange are rarely observed and a combination of the two are most often observed^{42,43}. The two processes are hugely important in describing transfer of matter in environmental contexts and immobilisation of contaminants. Sorption is thought to be the more effective mechanism in high ionic strength solutions such as groundwater or seawater⁴⁴.

2.2.2.1 Inner and outer sphere complexation

Another common classification of surface-complexed ions is to distinguish inner and outer sphere complexation. Outer sphere complexation is a binding mode with a surface, mediated *through* the sphere of hydration of an ion. The cation is

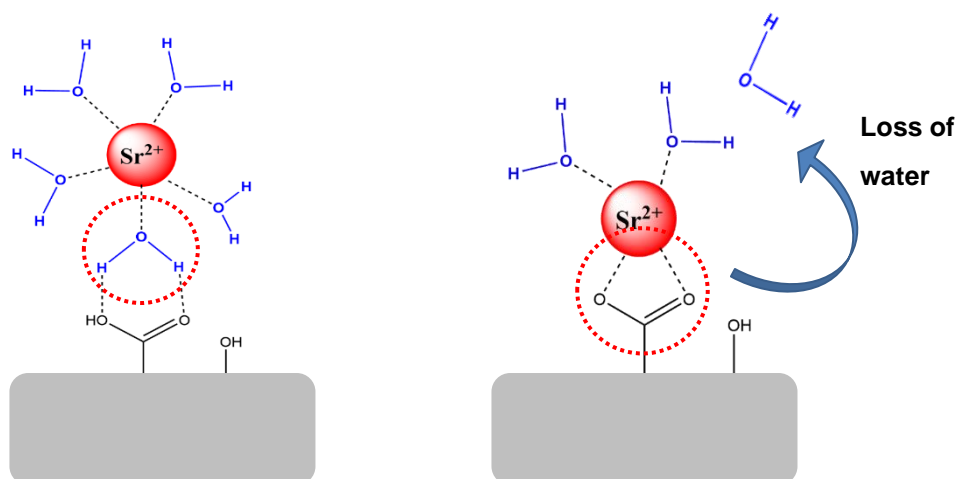


Figure 2-2 Outer sphere complexation (left) and inner sphere complexation (right) of a strontium ion to a surface

located at a greater distance from the surface and is less tightly bound than the inner sphere complex⁴⁵. Inner sphere complexation in contrast, is characterised by partial loss of hydration and a direct interaction between surface moieties and the ion⁴⁶. Figure 2-2 displays this difference. Formation of an inner sphere interaction implies a high affinity between the ion and surface binding sites. This can be achieved, in the case of the strontium cation, by σ -donation of surface oxygen lone pairs to the ion, increasing its electron density and forming a strong ionic interaction, much stronger than outer sphere complexation. This type of interaction would be most favourable with an electron rich adsorbent, i.e. one with delocalised π -bonding. Inner sphere complexation is typically a slower process than outer sphere complexation and is less reversible, thus more favourable in immobilisation or separation processes. The pH of a system can greatly influence binding, since this affects surface charge, which in turn affects electrostatically-driven (ionic) binding⁴⁷.

2.2.3 Absorbent classes

2.2.3.1 Inorganic ion-exchangers

Ion-exchange minerals, both naturally occurring and synthetic, have a long history in the nuclear industry and are the preferred method for the solid phase extraction of waste radionuclides from solution⁴. Ionic species located in interstitial layers or channels of the ion-exchange structure (Figure 2-3) are exchanged for a target ionic species in solution. As such, this is a reversible process, classed as physisorption^{49,50}. Ion-exchange materials exhibit high cation exchange capacities (on the order of 100s of mg cation per gram ion-exchange material)⁵¹, are highly uniform and consequently exhibit predictable adsorption properties. They possess some limitations however. Even small amounts of dissolved organic matter (DOM) can result in fouling of ion-exchange media⁵² – precluding its use in groundwater without significant pre-treatment⁵¹. Strongly oxidising elements such as nitrates (present in abundance in groundwater worldwide) can pose issues, as can the presence of other inorganic species which can also strongly inhibit the efficacy of the material⁴⁸. Scalability can also be an issue given the sometimes large throughput required⁵³. The ALPS plant at Fukushima⁵⁴ failed to perform as was hoped for removal of radionuclides such as cesium and strontium, with treated water still containing levels above regulatory limits⁴¹.

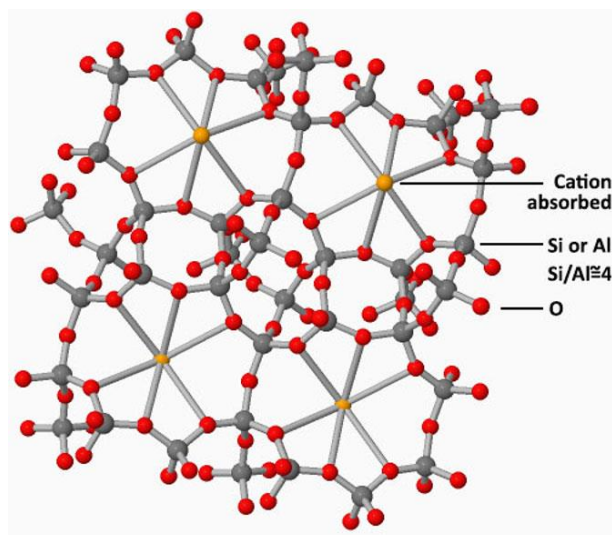


Figure 2-3 The structure of a zeolite and principle of its ion-exchange capacity

2.2.3.2 Biopolymers

Biopolymers are materials and polymers derived from natural sources, such as chitosan from chitin, the exoskeleton of crustaceans⁵⁵, alginate the anionic biopolymer which forms a major component of brown kelp⁵⁶, or biochar, the pyrolytic product of lignocellulosic material. Biopolymers are inherently environmentally benign, therefore compatible with environmental remediation applications. Biopolymer-based remediation materials could therefore be more suitable for *in-situ* remediation of soil and groundwater, such as in reactive barriers or for purification of contaminated water, and show promise of functioning well in acidic and high ionic strength solutions⁵⁷. As natural materials, biopolymers are sustainable and cheaper to produce than many synthetic remediation materials^{55,58}. Biopolymers also have the potential to undergo volume reduction steps post-uptake⁵⁹, with reports of volume reduction ratios for a Sr-loaded biochar of around 1000 times by Liu et al. 2016⁶⁰. Biopolymer based materials are still criticised for their variable nature and apparent lack of tunability⁵¹. This paradigm is currently being challenged by a new wave of research which is striving for ever greater physicochemical tunability and enhanced, targeted functionality^{61,62}. The main types of biopolymers used in adsorptive immobilisation of radionuclides are described below.

Biochar / Pyrolytic carbon

Biochar is the thermal decomposition product of biomass (cellulose, hemicellulose and lignin) and other bio-wastes under low oxygen conditions⁶³. The thermal treatment, known as pyrolysis, employs treatment temperatures typically ranging from 350 – 1200 °C, producing a stable, carbon-rich and highly porous material with abundant surface functionality, particularly oxygen-bearing groups such as carboxylates, hydroxyl, lactone and ether groups⁶⁴. Biochar is well suited for immobilisation of a range of cationic species due to the abundance of these surface groups. It is often highly aromatic and recalcitrant, since the pyrolysis process essentially reduces the biomass feedstock via loss of heteroatoms and condensation transformations⁶⁵. This recalcitrance conferred by increasingly high temperature is a beneficial property. These properties have seen it used as a contaminant immobilisation material for centuries⁶⁶ and at time of writing, is a thriving area of research for contaminant

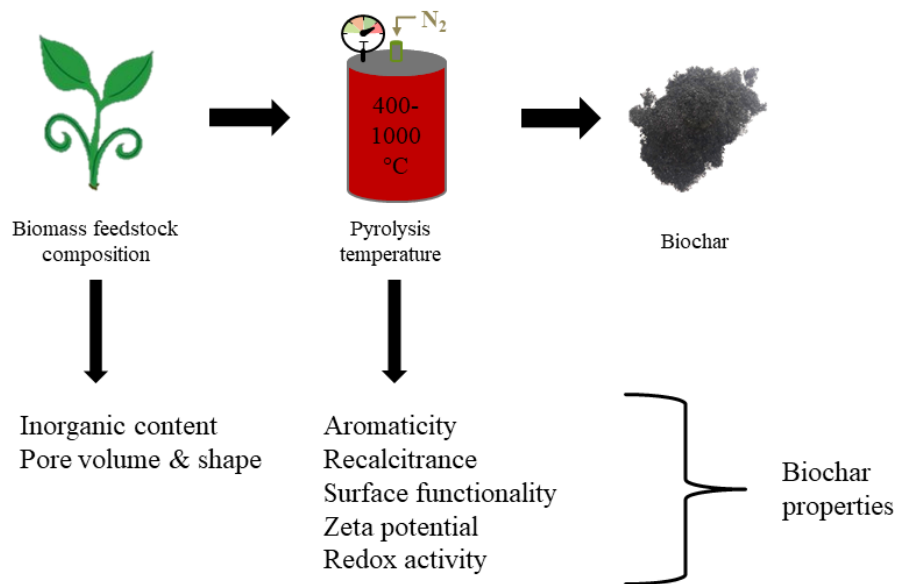


Figure 2-4 Relationship between feedstock type, pyrolysis regime and resulting physicochemical characteristics of biochar

immobilisation.

One of its major strengths is its versatility as a material, since its physicochemical characteristics can be tailored and optimised specifically for application (Figure 2-4), even to target specific contaminant species^{67,68} e.g. cation or anion immobilisation. Furthermore, it lends itself to functionalisation, both generalised in the form of activation (using acid, base, steam or pressure)⁶⁹⁻⁷², functionalisation via organic transformations^{73,74} or metal doping⁷⁵⁻⁷⁷, making it even more tailorable. In addition it can be produced both

inexpensively and rapidly from wastes or crop residues, making it sustainable, and not limited by dependence on specific feedstocks or geopolitical constraints^{78,79}, a consideration which becomes more important as fission technology is expected to expand globally. Biochar and activated biochars have been considered for immobilisation of uranium^{80–86}, cesium^{87–89}, strontium^{57,90}, iodine⁹¹, thorium⁹², europium⁹³, and technetium⁹⁴. The compositional make up of three common biomass feedstocks for biochar is presented in Appendix A.

Binding mechanism

Due to its amorphous nature, examining the binding mechanism of cations to biochar is challenging via techniques such as X-ray Diffraction (XRD) which work well for inorganic crystalline materials. Information about the nature of the bonding to biochar is typically examined via X-ray Photoelectron Spectroscopy (XPS), Fourier Transform Infra-red (FTIR) spectroscopy, by identification of changes to bond vibration and energy shifts, correlated with altered binding or bonding states before versus after uptake. Yet these are surface specific techniques and for a highly porous materials such as biochar, this reveals little of the bulk picture. Boehm titration provides another avenue of investigation, determining the absolute number of various acidic oxygen containing surface functional groups, and thus quantifies the major binding sites. In practice, this technique is not routinely used in studies of biochar owing to limitations and uncertainties in its accuracy specific to biochar^{95,96}. The complexation mechanism of uranium onto biochar have also been examined in one Extended X-ray Absorption Fine Structure Spectroscopy (EXAFS) study⁹⁷. The advantages of using EXAFS to examine the complexation mechanism of cations to biochar as discussed in Section 2.3.1 and Section 2.5.

Alginate

Alginate is an anionic biopolymer derived from brown algae (*Phaeophyceae*) such as brown Kelp but also from *Pseudomonas* and *Azotobacter bacterial genera*. It consists of (1 → 4)-linked (1 C4)-α-L-gulopyranuronate and (4 C1)-β-

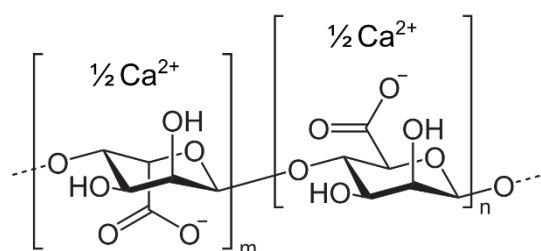


Figure 2-5 The calcium alginate biopolymer

D-mannopyranuronate unit⁹⁸, shown in Figure 2-5. It is well suited to uptake of cationic species since as an anionic polymer, cations naturally form part of its structure. Another of its most useful properties is its ability to form gels^{56,99} and thus form monolithic adsorbent materials. This property conveniently circumvents any issues with separation of fine particulate adsorbents or nano-phases. As well as monolith formation, alginate's carboxylate and hydroxyl functional groups make it well suited to immobilization of cationic species, particularly strontium¹⁰⁰. This is thought to largely occur via an ion-exchange mechanism with Ca^{2+} (or similar) within the gel structure and is described by the egg-box model⁹⁹. Formation of gels is examined further in Section 2.2.3.4.

Chitosan

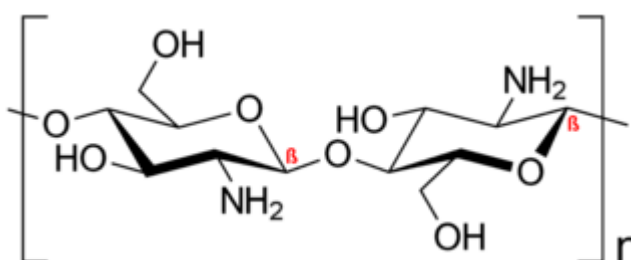


Figure 2.6 The structure of chitosan

Chitosan is the partially de-acylated product of Chitin, derived mainly from crustacean shells¹⁰¹ and as such it is a waste product of seafood production. Up to 8 million tonnes of crab, shrimp and lobster waste shells are generated annually¹⁰². Its structure consists of two β-1,4 linked N-acetyl-D-glucosamine units (Figure 2.6), and contains abundant amine, amide and hydroxyl functionality, making it well suited for cation uptake, particularly more labile ion species such as uranium. Chitosan as a standalone adsorbent exhibits poor to reasonable uptake of cationic contaminants however its real strength lies in providing a stable scaffold or support for secondary phases with even higher adsorption or reductive adsorption capacities within composites such as hexacyanoferrates¹⁰³, zero valent iron¹⁰⁴ or iron oxide phases¹⁰⁵.

Other notable biopolymers

Cellulose, starch¹⁰⁶ and pectin⁹⁹ also possess useful characteristics for cation complexation. Bacteria-derived cellulose membranes contain hydroxyl, carboxyl among other functionality useful for coordination with iron-bearing phases¹⁰⁷. Carboxyl methyl cellulose (CMC) and hydroxyethyl cellulose (HEC) are derivatives of cellulose which are also of interest due to their own absorptive capacity and crosslinking potential^{108–111}. CMC is also known as cellulose gum and it is formed by alkali-catalysed reaction of cellulose with chloroacetic acid,

conferring carboxylate groups which renders the material more polar and therefore soluble¹¹².

2.2.3.3 Activation

Activation is a collective term for treatments (chemical, physical, thermal etc.) that alter surface chemistry, chemical composition and/or physical morphology of a material in a form that is favourable to the desired application. For adsorptive immobilisation, the major purposes of activation are increasing surface functional groups which will complex, bind or chelate to the target contaminant and enhancing porosity and surface area¹¹³. Chemical activation agents are generally viewed as the most effective at this dual modification^{114–117} rather than physical activation methods. There are a wide range of chemical agents employed to activate biochars or similar biopolymers. Some of these include boric acid, ammonia, phosphoric, sulfuric, nitric or hydrochloric acids¹¹⁸, bases such as sodium or potassium hydroxide^{67,69,119}. There is some overlap between activation and ‘doping’ or impregnation techniques which, in addition to forming a composite material may also chemically activate the starting material¹²⁰. Inorganics such as metal oxides or heteroatoms¹²¹ are common examples of dopants. Inorganics which are capable of both ion-exchange and redox transformations generally exhibit very favourable adsorption capacities^{7,122,123}. Iron and manganese oxides are among the most common of biochar dopants, and due to their abundance in nature are a natural pairing with biochar, with some evidence of a synergistic effect on stability and/or adsorption^{124–126}. Pyro-processing of biomass into biochar also provides favourable thermodynamic conditions and a source for electrons for reduction of iron in a convenient one-pot synthesis.

Four common activation methods were selected for further review based upon their favourable adsorptive characteristics for strontium immobilisation. The Lewis acid zinc(II)chloride, the mineral acid nitric acid, and manganese and iron oxides.

ZnCl₂ activation

Zinc (II) chloride dihydrate (ZnCl₂•2H₂O) is common chemical activator and has been applied to a range of carbonaceous biomass precursors including spent coffee grounds^{127–129}, rice husk¹³⁰, wood sawdust¹³¹, biogas residues¹³², cellulose¹³³, lignin-rich residue¹³⁴, sewage sludge⁷⁵, anaerobic digestion sludge¹³⁵, shiitake substrate¹³⁶, olive stones¹³⁷, grape stalk¹³⁸, safflower seed press cake¹³⁹ and shaddock skin¹⁴⁰ among others. It has also been used to

activate kerogenic carbons such as coal¹⁴¹ and has also been employed to create biochar-ZnO nanocomposites for photocatalytic degradation of contaminants¹⁴². It has been shown to be a useful activator for electrochemical, catalytic and energy storage applications, with ability to increase carbon aromaticity at high temperature and increase specific capacitance^{72,143} as well as for activated carbon wound dressings¹⁴⁴. Its application to biomass can reduce the treatment temperature needed by reducing the activation energy required for the condensations reactions that are characteristic of the pyrolysis treatment. It can also increase biochar yield¹¹⁶.

Adsorption

For application in adsorptive processes, ZnCl₂ is known to enhance micro pore surface area and volume¹¹⁸ as well as increase surface oxygen group functionality¹³⁹. However, few studies examine immobilisation of cationic species^{130,137} to ZnCl₂ activated biochars. This is in part due to concerns of leaching of residual Zn²⁺ ions during wastewater treatment.

Porosity

As a Lewis acid, ZnCl₂ interacts with oxygen electron lone pairs in lignin, cellulose and hemicellulose. This Zn-O interaction promotes the degradation of biomass components during pyrolysis via loss of water has a major effect on pore structure. It is thought to widen existing pore structures and also create new cavities in the resulting biochar⁷². It provides a 'skeleton' or scaffold around which carbonisation of the biomass occurs. Once the activator is removed, the porous structure of the biochar is retained¹¹⁶. Activation with this method routinely increases the specific surface area (SSA) of a biochar from 10s m² g⁻¹ to well in excess of 1000 m² g⁻¹¹⁴⁵. This is summarised in Table A-2. Impregnation ratio (ZnCl₂:biomass feedstock) is an important variable which affects resulting properties such as yield, SSA and pore size distributions as well as weight % elemental composition, and notably for adsorptive processes, oxygen content¹³⁹. Higher ratios favour high pore space values but lower yield and oxygen content.

HNO₃ activation

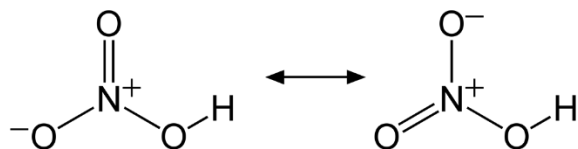


Figure 2-7 Nitric acid mesomeric forms

Nitric acid is a small mineral acid with a pKa of -1.4 which also possesses strongly oxidising properties (Figure 2-6). It is well known to add a range of oxygen and nitrogen containing groups. Oxidation reactions add carboxyl groups in particular and to a lesser extent nitrogen groups to aromatic (graphitic) carbon^{113,146–148}. For this reason, it has been a popular choice for activation of carbonaceous biopolymers such as biochar derived from cactus¹⁴⁹, red cedarwood¹⁵⁰, sunflower seed husks¹⁵¹, or weeds¹¹³ for purposes which require addition of electronegative oxygen groups.

Adsorption

A study by Yakout et al. 2018¹⁵² showed that carboxylate groups in biochar are instrumental in strontium adsorption, more so than any other oxygen containing group, with a similar conclusion by Shawabekeh et al. 2002 using a pecan shell biochar¹⁵³. As a bidentate moiety, carboxylates are subject to *the chelate effect*¹⁵⁴, meaning complexation of an hydrated cation is both more enthalpically and entropically favourable. Combining this with the graphitic nature of biochar, which possesses delocalised electrons^{155,156}, this aromaticity may be capable of further increasing electron density around a charge dense, electropositive cation such as strontium, through a surface carboxylate, further strengthening the interaction. HNO₃ activation has been shown to increase uptake and immobilisation of other cationic species including uranium^{85,157,158}.

Porosity

HNO₃ appears to have a variable effect on SSA (Table A-2). Some studies suggest a small decrease in SSA with activation. It appears that increasing the acid concentration decreases resulting SSA while increasing oxygen surface functionalisation¹¹³. It is theorised that the addition of such oxygen groups in such confined spaces as micro pores may have a blocking effect, thus reducing the measured SSA of the material. Another likely mode of action on the pore space

is corrosive widening of meso pores into larger macro pores which are not possible to measure via the BET gas adsorption derived SSA. As a mineral acid it also will dissolve crystalline inorganic phases, many of which are present in biopolymers such as biochar. Thus, one mode of action of HNO_3 on surface morphology is thought to be to remove said crystalline phases and create void spaces in this manner. This has the added benefit of removing unwanted phases present in the raw biochar and increasing batch-to-batch consistency.

Manganese oxide activation

Oxides of manganese (MnO_x) are abundant in environmental systems¹⁵⁹ and exist in a large number of polymorphic structures^{160,161}. As a redox active metal, manganese is able to exist in a number of oxidation states¹⁶² and for this reason MnO_x is of interest across a wide range of domains, from capacitance and redox applications, catalysis as well as adsorption science. This wide-ranging application is reflected in the numerous synthesis routes possible. Doping of biochar is typically performed post-pyrolysis; evidence points to poorer adsorptive performance in composites in which the Mn phase is co-pyrolysed^{163,164}. It is thought that the strongly oxidising properties of Mn(VII) may not only provide a source of Mn for the synthesis, but also oxidise the biochar phase too, further enhancing surface functionality^{165–167}. Indeed, it is not clear in biochar- MnO_x composites created in this way, whether uptake enhancement is due to biochar oxidation or MnO_x ion-exchange processes.

Adsorption

Layered MnO_x structures have also shown excellent ion-exchange properties¹²³, as well as a high selectivity for strontium, outperforming several adsorbents including the zeolite clinoptilolite in a MnO_2 -carbon fibre composite⁴⁴. Studies also show success at removing strontium from seawater^{168,169}, and a high uptake of $Q_m = 200 \text{ mg g}^{-1}$ strontium was reported by Ivanets et al. 2015 to a mesoporous manganese oxide¹⁷⁰, further highlighting its high selectivity. This is, in part since MnO_x are noted to typically exist as non-stoichiometric minerals (with a few exceptions,) which display complex crystal structures and many substitutions of other cations in place of manganese¹⁷¹. Surprisingly few studies have examined strontium uptake to biopolymer- MnO_x composites. However, biochar- MnO_x composites do report considerable improvement in heavy metal uptake over control biochars, including lead^{163,172,173}, arsenic, cadmium, zinc and copper¹⁷⁴.

Porosity

Application of the oxidation of biochar to enhance pore space via Mn(VII) has been utilised previously^{159,167,175,176}. Such a treatment not only oxidises biochar but also impregnates it with MnO_x phases. This can therefore act to both widen pores and potentially block pores by deposition of MnO_x. Song et al. 2014 found that a 10 wt% KMnO₄ on a corn straw biochar decreased the SSA significantly from 61 to 3.2 m²g⁻¹, while the average pore width (as determined by BET gas adsorption) increased from 24 to 70 nm. This suggests that KMnO₄ treatment blocks or fills smaller pores via deposition of MnO_x phases. Another possible mode of action is corrosive pore widening by the highly oxidising KMnO₄. The authors suggest that at lower wt% of KMnO₄ treatments, pore blocking is the dominant mechanism, while at higher KMnO₄ ratios, the oxidative pore widening effect became more dominant¹⁵⁹. This theory is supported by the work of Yang et al. 2017 who created a 2 wt% KMnO₄ treated rape straw biochar, finding a SSA decrease from 111 to 19 m²g⁻¹ over the unactivated biochar but a pore width decrease from 7.2 to 3.1 nm¹⁷⁷. Uptake of their target contaminant (Cd²⁺) increased from 33 to 81 mg g⁻¹ upon KMnO₄ activation, proving that addition of MnO_x enhances uptake, in spite of some pore blocking. Meanwhile Wu et al. 2020 created a 17.4 wt% KMnO₄ activated rice husk biochar which led to a decrease in the SSA of 128 to 93.8 m²g⁻¹, and a slight increase in pore width from 2.7 to 3.6 nm⁷⁷. Uptake of the target contaminants were still enhanced with the addition of the Mn-phase. Other recent works report the same trend^{163,178,179}.

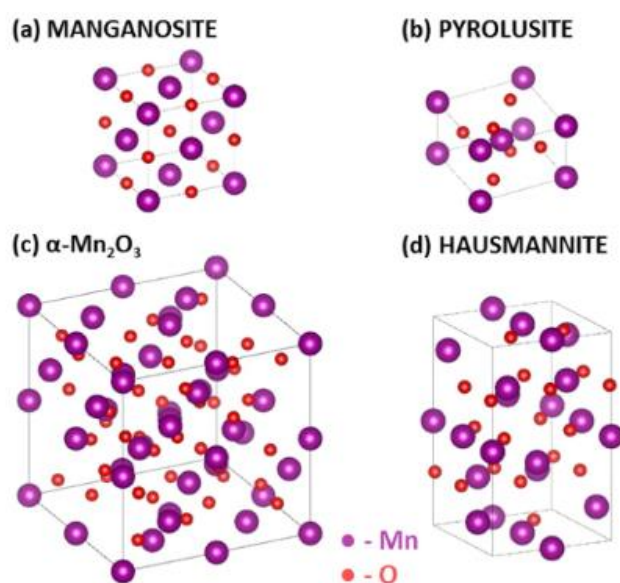


Figure 2.8 Common Manganese oxide structures. Adapted from Qiao & Swihart 2017

2.2.3.4 Biopolymer gels

Formation of gels via crosslinking reactions is an increasingly attractive method for creating a material which immobilises fine powdery adsorbents within a readily separable monolithic matrix. This builds on years of research into carbon aerogels^{180–182} and metal alkoxide sol-gels. Several biopolymers are capable of crosslinking via gelation or variations on the sol-gel method¹⁸², such as alginate^{183,184}, pectin⁹⁹ and gellan gum¹⁸⁵, with alginate being the most common. A number of studies also incorporate biopolymers into gels cross linked using reagents such as glutaraldehyde¹⁸⁶ or thiourea¹⁸⁷. Along with crosslinking agent, the drying method also affects end porosity and mechanical stability, largely due to shrinkage during drying as the solvent is lost from pore space. Gelation of the alginate phase can be pH-induced¹⁸⁸, carbon dioxide induced¹⁸⁹, cryotropic¹⁹⁰, using ambient pressure techniques¹⁹¹, using green solvents¹⁹², freeze-drying¹⁹³ or ion-exchange (Figure 2-8). Each method produces a gel with different microstructure and physical characteristics which impact upon end use efficacy and as such, gelation is a tuneable production method for green adsorbent materials⁵⁶.

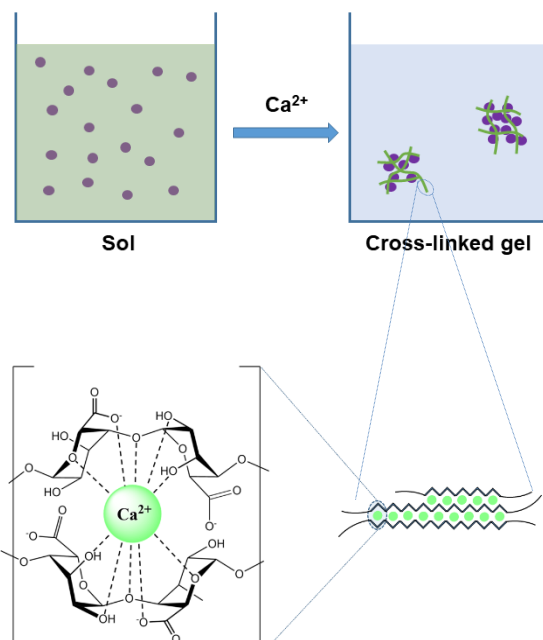


Figure 2-9 Ionotropic gelation of an alginate hydrogel composite (top) and the egg-box model of the gelation cross-linking process (below)

Cryo and supercritical methods appear to produce the most extensive pore structures. Gels are variously classed by the prefixes “aero-“, “hydro-“, “cryo-“ and “xero-“ depending on the method of drying. However, definitions of these sub-classes are not standardised in literature¹⁹⁴, thus the term “gel” or “hydrogel” will be used henceforth to describe generalised gels and gels prepared in aqueous solution respectively. Biopolymer hydrogel monoliths have been successfully used for removal of strontium^{195,196}, cesium^{197,198} and both at once^{184,199}. The advantage of a composite gel is the ability to combine distinct phases, such as nano-particle phases, each tailored to a specific radionuclide, into one universal, monolithic adsorbent. A further advantage is stability. While alginate-only hydrogels show excellent removal rates for strontium in laboratory settings²⁰⁰, their poor mechanical strength and stability tend preclude their use in real world settings. Wu et al. 2020 indicate that incorporation of biochar into an alginate hydrogel improves mechanical stability of the monolith adsorbent⁷⁷. Inorganic phases, such as hexacyanoferrates can also be immobilised in hydrogels. This appears to improve uptake capacity via dispersion of the ion-exchange media²⁰¹. Alginate hydrogels also exhibit good macro porosity (Figure 2-9), allowing rapid movement of contaminated water through the pore network.

2.3 The binding mechanism of strontium to adsorbents

Strontium, as a relatively charge-dense group (II) divalent cation, with electronic structure [Kr] 5s², tends to remain strongly hydrated in aqueous systems at low

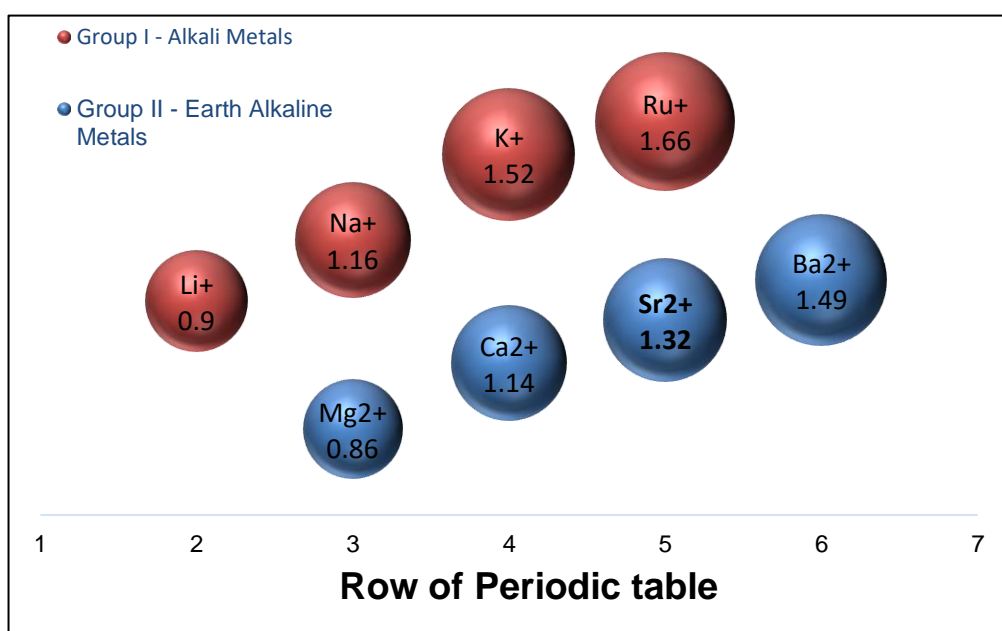


Figure 2-10 SEM image on a cross-sectioned alginate hydrogel monolith bead

Figure 2-11 Selected ionic radii values of group I and II metals for visual comparison. Adapted from Shannon 1975

and circumneutral pH making it particularly difficult to remediate from aqueous systems as it is highly soluble and thus mobile. It does not possess directional valence electron orbitals unlike transition metals, and so rationally designed adsorbents cannot take advantage of specific coordination geometry to aid binding selectivity. Strontium is typically not thought to complex strongly with any oxides or clays²⁰², as a consequence of its filled valence shell. The only discriminating features of such ions are their ionic radii, and to some extent charge density. Strontium has a similar ionic radius to several abundant and bio essential group I and II metals²⁰³, with calcium and sodium being the most similar (Figure 2-10). Thus, selectivity is a major issue⁴⁴.

2.3.1 Binding in Biochar

The binding modes of strontium to biopolymers such as biochar have been somewhat neglected on a mechanistic basis, due to the difficulties of analysis of such an amorphous and highly porous material, for which surface sensitive techniques such as XPS or FT-IR cannot necessarily reveal the bulk picture. Many studies rely on modelling methods or non-empirical approaches to deriving information about the mechanism. While these can provide useful indications, such techniques provide limited molecular scale insight into binding mechanism and modes. Pourret and Houben 2018 examined the relative contributions of distinct binding sites of biochar for strontium uptake under varying environmentally relevant conditions²⁰⁴. Their findings show that, in accord with previous studies on humic acids, the nature and strength of binding sites that are occupied vary with ionic strength and pH, in addition to overall uptake capacity. Strength of metal binding to biochar increases with increasing ionic strength and pH, and that carboxy-phenolic and phenolic groups provide the major binding contribution. This is confirmed by related works^{152,205}. Rae et al. examined the uptake of Sr to crab carapace and spent distillery grain²⁰⁶ biochar ($Q_m = 4 \text{ mg g}^{-1}$), determining the mechanism to be a mixture of ion-exchange, inner sphere and outer sphere complexation. This conclusion was reliant on the Dubinin–Radushkevich isotherm E parameter, said to confer information about the nature of binding. Their E value of 1.06 kJ mol^{-1} is on the low end of the physisorption range. Guo et al. 2022 describe a proton exchange mechanism with carboxylates and hydroxyl groups for the uptake of strontium to a biochar²⁰⁷. Similarly, Shawabkeh et al. attribute strontium uptake ($Q_m = 180 \text{ mg g}^{-1}$) to an activated pecan shell biochar to ion-exchange¹⁵³. Yakout et al.²⁰⁸ examine strontium uptake to a rice husk biochar ($Q_m = 198 \text{ mg g}^{-1}$), providing a theoretical basis for their claim that the binding mechanism of strontium to straw

biochar is “probably” ion-exchange. Shin et al. 2021²⁰⁹ examine strontium uptake to spent coffee ground biochar, suggesting a chemisorption type complexation from thermodynamic parameters and kinetic data. Sumalatha et al. 2022 also concluded a chemisorption type binding ($Q_m = 133 \text{ mg g}^{-1}$) from thermodynamic and kinetic data for strontium to a KOH-activated peanut shell biochar²¹⁰. Despite somewhat conflicting data on the binding of strontium to biochar, it is clear that biochar has potential for efficient immobilisation of strontium.

2.3.2 Alginate and alginate-biochar composites

Gok et al. 2013 studied the uptake of strontium to alginate beads¹⁰⁰ finding that the Langmuir model was most consistent with their data, with indication of monolayer sorption to homogenous surface sites. The Dubinin–Radushkevich isotherm model E value indicated physisorption and weak ionic interaction of strontium to the alginate. Overall uptake was reasonable, at around 50 mg g^{-1} . The authors speculate as to the exact nature of the binding mechanism without reaching firm conclusions, noting the complex nature of alginate gelation likely leads to a mixture of several binding mechanisms or modes. A rice husk biochar-alginate hydrogel was created by Jang et al. 2018 ($Q_m = 176 \text{ mg g}^{-1}$), showing good selectivity for strontium and good performance at low pH²¹¹. Models indicated low desorption rates, suggesting a strong and irreversible interaction with strontium. Similar work also indicated good selectivity of alginate hydrogels for strontium²¹². Zhang et al. 2020 examined the binding of strontium in alginate hydrogel fibres using circular dichroism. They concluded not only that binding was analogous to the egg-box model (Figure 2-8) but that strontium crosslinking was stronger than calcium crosslinking, based upon mechanical strength²¹³. A possible explanation for the enhanced crosslinking strength is the increased charge density of strontium over calcium. Such composites could prove useful in removal of strontium from high ionic strength and slightly acidic seawater, a medium for which separation is challenging²¹⁴.

2.3.3 Strontium EXAFS literature

The same features that make strontium challenging to remediate (Section 2.3) complicate its study via EXAFS experiments²¹⁵. Strontium XAS spectra possess fewer features than many other elements. Since it does not possess multiple oxidation states, edge and near-edge studies yield little useful data, although these can be appraised in qualitative sense to identify differences or similarities in the binding environment of strontium²¹⁶. Strongly oxyphilic, strontium shows a strong preference for oxygen binding. EXAFS data and computational modelling methods always yield a 1st shell of oxygen with a high coordination number between 8 - 12^{37,217}. Crystallographic diffraction studies confirm this, yielding values for formaldehyde of $N = 8$ ²¹⁸, carbonate of $N = 9$ ²¹⁹ and oxalate of $N = 9$ ²²⁰. EXAFS R-space spectra show a large and broad peak around 2 Å (Figure 2-11). Accounting for phase shift, this typically yields first shell Sr-O distances between 2.5 – 2.8 Å. The broadness of the first shell backscattering peak is attributed to a relatively large degree of static and substitutional disorder, which is observed even in solid state complexes²²¹. Since strontium tends to remain hydrated, the first shell peak can contain contributions from both solid state oxygen functional groups and water molecules forming a full or partial sphere of hydration, with water molecules yielding slightly longer Sr-O distances^{37,222}. The lack of directional valence orbitals and well-defined bonding

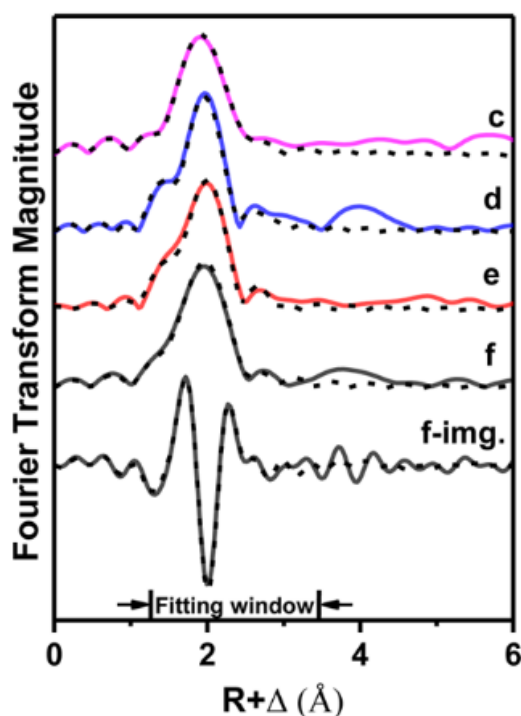


Figure 2-12 A typical set Sr EXAFS spectra of Sr adsorbed on Goethite, dominated by first shell oxygen backscattering signal. Adapted from Nie et al. 2017

geometries contribute to anharmonicity in bond vibration. Variable coordination also increases disorder in the system. These factors, coupled with the fact that strontium is thought to form outer sphere hydrated complexes at circumneutral pH make it challenging to derive structural data via EXAFS.

2.3.3.1 System pH

Much of the Sr EXAFS data in the literature concerns strontium in or adsorbed to inorganic materials with a portion focusing on hyper-alkaline conditions^{223,224}. Such high pH systems are highly relevant to nuclear waste processing due to the effect of young cement water and since wastewaters containing activation products are often stored as high pH. EXAFS of high pH systems typically yield more structural information, since inner sphere complexation of strontium is all but guaranteed in hyperalkaline conditions. Strontium binding at circumneutral pH is also examined in the literature to a range of materials, as this is a scenario relevant to accidental release. It has been suggested that strontium always forms hydrated outer sphere complexes at neutral pH²²⁵, for reasons outlined above. This is examined in more detail in subsequent sections.

2.3.3.2 Data interpretation: Inner vs outer sphere

EXAFS can provide unparalleled information about the binding environment(s) of a target element. This is particularly so in amorphous systems where crystallographic techniques such as XRD are not appropriate, and surface specific techniques such as XPS or FTIR cannot reveal the bulk picture. EXAFS can provide information about the number of atoms surrounding strontium, their average distances and their approximate atomic mass. Presence of a second shell backscattering signal is typically attributed as evidence of inner-sphere binding²²⁵, even if such second shell components are perhaps minor (e.g. N = 1 or 2 bidentate edge sharing)^{226,227}. Lack of a second shell signal is thus assigned as outer sphere complexation²²⁸. Yet Sahai et al. 2000 caution against the assumption that lack of signal is evidence of an outer sphere or “hydrated electrostatic complex”, calling this an “overinterpretation”³⁷ of the EXAFS. This is again due to the difficulty in obtaining data in strontium EXAFS on the backscattering shell beyond the 1st shell. The EXAFS signal beyond the first shell of most large and strongly hydrated cations is often weak, often too weak to perform a meaningful fit. Sahai et al. point out that in aqueous samples at RT, no evidence of the second shell of hydration is observed, which undeniably must be present. This is thought to be due to static and substitutional disorder around the cation, anharmonicity in bond vibration and bond length distributions for a given shell, varying coordination numbers and often long interatomic

distances²¹⁵. Multi-electron excitation (MEE) are also sometimes observed which affect the magnitude of observed backscattering particularly at higher wavenumber²²⁹. Other studies indicate that the second hydration shell of strontium in aqueous solution lies at around 4.7 - 4.95 Å²³⁰. These factors can make it difficult to obtain precise information about the nature of strontium complexation via EXAFS.

2.3.3.3 Binding to inorganic adsorbents

Weak binding is typically observed in clay based adsorbents such as zeolites, with studies showing strontium adsorbed to the clay-mineral interface in outer sphere, partially hydrated complexes^{37,215,216,231,232}. This consistent with established wisdom, that metals such as strontium are generally taken up via cation exchange^{221,233}. Carroll et al. 2008 used EXAFS and modelling to conclude an outer sphere binding of strontium to silica and goethite over pH range 6 - 10²³⁴. Collins et al. 1998 examined strontium uptake to iron-bearing minerals such as goethite²²⁴, finding no second shell at pH 9.2 but a N = 1.8 Fe second shell signal at pH 10.2. They assign this signal to a binding through two adjacent Fe-OH surface moieties. Nie et al. 2017 found no second shell signal of Sr adsorbed to goethite at pH 6, although at pH 10.5 data showed N = 8 first shell oxygen and curiously a second O shell N = 1.2 at around 3.3 Å²³⁵. Axe et al. 1998²³⁶ examined uptake to a hydrous ferric oxide, and found Strontium complexed with large number of oxygen/waters at varying distance in the first shell. Bond lengths followed a non-gaussian distribution, so a cumulant expansion was used to fit the data²³⁷. The authors included a second shell iron signal in their fit however, uncertainties in the coordination numbers were higher than stated values themselves. Bonding was characterised as weak, surface physisorption. Fuller et al. 2016 examined uptake to goethite, illite and chlorite²²⁵ surfaces, finding no second shell contribution at pH 6.6, and stating that at circumneutral pH strontium exists only as an hydrated, and therefore outer sphere complexing cation. Evidence of second shell iron was only found at hyper-alkaline conditions, due to surface adsorption of SrOH⁺ formed at high pH. A 2012 study by Wallace et al. examined strontium binding to sediments from around the Sellafield reprocessing site, UK, finding a weakly bound state to soil sediments that was largely controlled by ionic strength of groundwater²³⁸. A 2003 study of strontium uptake to clinoptilolite suggests it is preferentially taken up in outer sphere, hydrated form to Ca²⁺ channel positions within the crystal structure, as opposed to K or Na sites, which are slightly too large for strontium²³³. Uptake was found to be governed by ionic strength and pH. Parkman et al. studied uptake to kaolinite, determining that strontium was

bound to partially hydrated octahedral sites on the kaolinite surface²¹⁶. The fate of strontium has also been studied in sediments. Thorpe et al. 2012 showed that bio reduction of nitrates caused a pH rise, which was in turn responsible for reducing the solubility of strontium. Only outer sphere complexation was observed below pH 9, with only 1st shell oxygen signals observed in the EXAFS²³⁹. Cleary et al. 2019 showed that aqueous strontium in waste waters could be somewhat immobilised by a bio mineralization of glycerol phosphate²⁴⁰. Their EXAFS showed a second shell coordination of 0.8 phosphorus consistent with ~25 % of aqueous strontium being incorporated into insoluble hydroxyapatite, which has a second shell coordination number of 3 for P. Bots et al. 2021 developed a bidentate edge sharing model for strontium with anatase and illite-smectite in clayey soils²⁴¹. Typically, strontium uptake is found to be governed by pH, with little evidence found of inner sphere complexation at circumneutral pH. With the ion-exchanger clinoptilolite, Strontium seems to interchange with Ca²⁺ sites (N = 8). EXAFS showed only small difference in signal between free hydrated Sr and adsorbed Sr, leading Bots et al. to conclude that sorption occurred via loss of some water but as “outer sphere”²⁴².

2.3.3.4 Binding to organic adsorbents

EXAFS has been used to examine strontium bound to calcium oxalate (Figure 2-12)²²⁹. Calcium oxalate (CaOx) is produced by a wide range of plants and presents as an attractive system for strontium uptake due to the electronic and dimensional similarities of calcium and strontium. These data showed strong second shell carbon signals in the Sr-CaOx complex at pH 4, 6 and 10, indicating that strontium uptake is not affected across this pH range. The 2nd shell Sr-C distance was also stable at 3.4 Å, which is intermediate in length between the shortest 2nd shell Sr-C reported distances (~3.0-3.1 Å), typical of bidentate binding mode^{37,239}, and mono dentate Sr-C (~3.5-3.8 Å) as seen in Sr-formate^{218–220}. Crystallographic data show that bidentate binding e.g. with carboxyl groups give a Sr-C distance 0.2-0.4 Å shorter than mono dentate binding e.g. hydroxyls, lactones, ethers etc. The authors attribute a failure to

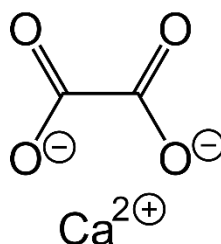


Figure 2-13 The calcium oxalate monomer

find a Sr-Ca signal as evidence the Sr is not bound in an inner sphere environment; instead, it is believed the data more closely resembles a SrOx.nH₂O environment with outer sphere type binding. However, they do put forward an explanation of their second shell carbon N = 6 result. It seems plausible, given the strontium-specific issues with disorder and signal decay outlined above, that the Sr-Ca distance is too large to register as a backscattering signal – perhaps just the over interpretation of results that Sahai et al. cautioned against. Another study by Dietz and Jensen 2003 neatly characterised strontium binding from a nitric acid solution to a crown ether complex dispersed on a solid polymer support²⁴³. Complexation with the crown ether and two axial nitrate ions above and below the plane of the crown ether in a bidentate arrangement best described the EXAFS spectra²⁴³.

2.3.3.5 Binding to cements and other industrial materials

Bower et al. 2016 used microfocus X-ray fluorescence mapping as well as EXAFS to characterise the distribution and binding environment of strontium in nuclear fuel pond contexts, finding that strontium was bound to TiO₂ paint layers. Further EXAFS experiments by Wieland et al. 2008 on concrete samples showed that strontium remained partially hydrated at pH 12.5 at the cement surface, consistent with previous reports²⁴⁴, and in contrast to cesium which was associated with clay aggregates within the cement. Wallace et al. 2019 examined strontium interaction with sediment in hyperalkaline cement leachate relevant to waste storage ponds²²³. After simulating pond conditions for 365 days, it was found that time, temperature and pH had an effect of strontium binding and incorporation into aluminosilicates.

2.3.3.6 Measurement Temperature

Thermal disorder can be somewhat offset by cryo-cooling of the sample stage during scan acquisition. Sahai et al. 2000 discusses changes to bond length associated with temp²⁴⁵. A number of studies choose a range of lowered temperatures in which to conduct EXAFS measurements, the most common of which being 77 K, using liquid nitrogen cryocoolant. While this does not reduce static disorder, known to be a prominent feature of hydrated ions, it will reduce the thermal disorder component of the Debye-Waller factor³⁷. Although the gains in signal to noise are modest in comparison to room temperature measurement, these gains can still greatly aid spectral deconvolution and interpretation particularly for second and third shell backscattering, where the signal is known to be weak and also is precisely where the most interesting

spectral features are to be found. Therefore, even with modest gains, cryo-cooling of samples during the measurement of EXAFS is worthwhile.

2.3.4 Knowledge gaps

1. Knowledge of the binding mechanism of strontium to biopolymers such as biochar and alginate, as well as their composites is incomplete, in part due to their amorphous nature. Very few EXAFS studies have attempted to examine the binding of radionuclides to biochar, alginate or other biopolymers. These studies are limited to uranium^{97,246,247} and europium⁹³ and to our knowledge none have examined strontium uptake, save for studies by this author.
2. Activation is widely employed to biochar and is known to enhance overall uptake capacity of strontium to biochar. Yet little is known about how the binding environment may be altered in activated biochar, compared with control biochars. Coordination number and crucially, degree of inner sphere binding may be altered through activation, and this should be investigated.
3. Alginate is increasingly deployed as a gelation agent, in addition to its metal complexing ability, to immobilise particulate ion-exchange and/or adsorbent materials. A good deal of work examines the structure of the alginate gel around metals, specifically the egg-box model. Yet to our knowledge none have used EXAFS to examine strontium binding environment in alginate, save for studies by this author.
4. Manganese oxides show tantalising potential as strontium immobilisation materials. Little work has been conducted on the binding mechanism in biochar-MnOx composites .

2.4 The physical and morphological features of biopolymers

“Independent of the application, it is of interest to clearly identify how pores of different sizes are interconnected and how the overall architecture of the porous medium can be broken down into the local pore structure.”

- Vorhauer-Huget et al. 2020, “Computational Optimization of Porous Structures for Electrochemical Processes”²⁴⁸

Porous materials play important roles across a range of domains, both in natural systems and engineered systems for a wide variety of applications. This is certainly true in immobilisation of radionuclides, where porosity is a key feature of virtually every material studied⁵¹. Figure 2-14 highlights the emergent and expanding nature of understanding that the pore space architecture spans several orders of magnitude, from nm to mm scales. This understanding is captured in the term **hierarchical porosity** (or multiscale porosity), and through which, new research attempts to link pore space architecture to performance efficacy. In other words, the **structure-function relationship**. Figure 2-13 represents this concept as it applies to porous biopolymers.

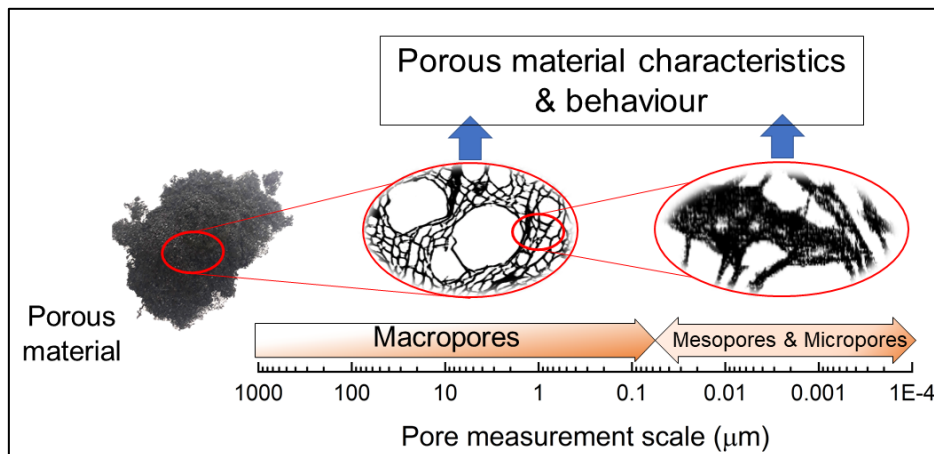


Figure 2-14 Schematic representation of hierarchical porosity - how pores of all sizes contribute to overall performance of a porous material

The vast majority of research in porous materials the past several decades has focussed on understanding how the smallest pores, the meso and micro pores (> 50 nm) affect performance, and this is especially the case in adsorption sciences. This is due to the fact that the presence of smallest pores are often correlated with adsorption capacity. Micro pores are thought to provide binding pockets and/or increase surface area which in turn increases surface group abundance. Pores which are of the same scale as a contaminant of interest (e.g. CO₂ or mustard gas) can play a key role in the uptake and retention of said

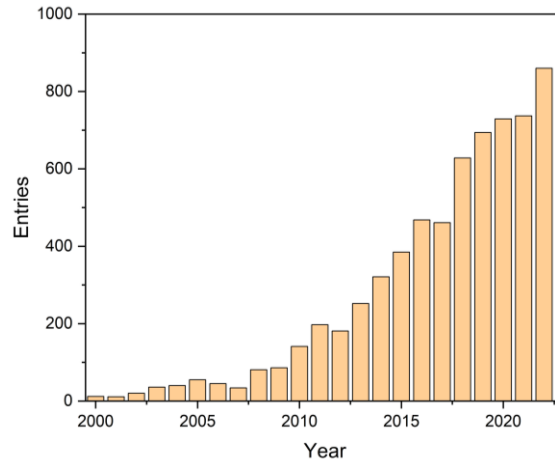


Figure 2-15 Number of entries returned for the term "hierarchical porosity" using the Scopus search tool (www.scopus.com) 2000 - 2022 (accessed 28/11/2022)

contaminants to porous media. Yet far less attention has been paid to larger pores, the interplay between smaller and larger pores, and their role in the bulk behaviour of porous materials. This represents a significant knowledge gap in porous materials.

2.4.1 Pore structure

Pores are voids or spaces within a (usually) solid-state material, which can facilitate the transport of gaseous or liquid state matter either in, through or out of the pore structure. Figure 2-15 depicts a representation of some common pore features. It can also be expressed mathematically as:

$$\phi = \frac{V_T - V_S}{V_T} \quad (1)$$

Where Φ denotes porosity or fraction of pore volume, V_T is the total or bulk volume of the material and V_S is the volume of the solid-state portion of the material.

2.4.1.1 Pore size definition and classification

The IUPAC²⁴⁹ convention on pore size classification denotes pore size ranges as the following²⁵⁰:

Table 2-2 IUPAC pore size classifications

Name	Pore diameter
Micro pore	< 2 nm
Meso pore	2 - 50 nm
Macro pore	> 50 nm

It is noted that several alternative (and often more complicated) classification systems have been proposed recently^{251,252}. This reflects the emergent nature of pore space studies, with need for more detailed classification to distinguish different pore sizes. Although there are some benefits to an updated classification system, herein the IUPAC definitions are used throughout, because such terminology is still most widely used.

2.4.1.2 Macro pores

Macro pores are defined by IUPAC as pores larger than 50 nm in diameter, and encompass pores throughout the micrometre range (10^{-3} - 10^{-6} m). As well as playing a crucial role in the kinetics of flow through an engineered pressure gradient, such as in the case of aqueous contaminant pumped through a column filtration system, such pores are also subject to capillary flow and capillary effects²⁵³ which is relevant for soil and permeable reactive barrier type scenarios. Pores of this diameter range in carbonaceous materials are known to retain water in soils²⁵⁴, which in turn improves the retention of nutrients in soil.

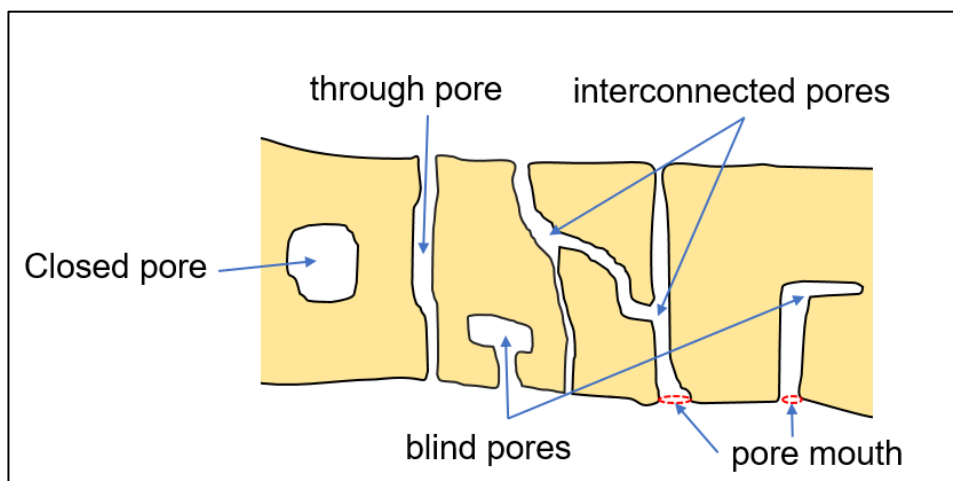


Figure 2-16 Schematic representation of pores and pore features

The role of macro pores in adsorption is also increasingly recognised as “transport pores”²⁵⁵, acting as conduits and moving target molecules or ions through a porous framework to the active adsorption sites, located within smaller micro pores. As such they can affect the kinetics of diffusion through the pore network²⁴⁸. This is recognised across a range of different materials for adsorptive removal or immobilisation applications, including MOFs^{256,257}, zeolites^{258,259} and carbon based adsorbents^{12,150,260–266}. When used as a soil amendment, biochar macro pores are also thought to provide habitat for microbiota such as bacteria, fungi and protozoa²⁶⁷ which can alter soil micro biodiversity and nutrient availability²⁶⁸.

2.4.1.3 Meso pores

Intermediate between macro and micro pores, the meso pores (2 – 50 nm) quite literally connect the two pore sizes. Their roles and functions in the overall pore structure accordingly straddle both groups, said to contribute to surface area (typically associated with micro pores) and also acting as diffusion conduits²⁶⁹ or niches for microbial support²⁷⁰ (associated with macro pores). Meso porous materials such as silica, alumina and carbons among others are highly prized for energy storage^{271–273} and catalysis^{274,275}. High meso porosity is also said to correlate with high contaminant adsorption efficiencies^{276–278}, particularly for higher molecular weight contaminants¹¹⁶. Meso pores have also been found to be suitable in carbons to stabilise redox active nano zero valent metals such as nZVI²⁷⁹.

2.4.1.4 Micro pores

Micro pore volume (most often determined via BET gas adsorption analysis, Section 2.4.4.1) typically correlates well with adsorptive contaminant uptake capacity for a porous material, and is usually second only in importance to surface functionality in this regard. Maximising the micro pore volume and surface area is one of the most commonly employed strategies for optimisation of a porous material’s contaminant uptake capacity. This is usually achieved via activation protocols such as acid treatment (Section 2.2.3.3). Micro pores, since they are on a molecular-relevant sizing, are thought to act as binding pockets for contaminants, ions or organic small molecules²⁸⁰.

2.4.1.5 Other useful pore metrics

Tortuosity is widely referred to in discussions of porous media, as well as the closely related permeability. Confusingly, there are numerous ways to define tortuosity depending on the porous media and research focus in question. For

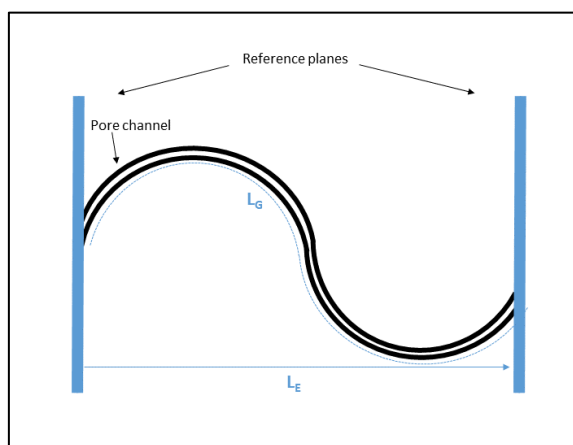


Figure 2-17 Schematic representation of a pore running between two parallel planes. This also visually represents the definition of a definition of tortuosity defined in equation 2

example, geometric, hydraulic, electrical and diffusional tortuosity all have distinct meanings²⁸¹. In general terms, tortuosity describes the interconnectivity and twisted character of a pore path. A more tortuous pore structure will have a longer and more twisted path in general. A simple mathematical definition (equation 2) of the tortuosity of a pore is the ratio of the length of its path (L_G) to the Euclidian distance (L_E), or the shortest possible distance, between the pore mouths, as is represented in Figure 2-16. Standardised methods to empirically and experimentally test, quantify and compare this property do not exist. Instead, there has been a heavy reliance on modelling methods to depict and analyse pore space tortuosity (τ).

$$\tau = \frac{L_G}{L_E} \quad (2)$$

Modelling the tortuosity requires significant simplification of the pore space, such as selecting a representative pore size and ignoring the pore size distribution²⁸² or employing the pore diffusion model (PDM) coupled with the Freundlich isotherm²⁸³. The related parameter, permeability (k) depends directly on tortuosity according to the Kozeny-Carman model, which is used to estimate of tortuosity and permeability in rocks²⁸⁴. It is clear from qualitative examination that certain biochars exhibit orientation-dependent tortuosity (Figure 2-18). Further, at the macro pore scale (> 50 nm), biochar pores can vary greatly in thickness. Earlier tortuosity estimation algorithms such as the build-in Skeletonisation tool in ImageJ²⁸⁵ do not take thickness variation (i.e. pore diameter) into account and does not as accurately reflect the distribution of possible paths through larger pore systems.

2.4.1.6 Hierarchical porosity

The term hierarchical porosity has been in use for several decades and Schwieger et al. attempted to define and classify hierarchical zeolite porosity in 2016 (Figure 2-17)²⁸⁶. The importance of hierarchical porosity is highlighted by Kerstens et al. 2020, who describe two key issues that highly microporous zeolites suffer - diffusional limitations as well as micro pore blocking²⁸⁷. The solution to which is a hierarchical pore structure via the introduction of larger pores to both deliver target molecules to micro pore active sites more efficiently and minimise unwanted pore blocking²⁸⁸. The recent nature of this work highlights that this is very much an active area of research, and underscores that performance enhancement of porous materials through improved optimisation in both diffusional kinetics and pore blocking, or lack thereof, can be significant. The arc of understanding of zeolite pore space is much more advanced than in porous carbon materials, especially biopolymer-derived porous materials, despite the fact that it is clear that porous biopolymers such as biochar possess extensive hierarchical porosity. The reasons for this are explained in domains such as adsorption, catalysis or energy storage, it surely must be possible – even vital – that full understanding and control of hierarchical pore space is gained, in order to tune and optimise them.

2.4.1.7 Amorphous pore space

The bulk of research focus on porous materials has, in several previous decades, striven for highly ordered, crystalline porous materials and this is often seen as the benchmark or as advantageous in a pore structure; this type of structure is also easier to conceptualise than disordered pores. Myriad examples of these highly ordered crystalline structures in zeolites or metal organic frameworks (MOFs) exist. This paradigm is undergoing something of a rethink in more recent years by some sections of porous materials research, with a deeper understanding that disorder and defects in a porous structure can in fact be advantageous²⁸⁹ for some applications. Such disorder can in fact prove crucial in controlling the catalytic properties of porous materials²⁹⁰, improving superconducting properties²⁹¹ or affecting the diffusion of a phase through a pore network. Such work has opened up an area of research dedicated to introducing disorder into ordered porous systems, to design, engineer or tune disorder into porous systems^{292–294}. Biochar and other porous

biopolymers as amorphous materials could prove to be of great potential for such systems.

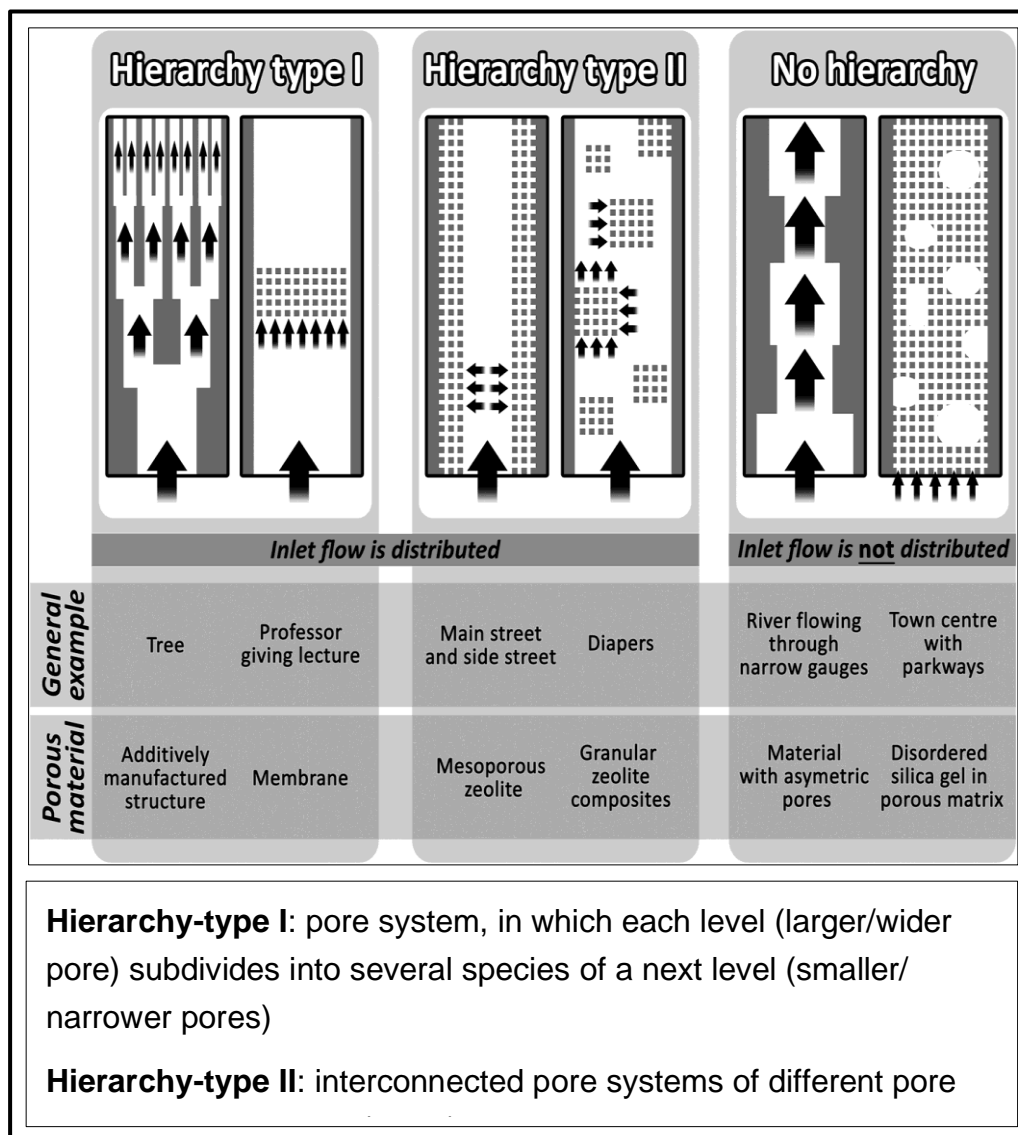


Figure 2-18 Schematic representation of the proposed hierarchical pore space classification system, with proposed definitions below. Adapted from Schwieger et al. 2016

2.4.2 Porosity in biopolymers

“the wide range of biochar pore sizes complicates biochar porosity characterization, making it challenging to find methods appropriate to connect the fundamental physical properties of density and porosity to environmental outcomes.”

- Brewer et al. 2014 “New approaches to measuring biochar density and porosity”²⁹⁵

While hierarchical porosity may be an advantageous property in a material, it can prove challenging to study. As Brewer et al. 2014 point out, biochar pores span some five orders of magnitude and are shaped in every possible manner, from nano-sized slits in between graphitic-like sheets through to preserved plant vesicles on the micrometre scale²⁹⁵. This can make it impossible to evaluate the whole pore space range using the commonly employed pore space measurement techniques. See Section 2.4.4 and for an overview of pore space measurement techniques including limitations and strengths.

2.4.2.1 Porosity in biochar

Biochar’s porous structure comes in to play in energy storage²⁷³, soil fertility, electrochemical (electrode, capacitance)^{150,261,262} and catalysis^{296,297}, in “slow releasing” materials as well as in templating¹¹⁶. Qiu et al .2018²⁹⁸ used a combination of microscopy and BET gas adsorption analysis to conclude that their hierarchical KOH activated biochar-based carbon super capacitor material possessed increased surface area and faster diffusional kinetics, resulting in higher specific capacitance and rate performance due to the contribution of macro pores. Feng et al. 2016, reached similar conclusions with a KOH activated bagasse waste-derived biochar superconductor. Stating that macro

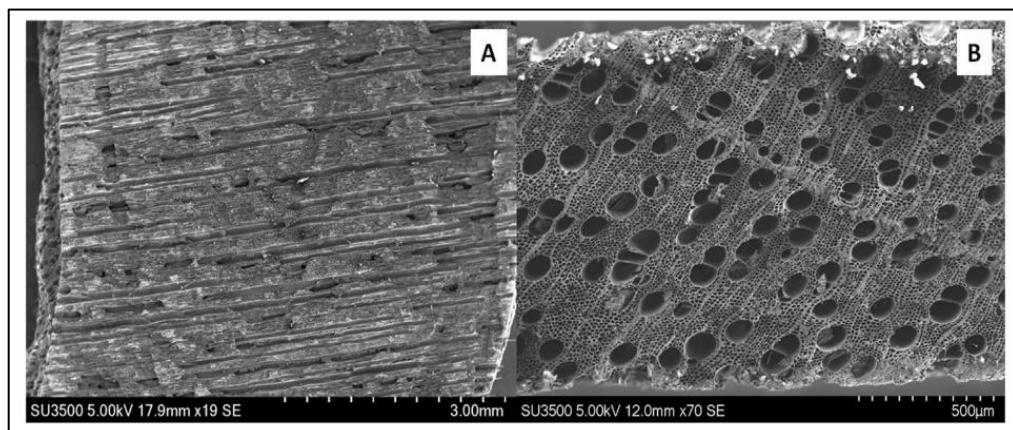


Figure 2-19 Caguiat et al. 2018 tested the capacitance of wood-based biochar in different orientation, finding significant differences in performance

pores served as “ion-buffering reservoirs” within the interior pore space, facilitating rapid transport of electrolytes through the pore network²⁹⁹. Caguiat et al. 2018 found that the macro pore structure plays a significant role in performance of monolithic biochar electrodes³⁰⁰. They tested the capacitance of thin sections of wood derived biochar in two orientations: with grain (WG) and against grain (AG), finding significant differences in performance with the altered geometry Figure 2-18. This is thought to be due to the differences in electrolyte access to the materials pore network, and show that not only does the macro pore structure play a key role, but the orientation of an anisotropic material is significant too. In adsorption, macro pores are thought to be crucial for mass transfer kinetics^{121,301} as well as fouling resistance³⁰² and desorption behaviour³⁰³. Hou et al. 2023³⁰⁴ note that commercially available activated carbons are predominantly micro porous, leaving a need for porous carbons with hierarchical pore structures for adsorptive applications. Comparing porosity in other adsorbent classes, it is observed that micro porous zeolites also suffer from diffusion related performance limitations due to fouling of narrow pores²⁸⁷. Fouling is an especially important consideration in treatment of contaminated groundwater rich in dissolved organic and inorganic matter. Synthetic hierarchical porous materials typically require templating methods and/or chemical/physical activation in order to avoid such issues. This can be time-consuming and costly. Biochar is known to be inherently macro porous and as such is well suited to avoid such fouling issues, without templating steps or activation necessarily³⁰⁵. Biochar is also widely used as a soil additive and macro pores are known to play a key role in water retention function³⁰⁶. However as Edeh et al. 2021 point out, conflicting results exist on water retention performance^{307–310}, suggesting an incomplete understanding and that other factors are at play which affect soil water retention. This could relate to distinct biochar feedstocks having different macro pore size ranges, interconnectivity or tortuosity characteristics. Lee et al. 2022 examined the use of biochar as a microbial and agricultural inoculant (used to improve soil microorganism diversity), also concluding that macro pores played a key role in the use of biochar as a soil aid²⁷⁰, while Bello et al. 2020 concluded similar³¹¹.

Capillary flow modelling

Related to mass transfer through a pore network, modelling of capillary flow is of increasing interest in porous materials³¹². Capillary flow is the spontaneous movement of a fluid through a small channel without application of external force³¹³. Modelling capillary flow through macro porous media is often based on the Lucas–Washburn (LW) equation and its various modifications³¹⁴. Modelling tends to rely on a number of theoretical assumptions or simplification depending on the choice of model parameter employed. Simplifications to pore space

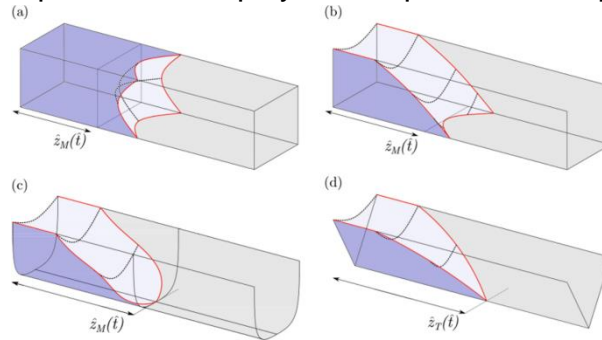


Figure 2-20 A schematic representation of various models of capillary flow in (a) closed rectangular, (b) open rectangular, (c) open U-shaped, and (d) open V-shaped microchannels. Adapted from Kolliopoulos et al. 2021

isotropy (homogeneity)³¹⁵, pore space radii³¹⁴, pore shape³¹⁴, and pore surface roughness³¹³, among others are employed, as can be seen in Figure 2-19. These simplifications are necessary to build a working model but inevitably lead to loss of accuracy with respect to the real-world flow conditions that are the focus of study. This is especially pertinent to biopolymers and biochars, which can be highly amorphous or heterogeneous, and which varies depending on feedstock and preparation protocol (pyrolysis treatment temperature and activation protocol). The result of which is that biochars and associated composites are especially difficult to accurately model.

2.4.3 Pore space tunability via activation

In a step beyond simply exploiting the native pore structure of biochar, tunability of the pore structure is desirable for adsorptive applications³¹⁶. While materials such as MOFs are often sold as a class of materials whose pore structure is readily tuneable²⁵⁷, activated carbons and zeolites have traditionally been thought of as only minimally tuneable, with a set of defined pore features⁵¹. That paradigm, for biomass-derived activated carbons, has been recently successfully challenged by a newer generation of researchers utilising a wide range of activation protocols to explore the effect on such treatments on the pore structure^{114,317,318}. As knowledge of the pyrolysis process and other related

facets of the biochar production process increases, it has become clear that biochar and its derivatives are vastly tuneable. Simple alteration of the pyrolysis process, e.g. change of pyrolysis temperature, treatment time or pre-drying step all have an effect on the resulting pore structure. This is a rudimentary form of pore tuning. Activation treatments are known to further alter the pore space widely. The following three case studies (boxed) display recent examples from literature of the significance of tunability control of the pore space of carbonaceous materials, and its effect on performance.

Case Study 2.1 Novel and wet-resilient cellulose nanofiber cryogels with tuneable porosity and improved mechanical strength for methyl orange dyes removal³¹⁸

Zhang et al. 2021 created a tuneable macro porous cellulose cryogel adsorbent, using a aqueous NaIO₄ treatment to tune the size of macro pores as a function of NaIO₄ concentration and treatment time. Not only does this alter solution phase kinetics through the pore network, but it also enhanced the mechanical strength of the cryogel.

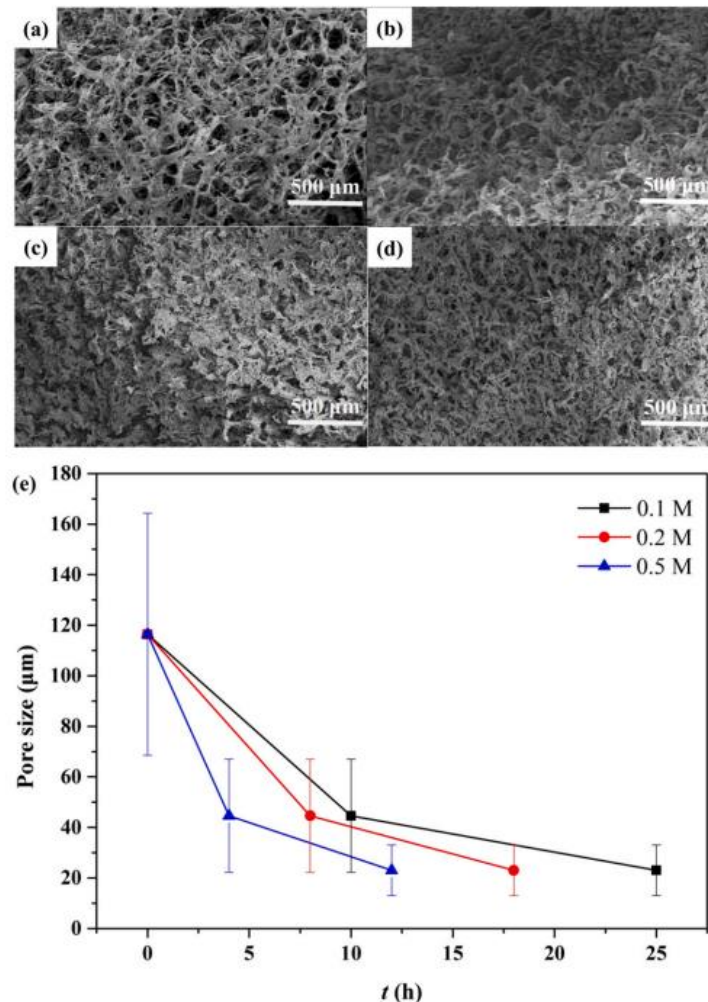


Fig. 3. SEM images of dried MFC-36 (a), MFC-25 (b), MFC-19 (c), and PEI-MFC (d) cryogels and (e) influence of soaking time in different NaIO₄ solution on the pore sizes of MFC cryogels.

In this work, macro pore size has been measured via SEM image analysis and thus is only an analysis of surface pore mouth diameter, not internal macro pore structure

Case Study 2-2 Honeycomb-like carbon with tuneable pore size from bio-oil for super capacitor³¹⁹

Wang et al 2020 used a bio-oil based material (side-product from pyrolysis of biomass) in conjunction with a macro-molecule, a “pore-adjusting material”, to create a multi-scale porous carbon material for enhanced supercapacitance for energy storage application.

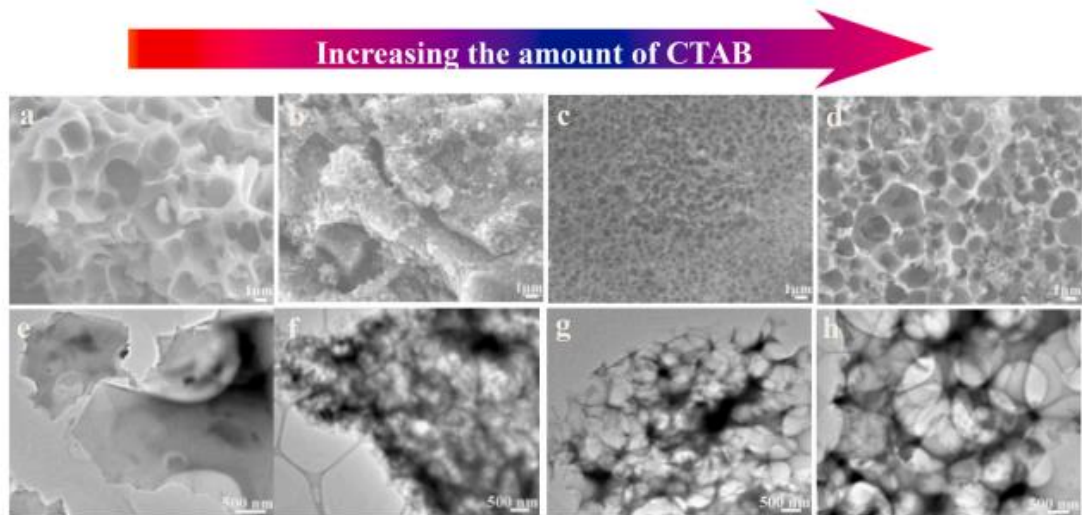


Fig. 1. SEM images and TEM images of B (a and e), B-1.6C-Ni (b and f), B-3.2C-Ni (c and g) and B-6.4C-Ni (d and h).

They highlight the important role of macro pores, stating that:

“3D interconnected macro porous frameworks serve as ion buffering reservoirs, micropores provide charge storage sites and mesopores as ion-highways to guarantee the rapid diffusion of ions. The unimpeded ion transport pathways are important for achieving high rate capability”

Analysis of macro pore (and to some extent, meso pore) architecture is through a combination of SEM pore mouth image analysis and inference from BET gas adsorption micro pore analysis.

Case Study 2-3 Floatable, macro porous structured alginate sphere supporting iron nanoparticles used for emergent Cr(VI) spill treatment³²⁰

Huang et al. 2016 used an alginate-nZVI composite cryogel for reductive adsorption of Cr(VI) from wastewater. The “cabbage-like” macro porous structure was driven by a diffusion effect of the cross-linking cation Fe^{3+} which forced the assembly of micro droplets of water within the composite. Once removed by freeze-drying, these became cavities and macro pore structure which not only facilitate effective transport of Cr(VI) contaminated water through the structure to active nZVI sites within the micro pores but also induce floatation of the cryogel monoliths, aiding effective separation from solution.

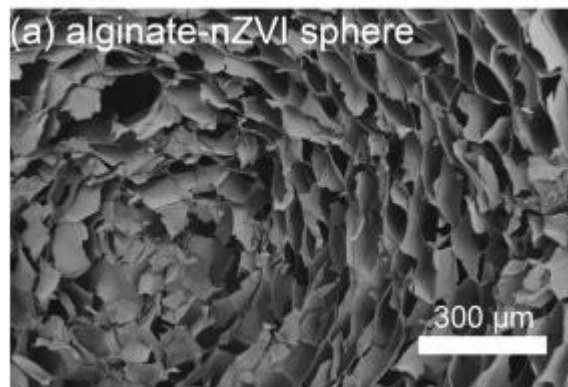


Figure 2-21 FESEM of a cross-sectioned alginate-nZVI composite monolith. Adapted from Huang et al. 2016

Analysis of the macro pore structure utilises SEM of a cross-sectioned monolith (cross-sectioning method not stated) and BET isotherm shape (type II isotherm) to infer porous structure.

2.4.4 Pore space measurement techniques

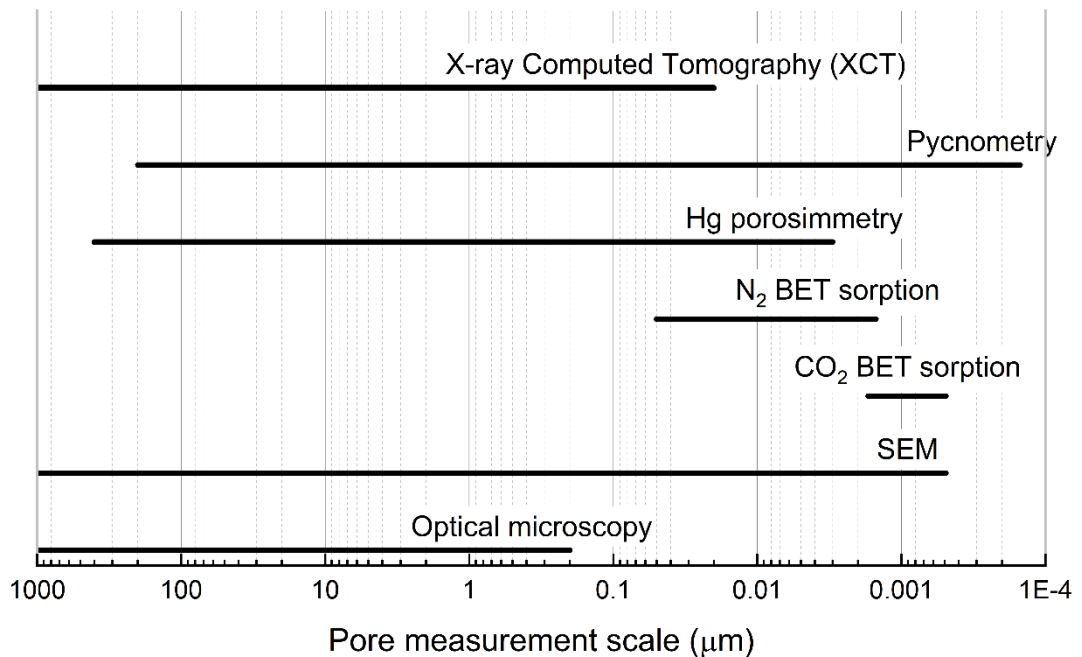


Figure 2.22 Scale of pore size ranges spanning five orders of magnitude, showing the working ranges of the most common pore space measurement techniques

The most common pore space analysis techniques and their working ranges are plotted across macro, meso and micro pore size ranges in . Optical techniques capable of surface only pore space analysis are displayed towards the lower region while techniques capable of analysis of internal pore spaces are displayed above. Few analysis techniques are capable of spanning across all pore space sizes. Those that do, possess various limitations which are summarised in subsequent sections below.

2.4.4.1 Brunauer-Emmett-Teller (BET) surface area analysis³²¹

This technique is an extension of the Langmuir model, which describes adsorption of a gas onto a surface and has been a hugely successful technique in measuring meso and micro pores of many types of porous solids. The technique makes the following empirical assumptions:

- Gas being adsorbed behaves as an ideal gas
- Only one monolayer formation
- All surface sites are of equal energy
- No interaction occurs between neighbouring adsorbate gas molecules
- Sample surface is homogeneous

- Adsorption of the adsorbate can occur in infinite layers
- Each layer can be treated equally

However, this technique cannot detect or measure pores larger than small meso pores¹⁹⁴ despite the fact that the majority of pore volume is said to be composed of macro pores (> 50 nm)²⁹⁵. There is also a reliance on effective and thorough degassing pre-treatment to remove any gases entrapped in the pore space whose presence would otherwise yield inaccurate results³²². This can be of particular concern for biochars, with extensive and disordered pore structure, as well as varying degrees of high MW waxy media within the pores can make effective degassing very difficult. A further difficulty specific to biochar is that N₂, the most often used gas, diffuses poorly and quite variably into the ultra-micro pores of such carbons³²³, yielding inconsistent results. Indeed Blankenship et al. 2022 recommend the modified technique of dual isotherm measurements using two distinct gases (e.g. N₂ and H₂), stating that an N₂ isotherm alone cannot fully and accurately determine pore sizes across the entire micro pore range³²³. This technique has been used to indirectly estimate macro pores³²⁴. However due to a limit of sensitivity up to 100 nm, this is likely to lead to erroneous estimations.

2.4.4.2 Mercury porosimetry

This technique measures pore size distribution, total pore volume (porosity), skeletal and apparent density and specific surface area over the size range 3.5 nm – 500 µm. The limitations of the technique are that it actually measures the largest entrance (pore mouth) towards a pore not the actual inner size of a pore (Figure 2-15). Closed pores (Figure 2-15) cannot be measured since mercury is unable to permeate such spaces. The sample is also destroyed during analysis. While this technique can provide useful and detailed pore space analysis^{325,326}, it is not commonly used in analysis, certainly not near the levels that BET gas adsorption analysis is used^{327,328}, in part due to the numerous limitations and assumptions²⁹⁵. A brittle, amorphous and powdery material such as biochar is also likely to prove among the most challenging of materials for such a technique, due to the significant pressures involved in measurement.

2.4.4.3 Gas pycnometry

Helium pycnometry has also been used to measure the associated property of biochar density³²². The technique is based upon the Boyle–Mariotte law, which relates volume to pressure and thus derives a value for the volume of a sample via gas displacement. Along with the known mass, the density of a sample can

be calculated. The technique is relatively trivial and rapid, but can only derive a bulk density value for a given sample and thus provides useful but limited information.

2.4.4.4 Other techniques

Small Angle X-ray Scattering (SAXS) is a relatively new technique that is capable of measuring minute density differences and thus minute pore structures in the range of 1-150 nm. Although it does not require crystalline samples, the disorder in the structure of biochar somewhat complicates analysis of such measurements. Optical techniques such as image analysis of SEM are also used to analyse surface pore structures but are unable to deduce information about any internal structure.

2.4.4.5 X-ray Computed Tomography (XCT)

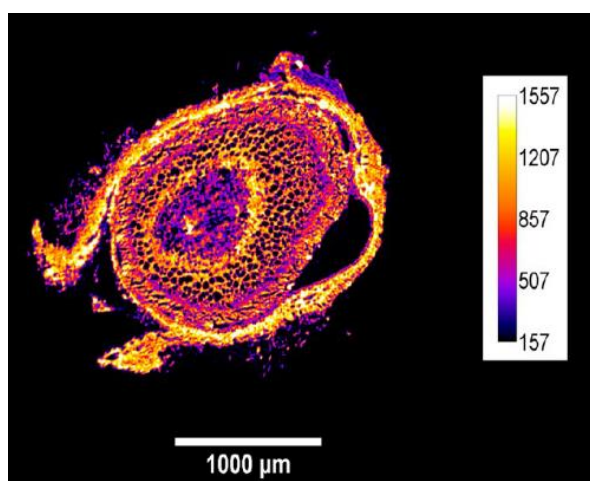


Figure 2.23 A 2D XCT image of Jones et al.'s cotton hull biochar in false colour (dark regions indicate pore space).

X-ray Computed Tomography (XCT) is not especially novel but the computing power required to complete in-depth quantitative image analysis has only more recently become widely available. Accordingly, software development of tools to meet this need is still an emergent area. For this reason, only a handful of studies have attempted to use XCT to examine the pore space of biochar. Jones et al. 2015 investigated the porosity of cotton hull biochars pyrolysed at increasing temperatures³²⁹. Using a synchrotron X-ray source (X2B beamline at NSLS, Brookhaven National Laboratory, USA) and an effective pixel size of 4 μm they were able to reconstruct sections of cotton hull biochar (. Using the linear attenuation coefficient (the product of the X-ray mass attenuation coefficient and sample density), they were able to estimate a value of overall porosity of the biochars. Values between 23 and 29 % porosity were calculated

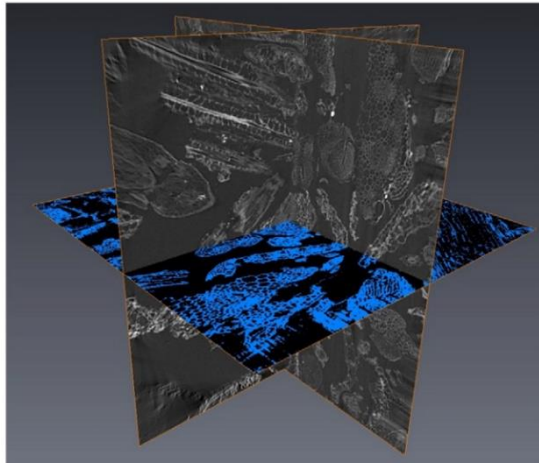


Figure 2-24 Orthogonal XCT reconstruction of Jeffrey et al.'s straw biochar. The field of view represents 4.9 mm³. Adapted from Jeffrey et al. 2015

for biochars created at 350 – 800 °C pyrolysis treatment temperature and macro pores began developing below 350 °C. No image analysis method was attempted. Another paper published the same year also examined biochar pore space using XCT, but for the purposes of evaluating biochar as a soil amendment. Jeffrey et al. 2015 focussed on biochar pores as a water reservoir in sandy soils and used a laboratory X-ray source with a 2.56 µm voxel size to examine biochar porosity (Figure 2-23) finding 48 and 57 % porosity for 400 and 600 °C treated hay-derived biochars respectively³³⁰. The software package Avizo was used to deduce porosity values. Error was estimated by manually varying the threshold values within reasonable tolerance, and was found to be < 5 %. In conjunction with a range of other analyses such as biochar hydrophobicity and field measurements, they concluded that this biochar in this system did not aid soil hydrological function. A 2014 study by Quin et al. also examined the effect of biochar on soil properties, conducting XCT on biochar-treated soil (Figure 2-24) with a voxel size of 70 µm³³¹. Authors used a manual (visual comparison) thresholding in ImageJ after finding automated thresholding to be unsatisfactory. Bird et al. 2008 examined the porosity of a scots pine-derived “natural charcoal” using XCT with a 21 µm voxel size. Authors also used a manual visual inspection method to threshold XCT images for analysis, highlighting the lack of availability of consistent and accurate automatic thresholding methods. The issue is that contrast between phases for materials such as these is poor. This is in part due to a predominance in composition of low mass elements (biochar is often 70-90 % carbon) which offers less X-ray attenuation than higher mass elements. The linear attenuation coefficient depends on both the atomic number of absorbing elements, density of the

material, as well as the incident X-ray energy³³². Hyväluoma et al. 2018 also studied water retention using XCT, to several unactivated biochars, to a resolution of 1.44 μm ²⁵⁵, deriving porosity, pore size distributions and random walk modelling values. Barr et al. 2021 also used in-situ pyrolysis to examine particle shrinkage and better understand the pyrolysis process³³³. These studies reveal that XCT is a suitable technique for biochar macro pore space analysis. They also reveal the resolution improvements achieved in recent years, with further enhancements possible as detector technology develops. Further, the associated technique of ptychography (“nano-tomography”) is capable of image resolutions well into the nanometre range³³⁴. This is not depicted in . There is a great deal of potential in X-ray tomography techniques for pore space analysis.

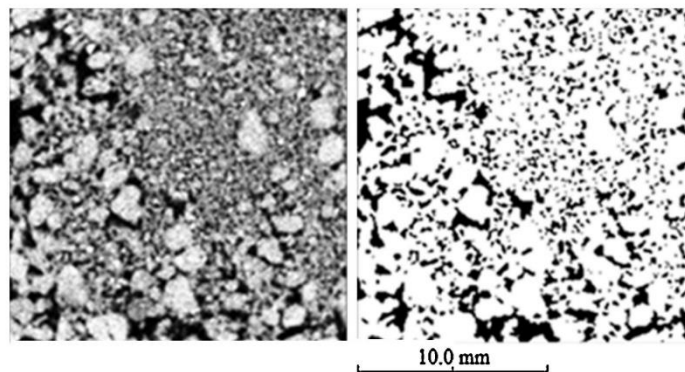


Figure 2-25 An example of the manual thresholding (right) from reconstructed XCT image slice (left) by Quin et al. 2014 on biochar-treated soil. Adapted from Quin et al. 2014

2.4.5 Knowledge Gaps

1. Analysis techniques and limitations

“The clear need for a new or optimized technique that could determine the pore size of aerogels in a broad range is highly desired”

- Horvat et al. in their 2022 paper, *A Brief Evaluation of Pore Structure Determination for Bioaerogels*,

BET derived surface area measurements are **the** metrics of choice for comparative pore space analysis. While it is a powerful micro pore analysis, it does not capture any information about macro pore space. As case studies 2.1 - 2.3 demonstrate, where macro pore structure is considered, it is typically analysed via SEM, which only allows for investigation of internal pore structure (or quantification thereof) after time consuming and potentially sample-damaging cross sectioning. While this can provide a ‘snapshot’ of internal macro pore structure, the statistical value of any quantitative analysis would be

low due to the small sample size available via a single cross section. Therefore, **more comprehensive techniques are required for investigation of macro pore space**, and crucially to understand the structure-function relationship.

2. Modelling of mass transport

Modelling of pore space dynamics, while making great strides in recent years, cannot effectively model for the wide variety of pore shapes that are observed in biochar. Different biochar feedstocks tend to produce different macro pore shapes.

3. Activation, modification and tuning of pore space

Pore space tuning is increasingly being employed to enhance performance, both in adsorption science and beyond, by means of activation or doping protocols. The influence of activators or dopants on the macro pore structure is not well understood, even though macro pore space architecture is known to affect performance. There is a need for accurate analysis, which will lead to greater understanding in the structure-function relationship and allow for further optimisation.

X-ray Tomography is a technique well suited to address all of these knowledge gaps.

2.5 Iron-biopolymer composites

Iron-bearing minerals are often studied for the immobilisation and remediation of radionuclides, among many other contaminants. Abundant throughout the biogeosphere, iron-bearing minerals have the potential to influence radionuclide mobility in both incidents of accidental release as well as in a geological disposal (GDF) setting. Iron is both redox active and possesses adsorptive properties useful for radionuclide immobilisation. Rationally designed composite materials comprising of i) biopolymer phase and ii) an iron-bearing phase are effective at immobilising radionuclides such as uranium, strontium 90 or cesium 137. Increasingly biopolymer materials are paired with iron-bearing phases such as metallic zero valent iron (zvi), iron oxides and hexacyanoferrates (HCF) to form composite materials which combine the favourable immobilisation characteristics of both phases individually and even create synergistic immobilisation effects^{335–337}. Such materials also have application beyond radionuclide remediation, since their chemistry is appropriate in stable isotope heavy metal remediation and organic pollutant removal, as well as in wider fields such as catalysis.

2.5.1 Overview of iron-bearing minerals

Metallic iron and iron minerals are widely used for adsorption and contaminant immobilisation. Zero valent iron (zvi) and mixed Fe(II/III) oxide magnetite (Fe_3O_4), are capable of redox transformations, making them ideal for reductive immobilisation of redox active metals such as uranium^{338–341}, selenium^{342,343} and technetium^{340,344–346}. Non-reductive immobilisation (adsorption or surface complexation) of metals e.g. strontium^{347,348} and cesium^{342,349} is also observed to these iron minerals as well as to non-redox active minerals such as iron oxyhydroxides ($\text{FeO}(\text{OH})$) and hematite (Fe_2O_3). Iron oxyhydroxides, such as goethite, and oxides generally have high surface areas favourable to adsorption³⁴² and possess surface oxides or hydroxides, suitable for cation complexation. Hexacyanoferrates (HCF) are a distinct class of iron-bearing minerals that are capable of highly selective ion-exchange, based upon electronic charge and ionic radius and are particularly suited to cesium immobilisation¹⁰³. Iron-bearing minerals, similarly to biopolymers, are low cost, abundant and widely available. They are safe and convenient to work with and prepare, as well as the benefit of having been studied and characterised thoroughly.

2.5.1.1 Zero Valent Iron (zvi)

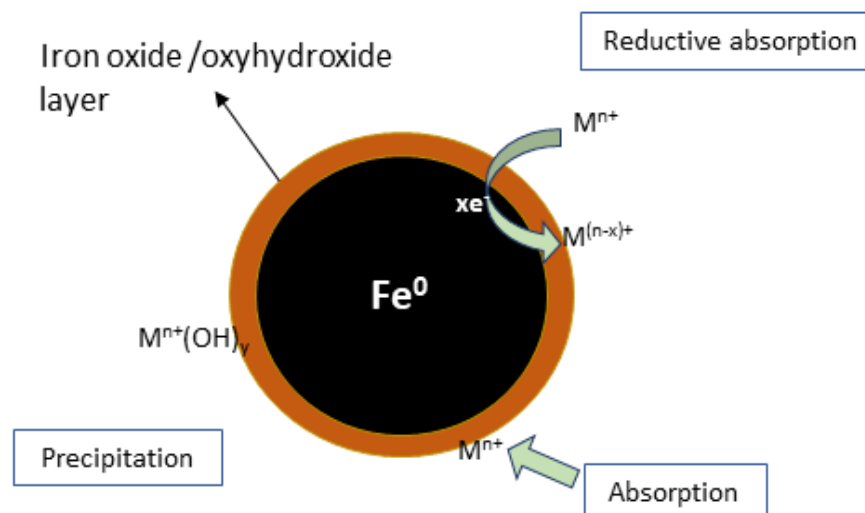


Figure 2.26 Core-shell model of zero valent iron nanoparticles

Zero valent iron and particularly nano zero valent iron (nzvi) has a number of key advantages for adsorptive immobilisation, reduction and degradation of a wide range of contaminants, ranging from pesticides³⁵⁰, industrial wastes^{351,352} and other organic pollutants, heavy metals^{104,353}. They are capable of achieving high contaminant immobilisation loading and can be retrieved easily once spent by virtue of their magnetism. zvi readily reduces redox active cations such as uranium, technetium or cobalt, rendering them less soluble and much more likely to become immobilised at active sites on or around the zvi phase, a process known as *reductive immobilisation*. According to the core-shell model (), zvi particles consist of a core of zero valent iron surrounded by a corroded surface layer of mixed iron oxides. This surface layer protects the iron core from further corrosion and plays an important role in mediating reduction, adsorption and precipitation during contaminant immobilisation^{351,352,354}. A STEM XEDS mapping study by Ling et al. 2015 showed that uranium adsorbed from solution became concentrated in the core of a zvi particle 24 h post sorption^{355,356} (Figure 2.27i). This is in contrast to a hematite particle tested, onto which uranium was distributed on the particle's surface (Figure 2.27n). In addition, as the zvi phase is oxidised it also creates Fe³⁺ phases e.g. FeOOH, Fe₂O₃, known to possess active sorption sites for cationic species³⁵⁷. Thus zvi itself has at least two distinct modes of contaminant immobilisation, depending on the physicochemical characteristics of the target radionuclide.

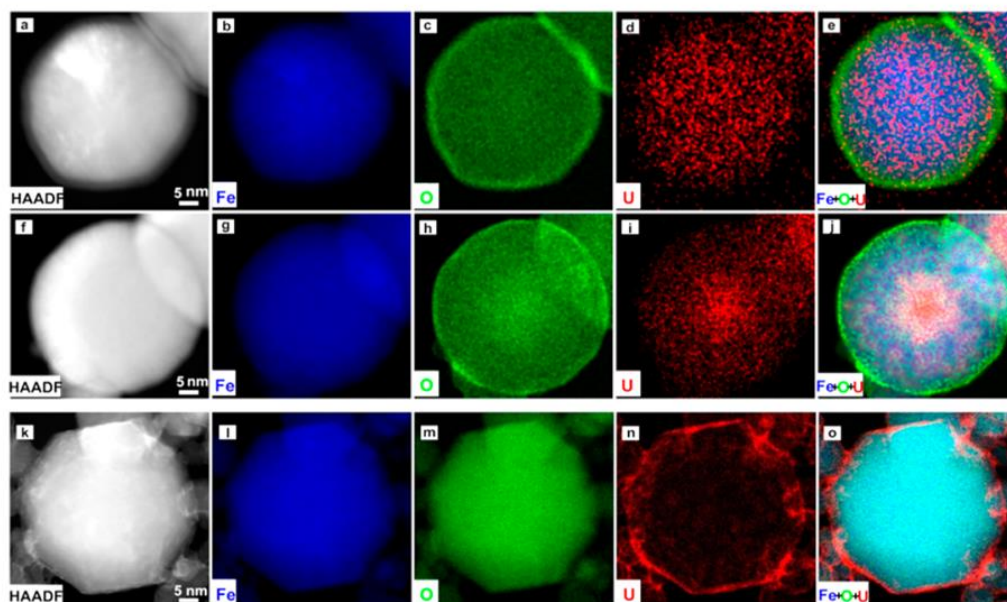


Figure 2. STEM XEDS mappings of uranium reactions with hematite (Fe_2O_3) and nZVI: (a–e) after 1 h with nZVI; (f–j) after 24 h with nZVI; (k–o) after 24 h with hematite. (a,f,k) HAADF images; (b,g,l) Fe mapping; (c,h,m) O mapping; (d,i,n) U mapping; (e,j,o) Fe + O + U color overlays.

Figure 2.27 adapted from Ling et al. 2018 showing the different distribution of uranium adsorbed to zvi and hematite. HAADF and element mapping (Fe, O, U and Fe+O+U from left to right) showing zvi at 1 hr (a–e), zvi at 24 hr (f–j) and hematite at 24 hr (k–o)

Smaller zvi particles confer larger surface areas and higher energy surface sites thus higher reactivity. Synthesis of nano-zvi is therefore highly desired, although the downside of such high reactivity particles is that they are more susceptible to unwanted and rapid oxidation³⁵⁸ and tend to agglomerate, both due to their magnetism and the high surface energy, which can lead to significant reduction in redox and adsorption performance. Therefore, zvi particle size must be carefully balanced between stability and activity to achieve highest uptake. A more promising strategy to stabilise nzvi is to incorporate the iron phase within a protective composite material, thereby preserving the particle size, dispersibility and high redox activity of nano-zvi. Methods employed include coating zvi with a protective layer of polymeric surfactants or a second metallic phase such as nickel, incorporation into oil-water dispersions or incorporation into a range of solid support materials^{359,360}. Biopolymers, such as pyrolytic carbon (biochar) have proved successful as a protective support for nzvi due to their stability and electronic properties^{357,361}. This is discussed in detail in Section.2.5.2.1

2.5.1.2 Iron (II/III) oxides

Iron oxides can take a number of forms and oxidation states. Among the most common iron oxides for cation immobilisation are goethite ($\alpha\text{-FeO(OH)}$),

hematite ($\alpha\text{-Fe}_2\text{O}_3$) and magnetite (Fe_3O_4). Iron oxides are low cost³⁶² and abundant materials which are facile to synthesise, well studied and well characterised. Iron oxyhydroxides and oxides generally have high surface areas and their surface oxides present abundant cation binding sites³⁶³[49]. Magnetite also has the benefit of strong magnetism, and is thus widely used in composites purely for the ease of separation that magnetism confers^{67,364,365}. Mixed iron (II/III) oxides and magnetite also exhibit redox activity, although this is to a lesser degree than zvi. Formation of composites necessitates the immobilisation of an iron oxide phase within a secondary (biopolymer) phase, and there are a number of common procedures to achieve this. The in-situ preparation of iron oxide-biochar composites during pyrolysis (carbothermal reduction) immobilises iron oxide within the carbonaceous biochar phase. The presence of iron oxides appears to have a beneficial effect of inhibiting the formation of water soluble organic matter and increases biochar (carbonaceous phase) yield³⁶⁶. Such mobile water soluble organics may coordinate to cationic radionuclides and reduce uptake and immobilization. The Massart procedure³⁶⁷ utilises a base such as NaOH to catalyse the co-precipitation of iron II/III salts. This is a facile and economical method to generate iron oxide phases³⁶⁸ and can be employed in the presence of another phase such as a biopolymer³⁶⁹. However, it does require an anoxic environment during reaction.

2.5.1.3 Metal hexacyanoferrates

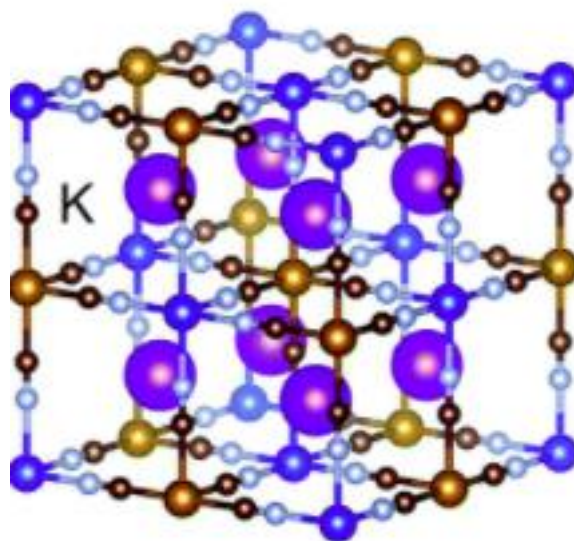


Figure 2.28 Example of the Molecular Structure of Prussian blue (Akira Takahashi, 2018)

Metal hexacyanoferrates (HCF) are cubic face-centred inorganic minerals known to possess excellent cation exchange capacity for radio cesium (^{137}Cs). The

specifics of HCF uptake are not the focus of this review and are covered elsewhere¹⁰³. In brief, HCFs have a basic structure of $A_yM[Fe(CN)_6]_x$, where A is any monovalent cation e.g. potassium, sodium etc. and M is a metal ion e.g. copper, manganese, iron, cadmium, nickel or zinc. The basic cubic structure consists of alternating low spin iron (II) ligated by six carbon atoms and high spin iron (III) ligated octahedrally by six nitrogen atom (. The choice of M affects the pore size which is a crucial factor to consider in ion-exchange since the group I monovalent ions and hence ion-exchange site are located, or intercalated, in the inter-layer region³⁷⁰. It is therefore possible to tune pore size based upon choice of M. It is also possible to tune the synthesis parameters to alter surface area and particle size³⁷¹. Some studies suggest that naked HCF adsorbents can perform better than when incorporated into some biopolymer composites³⁷², while others suggest that the formation of composites have stabilising effect. HCFs tend to decompose at elevated pH due to interaction of the ferric ion with abundant hydroxyls in solution. However, composites can help resist this degradation²⁰¹ as is detailed in Section 2.5.2.

A wide variety of iron-bearing minerals exhibit favourable uptake and immobilisation of radionuclides. This versatility is not commonly observed in most other metal-based adsorbents. On the other hand multiple iron minerals, created via multiple synthesis routes leads to many possible mechanisms of binding³⁷³, which necessitates careful study and comparison of each in order to fully understand uptake mechanism(s).

2.5.2 Iron-biopolymer composites

The various combinations of iron phase and biopolymer pairings which have been tested for radionuclide uptake and immobilisation are summarised in , and detailed in the following sections.

2.5.2.1 Biochar

Iron-biochar composites have been studied for a wide range of uses mostly comprising pollutant immobilisation and/or degradation, but also as a soil amendment³⁷⁴. Contaminants range from organics such as tetrachloroethene(TCE)^{352,375}, pentachlorophenol (PCP)³⁵⁰ and dyes such as methylene blue (MB)³⁷⁶, arsenate³⁷⁷, chromate³⁷⁸ among many other heavy metals and radionuclides³⁵⁵. There are biochar composites of zvi, mixed

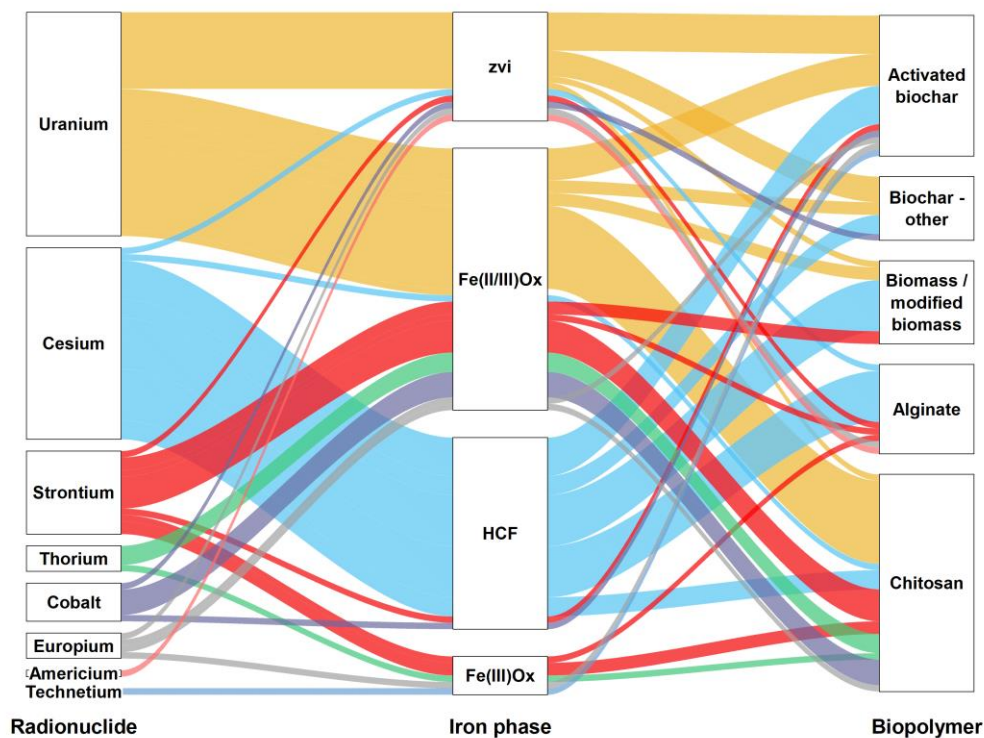


Figure 2.29 Summary of biopolymer-iron composites examined for radionuclide immobilisation. Classified by radionuclide (left), iron phase (middle) and by biopolymer type (right). Colour groupings refer to radionuclide

Fe(II/III) oxides, Fe(III) oxides and hexacyanoferrates³⁷⁹. Zvi and iron oxides in biochar composites can play several roles: Firstly they provide adsorption sites. Zvi and magnetite, due to their high redox power provide a secondary mechanism of reductive immobilisation³⁵⁷. They can also aid separation due to magnetism. Biochar plays a key supporting role in protecting the activity of the iron phase(s) from unwanted or premature oxidation. It has also been demonstrated that iron-biochar composites not only enhance overall uptake but also exhibit faster uptake kinetics than either solely iron or biochar phases alone³⁸⁰, suggesting that the combination of both in a composite has a synergistic effect. It is thought that biochar's surface functionality throughout its extensive pore network binds to iron phases³⁵⁵ forming tightly bound composites. Pang et al 2019 highlight the crucial role of the carbon phase in such composites, carefully comparing controls and showing that addition of a carbonaceous phase versus the naked iron phase more than doubles uranium uptake, underscoring the role of the carbon-based support in uptake capacity³⁵⁷. Another such study points to a key role of an organic phase in cesium adsorption. Kikuchi et al. 2019 ascribe an increase in Cs⁺ adsorption on

biogenic ferrihydrite to the presence of biogenic organic matter such as plant stalks³⁴². Several studies show that biochar increases the stability of the iron phase and several more indicate that the iron phase enhances the stability of the biochar phase too^{374,381}.

Biochar-nzvi

Graphitic, electron-active carbon materials such as biochar are thought to have a protective effect on the zero valency state of iron³⁵⁷. Although it has been shown that single phase nzvi alone has a higher reductive potential than when incorporated into carbon-based bio-adsorbent composites³⁸², it is highly susceptible to agglomeration or oxidation (from water or air) as a single phase, rendering it ineffective³⁵⁵. Therefore, the highest immobilisation capacities are seen using a combination of both phases. Stabilisation of the zvi phase by incorporation with a porous solid phase improves uptake significantly³⁸³. Biomass-based carbons are ideally suited to this role, since they exhibit extensive porosity and surface functional chemistry suited to metal uptake. They can also be surprisingly electroactive³⁸⁴ and have been shown to shuttle electrons from soil bacteria to iron-bearing soil minerals, reducing Fe(III) → Fe(II)³⁸⁵. Thus they show promise in providing protection from oxidation and provide active adsorption sites, secondary to those from zvi.

Synthesis of zvi and Fe-oxides

There are three main methods for synthesis of iron-biochar composites - reduction via either thermal or chemical processing. Chemical Reduction of iron using sodium borohydride (NaBH₄) directly onto biochar is common^{337,357,375,382,386,387}. This powerful reductant rapidly and reliably reduces iron(III) fully to zvi. It requires preparation under inert atmosphere, as well as the use of costly and toxic chemicals, and produces boric acid as a by-product³⁸⁸. It is also thought to produce larger zvi nanoparticles (10-100 nm) than other synthesis methods²⁷⁹. These factors tends to somewhat negate the advantages and motivation for using sustainable processing and materials such as biopolymers. Carbothermal reduction is a second technique well-suited to carbonaceous materials such as biochar. Iron salts are mixed with a biomass feedstock and the resulting mixture is pyrolyzed (thermally treated under anoxic conditions), creating both biochar and zvi or Fe(II) oxides in a one-step process³⁸⁸. The high temperatures (400-1000 °C) employed during pyrolysis provides the thermodynamic input required, and the decomposition of biomass carbon to CO and CO₂ provides a source of electrons required to reduce iron. Other reducing gases formed during pyrolysis (CH₄ and H₂) are also thought to

play a role in iron reduction. No toxic by-products are generated in this one-step process and the relative phases of zvi to Fe(II)oxide, usually magnetite, can be tuned by careful selection of the pyrolysis treatment temperature. Finally, co-precipitation of aqueous Fe(II/III) salts onto biochar is a third such method which uses high pH to induce precipitation[106], in a modified version of the Massart method³⁶⁷.

Biomass feedstock composition

The mineral phases present in biochar varies significantly depending on the biomass feedstock, which may affect performance. Lawrinenko et al. 2017 studied the effect of feedstock composition on the formation and stability of carbothermal biochar-zvi composites, finding that the presence of silicon and phosphorus not only inhibited the formation of zvi during pyrolysis, but also accelerated the oxidation of zvi³⁵⁸ in the resulting zvi-biochar composites. zvi prepared identically using red oak, a low mineral content feedstock, exhibited prolonged zvi stability over other feedstocks. Feedstocks such as switchgrass, bamboo, rattan, rice husk, corn stover or coconut coir which tend to be high in Si content^{389–391} are likely to produce less stable zvi phases. It is also quite possible that the generation of reductive gases and rate of electron transfer of the chosen biomass at a given HTT varies as a function of its precise chemical makeup, thus modulating the formation of zvi at a given pyrolysis temperature^{358,384,392}. The relationship between zvi content and the pyrolysis treatment temperature is not yet fully clear, with optimal values ranging between 600- 900 °C. However Su et al. 2013³⁵² showed that increasing the temperature and residence time increased overall iron content, although the latter appeared to decrease zvi content and increased Fe(III) content. This achieved the greatest zvi content on a coconut coir pith biochar with a 600 °C HTT for only 15 minutes.

Iron salt precursor effect on zvi phases

Often overlooked as a 'bystander', the counter anion of the iron salt precursor also appears to have a significant effect on the resulting performance of zvi-biochar composites. Although the precise mechanism of this is less clear since the counter anion is rarely the focus of such work this has been examined by Hoch et al. 2008, who produced carbon-zvi composites via carbothermal reduction using three organic (citrate, oxalate and acetate) and one inorganic counter anion (nitrate) to Fe(III) precursor salts. The organic counter ions resulted in smaller iron particles than for the nitrate precursor salt³⁷⁸. The differing thermodynamic properties of iron salts such as chloride, nitrate or

sulfate most likely cause key iron reduction to occur at different pyrolysis temperatures. This is highlighted by Zhang et al 2019 who found that zvi formation onto a starch-based biochar occurred at different HTT for chloride vs nitrate precursor ions. A ferric chloride salt precursor results in zvi formation at 800 °C, in contrast to the ferric nitrate precursor in which XRD confirms the presence of zvi only at a higher HTT of 900 °C. Sulfate as precursor counter ion didn't produce zvi even at 900 °C, resulting instead in pyrrhotite ($\text{Fe}_{(1-x)}\text{S}$). The consequence of this is shown clearly in resulting uranium removal efficiency³⁹³. Slower uranium uptake kinetics are also observed with Zhang et al.'s nitrate precursor sample, while overall it yields an uptake capacity around 1.6 times higher than that of the chloride precursor sample. Another key consideration is the weight ratio of iron salt to carbon used in carbothermal reduction. Too much iron will result in a composite with partially reduced iron with a corresponding lower reductive activity. Too little iron will fully reduce but be present in too low quantities for overall adsorptive capacity³⁹³. A mass ratio of between 1:4 to 1.6 iron:carbon/biomass was found to be optimal^{335,393}. A final consideration is the speciation of the iron precursor. Hu et al. 2017 used a mixed Fe(II)/Fe(III) chloride precursor, showing that a higher Fe(II)/(III) ratio favoured a higher zvi yield³⁹⁴. This would of course require fewer electrons to fully reduce to Fe(0). Since Fe(III) salts are usually employed in carbothermal reduction, this is an important observation.

2.5.2.2 Chitosan

A natural pairing with chitosan is a magnetic iron phase – typically magnetite – since chitosan takes a fine powdery form which can make it more challenging to separate post-sorption. Another common pairing in literature is the extensive work published around chitosan-prussian blue composites (HCFs) for immobilisation of cesium. Both chitosan and HCFs are powdery particulate matter and so more recent work incorporates a third crosslinking agent. Chitosan confers excellent mechanical stability^{395,396} to such composite materials and is resistant to oxidative processes. Its functionality provides means of relatively facile further functionalisation or crosslinking via condensation reactions or similar. Typically crosslinking agents include glutaraldehyde^{187,397,398}, glycine³⁹⁹ and maleic anhydride⁴⁰⁰ which can achieve both crosslinking and enhanced functionality for complexation of cationic species.

2.5.2.3 Other biopolymers

Although alginate has no natural affinity with iron, the gelation properties of alginate are utilised to suspend iron-bearing nano particles (e.g. HCFs)⁴⁰¹, as well as in combination with magnetic iron to create magnetically separable gels^{402,403}

2.5.3 Uranium uptake

2.5.3.1 Zvi adsorbents

A wide range of biopolymers have been employed to form composites with zvi, from green carbons ('biochar') derived from pine needles³⁸⁸, sewage sludge³⁸⁰, starch derivatives³⁹³, collagen fiber⁴⁰⁴, chitosan³³⁷ or bacterial cellulose³⁸².

Uranium reduction

The reduction of uranium is a key mechanism for the immobilisation or capture of uranium since it renders uranyl ions less soluble and therefore less mobile in aqueous systems, including environmental systems. This is apparently confirmed in density function theory (DFT) calculations performed by Chen et al. that indicate that reduced U(IV) is more tightly bound to a coal-fly ash nZVI composite than U(VI)³⁸⁶. Uptake experiments on the same composite achieved 148 mg g⁻¹ loading of uranium. The fraction of U(VI) that is reduced was examined by several authors. Hu et al. 2017 achieved a 28 % reduction of U(VI) to U(IV) from a total of 54 mg g⁻¹ uranium loading³⁸² while Kong et al. 2016 showed a 54.4% reduction of 149 mg g⁻¹ uranium loaded, using an efficient starting material of iron-rich sewage sludge. By employing the carbothermal reduction process directly on the iron-rich sludge, no additional starting material is required to introduce iron into the composite which is attractive from an economic perspective³⁸⁰. Liao et al. 2020 showed a 70.6 % reduction of a total 130 mg g⁻¹ of uranium loaded to a collagen zvi-Ni⁰ composite⁴⁰⁴, attributing the addition of nickel as the crucial factor to its high reductive capacity. It was believed that Ni⁰ played a similar protecting role to the zvi as that of iron oxide in the core-shell model (), but also helps to regenerate zvi by sacrifice of its own electrons. Quantification of the reduction of uranium is typically achieved by X-ray Photoelectron Spectroscopy (XPS), specifically by examination of a shift from metallic Fe 2p_{1/2} and 2p_{3/2} peaks to ionic 2p_{3/2} peaks. Equally, examination of the uranium 4f_{5/2} and 4f_{7/2} peaks can distinguish U(IV) from U(VI)³⁸⁸ as the two ions exhibit slightly different binding energies. This can however be a challenging quantification if uranium loading is not particularly high, a challenge

which is compounded by the fact that surface specific techniques such as XPS cannot penetrate and accurately quantify binding that may occur to interior surfaces and binding sites. A technique such as X-ray Absorption Spectroscopy (XAS) which utilises higher energy, penetrating X-rays gives accurate quantification of uranium oxidation states, with the added possibility of gaining further binding mechanism insight through examination of the photoelectron fine structure⁴⁰⁵.

Optimal carbothermal reduction temperature for uranium uptake

In a comparison of optimal pyrolysis temperatures (600-900 °C) for zvi-biochar composites for uptake of uranium, Kong et al. 2016 found carbothermal reduction at 800 °C produced the highest uranium uptake of around 150 mg g⁻¹, using a wastewater sludge as biochar precursor³⁸⁰. This uptake was significantly greater than uptake from either the component carbon phase or iron phase alone. The authors also found that below a 600 °C pyrolysis treatment did not appear to convert significant quantities of the iron(III) precursor into zvi. Other authors have reported similar temperatures for zvi formation, at pyrolysis temperatures of 700 °C³⁶⁵ or as low as 600 °C²⁷⁹.

Surface area and uptake

Little correlation between uranium uptake capacity and micropore surface area is observed. Pang et al. 2019's Dictyophora indusiata sulfur doped biochar-zvi composite³⁵⁷ showed a low surface area of 16.2 m²g⁻¹ despite being one of the highest performers in uranium uptake at around 428 mg g⁻¹. Conversely, Zhang et al. 2019's starch based composite³⁹³ showed a high surface area of 782 m²g⁻¹ with more moderate uranium uptake of 55 mg g⁻¹. Although surface area is usually well correlated to uptake capacity in porous media such as biochar and activated biochars, there is clearly a more complex relationship with uptake in composites. This is likely in part due to biochar's pore system becoming blocked and filled by the zvi or other phases present.

Functionalisation strategies

More complex rationally designed composites continue to push the envelope. In particular, the addition of a third phase in addition to the biopolymer and zvi phases serves several purposes. Addition of carefully chosen heteroatoms can have a protective effect on the dispersion and activity of nzvi particles within the composite, enhancing its adsorptive capacity. For example the addition of sulfur forms a protective FeS shell to zvi particles embedded in biochar^{357,406}. Nickel is also thought to regenerate the redox active Fe⁰ by supplying the necessary

electrons⁴⁰⁴. Nitrogen and sulfur are both known to bind strongly to uranium and so the facile addition of these atoms can greatly enhance the number of uranium binding sites in such composites. Pang et al. 2022 showed that the ratio of sulfur and biomass starting material to iron was a crucial consideration for optimal uptake, with the S:Fe particularly sensitive. Uranium percent removal varied between 25 – 70 % depending on this ratio⁴⁰⁶. Other strategies employed include derivative composites such as a carboxymethyl cellulose (CMC) zvi composite¹¹¹. CMC is derived from cellulose through a process of mercerization then etherification to fine tune the surface functional chemistry.

It is perhaps notable how few uranium immobilisation studies using biopolymers have examined chitosan-zvi composites. Biochar is well known for its redox activity, particularly electron donating capacity^{384,392,407} due to its reduced, graphitic and highly aromatic structure. In contrast, chitosan is a poor electrical and thermal conductor^{396,408}. Thus it likely does not provide the same protective and/or regenerative effect on reduced iron that biochar is capable of. One notable exception however, Zhang et al. 2019 achieved an uranium loading of 592 mg g⁻¹ onto a zvi-loaded chitosan composite³³⁷. Therefore chitosan-zvi composites can be effective, although stability of the composite was not discussed. Clearly, further investigation of chitosan composites are needed to explore this potential and this is like to be an area of active research in the next few years.

Table 2-3 A summary of zero valent iron – biopolymer composites studied for uranium uptake (1/2)

Biopolymer and iron source	Reductant method	Q max / mg g ⁻¹	pH	T / K	Equilibrium time / h	Kinetic model	isotherm model	Selectivity	Reference
Activated Charcoal Fe(II)SO ₄	NaBH ₄	493	5	308	1	PSO	Freundlich	-	Liu 2016 ³⁸⁷
Pine biochar Fe(III)(NO ₃) ₃	Carbothermal	204	4	298	1.7	PSO	Langmuir	-	Lv 2019 ³⁸⁸
Dictyophora indusiata-derived biochar Fe(II)SO ₄ - dithionite	NaBH ₄	428	5	298	3	PSO	Langmuir	Simulated seawater	Pang 2019 ³⁵⁷
Fe-rich sludge wastewater biochar	Carbothermal	149	3.5	298	0.5	PSO	Langmuir	-	Kong 2016 ³⁸⁰
Bacterial Cellulose biochar Fe(III)Cl ₃	NaBH ₄	54	3.5	298	24	PSO	Langmuir		Hu 2017 ³⁸²
Coal Fly ash FeSO ₄	NaBH ₄	148	6	298	10	PSO	Langmuir		Chen 2018 ³⁸⁶

Table 2-3 continued (2/2)

Biopolymer and iron source	Reductant method	Q max / mg g ⁻¹	pH	T / K	Equilibrium time / h	Kinetic model	isotherm model	Selectivity	Reference
Starch Fe ₂ (SO ₄) ₃ , FeCl ₃ , FeNO ₃	Carbothermal	55.1		303	1	PSO	Langmuir	-	Zhang 2019 ³⁹³
Dictyophora indusiate biochar FeSO ₄	NaBH ₄	300	-	298	1	PSO	Langmuir	-	Pang et al. 2022 ⁴⁰⁶
Longan shell biochar FeCl ₃	NaBH ₄	331	6	298	3.4	PSO	Langmuir	-	Zhang et al 2021 ⁴⁰⁹
Collagen fibre, bayberry tannin crosslinker FeCl ₃ - NiCl ₂	NaBH ₄	130	5	328	5	PSO	Langmuir	-	Liau 2020 ⁴⁰⁴
Chitosan FeCl ₂	NaBH ₄	592	5	298	Rapid but not explicitly stated	PSO	Langmuir		Zhang 201 ³³⁷
CMC FeSO ₄ ·7H ₂ O	NaBH ₄	323	5	298	48	-	Freundlich	-	Popescu 2013 ¹¹¹

2.5.3.2 Iron oxide adsorbents

Although not as powerful a reducing agent as zvi, mixed $\text{Fe}^{2+}/\text{Fe}^{3+}$ iron oxide (Magnetite) is also capable of reducing uranium (VI)³⁴¹. However it is its magnetism, exploited for facile separation of composite adsorbents, that appears to be the focus of its use in biopolymer composites for uranium uptake⁴¹⁰, with little data specifically examining the magnetite mediated reduction of U(VI) to U(IV). Magnetic separation is a highly useful feature for particulate adsorption materials. The addition of magnetite is also thought to enhance the mechanical properties of some biopolymer composites, e.g. chitosan⁴¹¹. One of the few studies to examine uranium reduction in this subgroup showed intriguing XANES data on 2-day and 14-day aged samples post uranium sorption⁴¹². Reduction of uranium on their magnetite-biochar composite appeared to occur over the course of days/weeks, with a 2-day post uptake sample indicating mostly U(VI) adsorbed, while at 14-days post uptake, the edge more closely resembles U(IV) (Figure 2.30). This suggests that reduction of uranium on such composites is a relatively slow process characterised by first adsorption and subsequent reduction and further immobilisation. Studies have shown the kinetics of biochar-mediated reduction is slow, on the timescale of days or longer^{384,392} thus it seems likely that the redox activity of the biochar is contributing to the slow reduction of uranium. If so, biochar-magnetite composites may be particularly suited to long-term remediation techniques such as in-situ reactive barriers. This study also highlights the need to consider processes which can occur on timescales longer than the uptake experiments themselves. The most common preparation method for magnetite composites, irrespective of the biopolymer type, was via the Massart method³⁶⁷, the precipitation of iron oxides in sparingly soluble high pH conditions. This reflects the relative simplicity and reliability of this method. However when considering biochar-based composites it should be noted that mixed $\text{Fe}^{2+}/\text{Fe}^{3+}$ oxides are synthesized simultaneously during biochar production in a one-step pyrolysis, which is favourable in terms of starting materials and steps required. Although Table 2-4 contains one sole entry for such a one step process, Li et al.'s magnetic rice husk biochar⁴¹², which at face value seems to suggest this is not a particularly favoured method, it should also be noted that mixed $\text{Fe}^{2+}/\text{Fe}^{3+}$ were often generated in significant quantities during the carbothermal synthesis of zvi, particularly at lower pyrolysis temperatures (500-700 °C), which is covered in Section 2.5. The addition of magnetite, or other iron oxide phases, to biochar has variable effects on uranium uptake. Wang et al. 2020 found that an acid-activated *Microcystis* biochar performed slightly better in uranium uptake

experiments than a magnetite-containing analogue⁴¹³. Blocking of the extensive pore network and reduction in surface area of biochar by addition of mineral phases is well documented^{414–416}. This likely blocks access to complexation sites within the pore network, reducing overall uranium uptake. However, this is not always the case: Wang et al. 2018 observed that the presence of magnetite increased uranium uptake to an unactivated rice husk biochar⁴¹⁷ over the unmodified control. A wide range of uptake capacities are observed among the biochar composites (Table 2-4). A novel *Citrullus lanatus* L. seed biochar-MnFe₂O₄ spinel ferrite nano-composite achieved a relative modest uptake of 28 mg g⁻¹ while a magnetic Pine needle biochar achieved an impressive 624 mg g⁻¹ by employing an acid activation step to maximise oxygen surface

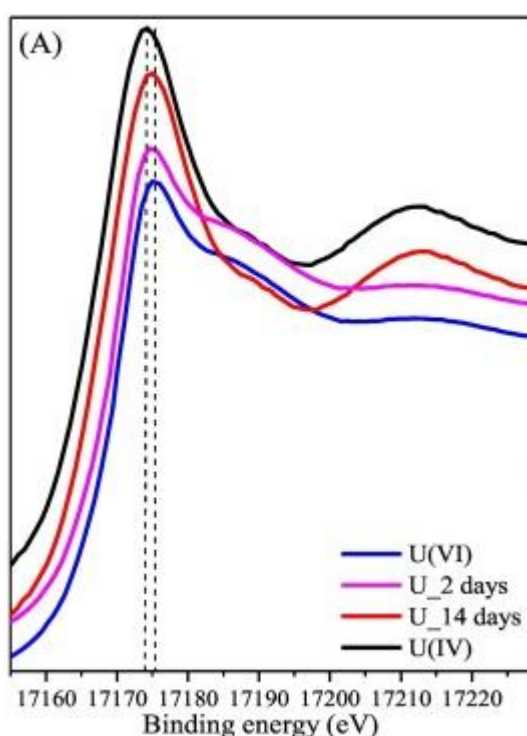


Figure 2.30 L3-edge uranium XANES data from Li et al. 2019 showing the slow reduction of U(VI) to U(IV)

functional groups for uranium binding⁴¹⁸. This reflects the emergent nature of biopolymer-iron composites, that multiple possible strategies are being investigated and many possible combination exist. In general, the consensus was that oxygen surface functional groups of biochar and particularly activated biochar played a major role in uranyl binding^{412,413,419} with some contribution from Fe-O moieties, evidenced by energy shifts in Fe 2p_{3/2} XPS spectra. A far greater range of chitosan-mixed Fe(II/III) composites are reported in the literature. In general, chitosan is a more uniform biopolymer than biochar⁴¹⁰. It is therefore possible to suggest and execute a more targeted functionalisation protocol which is reflected in the wide range of functionalisation and crosslinking

strategies deployed to target uranium uptake. The most common chitosan functionalisations contain nitrogen containing groups such as amidoxime functionalisation^{420,421}, ethylenediamine⁴²², triethylene-tetramine¹⁰⁵, Schiff's base¹⁸⁷, derivatives of hydrazine^{399,420,423} as well as oxygen containing groups maleic anhydride⁴⁰⁰ and phosphonobutane-1,2,4-tri- carboxylic acid (PBTCA)⁴²⁴. The final of these by Huang et al. (2020) achieved a good but relatively modest uranium uptake capacity of 83.16 mg g⁻¹ onto a (PBTCA)-decorated chitosan-coated magnetic silica nanoparticle adsorbent. Its real strength however is its excellent selectivity shown for uranyl ions in competitive uptake experiments with 14 other cations. Shehzad et al. also increased uranium selectivity onto magnetic chitosan via functionalisation with maleic anhydride groups⁴⁰⁰, almost doubling the quantity of uranium adsorbed from a multi-ion solution. Other highly functionalised adsorbents such as a magnetic Schiff's base chitosan composite¹⁸⁷ show good uptake for several ions simultaneously, including uranium, from a multi-element solution, thus positioning itself as a potential multi-element adsorbent. The complex functionalisation of biopolymers is a trade-off between sustainability and economics of the adsorbents vs uptake capacity and selectivity.

Crosslinking strategies also play a role in selectivity. Zhou et al. 2012 used uranyl ions as a template during the crosslinking process in order to create binding pockets perfectly suited both sterically and electronically for uptake of uranium³⁹⁷. Of course this necessitated multiple acid rinsing steps to remove the uranyl ions used for templating prior to use and only increased uranium uptake from 161 to 187 mg g⁻¹, suggesting the chitosan composite is reasonably effective without templating. However, the benefit of this method is perhaps more prominent when the authors considered the effect of competitive uptake, finding a 3-fold increase for ion selectivity in the presence of a range of relevant competitive cations. Crosslinking agents used include glutaraldehyde^{187,410,424}, epichlorohydrin^{399,400,421} and glycine³⁹⁹. Another strategy for ion selectivity was utilised by Hamza et al. 2018, who were able to show pH-dependant uptake onto an amidoxime functionalised magnetic chitosan composite, with uranium predominantly taken up at pH 4.9 but europium uptake dominating at pH 2.3⁴²¹. In general, chitosan composites showed excellent uptake capacity, with good reusability⁴²⁰⁻⁴²² and evidence of good ion selectivity^{400,420}. Complexation was attributed mostly to nitrogen lone pair interaction with a contribution from oxygen groups such as hydroxyls, phosphonates and carboxylates.

Table 2-4 Summary of selected iron oxide biopolymer composite materials examined for uranium uptake (1/3)

Biopolymer and iron source	Oxide prep method	Q max / mg g ⁻¹	pH	T / K	Equilibriu m time / h	Kinetic model	Isotherm model ^b	Reference
<i>microcystis</i> biochar ferric ammonium citrate	^a Base precipitation + Hydrothermal treatment	52.06	6	298	12	PSO	Freundlic h	Wang 2020 ⁴¹³
oxidised pine needle biochar FeSO ₄ , FeCl ₃	^a Base precipitation	623.7	6	298	-	PSO	Langmuir	Philippou 2019 ⁴¹⁸
citrullus lanatus L. biochar FeSO ₄ , KMnO ₄	^a Base precipitation	27.61	4	298	1	PSO	Langmuir	Ahmed 2021 ⁴¹⁹
rice husk biochar siderite	Carbothermal reduction	52.63	4	318	25	-	Langmuir	Li 2019 ⁴¹²
rice husk biochar FeSO ₄	^a Base precipitation	118	-	328	-	PSO	Langmuir	Wang 2018 ⁴¹⁷
humic acid FeSO ₄ , FeCl ₃	^a Base precipitation	10.5	-	-	-	-	Langmuir	Singhal 2017 ⁴²⁵
coal fly ash FeCl ₂ , FeCl ₃	^a Base precipitation	329	6	298	24	PSO	Langmuir	Chen 2017 ⁴²⁶
hydrazide grafted chitosan FeSO ₄ , FeCl ₃	^a Base precipitation	369	5	295	1	PSO	Langmuir	Hamza 2020 ⁴²³

Table 2-4 continued (2/3)

Biopolymer and iron source	Oxide prep method	Q max / mg g ⁻¹	pH	T / K	Equilibriu m time / h	Kinetic model	Isotherm model ^b	Reference
PBTCA decorated chitosan CoFe ₂ O ₄ @SiO ₂	Multi-step	105.3	4	298	2	PSO	Langmuir	Huang 2020 ⁴²⁴
Schiff base-modified chitosan Fe ₃ O ₄	Multi-step	552	4	298	0.42	PSO	Langmuir	Elwakeel 2014 ¹⁸⁷
amidoxime-functionalised chitosan FeSO ₄ , FeCl ₃	^a Base precipitation	357	4	-	1-1.5	PSO	Langmuir	Hamza 2018 ⁴²¹
ethylenediamine-modified chitosan FeSO ₄ , FeCl ₃	^a Base precipitation	82.83	3	303	0.5	PSO	Langmuir	Wang 2011 ⁴²²
amidoxime-functionalised chitosan FeSO ₄ , FeCl ₃	^a Base precipitation	328	3	-	1	PFO	Langmuir	Hamza 2019 ⁴²⁰
glycine-grafted chitosan FeSO ₄ , FeCl ₃	^a Base precipitation	271		-	-	PSO	-	Hamza 2017 ³⁹⁹
triethylene-tetramine functionalized chitosan Fe(NH ₄) ₂ (SO ₄) ₂	^a Base precipitation under N ₂	166.6	5	293	1	PSO	Langmuir	Jin 2015 ¹⁰⁵
maleic anhydride chitosan FeSO ₄ , FeCl ₃	^a Base precipitation	187.9	4.5	298	3	PSO	Langmuir	Shehzad 2018 ⁴⁰⁰

Table 2-4 continued (3/3)

Biopolymer and iron source	Oxide prep method	Q max / mg g ⁻¹	pH	T / K	Equilibriu m time / h	Kinetic model	Isotherm model ^b	Reference
chitosan FeCl ₂ , KNO ₃	^a Base precipitation under N ₂	588	4	298	2	-	Langmuir	Hritcu 2012 ⁴¹⁰
ion-imprinted chitosan FeCl ₂ , FeCl ₃	^a Base precipitation	187.3	5	298	2	PSO	Langmuir	Zhou 2012 ³⁹⁷
arachis hypogaea leaves powder/ chitosan FeCl ₂ , FeCl ₃	^a Base precipitation	232.4	5	303	1.5	PSO	Langmuir	Yuvaraja 2020 ⁴²⁷
diethylenetriamine grafted chitosan FeSO ₄ , FeCl ₃	^a Base precipitation	185	4	298	1	PSO	Langmuir	Galhoum 2017 ⁴²⁸

^aThe Massart or a modified Massart method

2.5.4 Strontium uptake

2.5.4.1 Spectroscopic studies

A few X-ray Absorption Spectroscopy (XAS) studies to various iron phases show that strontium tends to form outer sphere complexes with Goethite²³⁵, hydrous ferric oxide²³⁶ (Sr not incorporated into HFO). Indeed, Collins et al 1998 showed that Sr only forms inner sphere complexation with Goethite at elevated pH (> 10.2)²²⁸ which is likely due to the zero point charge (pH_{ZPC}) of Goethite, above which FeOOH groups become negatively charged. Literature puts the pH_{ZPC} of Goethite between 7-9 pH⁴²⁹. This is consistent with a study of Sr sorption to Fe in sediments, which showed that the outer sphere complexation mechanism dominated below pH 9²³⁹, below which no signal of second shell nearest neighbours could be found. Thus, at circumneutral pH Goethite is protonated and does not appear to show much affinity for Sr. This is reflected in moderate uptake values for Goethite, particularly at circumneutral pH^{228,429,430}. One interesting point is that amorphous (freshly base-precipitated) goethite showed 25 % better uptake than 40 h aged⁴³⁰. No such studies were found which examined Sr uptake to zvi phases, either naked or incorporated into biopolymer supports of any type. Pertinent to iron-containing composites, strontium is not redox active, thus some of the advantages of incorporating an iron phase are not applicable. The majority of studies appear to include mixed Fe(II/III) phases for the purpose of conferring magnetic separation properties^{59,169,369,411,431-436} rather than to increase Sr uptake. Indeed, the addition of a mixed Fe(II/III) phase largely did not increase Sr uptake.

2.5.4.2 Chitosan

Zemskova et al. 2018 created a chitosan-magnetite composite via the base co-precipitation method, finding that Sr uptake efficiency decreased with increasing Fe-fraction, due to greater instability in solution³⁶⁹. It is notable that this composite achieved a lower theoretical max uptake than a naked magnetite control. This suggest that chitosan may not be the most suitable of biopolymer adsorbents for strontium. Chitosan possesses a number of advantages such as mechanical strength, polymorphism, stability, ease of crosslinking and abundant surface hydroxyl and amino groups^{55,369,437}. Although chitosan is hampered as a sorption material due to low porosity, poor stability in acidic media and poor thermal stability⁴³². In addition to this, oxyphilic strontium appears to exhibit low affinity for chitosan's amino groups⁴¹¹. Indeed, the highest performing chitosan-iron composite examined here achieved a respectable max uptake of 82 mg/g

Sr, Yin et al. 2017's chitosan-Fe(II/III) microspheres also containing *Saccharomyces Cerevisiae* (brewer's yeast). However, the *S. Cerevisiae* control alone was reported to achieve a Q_{max} of 78 mg/g, suggesting that the chitosan contributed little if any to Sr binding sites. Ji et al. 2010 created a similar yeast cell-magnetite composite using the base precipitation method, although without chitosan⁴³¹, achieving a Q_{max} of around 141 mg/g (Table 2-5). This supports the notion that chitosan adds little in the way of strontium binding sites. However, no controls (yeast or magnetite only) were reported for this study precluding further inference of binding site locations.

2.5.4.3 Alginate

One of the most attractive biopolymers for strontium immobilisation is alginic acid, the anionic polysaccharide found in the cell walls of brown algae. Containing carboxylate functional groups, it is well suited to group I and II metal complexation due to the favourable ionic attraction. In addition it has mild gelation properties⁵⁶ allowing facile formation of composite beads that do not require strong bases as with chitosan based composites. The literature pertaining to alginate composites for Sr remediation is reasonably extensive⁴³⁸, however few papers combine it with any iron phases for the aforementioned reasons: that iron does not contribute to Sr sorption and the only reason for addition of iron would be for magnetic separation. Hong et al. 2016 did examine just this, forming an alginate-magnetite composite via the ionotropic gelation method⁴³⁵ and achieving an impressive maximal uptake of 400 mg/g. Fuks et al. 2018 created a similar composite bead using iron carbonyl⁵⁹, and achieved a 50 % Sr removal efficiency. Another approach is to incorporate hexacyanoferrate particles into an alginate gel composite⁴⁰¹, attempting to create a bi-functional sorbent with high-affinity site for both strontium (alginate residues) and cesium (hexacyanoferrates) simultaneously.

2.5.4.4 Activated carbons

A similar composite was fabricated by Ali et al. 2020, this time using activated carbon (instead of alginate) coated with hexacyanoferrate particles⁴³⁹ which they examined for strontium, cesium and cobalt uptake. Activated carbon is similar in physicochemical structure to biochar and particularly activated biochar and as such is a useful indicator of biochar performance. Controls showed that in this case, Sr uptake occurred exclusively to the carbon phase i.e. HCF did not enhance Sr uptake as would be expected) achieving a modest Sr uptake of 30 mg/g. Although this didn't show huge uptakes, it is important work nonetheless since it proves it is able to immobilise multiple radionuclides

simultaneously. Lu et al. 2015 used a commercially available activated carbon to create a magnetic composite. Sr uptake of 40 mg g^{-1} actually decreased slightly once the activated carbon was combined with the iron oxide phase – the activated carbon alone showed better uptake. This could be because iron oxides block pore spaces of the activated carbon and occupy active adsorption sites/oxygen surface functionality. It is perhaps of little surprise that few publications have examined biochar-iron oxide composites; although the magnetic properties of iron oxide confer easy separation of composite adsorbents, their incorporation to biochars appear to reduce Sr uptake at environmentally relevant pH.

2.5.4.5 Other biopolymers

Of final note is the fabrication of biologically derived speciality chemicals, fulvic and/or humic acids. Humic acids are a complex mix of small organic molecules derived from humus, itself a major component of soil and peat. Humic acids contain an abundance of oxygen functionality such as carboxylates, quinones, catecholates, phenol, alcohol and sugars, making them an attractive candidate for strontium complexation and chelation¹⁶⁸. They were incorporated into an alginate-Fe-aminoclay composite by Choe et al. 2018., achieving a strontium uptake of 46 mg/g ⁴⁴⁰. Unusually, iron in this case was incorporated in an aminoclay matrix that was added for mechanical stability and crosslinking of the composite. A sub-family of humic acids – fulvic acids, which are the humic acids remaining in solution after acidification, were incorporated into a magnetic composite for the removal of strontium from seawater, by Ghaeni et al. 2019¹⁶⁹, achieving an impressive max uptake of 227 mg/g Sr. This composite, in addition to magnetite, also incorporated a manganese dioxide phase. Manganese oxides are well known, although not well understood, in cation adsorption. Such a high strontium uptake capacity shows great promise for manganese dioxide as an adsorbent in this setting^{168,441}. It is possible that base precipitation synthesis methods (e.g. the Massart procedure) could inadvertently show higher uptake than expected, particularly with porous materials, such as biopolymers. This is because unless the final materials are thoroughly rinsed after synthesis, basic solution can remain in the pore network. Since Sr is known to precipitate as insoluble $\text{Sr}(\text{OH})_2$ at elevated pH²¹⁶, this could be a mechanism as yet unaccounted for. In batch uptake experiments, as many as nine distinct pH control regimes are recorded in a review of uptake isotherm experiments⁴⁴². Residual pore-bound basicity could then increase the pH *during* batch uptake, precipitating Sr and giving erroneous uptake data. Base precipitation of both Fe(II/III) phases and chitosan composites are common¹⁶⁹

and careful attention much be paid to this. Buffering of batch uptake experiments with pre-equilibration, or careful monitoring of pH throughout should prevent issues with this.

Table 2-5 Summary of iron-biopolymer composites studied in strontium uptake experiments

Biopolymer	Iron phase	Q _{MAX} (mg/g)	Experimental conditions	Reference
fulvic acid / MnO ₂ nanocomposite	Fe ₃ O ₄	227	25 °C, pH 8	Ghaeni 2019 ¹⁶⁹
Chitosan-modified sawdust	Fe ₃ O ₄	12.6	20 °C, pH 6.74,	Cheng 2012 ⁴³⁶
Calcium alginate	Fe ₃ O ₄	400	pH 6	Hong 2016 ⁴³⁵
Purchased activated carbon	Fe ₃ O ₄	39.8	20 °C, pH 5	Lu 2015 ⁴³⁴
Activated carbon	Cobalt Prussian Blue (CoHCF)	29.6	pH 6.8	Ali 2020 ⁴³⁹
Chitosan/brewer's yeast/alginate/	Fe(II/III)	82	30 °C, pH 8	Yin 2017 ⁴³³
Chitosan	Fe ₃ O ₄	54	-	Zemskova 2018 ³⁶⁹
Chitosan	Fe ₃ O ₄	11.6	pH 8.2	Chen 2012 ⁴¹¹
Chitosan	-	2.5	-	Egorin 2020 ⁴³²
alginate/humic acid/Fe-aminoclay	aminoclay	45.7	25 °C, pH 7	Choe 2018m ⁴⁴⁰
Yeast cells	Magnetite	141	20 °C, pH 7.0	Ji 2010 ⁴³¹
alginate beads/CNT	Sodium cobalt hexacyanoferrate	72		Vipin 2014 ⁴⁰¹
Waste FeOx from Fenton fluidised bed	goethite phase (α-FeOOH)	38.5	pH 10.5	Liu 2014 ⁴²⁹

2.5.5 Cesium uptake

The majority of the literature on cesium uptake to iron-bearing minerals is focussed on metal hexacyanoferrates (HCF), and in optimising such sorbents. Being non redox active, adsorption of cesium is typically via ion-exchange and complexation. The uptake mechanism of HCFs is via ion-exchange, typically replacing K^+ from the interstitial sites. This is generally endothermic and spontaneous. Although HCFs have been known to be effective ion-exchangers for group I metals for a number of years, the vast majority of literature concerned with in this review are from recent years – this reflects the explosion of recent research in using biopolymers as in composites with HCFs. HCFs are fine particulate matter and therefore benefit from composite formation to ease separation of the spent sorbent post-uptake. One of two strategies are commonly employed in order to facilitate easy separation: HCFs are either combined with magnetic phases⁴⁴³, or are incorporated into monolithic composite such as cross-linked hydrogel beads^{401,444} (which may also be magnetic). Cesium uptake to HCFs are concerned with the following factors: choice of the metal in the HCF phase (e.g. copper, iron, nickel etc.), method of immobilisation, and optimal weight fraction HCF in composites. Another active area of research is in strategies to minimise leaching of metals from the HCF phase, as this is a common issue with the material⁴⁴⁵. These could be Fe^{3+} or any other metal that is chosen in the synthesis stage such as Ni^{2+} ^{107,445} or Cu^{2+} ^{108,379}. The choice of metal (M) in the HCF phase is observed to alter uptake behaviour in several distinct ways. Parajuli et al. 2016 observed faster uptake kinetics to a Cu HCF over an equivalent Fe HCF as well as 57 % increased uptake in an alginate-HCF composite. This was rationalised due to a greater quantity of K^+ in Cu HCF. They concluded that Cu HCF was more stable over a wide pH range, in terms of metal leaching⁴⁴⁶. It is thought that cesium absorption capacity decreases from $Co^{2+} > Ni^{2+} > Zn^{2+} > Cu^{2+} > Fe^{2+}$ ⁴⁴⁷ and this trend was also observed in a recent study by Fuks et al, achieving an uptake of 100 % to a Co HCF compared with 30 % to a FeHCF⁴⁰³.

2.5.5.1 Alginate

Alginate is the most common biopolymer paired with HCF for cesium immobilisation. It is common that a third phase is more often than not added to alginate-HCF composites for ‘reinforcement’ – added mechanical strength⁴⁴⁴ e.g. carbon nanotubes (CNTs)^{401,448}, as well as providing crosslinking and adsorption sites e.g. graphene oxide⁴⁴⁹, poly vinyl alcohol (PVA)⁴⁴⁴ or magnetite for ease of separation⁴⁰³. Gelation of alginate is often initiated via ionotropic

gelation, typically utilising divalent calcium to crosslink alginate branches. The resulting hydrogel appears to exhibit a highly macro porous structure (Figure 2-30). An innovative approach of some work removes the need for calcium as the crosslinking agent, instead employing Fe^{3+} in a dual mode as both alginate crosslinker and for in-situ precipitation of the Fe HCF phase^{201,450}. This lead to an improvement in cesium uptake. A similar approach was taken by Eun et al. 2020 with a carboxymethyl cellulose (CMC) Fe HCF composite¹¹⁰ and also Jang et al. 2016 in which aminopropyl-functionalized iron phyllosilicate bound iron was used to crosslink alginate to clay and HCF phases³³⁶. In terms of cesium uptake, the CMC composite outperforms the alginate composite substantially. Mihara et al. Compared two different synthesis routes for HCF-alginate composites (). The HCF phase of (A) was formed in-situ by immersing alginate beads containing $\text{K}_4\text{Fe}(\text{CN})_6$ in a solution of FeCl_3 , while an ex-situ preformed HCF powder was added to the sodium alginate mixture in (B). (A) showed faster uptake kinetics and a modest improvement to overall cesium uptake, likely due to better dispersion and smaller particle size of the HCF phase within⁴⁵⁰.

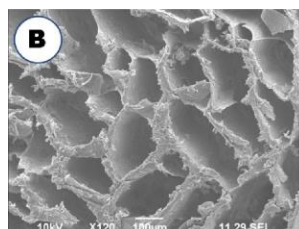


Figure 2-31 SEM Cross-sectional image of a HCF-alginate hydrogel.
Adapted from Vipin et al. 2014

The standout performer among alginate-HCF composites was a graphene-oxide HCF alginate composite, achieving 291 mg g^{-1} uptake⁴⁴⁹. The authors found a 5 wt.% HCF-GO : 4 wt.% alginate solutions to be optimal (of 1-15 %) finding that higher loadings resulted in brittle beads. Although not strictly a biopolymer, this graphene oxide composite was included owing to its similarity with high temperature biochar, which is often highly graphitic. Parajuli et al. 2016 achieve an uptake of 163 mg g^{-1} with an 80 % overall CuHCF loaded alginate hydrogel without any carbonaceous phase⁴⁴⁶. Clearly, the carbon phase has a role to play in uptake. Kim et al. 2017 report the HCF fraction as a *metal* wt.% (i.e. wt.% $\text{K}^{+} + \text{Fe}^{2/3+} + \text{Cu}^{2+}$)¹⁰⁸ finding a 57 wt.% to be more favourable than 28 or 39 % for cesium uptake. Elsewhere, HCF loadings are not specifically noted and as such it would be beneficial to standardise the reporting of this

parameter, preferably as a final mass fraction (dry or wet) since some losses may occur during wet synthesis.

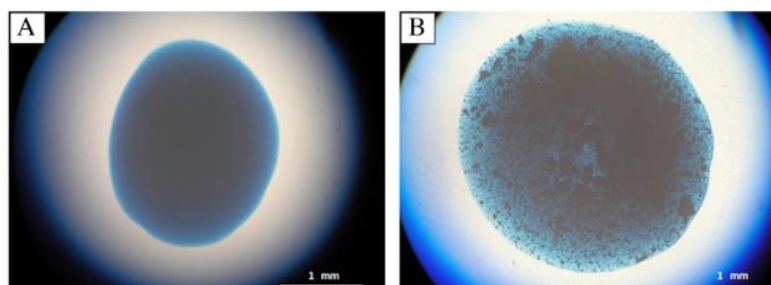


Figure 2.32 Synthesis of HCF-alginate hydrogels via an in-situ HCF synthesis (A) versus incorporation of HCF powder (B). Adapted from Mihara et al

2.5.5.2 Activated carbons

A key factor in using carbothermal materials such as biochar appears to be an activation step. For example, Tao et al. 2019 fabricated a pomelo peel biochar-Cu HCF composite with an uptake of 30 mg g^{-1} ³⁷⁹ (nonetheless performing better than its component parts), while Lalhmunsiamma et al. 2014 created a similar rice husk biochar-Ni HCF composite with roughly equivalent uptake (31 mg g^{-1})⁴⁵¹. While these results demonstrate the beneficial aspects of encapsulating HCFs in biochar composites, further functionalisation steps, such as addition of a crosslinking or complexation agent, but especially activation, can dramatically improve uptake. Li et al. 2020 created a porous cattle bone derived activated carbon-HCF composite²⁶⁰, achieving 125 mg g^{-1} cesium uptake. One of the strengths of activated carbons over unactivated analogues are their high surface area, $1884 \text{ m}^2/\text{g}$ in this case, which confers a large area over which HCFs can disperse. As the authors note, HCF performance can be dramatically affected due to poor dispersion/agglomeration in composites with low specific surface areas. This finding seems to be confirmed by the work of Adibmehr et al. 2019 who activated an oak shell carbon, forming a magnetic Ni HCF composite with an uptake of 135 mg g^{-1} ⁴⁵². As well as increased surface area, activation increases the surface functionality, mostly oxygen surface groups but also sulfur or nitrogen depending on the activation agent⁴⁵³. This may also promote good dispersibility of a HCF phase by providing a larger number of binding sites for it during composite formation, as well as playing a minor role in cesium binding.

Another interesting property of activated carbons are their electro activity, particularly the graphitic carbons generated at high temperatures. This makes carbon-based materials of interest to electrochemical immobilisation

techniques^{454,455}. The advantage of electrochemical immobilisation is that HCF phases can be synthesized in-situ rapidly by careful selection of electrode potential to direct modification and direct the immobilisation of cesium in the same process.

2.5.5.3 Chitosan

HCF-chitosan composites have been successfully magnetized, encapsulated into monolithic beads⁴⁴³, a porous sponge³⁹⁵ or immobilized into a membrane⁴⁵⁶ or to ease separation. Chitosan is known to be stable at high pH and thus is thought to enhance the stability of HCFs at high pH^{443,457}. It is also said to reduce agglomeration of tertiary phases⁴⁵⁸ and act as a “intermediate carrier” to prevent unwanted reaction between inorganic phases⁴⁵⁹. Tertiary phases are often introduced to promote crosslinking or counteract the negative effect that HCF inclusion has on mechanical stability, materials such as graphene oxide⁴⁶⁰, polyethylene glycol⁴⁵⁶ and carbon nanotubes⁴⁵⁸. Chitosan-HCF composites appear to demonstrate rapid uptake kinetics[129], good recyclability^{443,461} and good selectivity^{443,459,461} for cesium. Data tend to demonstrate that cesium is immobilized via ion-exchange in the HCF phase and also via complexation with the abundant amine and amide functional groups of the chitosan^{461,462}. Since the techniques routinely used to determine binding mechanism, such as FTIR are not quantitative, the relative contribution of each is not fully understood, especially under different ionic strength regimes. However the major contribution is likely to be ion-exchange in the HCF since studies show cesium uptake capacity is highly sensitive to the % weight fraction of HCF. This is supported by thermodynamic data which indicates the dominant mechanism is that of ion-exchange. Further to this, a magnetic-chitosan composite showed that composites lacking a HCF or similar phase performed poorly¹⁸⁶. The performance of HCFs are pH dependant, with Fe HCF performing well in acidic solution, Cu HCF in mildly acidic conditions and Ni HCF in alkaline solution^{103,457}. Another key area for study is in binding strength and reversibility. Cetin et al examined cesium uptake to a magnetic chitosan-HCF composite, finding loading actually decreased over time from > 90 % removal at 60 min to < 40 % removal at 120 min⁴⁶². This was a novel and unusual synthesis route using ZnCl₂ to create tetrahedrally coordinated Zn²⁺ to four nitrogen cyano ligands in an attempt to create a more thermally stable and more porous framework. The drop in cesium loading could be due to desorption of weakly bound cesium or possibly the leaching of the HCF phase. Applicability of the desorption test to other metal HCF (e.g. Fe HCF or Cu HCF) is not established but should be considered carefully since irreversible binding is a highly

desirable feature of radionuclide immobilisation materials. It seems as though enhancements to uptake performance and materials stability (leaching, durability and thermal stability) could also be made within innovative composite formation methods. Such processing clearly has a major impact on the accessibility and/or activity of the HCF phase, as is shown in increased uptake upon formation of composites. For example, in a treatment mimicking the activation protocols used on activated carbons, Li et al. 2016 improved the porosity of a chitosan-HCF-CNT composite via gamma radiolysis⁴⁵⁸.

2.5.5.4 Other biopolymers

Cellulose^{107,463,464} and its derivatives, hydroxyethyl cellulose (HEC)¹⁰⁸, carboxymethyl cellulose (CMC)^{109,110} are thought to provide good support onto which nano-sized HCF particles can be well dispersed. The hydroxyl groups of cellulose are not thought to play a role in immobilisation¹⁰⁷, however carboxyl groups on the more heavily functionalized CMC are found to contribute to cesium immobilization, as well as the ion-exchange contribution from the HCF phase¹⁰⁸. A 90 % selectivity for cesium in seawater was shown for a CMC/HEC-CuHCF composite¹⁰⁸. Another biopolymer of note is pectin, whose gelation properties, similarly to alginate, are of use in creating monolith composites containing and stabilizing nano-HCF^{372,465}. Of these two studies, the simpler pectin-HCF composite performed significantly more poorly than the more complex pectin-stabilized magnetic graphene oxide HCF composite⁴⁶⁵. Pectin is thought to inhibit stacking of GO sheets which promotes better dispersibility of HCF and magnetite nano particles. A green pectin-based FeHCF composite was created by Chang et al. 2018 from pectin-rich apple and pomelo peel wastes using a Co-60 γ radiation method⁴⁶⁶, eliminating the need for chemical or energy intensive reaction conditions.

2.5.5.5 Leaching

Encapsulation of HCFs in biopolymers such as alginate or chitin is thought to be reduce the leaching of metals into wastewaters⁴⁴⁹. Addition of a third phase, such as a resin has been shown to reduce leaching of Fe³⁺ from the HCF phase⁴⁶⁷. Chang et al. 2018 used colour change to assess the leaching of HCF from their biomass-HCF, finding no colour change⁴⁶⁶ while Fuchs et al. 2018 analysed process waters, finding a consistent 0.01-0.05 ppm of iron leachate from their alginic carbonyl ferrogel over three cycles⁵⁹. Leaching of metals from a brewer's yeast carbon-NiHCF composite was found to be dependent on the carbon type, as well as the leaching solution⁴⁴⁵. Minimal iron leaching was reported from a modified cellulose-CuHCF composite¹⁰⁸, while a magnetic

chitosan-HCF nanoparticle composite showed < 0.05 ppm Fe leaching at pH 2 and above⁴⁴³, showing good recyclability in repeat experiments. Although Çetin et al. 2022 didn't directly study leaching, a drop in cesium loading to their ZnHCF-chitosan composite over time was noticed which could indicate leaching of the HCF phase after 30 minutes⁴⁶².

2.5.6 Other radionuclides

Iron-biopolymer composites have also been examined for immobilisation of some actinides and other radioactive elements. As with uranium, zvi and magnetite have the ability to reduce metals such as plutonium⁴⁶⁸ or technetium³⁴⁵. Europium(III) which is used as an analogue for radioactive actinides, has been used to study uptake to magnetic biochar^{415,469} and an amidoxime functionalised magnetic chitosan composite⁴²¹. A range of metal-modified biochars were tested for technetium uptake, one of which was an iron(III) composite¹³³. A magnetic-alginate-CoHCF was also tested for Technetium uptake⁴⁰³. Cobalt immobilisation was also studied on several magnetic chitosan composites^{470–472}.

2.5.7 Future perspectives

There is a need to fully understand the mechanisms of adsorption, especially in biochar which is amorphous. The complex composition and physicochemical dynamics of such materials mean that multiple factors are often responsible for observed adsorption capacity, yet the underlying mechanisms are often unclear, leading to erroneous assumptions. For example, biochar is also known to increase the pH in aqueous media. This can lead to precipitation of some heavy metal species when it is erroneously assumed that complexation with surface functional groups is the dominant mechanism.

Chapter 3 Analytical Theory

This chapter sets out the theoretical basis for core analysis techniques employed in later results chapters.

3.1 Adsorption Isotherms

3.1.1 Isotherm models

An adsorption isotherm describes the dynamic equilibrium of adsorbate that is absorbed or in solution at a given at a range of initial adsorbate concentrations, and at a fixed temperature and pH. The Langmuir and Freundlich are among the most frequently employed in solution phase adsorption. Several authors have called for standardisation of the use of non-linearised isotherm modelling over linearized forms⁴⁷³. Therefore, non-linear forms of isotherm models will be employed in this work.

3.1.2 Langmuir

The Langmuir equation, first described in 1918⁴⁷⁴ is based on a dynamic equilibrium of an adsorbate in a solution and adsorbed to a surface, where the surface coverage, Θ (eqn 3) is:

$$\theta = \frac{\text{Number of adsorption sites occupied}}{\text{Number of adsorption sites available}} \quad (3)$$

Several theoretical assumptions underpin the model:

1. Adsorbate coverage is monolayer only
2. Each site can hold only one adsorbate ion or molecule
3. All binding sites are energetically equivalent
4. The affinity of a site is not altered by occupancy of neighbouring sites

The Langmuir equation takes the form:

$$q_e = \frac{q_m K_L C_e}{1 + K_L C_e} \quad (4)$$

Where q_e and q_m (mg/g) describe the adsorption capacity at equilibrium and adsorption capacity respectively (mg g⁻¹), K_L is the Langmuir constant and C_e the equilibrium solution concentration (mg L⁻¹)⁴⁷⁵.

3.1.3 Freundlich equation

Unlike the Langmuir isotherm model, this model describes adsorption onto a heterogeneous surface, as opposed to sites of equal energy. Nor does it

describe saturation loading of an adsorbent. It is an empirical equation without any theoretical background⁴⁷⁶. It takes the form:

$$q_e = k_F C_e^{1/n} \quad (5)$$

Where k_F is the Freundlich constant and $1/n$ is the heterogeneity factor.

3.2 X-ray techniques

3.2.1 X-Ray Absorption Spectroscopy

3.2.1.1 Background

Although the fine structure oscillations that underpin EXAFS have been observed for around 100 years, application of such data into a practical technique was first described in a seminal 1971 paper by Sayers, Stern and Lytle^{477,478}. The authors noted that the Fourier transform of the fine structure oscillations was a radial distribution function of backscattering signal around the absorbing atom, which clearly yielded information about the local structure surrounding the absorbing atom.

3.2.1.2 Theory

EXAFS is a technique by which X-rays with a fine energy resolution are used to excite a core electron and subsequently eject a photoelectron. Typically this is electrons from the $n = 1$ or $n = 2$ principal quantum number shells (denoted K, L etc.) The X-ray absorption coefficient, $\mu(E)$ is recorded as a function of incident X-ray energy I_0 according to the Beer-Lambert law (eqn 6) where I is transmitted (measured) X-ray energy and x is sample thickness through which X-rays are attenuated.

$$I = I_0 e^{-\mu(E)x} \quad (6)$$

Once incident X-rays reach the threshold energy to excite a core electron (Figure 3-1 left), a sharp increase in absorption is observed, known as the

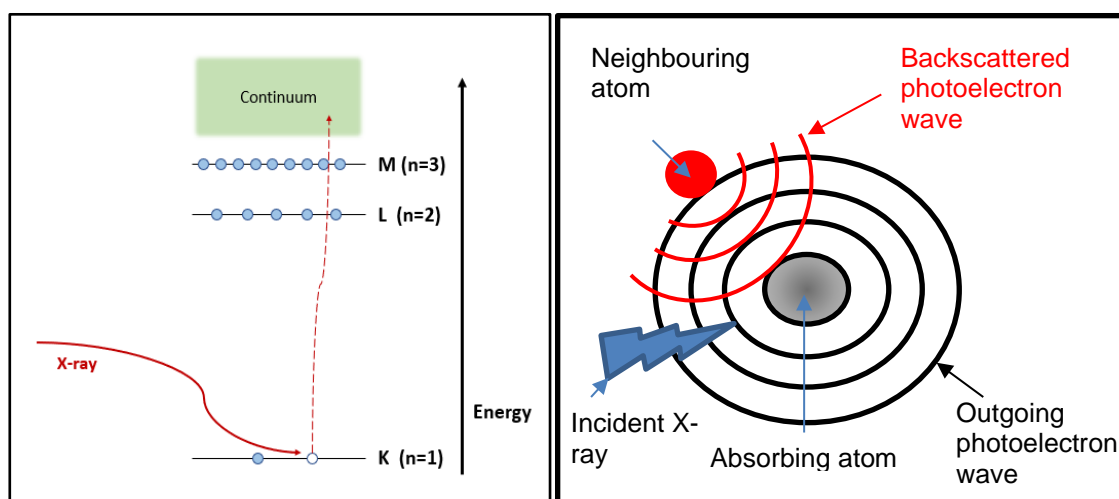


Figure 3-1 Excitation of a core electron from the K ($n = 1$) shell (left) and a schematic representation of photoelectron backscattering due to neighbouring atoms (right)

absorption edge (Figure 3-2). As incident X-ray energy is increased further, photoelectrons are ejected with kinetic energy equal to that of the incident X-rays minus the ionisation energy required to excite the core electron, $\frac{p^2}{2m} = h\nu - E_0$ where incident X-ray photo has energy $h\nu$ and the ionisation energy is E_0 . The wave-like property of a photoelectron causes backscattering of the photoelectron dependent on the local environment of the absorbing atom. In the case of an isolated atom, the outgoing photoelectron is not backscattered (Figure 3-1 right, black lines only). In the case of nearby atoms surrounding the absorbing atom, backscattering occurs (red lines) and the final state is the superposition of all outgoing and backscattered waves. This is observed as an oscillation in absorption above the absorption edge as a function of incident X-ray energy due to regions of constructive and destructive interference. Depending on the distance of neighbouring atoms, the phase of the backscattering wave will present as constructive or destructive interference. Similarly, the amplitude of backscattering, as a function of energy, depends on relative atomic mass of the backscattering atom. As such, it is possible to derive information about the binding environment of the central absorbing atom. The technique does not rely on any theoretical assumptions about solid-state atomic periodicity or symmetry and is thus as applicable to amorphous solids as to crystalline solids. Since EXAFS is fundamentally the process of exciting a core electron, it is also element specific. Therefore, it is relevant to dilute systems as well as systems that are more concentrated. A final advantage of using high energy X-rays is that penetration of X-rays through the sample yields bulk – as opposed to surface specific – measurements.

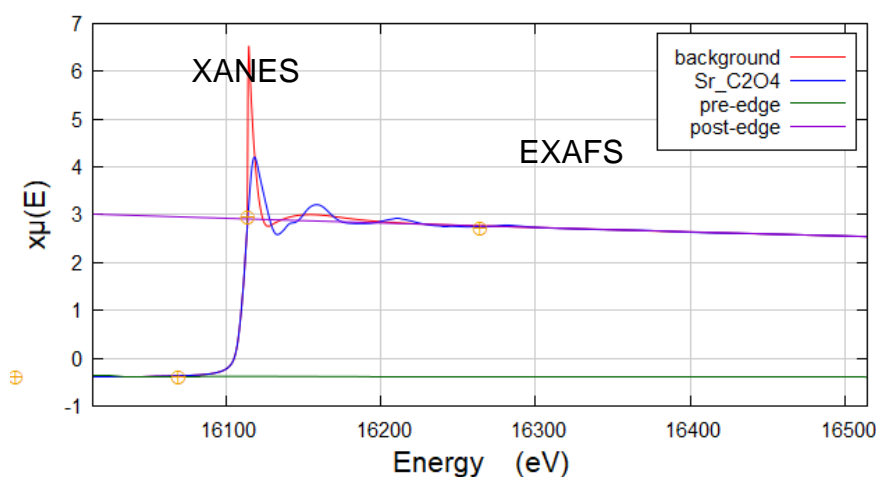


Figure 3-2 Example plot of X-ray absorption coefficient plotted with incident X-ray energy, showing the Sr K-absorption edge at 16105 keV and EXAFS or fine structure oscillations at higher energy for a strontium oxalate standard

3.2.1.3 The EXAFS equation

The X-ray Fine Structure is given by subtraction of the background function from the measured absorption data. A background removal algorithm⁴⁷⁹ is applied to remove background signal from the fine structure back scattering oscillations (eqn 7) via subtraction of the “bare atom” absorption background $\mu_0(k)$ and division by the edge step $\Delta\mu(k)$.

$$\chi(k) = \frac{\mu(k) - \mu_0(k)}{\Delta\mu(k)} \quad (7)$$

$\chi(k)$ is often multiplied by a power of k to emphasize the oscillations, e.g. $k^2\chi(k)$ (in units \AA^{-3}). For strontium, for example, k^3 -weighting is commonly used since oscillations die off rapidly in k , therefore the latter part of the k -space EXAFS requires more amplification. A complex Fourier transform (eqn 10) returns data in a form that can be quantitatively interpreted in terms of the coordination environment. The EXAFS equation (eqn 8) describes the backscattering signal of the photoelectron in terms of the scattering properties of neighbouring atoms. A systematic treatment of its derivation is published by Newville (2004)⁴⁸⁰. k is the wavenumber (\AA^{-1}), N the coordination number, R the distance to neighbouring atoms (\AA), σ^2 the Debeye-Waller factor (eqn 9), $f(k)$ is the amplitude term and $\delta(k)$ the phase shift.

$$\chi(k) = S_0^2 \sum_j \frac{N_j f_j(k) e^{-2k^2\sigma_j^2}}{kR_j^2} \sin [2kR_j + \delta_j k] \quad (8)$$

S_0^2 is the amplitude reduction factor and accounts for losses due to relaxation of electrons to the core level hole in the absorbing atom. This tends to reduce the observed EXAFS amplitude slightly and thus usually has a value of 0.7-1. The Debeye-Waller factor (σ^2) accounts for smearing of the EXAFS signal since all atoms have static disorder due to both static and thermal vibration. It is defined as the mean square relative displacement (MSRD) of the half path length

$$\sigma^2 = \langle (r - \bar{r})^2 \rangle \quad (9)$$

This term serves the additional function of correcting for discrepancy between experimentally and theoretically derived $\chi(k)$. The goal of EXAFS fitting is to model the EXAFS $\chi(k)$ which is a sum of scattering paths. This is compared to the experimental EXAFS $\chi(k)$ in order to determine the true contribution to the fine structure in terms of individual scattering paths.

$$FT(R) = \frac{1}{2\pi} \int_{k_{min}}^{k_{max}} k^n \cdot \chi(k) e^{2ikr} dk \quad (10)$$

3.2.2 X-ray Computed Tomography (XCT)

3.2.2.1 Background

'Tomography' is derived from the Greek words 'tomos', for slice and 'graph', referring to an image or depiction⁴⁸¹. X-ray computed tomography (XCT), also known as X-ray μ -tomography (X μ T) in the micron-scale working range, is similar in method to computed tomographic (CT) scanning of larger objects such as the human body in hospitals. A sample is scanned at incrementally increasing angles as it is rotated in the vertical (y) plane between 0-180 degrees.

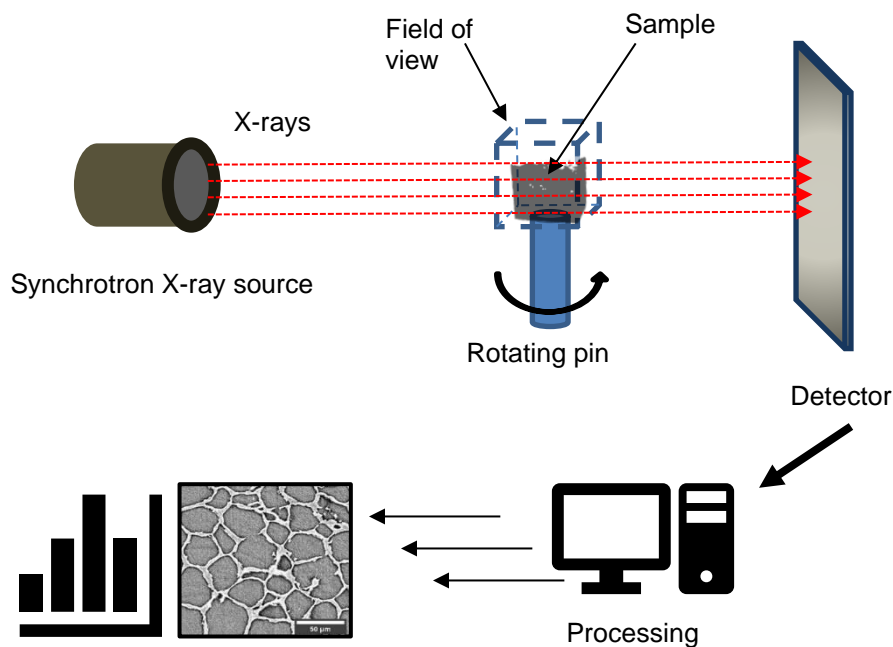


Figure 3.3 Schematic of the principle steps of the parallel beam X-ray computed tomography

As X-rays pass through the sample, they are attenuated by the sample absorbing a portion of the X-ray energy. Attenuation is measured at each distinct orientation in order to acquire projections at different angles used to construct the sinogram⁴⁸² (Figure 3-4). Regions within the sample that are distinct in density, structure or chemical composition will attenuate X-rays differently than the surroundings in accordance with the Beer-Lambert law

which relates transmitted X-ray intensity, I to incident X-ray intensity, I_0 with the attenuation coefficient μ and the path length x in equation 6. From these projections, reconstruction of a three-dimensional image of the sample is possible, including all internal and external features such as sub-structures or holes or pore space⁴⁸³. Regions with less attenuation are assigned darker greyscale colours while higher attenuation regions (i.e. denser regions of matter which scatter X-rays to a greater extent) are assigned lighter colours. The example image in depicts pore spaces in darker shades and solid sample phases in lighter shades. Based upon this greyscale distinction, it is possible to distinguish and classify pixels belonging to different phases. This is known as segmentation or thresholding and a range of methods have been employed to achieve it, most notably in the medical and geological fields. The elegance of using penetrating X-rays to image internal structures of a sample in a non-destructive manner also makes it an excellent technique for samples which are brittle and which may not withstand mechanically forceful cross-sectioning techniques. Samples containing intricate, brittle and extensive pore structure – such as biologically derived samples or biopolymers.

3.2.2.1.1 History

The development of XCT and attendant methods of analysis in two seemingly unrelated fields, medical and geological is likely no coincidence. As a non-destructive technique, the problem that XCT solves in both these fields is one of sample preparation. Alternative techniques yielding similar information are destructive e.g. cross sectioning, is not appropriate in most medical applications, and both technically challenging and expensive for geological samples. Thus, XCT was recognised as an important and unrivalled tool for 3D imaging in these fields. In medical fields where the X-ray dose and energy to the sample or patient was usually a limiting factor, high efficiency detectors⁴⁸⁴ and contrast enhancement techniques^{485,486} were developed. In geological settings where sample dose was often not a consideration, high energy X-rays and longer exposure times were employed. This led to gains in imaging resolution as smaller detectors could be used. Taud et al. 2000⁴⁸⁷ and Ketcham et al. 2001⁴⁸⁴ discuss and develop the use of XCT in geological applications. At this time, automated segmentation was in its infancy but has developed rapidly since. There are numerous experimental configurations and processing and reconstruction variations that exist within the family of 'tomography'. What follows is a description of the working principles of parallel beam full-field X-ray tomography with an iterative reconstruction algorithm. Initially used as a qualitative tool for visual appraisal of 3D structures and features, computing

power has increased the potential in the last 10-15 years for quantitative image processing. As quantitative analysis has come to the fore, a rapid proliferation of software tools and techniques⁴⁸¹ have been developed to explore density or phase changes, analysis of structures and sub-structures. The quantitative aspect of XCT has dramatically altered the potential of the technique to analyse and appraise materials and structures.

3.2.2.2 Outline of procedure

The basic steps involved in acquisition and pre-processing necessary to achieve 2D or 3D tomographic reconstruction of a sample are as follows:

Acquisition

X-rays are attenuated due to passing through the sample and are collected (projections) using a detector at incremental rotations, typically through 0-180° (). During measurement, there are several sources of erroneous and/or spurious signal pertaining to background signal. That is, the signal which the detector registers which does not pertain to signal from X-ray attenuation of the target sample. Dark current is so-called as it is a signal which is detected in the absence of any source X-rays. This includes 'true' dark current, which is proportional to the exposure time, and the digitization offset which is independent of exposure time. A flat field correction is also usually later applied during processing which accounts for and cancels the pixel-to-pixel variation in acquired signal. This involved acquisition of signal with X-ray source on, but without any sample present. The variation in the flat field can originate from non-uniformity from the incident X-ray beam e.g. due to defects in the X-ray beam beryllium window, non-uniform response of the scintillator and non-uniform response of the detector.

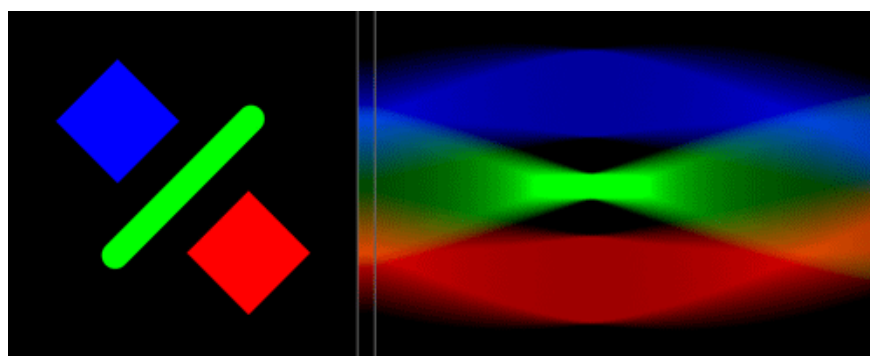


Figure 3-4 As the sample (left, plan view) is rotated through 180° and exposed to X-rays, a sonogram (right) is generated from the attenuated signal. This represents the sequential X-ray signals at all projections or orientations between 0-180°

Determination of the centre of rotation (CoR) value

Finding the centre of rotation is crucial for accurate reconstruction of samples from sinogram projections. This can be done by a trial-and-error process but more recently a number of attempts to automate the process have been developed, such as using the centre of mass calculation, digital alignment or image registration, by using image metrics on the reconstruction space or based upon Fourier analysis of the sinogram⁴⁸⁸. Due to artefacts, optical errors or sample considerations, certain methods may prove more optimal, depending on the precise set up in question.

Reconstruction

Reconstruction is the process by which information from the sinogram is deconvoluted into the precise properties at all spatial points, which correspond to the those of the sample. As with CoR determination, a number of algorithms have been developed for reconstruction. Similarly, experimental constraints, artefacts or sample considerations can make this a challenge. Filtered back projection (FBP)^{489,490} is by far the most commonly used reconstruction technique⁴⁸¹ due to its reliability and well understood process. The basis for this is the inverse Radon transform (eqn 11) where f is the filtered data. This projects the data in the form of line integrals back onto the plane at their appropriate angles to reconstruct 2D images ().

$$f(x, y) = \int_0^{\pi} f'(x \cos \theta + y \sin \theta, \theta) \quad (11)$$

Iterative back projection and deep machine learning are two other notable examples which contain in-built noise reduction processing. A number of filters are often applied at this stage, such as ring artefact suppression and flat field correction, which remove optical experimental and reconstruction related errors from the images.

Analysis

Once 2D or 3D data set has been reconstructed, it can be interrogated in a wide variety of ways. Quantitative methods of processing 2D and 3D volumes of data have come to the fore of late⁴⁸¹, largely due to the availability of increased computing resources which large data sets such as tomographic data demands.

3.2.2.3 Advantages of synchrotron X-rays for X-ray tomography

Synchrotrons are capable of generating highly collimated, high resolution, polarised X-rays with a far higher flux, or brilliance, than laboratory X-ray sources. This increased flux allows synchrotron X-ray sources to bypass certain

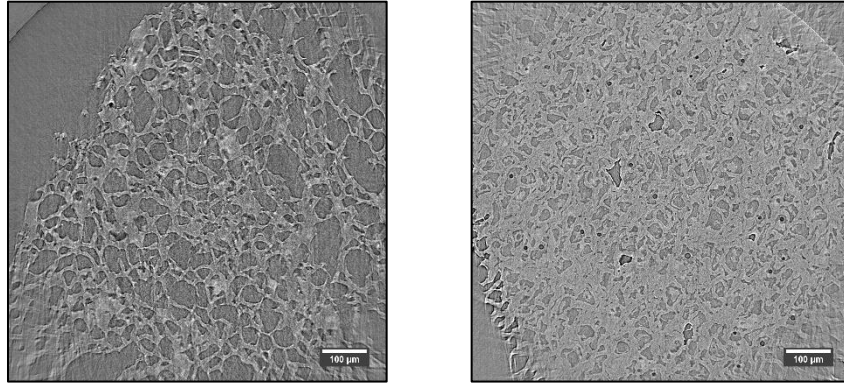


Figure 3.5 Examples of reconstructed 2D images

errors in the tomography acquisition process e.g. beam hardening artefacts that can be introduced by using a polychromatic beam⁴⁸³. Beam hardening describes the tendency of higher energy X-rays in a polychromatic (“white beam”) to absorb differently to lower energy X-rays, causing signal discrepancies. Further, the tunability and selectability of the X-ray energy also allows for element-specific examination of a sample via comparison of data above and below the target element absorption edge. A number of different acquisition modes are also possible, such as phase contrast or adsorption contrast mode depending on the suitability of the sample in question. Nonetheless, synchrotron X-ray sources are not without error either and can be subject to uneven pixel responses (ring artefacts)⁴⁸¹, super saturation and super penetration⁴⁹¹ errors, all of which must be corrected for or minimised by careful setup of acquisition parameters.

Chapter 4 Materials and Methods

4.1 Introduction

Three biomass types were selected as biochar precursors (). The choice of feedstocks were based upon several criteria. Firstly, to ensure that this work satisfied the requirement for sustainable materials, it was important to include at least one feedstock which is viewed as a waste material, in line with circular economy principles. Both rice husks and spent coffee grounds meet this criteria. A review of literature which indicated the suitability of certain feedstocks for creating of biochar most suited to adsorptive removal of cations. Rice husk biochars consistently generated biochar with good strontium uptake capacities (as reported in Section 2.2.3.2). Spent coffee ground biochar likewise has reported good cation uptake capacities. Both oakwood and rice husk are standard types of biochar, as categorised by the Biochar Research Centre, Edinburgh⁴⁹², which was another motivation for these decision to select these feedstocks over others. Availability and sourcing of feedstocks was another important factor, because replenishing stocks of a certain feedstock could result in a biomass batches with variable properties. Sufficient quantities of all three of the selected biomasses was assured. Finally, the three feedstocks were deemed sufficiently distinct from one another in terms of cellulose, hemicellulose, lignin and inorganic composition (Table A-1). It was hoped that these differences would translate to distinct adsorption behaviour.



Figure 4.1 Feedstocks selected for comparison in tomographic pore space analysis

4.2 Biopolymer composites synthesis

4.2.1 Biochar

All biomass feedstocks were rinsed repeatedly in ultrapure water (resistivity $\geq 18.2 \text{ M}\Omega \text{ cm}$) and dried at $105 \text{ }^\circ\text{C}$ and ambient pressure before further use, in order to remove any water-soluble organics. Rinsed biomass was stored under desiccant until pyrolysis. Feedstocks used were as follows: Rice husks (origin: northern Thailand), oak wood chips sourced via the UK Biochar Research Centre, Edinburgh and spent coffee grounds (single origin *coffea arabica*), sourced locally in Leeds, UK.

All biochars, activated or not, were produced in a fixed bed, vertical loading pyrolysis reactor at $450 \text{ }^\circ\text{C}$ (with one exception, see Section 4.2.1.1) using a ramp rate = $5 \text{ }^\circ\text{C min}^{-1}$, dwell time = 1 h under an N_2 flow rate of 140 mL min^{-1} . The resulting biochar was mechanically milled and sieved to $\leq 50\mu\text{m}$.

4.2.1.1 Biochar production for tomography

Biochar samples for tomography did not undergo ball milling in order to preserve the macro pore structure. The expanded tomography sample set was produced as above (at $450 \text{ }^\circ\text{C}$ using a ramp rate = $5 \text{ }^\circ\text{C min}^{-1}$, dwell time = 1 h under an N_2 flow rate of 140 mL min^{-1}) however the initial investigation tomography sample set (Section 4.6.1) were produced at $350 \text{ }^\circ\text{C}$. Namely SCG350 and SCG350-Zn. All other pyrolysis parameters as above.

4.2.2 Biochar activation and functionalisation protocols

4.2.2.1 Nitric acid activation

Activation followed an optimised nitric acid treatment process as reported previously¹¹³ and employed for enhancing cation uptake^{493,494}. Ball milled biochar is weighed (5g) into a clean and dry 250 mL round bottomed flask and a magnetic stirrer flea is added. 8 M nitric acid solution (125 mL) is added slowly under vigorous stirring, giving a final ratio of biochar to nitric acid of 1 g biochar : 25 mL nitric acid. The suspension is heated under reflux to $80 \text{ }^\circ\text{C}$ for 3 h under vigorous stirring. After the suspension has cooled, the spent nitric acid solution is removed by vacuum filtration. The activated biochar undergoes a comprehensive rinsing protocol to remove acidic residues. The activated biochar is re-suspended in 1 L of ultrapure water (resistivity $\geq 18.2 \text{ M}\Omega \text{ cm}$) and agitated on a horizontal orbital shaker for 24 h, before vacuum filtration followed by rinsing with 3 x 150 mL aliquots of ultrapure water. The resulting activated

biochar is dried at 105 °C and ambient pressure before being stored under desiccant.

4.2.2.2 Zinc (II) chloride activation

Zinc (II) chloride hexahydrate ($\text{Zn}\cdot\text{Cl}_2\cdot\text{H}_{12}\text{O}_6$) was weighed in a 2:1 weight ratio with dry biomass (2 g ($\text{ZnCl}_2\cdot 6\text{H}_2\text{O}$) : 1 g biomass) and mixed in a minimum of ultrapure water to form a slurry which was left to mix to homogeneity for 3 h under magnetic stirring. The mixture was transferred to an oven and dried overnight at 105 °C before being pyrolyzed following the protocol above. The resulting biochar was rinsed in 0.5 M HCl solution to remove latent Zn^{2+} before being dried and stored under desiccant. This activation protocol follows literature reported methodology^{75,130,495}.

4.2.2.3 EDTA activation

Disodium ethylenediaminetetraacetate dehydrate (EDTAD, $\text{C}_{10}\text{H}_{14}\text{N}_2\text{Na}_2\text{O}_8\cdot 2\text{H}_2\text{O}$), 1g, was added to 1 g of milled biochar in a 250 mL round bottomed flask with 100 mL of DMF (N,N-Dimethylformamide) and magnetically stirred at 60 °C for 4h with a few drops of H_2SO_4 10% in a modified esterification reaction⁴⁹⁶. Upon completion, vacuum filtration removed spent solvent. The resulting EDTA-grated biochar was rinsed with 2x20 mL DMF, 3x20 mL Na_2CO_3 to remove acidic residues and 3x20 mL of ultrapure water before being transferred to an oven and dried overnight at 105 °C. The EDTA grafted biochar was then stored under desiccant.

4.2.2.4 MnOx activation

This method followed a previously reported procedure by Wang et al. 2015¹⁷⁸. Briefly, 3.15 g KMnO_4 was dissolved in 50 mL of ultrapure water with 5 g of biochar and magnetically stirred for 2 h. The suspension was then held at the boiling point for 20 min, followed by a drop wise addition of 3.3 mL of concentrated HCl. The mixture was stirred under heating for a further 10 min before being allowed to cool to room temperature and filtered under vacuum. The resulting Manganese oxide-biochar composite was rinsed with 3x50 mL of ultrapure water then dried overnight at 105 °C and stored under desiccant.

4.2.2.5 FeOx activation

FeOx moieties were introduced following previously reported methodology³⁶⁵ Iron(III)chloride salts ($\text{FeCl}_2\cdot 6\text{H}_2\text{O}$) were dissolved in a minimum of ultrapure water to which biochar was added under stirring to form a mobile slurry. The weight ratio of iron salt to biochar was 1:1. The slurry was left to stir for 3 h then

placed in a drying oven and left to dry overnight before being pyrolyzed as above.

4.2.2.6 Control biochar

Control biochar for the above protocols in Section 4.2.2 was prepared by suspending and stirring 10 g of biochar (BC) in 100 mL ultra-pure water for 12 h, before filtration. This was then dried overnight at 105 °C before storage in a sealed container under desiccant until further use.

4.2.3 Hydrogel preparation

Sodium alginate (medium viscosity, 0.75 g) was stirred in 99 mL of ultrapure water for 24 h. Biochar (3 g) was added in a 1:0.25 ratio and the mixture was stirred for a further 24 h at 25 °C. The suspension was then agitated for 1 h in a sonic bath to ensure homogeneity. Aliquots of the BC-alginate suspension were then added dropwise to a 500 mL, 0.1 M calcium chloride solution under slow stirring (50 rpm). The resulting biochar-alginate beads were left to equilibrate for overnight then rinsed thoroughly with ultrapure water before being freeze-dried until dry and finally stored in airtight containers over desiccant until further use: samples were frozen at -20 °C overnight before being placed in a pre-cooled freeze drying chamber for 24 h at -58 °C and < 0.0006 bar. This method followed a previously reported method by Jiang et al. 2018²¹¹.

Alginate only beads (ALG) were created as a control, which was prepared as above excepting one modification. 8 g sodium alginate was dissolved in 300 mL water. It was necessary to alter the ratio of alginate: water both to account for the lack of biochar and to reduce the viscosity, which was too high to allow the above drop-wise ionotropic gelation.

4.3 Physical characterisation

4.3.1 Elemental Analysis

Around 3 mg of sample was precisely weighed and analysed using a Thermo Scientific Flash EA2000 organic elemental analyser for C, H N and S content. Oxygen analysis required around 4-5 mg per sample. All samples were run in duplicate, unless significant deviation was observed, in which case additional samples were prepared. Standards (Oatmeal and 2,5 Bis(5 tert butyl 2-benzo-oxazol-2-yl) thiophene (BBOT)) and blank capsules were run prior to measurement. Oxygen content was measured separately on the same equipment.

Van Krevelan diagram values were calculated by converting weight percent (wt%) values experimentally determined into atomic percent (at%) values via the following equations 12 and 13. The numerical values correspond to each element's relative atomic mass (RAM) (g mol^{-1}).

$$\text{At}\% \text{O}/\text{C} = \frac{\text{Wt}\% \text{Oxygen} / 15.999 \text{ g mol}^{-1}}{\text{Wt}\% \text{Carbon} / 12.001 \text{ g mol}^{-1}} \quad (12)$$

$$\text{At}\% \text{H}/\text{C} = \frac{\text{Wt}\% \text{Hydrogen} / 1.01 \text{ g mol}^{-1}}{\text{Wt}\% \text{Carbon} / 12.001 \text{ g mol}^{-1}} \quad (13)$$

4.3.2 Fourier Transform Infrared Spectroscopy (FTIR)

Biochar and hydrogel samples spectra were acquired on a Bruker Vertex V80 FT-IR spectrometer. Data processing was completed in Origin Pro.

4.4 Strontium uptake experiments

Strontium chloride hexahydrate ($\text{SrCl}_2 \cdot 6\text{H}_2\text{O}$) was purchased from Sigma Aldrich and stored under desiccant. This was used in the preparation of all subsequent strontium solutions.

4.4.1 SEM-EDX

Samples were mounted on carbon adhesive tape before low pressure measurement on a Carl Zeiss EVO MA15 microscope coupled with an Oxford Instruments AZtecEnergy EDX system with a CZ STEM detector.

4.4.2 Preliminary comparison of strontium uptake for several functionalised/activated biochars

Respective adsorbents (0.2 g) were weighed precisely into 100 mL Erlenmeyer flasks. Strontium stock solution, 50 mL of a 33 mg L^{-1} in deionised water, was quickly added to each flask, which was then sealed using parafilm and placed on a horizontal orbital shaker at 150 rpm. Samples were removed after 24 h and immediately filtered under vacuum. The filtered liquor was stored for AAS analysis of the remaining Sr^{2+} content. Laboratory temperature was monitored throughout to be $20 \pm 1.5 \text{ }^\circ\text{C}$.

4.4.3 Kinetic investigation of biochar and activated biochar

Respective adsorbents (0.2 g) were weighed precisely into 100 mL Erlenmeyer flasks. Strontium stock solution, 50 mL of a 100 mg L^{-1} in deionised water, was

quickly added to each flask, which was then sealed using parafilm and placed on a horizontal orbital shaker at 150 rpm. Samples were removed and immediately filtered under vacuum at the following time points post commencement: 30, 60, 180 and 360 minutes. Each time point was run in duplicate. The filtered liquor was stored for AAS analysis of the remaining Sr²⁺ content. Laboratory temperature was monitored throughout to be 20 ± 1.5 °C. Sorption kinetics were examined using the linear forms of the pseudo first (eqn 14) first reported by Lagergren in 1898⁴⁹⁷ and pseudo second (eqn 15) order equations as derived by Ho and McKay 1999⁴⁹⁸, where q_e is the maximum sorption capacity (mg/g) and q_t (mg/g) is the quantity of contaminant adsorbed at time t . The first and second order rate constants are k_1 (1/min) and k_2 (g/mg/min) respectively.

$$\ln(q_e - q_t) = \ln q_e - k_1 t \quad (14)$$

$$\frac{t}{q_t} = \frac{1}{k_2 \times q_e^2} + \frac{t}{q_e} \quad (15)$$

These kinetic models are

4.4.4 Strontium uptake isotherms

Respective adsorbents were weighed (0.2 g) into a sterile 50 mL centrifuge tube, before 2 mL of a 0.2 M MOPS (3-(N-morpholino)propanesulfonic acid) buffer was added and the system left to equilibrate for 12 h. Aliquots of a 1000 ppm Sr²⁺ stock solution (from SrCl₂·6H₂O) and 0.2 M MOPS buffer solution (pH 7) were quickly added to make the solutions up to 50 mL. Isotherms in Sections 6.1.1 and 6.1.2 used initial concentrations of 5, 25, 50, 75, 100, 150, 200, 250, 300, 400, 500 mg L⁻¹ Sr²⁺. Isotherms in Sections 0 and 0 used initial concentrations of 5, 25, 50, 75, 100, 150, 200, 250, 300, 400, 500, 1000, 3000 and 6000 mg L⁻¹ Sr²⁺. Each concentration value was completed in triplicate. Each sample was placed on a horizontal shaker at 150 rpm for 24 h before being filtered through a 0.45 µm cellulose syringe filter. The resulting solution was acidified to 2 % nitric acid and the remaining Sr²⁺ concentration measured via ICP-MS.

4.4.5 Atomic Absorption Spectrophotometry (AAS)

Initial uptake experiments were analysed via AAS in order to determine strontium concentration remaining in solution. An acetylene flame was used with a Strontium filament lamp. The carrier solution was mixed with a saturated

KCl solution in order to minimise matrix effects. The acetylene flame was oriented at 45° in order to extend the working range of the instrument. Samples were auto-diluted x10. Due to a degree of 'drift' in measurements over time, use of AAS for analysis was phased out in favour of ICP-MS which is capable of much higher precision.

4.4.6 Inductively-Coupled Plasma Mass Spectrometry (ICP-MS)

Strontium concentration in solution was measured using inductively-coupled plasma mass spectrometry on a PE Elan DRCe ICP/MS. Solutions were diluted x10-50 in order to achieve concentrations in the instrument working range. Calibration standards of 1, 10, 50, 100, 1000, 10000 and 15000 ppb Sr²⁺ were run every 10 measurements. External standards were also made up at every initial strontium concentration used in uptake experiments. Data analysis was completed in MS excel.

4.4.6.1 Uptake equations

Strontium loading on the adsorbent, q_e (mg/g) is given by eqn 16 which is derived using experimentally determined solution concentration, C_e (mg L⁻¹), initial strontium solution concentration C_i (mg L⁻¹), solution volume V (L) and adsorbent mass, m (g).

$$q_e = \frac{(C_i - C_e)V}{m} \quad (16)$$

The non-linear versions of the Langmuir (eqn) and Freundlich (eqn) isotherm models were employed and compared.

The decontamination factor, DF is derived by eqn 17, the initial strontium concentration divided by the final strontium concentration.

$$DF = \frac{[Sr^{2+}]_i}{[Sr^{2+}]_f} \quad (17)$$

4.5 X-ray Absorption Spectroscopy

4.5.1 Strontium EXAFS

Strontium-loaded samples were retained from batch uptake experiments. Samples were rinsed in 15 mL UHQ on filter paper to remove any surface precipitated strontium. Samples were then dried overnight at 105 °C before being ball milled and pressed into 6 mm pellets using a 20 wt% Cereox binder. EXAFS spectra were collected at B18, Diamond Light Source, UK in 2021. The

strontium K-edge (16105 eV) was measured in transmission mode at 77 K, as well as at room temperature, using a Si(111) monochromator. X-ray energy was calibrated using an yttrium foil (Y K-edge energy = 17038.4 eV). A minimum of three measurements (scans) were taken per sample. Standards measured were Strontium oxalate, strontium sulfate, strontium carbonate and strontium hydroxide.

The Demeter package was used for data reduction and background removal. Calibration and alignment of individual scans was completed using a reference standard (Strontium oxalate) in Athena before merging and deglitching was completed. Low temperature (LT) measurements were observed to exhibit improved spectral resolution with larger amplitudes of some spectral features, therefore LT scans were selected for EXAFS fitting. k^3 weighted fitting of the Fourier transform was completed in Artemis. A shell-by-shell approach to fitting was undertaken in order to examine the degree of inner or outer sphere complexation²²⁶. Fitting of standards yielded an optimum value of the amplitude reduction factor, S_0^2 , to be 1.0 ± 0.03 , which is in close agreement with several literature values^{215,235}.

4.5.2 Manganese XANES

Manganese K-edge XANES measurements were acquired at beamline 10-BM at the Advanced Photon Source, Argonne National Labs, USA. Transmission spectra were acquired at room temperature at 6539 eV using a 4-element Vortex SDD detector. The Demeter package was used for data reduction and background removal. Calibration and alignment of individual scans was completed using a reference standard in Athena before merging and deglitching was completed.

4.6 X-ray Computed Tomography (XCT)

4.6.1 Initial investigation

4.6.1.1 Acquisition parameters

An initial investigation with three samples was conducted: a spent coffee ground biochar (SCG350), its biomass precursor (SCG biomass) and a zinc activated analogue (SCG350-Zn) (see Section 4.2.1.1 for preparation method). Samples were mounted to pins and magnetic holders with a sparing quantity of cyanoacrylate adhesive (Figure 4-1). Samples were scanned on beamline i13-2 at Diamond Light Source, Harwell, UK in December 2018. A mono beam of 14 keV energy was used in absorption contrast mode. A pco.edge 5.5 scintillator-coupled detector was used at x10 magnification and giving an effective pixel size of 0.325 μm , a field of view of 0.83 x 0.70 x 0.7 mm. The angular resolution was 0.082°.



Figure 4-2 Photographic image of biochar sample SCG350 mounted to a pin and magnetic contact for tomographic image acquisition

4.6.1.2 Pre-processing - reconstruction

Raw data (.nxs files⁴⁹⁹) were first reconstructed into stacks of 2159 2D images (2268 x 2268 pixels) using 'Tomo Recon'⁵⁰⁰, a GPU cluster-based code written by Diamond Light Source. This allows for a user-led trial-and-error selection of the centre of rotation (CoR) value. Image bit-depth was reduced to from 16-bit to 8-bit using Tomo Recon to reduce the computational burden during subsequent processing. Volume used for quantitative analysis = 200 μm^3

4.6.2 Expanded Sample Set

Three biomass feedstocks were selected for comparison, oak wood (OAK), spent coffee grounds (SCG) and rice husk (RH), as summarised in . These

were chosen as commonly utilised feedstocks in biochar production, and as waste biomass from other processes such as food production. Further, SCG was used in the preliminary study (Section 8.1) at a lower pyrolysis temperature thus providing a means to compare the effect of pyrolysis temperature. Three common activation protocols were applied to all three feedstocks, yielding twelve biochar samples and three control samples, displayed in a matrix (Table 4-1). Activation protocols are described in Section 4.2.2.

4.6.2.1 Acquisition parameters

Samples were scanned on beamline i13-2 at Diamond Light Source, Harwell, UK in December 2018 using an automated 'robot' sample manipulator. A mono beam of 14 keV energy was used in phase contrast mode. A pco.edge 5.5 scintillator-coupled detector was used at x10 magnification and giving an effective pixel size of 0.325 μm , a field of view of 0.83 x 0.70 x 0.7 mm. The angular resolution was 0.072°.

4.6.2.2 Pre-processing - reconstruction

Raw data (.nxs files) were first reconstructed into stacks of 2159 2D images ((2268 x 2268 pixels). This was done via the Savu pipeline⁵⁰¹ using sample subsets to manually find and refine the centre of rotation value. Image bit-depth was reduced to from 16-bit to 8-bit, also using the Savu pipeline to reduce the computational burden during subsequent processing. Volume used for quantitative analysis = 350 μm^3

4.6.2.3 Processing methodology and development

Although qualitative examination of the pore structure was possible with basic pre-processing, several further processing steps were required for artefact removal such as ring suppression but most crucially in this case contrast enhancement, without which automated distinction between pore space and sample was inadequate due to poor image contrast (Figure 7-1). While direct application of automated pore space measurement techniques is typically possible for many material types, the low average atomic mass in biochar (which is around 80 % carbon) reduces X-ray absorption and resulting image contrast (between pore space and solid sample). Image contrast was insufficient to directly apply automated pore space quantification to these data. Two processing pathways were developed in parallel, with the results compared. This was to ensure that processing did not alter the results, since some contrast enhancement techniques are known to over or underestimate pore space. Details of the method development are discussed in Chapter 8.

Table 4-1 Sample matrix displaying samples for expanded sample set

	Control biomass	Control biochar	HNO ₃ activated	ZnCl ₂ activated	KMnO ₄ activated
Oakwood OAK					
Rice husk RH					
Spend coffee grounds SCG					

Chapter 5 Chemical characterisation: composition and functional groups

5.1 Elemental Analysis

5.1.1 Biochars and activated biochars

C, H, N, O and S weight % values of biochars, activated biochars and their feedstock precursors are shown in Table 5-1. It is typical for biochars to contain a significantly higher carbon fraction compared with their biomass precursors, with between 1.5 and 2.2 times more wt % carbon in biochar as compared with their respective biomasses. Pyrolysis is a thermally induced decomposition process resulting in loss of predominantly heteroatoms in the form of volatiles such as NO_x, SO_x, H₂O, as well as some CO, CO₂ and other gaseous species. This results in reduction of the non-volatile carbon phase via condensation reactions, resulting in a largely aromatic carbon rich material. Thus, elemental analysis is a useful indicator of the progression of pyrolysis, and the degree of carbonisation (Figure 5.1). Carbon weight fraction in all three unactivated biochars falls between 75-80 %, which is consistent with established pyro processing wisdom¹. In contrast to this trend for carbon, common heteroatom percent weight is typically reduced during pyrolysis, and this is observed in Table 5-1, with a handful of exceptions noted below. Surface functionality (and thus heteroatom abundance) is usually the most important factor for cation adsorption performance. As such, although loss of heteroatoms is undesirable, it is a known effect of pyrolysis, which more importantly transforms the biopolymer precursor into a recalcitrant and highly porous material. All three unactivated biochars show relatively consistent oxygen content (7.2–8.1 % wt) which is typical for biochars created at this relatively low pyrolysis treatment temperature of 450 °C⁴⁹². Nitrogen content varies with precursor feedstock but tends to fall between 0-3 wt%. Spent coffee grounds and rice husk biomass are typically higher in nitrogen content⁵⁰⁴ while oak wood biomass typically contains < 1 wt% N⁵⁰⁵. With the oak wood feedstock, pyrolysis apparently causes a slight drop in N weight fraction, 1.1 % to 0.9 % (although this is within experimental error of 0.2 %). With spent coffee and rice husk, nitrogen weight fraction is increased after pyrolysis, likely due to loss of considerably more oxygen and carbon. Activation has altered the chemical composition of the biochars, in some cases considerably so.

Table 5-1 Percent weight content of biochars, activated biochars and their feedstocks. Uncertainty is one standard deviation

		Wt %						
		C	O	H	N	S	molar O/C	molar H/C
Oak	biomass	42.6 ± 0.36	31.7 ± 0.62	4.1 ± 0.07	1.1 ± 0.21	0.00	0.56	1.15
	biochar	75.2 ± 0.07	8.1 ± 0.14	1.9 ± 0.01	0.9 ± 0.01	0.00	0.08	0.30
	HNO ₃ activated	63.2 ± 0.13	16.2 ± 0.09	1.7 ± 0.02	3.6 ± 0.00	0.00	0.19	0.32
	ZnCl ₂ activated	51.7 ± 0.19	2.8 ± 1.01	1.5 ± 0.22	0.7 ± 0.07	0.00	0.04	0.34
	KMnO ₄ activated	72.5 ± 0.5	8.6 ± 0.24	2.2 ± 0.3	0.8 ± 0.00	0.00	0.09	0.36
Spent Coffee	biomass	51.6 ± 1.44	29.2 ± 1.26	5.6 ± 0.22	2.3 ± 0.11	0.00	0.43	1.28
	biochar	76.6 ± 0.69	7.2 ± 0.05	2.6 ± 0.11	3.4 ± 2.2	0.00	0.07	0.41
	HNO ₃ activated	70.9 ± 1.13	10.6 ± 0.10	1.6 ± 0.06	6.3 ± 0.07	0.00	0.12	0.21
	ZnCl ₂ activated	80.0 ± 1.02	5.2 ± 0.19	1.7 ± 0.04	3.0 ± 0.04	0.22	0.05	0.25
	KMnO ₄ activated	75.4 ± 1.92	7.0 ± 0.05	2.6 ± 0.06	3.8 ± 0.01	0.00	0.07	0.41
Rice husk	biomass	36.2 ± 0.34	24.9 ± 0.25	3.9 ± 0.02	1.1 ± 0.09	0.00	0.52	1.27
	biochar	79.4 ± 0.24	7.5 ± 0.03	2.7 ± 0.24	3.3 ± 0.39	0.00	0.07	0.40
	HNO ₃ activated	69.8 ± 0.25	12.9 ± 0.28	1.7 ± 0.00	6.3 ± 0.05	0.00	0.14	0.30
	ZnCl ₂ activated	58.9 ± 0.03	3.4 ± 0.05	1.3 ± 0.02	1.0 ± 0.02	0.00	0.04	0.25
	KMnO ₄ activated	36.9 ± 0.37	8.3 ± 0.22	1.4 ± 0.03	0.9 ± 0.01	0.00	0.17	0.45

5.1.2 Nitric acid activation

Activation via HNO_3 consistently increases oxygen content in biochar, regardless of biomass precursor type types. HNO_3 activation doubles oxygen content in oak biochar from 8.1 to 16.2 wt%, in rice husk biochar from 7.5 to 12.9 wt%, while in spent coffee the increase is 7.2 to 10.6 wt%. Nitric acid treatment roughly doubles the O/C molar ratio of the biochars (also listed in Table 5-1). The types of oxygen functional groups that are added have been shown to predominantly consist of carboxylates as well as lactones, carbonyls and hydroxyls. HNO_3 also slightly increases nitrogen content in the activated biochars by around 3 %, over unactivated biochar controls. The increase is thought to be accounted for by oxidation reactions which variously add nitro, nitroso, amine, amide, imine and pyridinic groups to aromatic (graphitic) carbon^{113,146,147}.

5.1.3 Zinc (II) chloride activation

ZnCl_2 activation does not appear to have increased oxygen content in oak, spent coffee or rice husk biochars. Rather, this activation protocol appears to have reduced not only oxygen percent weight but also reduced the carbon percent weight in oak and rice husk by roughly 20 % (spent coffee shows a much smaller increase of around 3 %). The likely reason for this unusual trend is due to the preparation protocol (Section 4.2.2.2) which was optimised for X-ray μ -tomography. The result of this is the ZnCl_2 activated biochar is rinsed repeatedly in hot water in order to remove zinc post activation, which was adopted in order to ensure the integrity of tomographic results (Chapter 8). These data investigate the effect of the activation agent on macro pore structure.

5.1.4 Potassium permanganate activation

As with the above ZnCl_2 activation, the carbon wt% decreases upon activation, strongly indicating an increase in inorganic content which not accounted for in CHNOS wt% analysis. A small increase in wt% oxygen is observed upon activation in oak wood (0.5 wt %) and rice husk (0.8 wt%) biochars while a small decrease (-0.2 wt%) is observed in spent coffee ground biochar. KMnO_4 is a strong oxidiser therefore readily attacks most materials and adds oxygen surface functionality. The second action of this protocol is that it dopes or impregnates manganese oxides into the biochar pore structure. It is likely that the modest increases in oxygen content reflect the oxidising action of the protocol only, and not the added oxygen content due to the addition of

manganese oxide phases, due to the magnitude of the change. The oxygen analysis equipment uses a 900 °C (1173 K) temperature to volatilise all oxygen in the sample. Decomposition of pure MnO₂ (Mn⁴⁺) proceeds at around 482 °C (756 K), while Mn₂O₃ (Mn³⁺) begins to decompose only above 940 °C (1213 K)^{506,507}. The fact that no significant increase in oxygen content is detected with this activation protocol is highly suggestive that the MnO_x phase present is not decomposing at 900 °C, thus the Mn speciation is likely to largely if not wholly Mn³⁺ and/or Mn²⁺. Speciation of manganese is discussed further in Section 7.3

5.1.5 Van Krevelan diagram

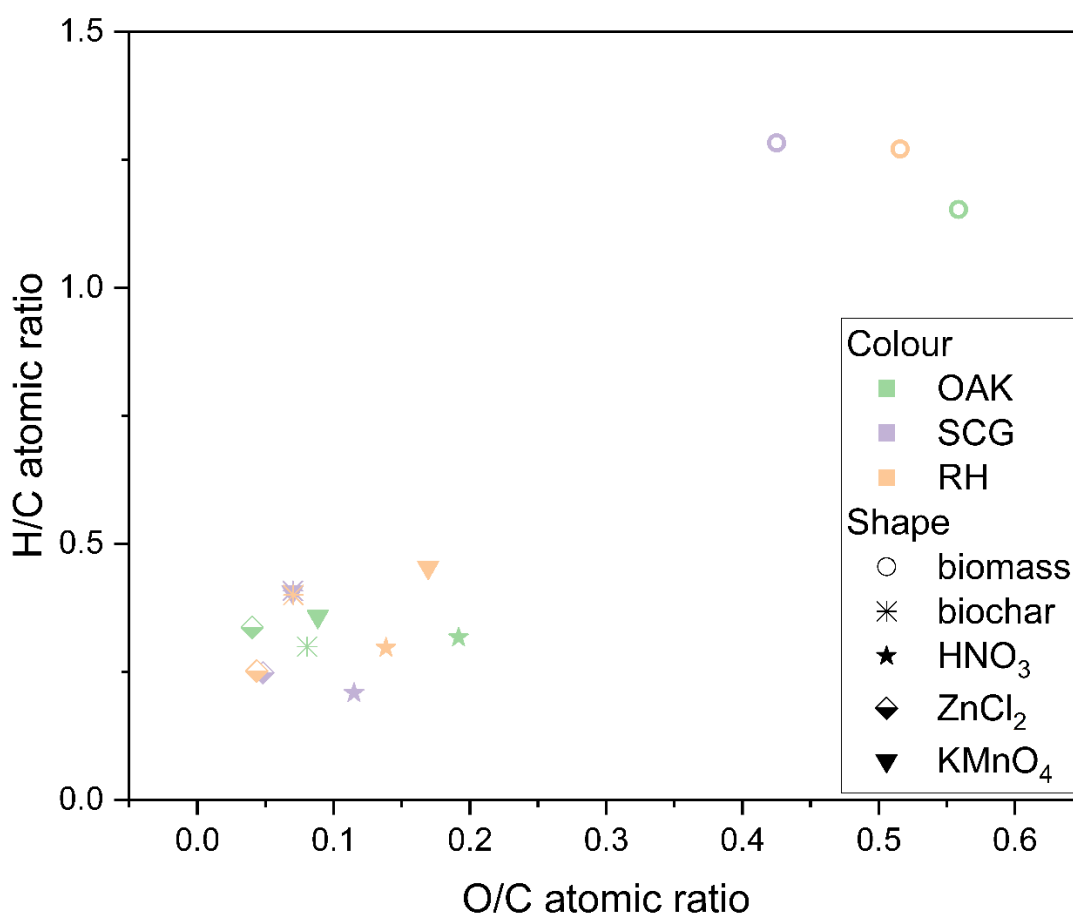


Figure 5.1 Van Krevelan diagram for biochars derived from Oak wood, spent coffee and rice husk, and their activated analogues

The Van Krevelan diagram cross plots atomic ratios of oxygen to carbon (x-axis) against hydrogen to carbon (y-axis). It was originally developed to evaluate and compare characteristics of petrols and kerogenic materials such as coal⁵⁰⁸. It has more recently been adopted by the biochar research community due to the obvious similarities in material classes^{509,510} as well as the importance of O/C and H/C molar ratios in biochar behaviour. The Van

Krevelan diagram is a useful visual summary and comparative tool for correlation of the aromaticity and dehydrogenation of pyrolytic carbon materials with pyrolysis treatment temperature⁴⁹², activation⁵¹¹ and feedstock type⁵¹². Lower molar O/C ratios indicate higher aromaticity and lower molar H/C ratios indicate greater dehydrogenation (Figure 5.1). Unpyrolysed biomass precursors are visible to the top right (open circle) indicating they exhibit far lower aromaticity and a higher degree of hydrogenation than biochars. Of these, OAK biomass (green open circle) exhibits the highest molar O/C ratio, and this trend is mirrored in the unactivated biochars, with OAK biochar (green star) displaying slightly higher molar O/C ratio than RH or SCG biochars, both of which fall in very close proximity. All biochars and activated biochars are clustered to the lower left, indicating greater aromaticity and dehydrogenation. It is notable that all three HNO₃ activated samples, indicated with the star symbol, fall at higher molar O/C ratio than their unactivated biochar analogues, as well as most of the activated KMnO₄ and ZnCl₂ samples. HNO₃ activation is well known to consistently increase oxygen content through oxidation reactions¹¹³. In contrast, ZnCl₂ activation yielded some of the lowest molar O/C ratios of the sample set. This is likely due to some degree of zinc retained within the samples (discussed in Section 5.1.3) which may be skewing the molar ratios of oxygen and carbon. A second possible reason for this apparently low molar O/C ratio is that some activation protocols can both increase oxygen content as well as increasing aromaticity⁵¹¹. However, from comparison of the wt% oxygen values of ZnCl₂ activated samples with other activation protocols, it is clear that oxygen content is typically lower, rather than abnormally high wt% carbon values, as would be indicative of higher aromaticity. KMnO₄ activated biochars show a range of molar O/C values. The SCG KMnO₄ sample is partially obscured in Figure 5.1 by both RH and SCG unactivated biochars, which all fall within very close proximity. OAK KMnO₄ shows a similar molar O/C value while RH KMnO₄ lies to a notably higher value, only surpassed by OAK HNO₃ in O/C ratio. The molar H/C ratio is relatively similar for all three KMnO₄ activated samples. Comparison of the three biomass types: oak, rice husk and spent coffee grounds, reveals a far narrower O/C distribution for spent coffee ground biochars. Oak and rice husk biochars in contrast have wider distribution, hinting that the choice of feedstock, and its precise chemical composition interacts with various activation processes to a greater extent in rice husk and oak based biochars. Looking a little more closely at these two feedstocks, it is well known that rice husks contain significant quantities of inorganics largely in the form of silica (around 16 wt% in dry biomass). These are naturally concentrated somewhat during the pyrolysis process with the loss of lighter elements, with the precise ash content

increasing with pyrolysis treatment temperature, and can exceed 70 wt%⁵¹³
Crucially, both nitric acid and permanganate activation regimes utilise an Brønsted-Lowry acid, more specifically an acid as defined by its proton donation tendency. Thus it is able to attack and dissolve inorganic phases such as silica or calcite present in the biochar and remove them much more readily than the Lewis acid regime of zinc (II) chloride activation.

5.1.6 Hydrogel composites

Elemental composition of hydrogel composites and their component materials are displayed in Table 5-2. Comparison of the effect of nitric acid activation, particularly on wt% oxygen content, between Table 5-1 and Table 5-2 show good agreement, with a slight increase in wt% oxygen content in the activated oak wood biochar from 16.2 wt% in Table 5-1 to 19.6 wt% in Table 5-2. Nitric acid activation again reliably slightly increases the wt% nitrogen content as detailed in Section 5.1.2 in both biochars and in subsequent activated hydrogel composites.

Hydrogel composites all reveal higher oxygen and lower carbon wt% than their biochar precursors, which is expected for a composite of biochar and calcium alginate, which contains the highest oxygen wt% of all component materials at 41.8 % and the lowest carbon wt% at 29.6 %. This is a curious result since the chemical formula of calcium alginate is $(C_{12}H_{14}CaO_{12})_n$ indicating parity in the number of oxygen and carbon atoms in the structure (see also Figure 2-5). Since the atomic masses of carbon (12.001 u) and oxygen (15.999 u) are relatively similar, a similar wt% value would be expected for both, in a pure material. In this case, the calcium alginate hydrogel was prepared following the ionotropic gelation method (Section 4.2.3) in which gelation is thought to create an “egg-box” structure around calcium ions (Figure 2-8). It is possible that water molecules may have been trapped within the gel structure such that they were not removed during freeze-drying, or else re-adsorbed into the material prior to analysis, due to time delay constraints between fabrication and analysis.

Table 5-2 Hydrogel composite beads weight percent chemical composition, with uncertainty is expressed as one SD

	Sample name	Wt %				
		C	O	H	N	S
Oak	biomass	42.6 ± 0.36	31.7 ± 0.62	4.1 ± 0.07	1.1 ± 0.21	0.0
	biochar	75.2 ± 0.07	8.1 ± 0.14	1.9 ± 0.01	0.9 ± 0.01	0.0
	HNO ₃ activated biochar	63.2 ± 0.13	19.6 ± 0.24	1.7 ± 0.02	3.6 ± 0.00	0.0
	KMnO ₄ activated biochar	52.8 ± 0.50	12.5 ± 0.02	2.1 ± 0.03	1.0 ± 0.00	0.0
	hydrogel	63.5 ± 0.19	15.2 ± 0.14	3.1 ± 0.03	1.1 ± 0.01	0.0
	HNO ₃ activated hydrogel	52.8 ± 0.25	23.4 ± 0.70	2.6 ± 0.06	3.0 ± 0.04	0.0
	KMnO ₄ activated hydrogel	51.3 ± 0.34	16.6 ± 0.26	2.6 ± 0.04	1.0 ± 0.03	0.0
Rice husk	biomass	36.2 ± 0.34	24.0 ± 0.25	3.9 ± 0.02	1.1 ± 0.09	0.0
	biochar	79.3 ± 0.24	7.5 ± 0.03	2.7 ± 0.24	3.3 ± 0.39	0.0
	HNO ₃ activated biochar	69.8 ± 0.25	12.9 ± 0.28	1.7 ± 0.00	6.3 ± 0.05	0.0
	KMnO ₄ activated biochar	45.1 ± 0.11	7.01 ± 0.01	1.8 ± 0.03	1.1 ± 0.01	0.0
	hydrogel	43.0 ± 0.18	10.3 ± 0.15	2.0 ± 0.04	0.9 ± 0.01	0.0
	HNO ₃ activated hydrogel	35.6 ± 0.30	15.1 ± 0.26	1.7 ± 0.09	2.4 ± 0.04	0.0
	Calcium alginate	29.6 ± 0.44	41.8 ± 0.64	4.1 ± 0.84	0.7 ± 0.00	0.0

5.2 Fourier Transform Infra-Red Spectroscopy

The chemical functionality of hydrogel composites was investigated relative to their component materials: calcium alginate, biochar and activated biochar to examine changes to surface functionality at respective stages of composite formation. Figure 5.2 displays oak derived biochar, activated biochar and their hydrogel composites, while Figure 5.3 displays rice husk (RH) equivalents. FTIR provides a useful 'fingerprint' – a comparative tool with which to distinguish differences in functional group or composition, as well as pinpointing specific functional groups present in the sample.

All spectra display a prominent and broad absorbance band between 2000 - 3700 cm^{-1} which is attributed mainly to water adsorbed within the pore network and surfaces. Since these materials are derived from relatively low temperature biochars (450 °C), the pore networks remain relatively hydrophilic due to the retention of extensive surface oxygen functionality. As an anionic polymer, alginate – with extensive oxygen surface functionality is also highly hydrophilic. This means that water is adsorbed rapidly and readily to these materials, and is retained. The presence of water may obscure certain functional group vibrations present in the materials, especially O-H vibrations from surface hydroxyl groups and C-H stretching vibrations. However in this case it does appear to provide soe useful 'fingerprinting', as there is a clear distinction in the shape of this broad peak between the biochars and their hydrogel analogues. This is particularly prominent in Figure 5.3, rice husk derived materials. The biochars and activated biochars (RH BC and A-RH BC) display a slightly broader and relatively flat water spectral absorbance section (2500 – 3500 cm^{-1}) followed by a steep and curved drop off in absorbance (1750 – 2000 cm^{-1}). In contrast, hydrogel composites display a more gradual and smooth decrease in absorbance across the same spectral region (1750 – 3500 cm^{-1}). Calcium alginate, as the second component of the hydrogel composites displays a shorter broad spectral feature (2250 – 3500 cm^{-1}) which drops off more rapidly than hydrogel composites. This is likely due to contributions to this broad spectral feature in the biochars and composites which comes from both aromatic (3020 – 3080 cm^{-1}) and aliphatic (2840 – 2990 cm^{-1}) –CH₃ and –CH₂ groups in the biochar component. This puts this spectral region in hydrogel composites intermediate between biochar and alginate. As would be expected.

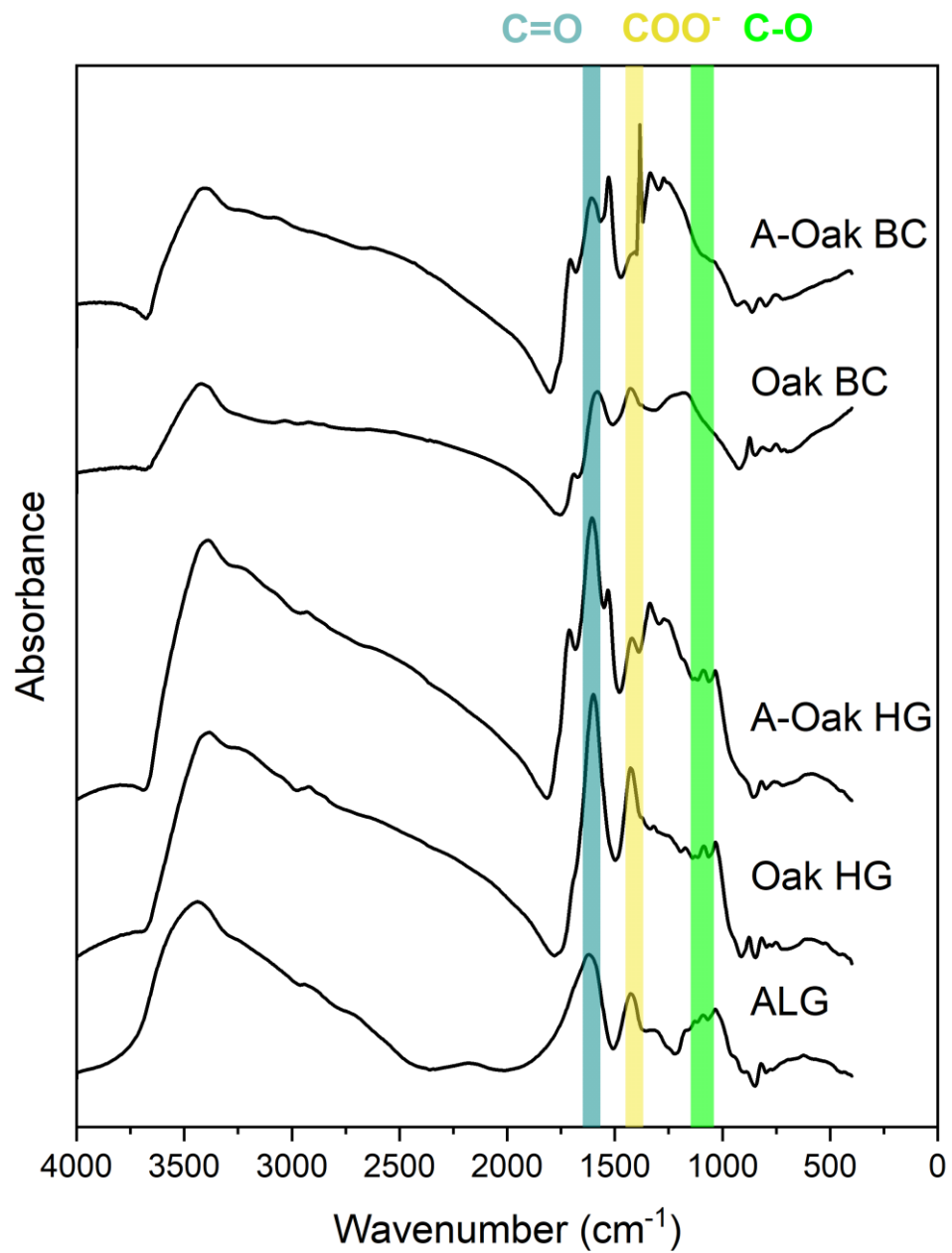


Figure 5.2 FTIR spectra for oak biochar (Oak BC), activated oak biochar (A-Oak BC), oak hydrogel composite (Oak HG) and activated oak hydrogel composite (A-Oak HG) as well as calcium alginate (ALG)

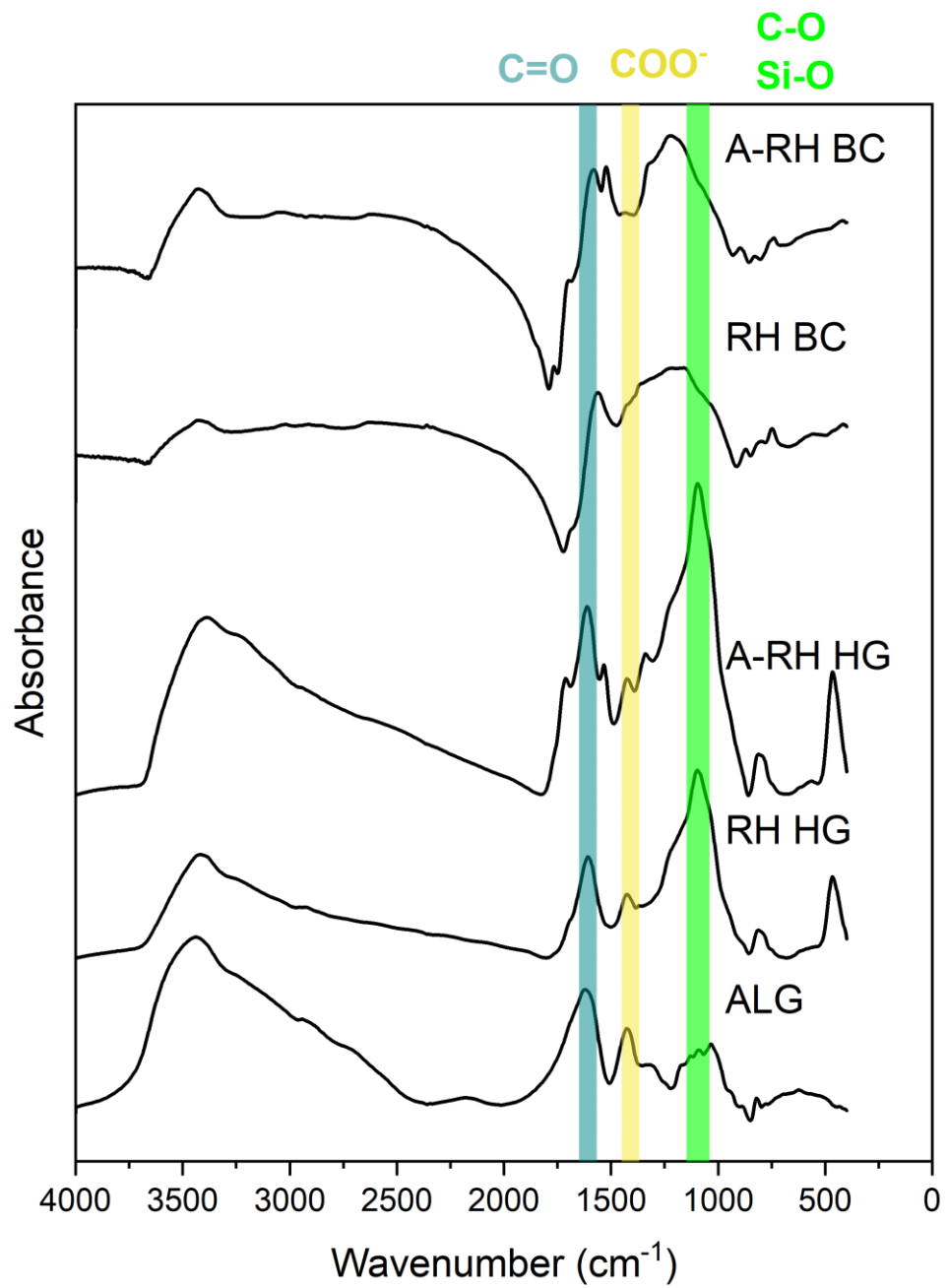


Figure 5.3 FTIR spectra for rice husk biochar (RH BC), activated rice husk biochar (A-RH BC), rice husk hydrogel composite (RH HG) and activated rice husk hydrogel composite (A-RH HG) as well as calcium alginate (ALG)

All samples display a prominent and well resolved peak, with some shoulder peaks present, in the region 1650 – 1740 cm^{-1} which is evidence of prominent carboxylate C=O stretching⁵¹⁴ (blue band, Figure 5.3 and Figure 5.2). Calcium alginate typically shows characteristic carboxylate C=O vibration at 1620 cm^{-1} ⁵¹⁵. This is also visible in the blue band (Figure 5.3 and Figure 5.2) and prominently in all hydrogel composites, indicating that carboxylate functionality is present in all samples to some extent. Curiously, both unactivated biochars Oak BC and RH BC show a small shift in this peak to lower wavenumber, indicating a lower bond energy.

The yellow band (around 1400 cm^{-1}) is region that could indicate both COO^- stretching and CH_3 symmetric stretching vibrations⁵¹⁶ from biochar carbon phases. Alginate displays a prominent peak in this region, as do all hydrogel composites, which is attributed to COO^- stretching since calcium alginate contains no CH_3 (Figure 5.3 alginate structure). Interpretation of this region for both Oak and RH biochars is a more complex, likely due to an overlap of the aforementioned groups. Biochar, being an amorphous material is likely to have wider range of group configurations and bond energies, yielding spectra with widened and overlapping peak areas.

5.2.1 Feedstock effects

Biochar precursor biomass is a key variable in any biochar-containing materials or composite, since precursor biomass types vary in chemical composition e.g. inorganic constituents, relative percent composition of lignin, cellulose & hemicellulose (Table A1). Rice husk is well known to contain significant inorganic constituents such as calcium, sodium & potassium and quantities of silica (SiO_x). Oak is typically regarded as a biochar precursor with relatively few inorganic constituents, but still contains appreciable quantities of bio essential minerals, especially calcium.

Clear differences are observed in RH and Oak biochar spectra, although a number of key common peaks are also observed. Differences are particularly observed in the 750-1500 cm^{-1} region, within which a silica Si-O bond vibration falls (1000-1140 cm^{-1}), which likely accounts for some of the increased signal in RH samples over Oak samples in this region. RH biochars display a broad signal peak around 750-1350 cm^{-1} , which is likely an overlap of carboxylate and hydroxylate vibration (1200-1280 cm^{-1}) with Si-O vibration (1040-1100 cm^{-1}), while the Oak biochars display a narrower peak without such a strong signal in the Si-O region. Analysis is further complicated by the presence of a polysaccharide C-O vibration in the same spectral region (1160-1120 cm^{-1})⁵¹⁷,

a signal which likely originate from alginate polysaccharide units. This spectral overlap could explain the greater prominence of the peak in this spectral region (indicated by the green band) for RH composite hydrogels over RH biochars, since it contains silica. Si-O bond vibration gives a characteristic broad peak with a shoulder at higher wavenumber⁵¹⁸. SiO₂ is an integral and abundant part of rice husk structure, providing protection from degradation.

The same region in Oak hydrogel composites is characterised by a series of small but well resolved peaks. This is a carboxylate C-O vibration at around 1200-1280 cm⁻¹ is observed in activated biochars and is sometimes described as a 'triple peak' of carboxylate vibration⁵¹⁴. This triple peak is clearly visible in Oak HG and A-Oak HG samples as well as calcium alginate since these samples do not contain appreciable levels of silica as RH biochars do.

5.2.2 Activation

Spectra of activated biochars and hydrogel composites all show a greater number of spectral features over their unactivated analogues, indicating a greater range of surface functional groups are present. Comparison of Oak-BC with Oak-O-BC reveal a greater number of peaks clustered around the two blue highlighted regions in A-Oak HG (Figure 5.2). This pattern is repeated consistently with the pairs Oak HG and A-Oak HG, RH BC and A-RH BC as well as RH HG and A-RH HG. Common to both feedstocks, two shoulder peaks appear either side of the 1600-1610 cm^{-1} C=O peak in the activated hydrogel composites A-Oak HG and A-RH HG (indicated by the blue band) which indicates several distinct C=O vibrations each with different bond energy. For example, some carbonyls present may pertain to different functional groups such as carboxylates, lactones or carbonyls, or may form part of a resonance structure or be coordinated to heavier atoms such as calcium, both of which would register at slightly lower the vibrational energy⁵¹⁹. Activation via oxidative acid treatment is well known to increase surface oxygen functional moieties, such as carboxylate, hydroxyl, lactone and carbonyl groups⁵²⁰. A sharp peak in the spectrum of A-Oak BC at 1385 cm^{-1} is attributed to N-O vibration. HNO_3 activation is known to increase the nitrogen content of the activated materials by addition of N-containing moieties. Nitrogen containing groups tend to display particularly sharp spectral features, similar to that observed in A-Oak BC.

5.3 Conclusions

The data presented in this chapter describe the compositional and functional group analysis of engineered materials – biochar and hydrogels – produced in this work. These data aid in understanding and explaining the adsorption behaviour and binding mechanism of strontium to biochar and biochar-hydrogel composites. Elemental analysis demonstrates that oxygen content is well correlated with both pyrolysis temperature and activation via nitric acid in particular. FTIR yields information about the functional groups present with a specific interest in the functional groups that oxygen forms. These data show an increase in carboxyl, carbonyl and hydroxyl groups in activated samples. The implications of these activation protocols on uptake behaviour and mechanism are discussed in subsequent chapters and are summarised in the conclusions chapter (Chapter 9).

Chapter 6 Strontium uptake – Biopolymer composites

In this chapter the uptake of strontium to several activated biopolymers and their composites are investigated through isotherm modelling. Two of the most successful biochar activation protocols are examined: first HNO_3 activation then MnO_x activation. These methods of biochar activation were identified as the most effective strontium removal in preliminary experiments (Appendix C). Uptake to alginate hydrogel composite adsorbents produced from these activated biochars are also compared with their precursor biochars. Two biochar feedstocks are compared in order to examine the role of the precursor biomass. Uptake data is paired with spectroscopic studies in Chapter 7 and discussed in final conclusions.

6.1 HNO_3 activated adsorbents

6.1.1 Biochar - uptake isotherms

The strontium uptake capacity of oak wood (OK) and rice husk (RH) biochar was examined in order to determine maximal uptake capacity and to compare the effect feedstock materials. HNO_3 activated analogues were also examined. Figure 5-1 demonstrates that rice husk biochar appears to exhibit more favourable uptake of strontium than oak wood. Activation increased uptake in

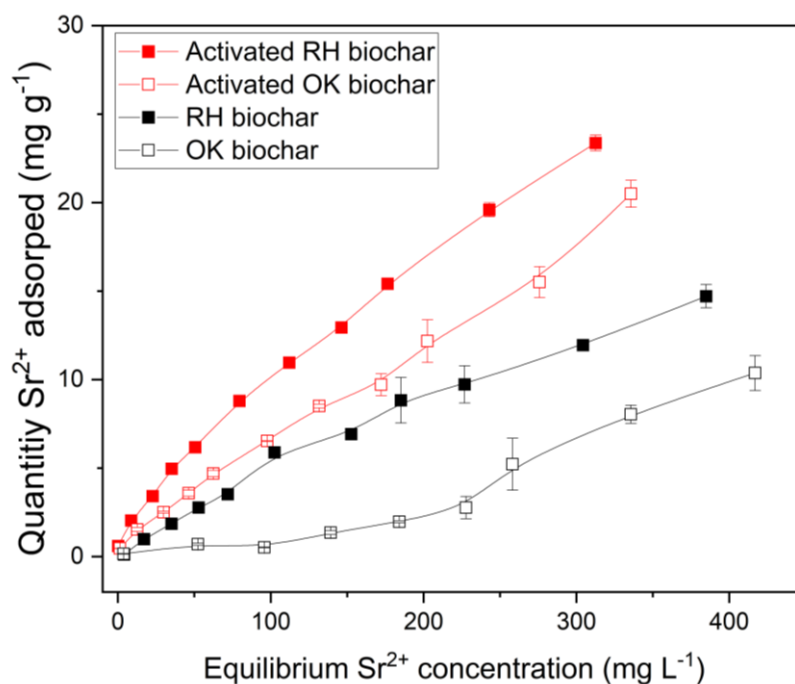


Figure 6-1 Uptake isotherm data for rice husk (RH) and oak wood (OK) biochars, both unactivated and HNO_3 activated.

both oak wood and rice husk biochars. The highest uptake was to activated rice husk biochar, which showed the highest strontium uptake values across the entire concentration range studied. Isotherm modelling fit parameters are displayed below for rice husk and activated rice husk biochars (Table 5-1) however oak wood biochar data series yielded models with unacceptably high uncertainty due to noise in the data series and are not displayed. A very obvious feature for all four data sets is that none reach saturation loading. Reaching saturation loading in an experimental series is desirable for accurate isotherm modelling fits because saturation is assumed in mathematical model. If saturation loading is not achieved, the model fits may underestimate maximal uptake as well as related model parameters. Saturation loading would be characterised by a reduction of the gradient of each series to nil at high initial strontium concentration (x-axis). This would indicate that all strontium binding sites have become occupied in the biochar, and no binding sites remain free. These biochars therefore all have higher uptake capacities than is represented by these data. Higher initial concentration series must be applied to accurately reach and determine their saturation loading for accurate isotherm adsorption models. Extended concentration range isotherms are presented in subsequent sections (Sections 0 and 0).

6.1.2 Hydrogel composites - uptake isotherms

Uptake of strontium to analogous biochar-alginate hydrogel composites was also investigated by means of uptake isotherms, including HNO₃ activated analogues. Isotherm data from control biochars in Section 6.1.1 are replotted below with their corresponding hydrogel composites for ease of comparison. Isotherm parameters captured in Table 5-1.

6.1.2.1 Rice husk hydrogels

Strontium uptake was examined onto rice husk biochar, activated rice husk biochar, a rice husk hydrogel composite and an activated rice husk hydrogel composite. The Langmuir and Freundlich isotherm models were applied to these data and maximal strontium uptake values were derived using the Langmuir model. The hydrogel composites (left) display a distinctly different strontium uptake profile than the biochar and activated biochar (right). This is evidenced by the steeper initial gradient of the hydrogel data series. In comparison, biochar uptake data series present as a more linear increase in uptake with initial concentration. It is also clear from comparison of plots in that strontium uptake is higher at lower Sr²⁺ initial concentration for hydrogels than biochars, particularly so for the activated hydrogel (A-RH hydrogel). Maximum

uptake for activated hydrogel composite was $42.6 \pm 2.1 \text{ mg g}^{-1}$. Although this is slightly lower than values for activated biochar at $53.6 \pm 6.4 \text{ mg g}^{-1}$ and unactivated biochar at $46.6 \pm 10.6 \text{ mg g}^{-1}$, the error on these latter two values are significantly higher. Unactivated hydrogel composite maximum uptake was also modelled at $24.4 \pm 0.1 \text{ mg g}^{-1}$. R^2 values indicating goodness of fit for the Langmuir and Freundlich models are comparable. It is clear that - somewhat

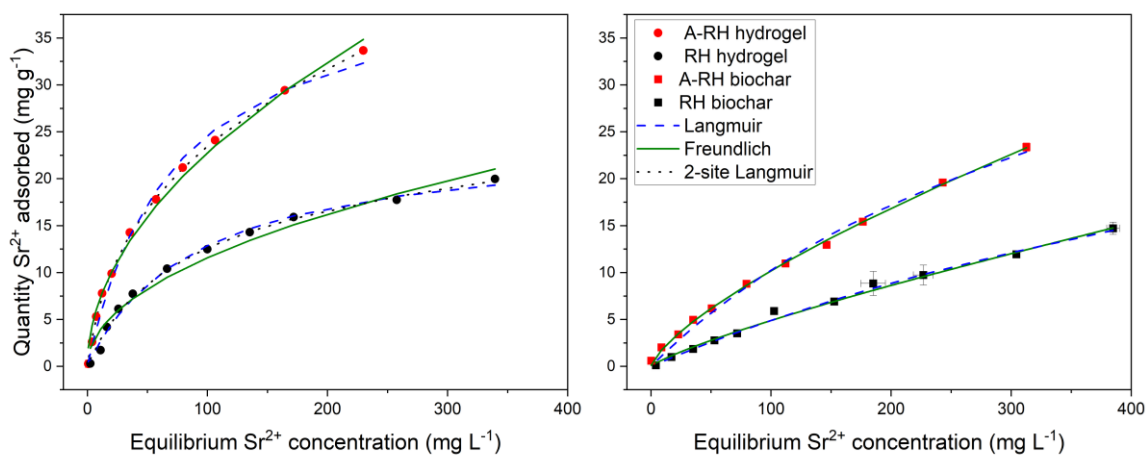


Figure 6.2 Strontium isotherm uptake data for rice husk (RH) hydrogels (left) and biochars (right). Data are plotted across identical axis for clarity. Error bars in x and y represent one SD; each data point was taken in triplicate

unexpectedly - none of the RH samples have reached saturation strontium loading by 500 mg L^{-1} initial concentration. This is discussed in more detail below.

6.1.2.2 Oak wood hydrogels

The oak wood biochar sample set display similar trends to rice husk biochar, with a few notable differences. Both hydrogel samples (, left panel) also exhibit steeper isotherm gradients at lower initial Sr^{2+} concentration than the biochars (right panel), indicating that hydrogel encapsulation of biochar into such composites results in higher strontium uptake at low ($0\text{-}100 \text{ mg L}^{-1} \text{ Sr}^{2+}$) concentrations. Uptake at higher concentrations also enhanced markedly. Langmuir model derived maximal uptake of strontium to activated oak wood biochar hydrogel composites was the highest at 109 mg g^{-1} , much higher than

unactivated hydrogel composite at 35.5 mg g⁻¹. Unfortunately, isotherm plots for both oak wood biochar samples returned with unacceptably high uncertainty¹, so fits are not displayed. It is clear however from examination of data plots in , that oak wood data series – both biochar and hydrogels – possess more ‘noise’ or variability in their data series than RH analogues and this feature is discussed jointly with subsequent results in Section 6.1.4.3. This is quite prominent for the activated hydrogel, which exhibits a significant step change in uptake behaviour at around 50 mg L⁻¹ initial Sr²⁺ concentration, - uptake appears to jump significantly at this point which is an unusual trend for an isotherm.

Table 6-1 Strontium uptake isotherm parameters for biochar and hydrogel composite adsorbents

	Langmuir			Freundlich		
	Q _{MAX} (mg/g)	K x10 ⁻³ (L/mg)	R ²	K _f (mg/g)	n	R ²
A-RH hydrogel	42.6 ± 2.1	13.7± 1.6	0.9917	2.16 ± 0.23	0.511±0.02	0.9915
RH hydrogel	24.4 ± 0.1	11.2± 1.0	0.9936	1.22 ± 0.25	0.488±0.04	0.9703
A-RH biochar	53.6 ± 6.4	2.4 ± 0.4	0.9927	0.36 ± 0.02	0.725±0.01	0.9988
RH biochar	46.6 ± 10.6	1.2 ± 0.3	0.9892	0.11 ± 0.03	0.818±0.04	0.9890
A-OAK hydrogel	109 ± 0.3	2.8 ± 0.01	0.9631	0.397 ± 0.09	0.888 ± 0.05	0.9906
OAK hydrogel	35.5 ± 2.9	4.0 ± 0.6	0.9914	0.647 ± 0.04	0.4897 ± 0.11	0.9796

¹ Non-linear Langmuir and Freundlich isotherm fits were returned with uncertainty 5-10 times greater than modelled values, indicating the mathematical models did not accurately describe uptake. Non-linear fitting was attempted with two different fitting programs (Origin Pro and a custom-built excel macro) with similar results.

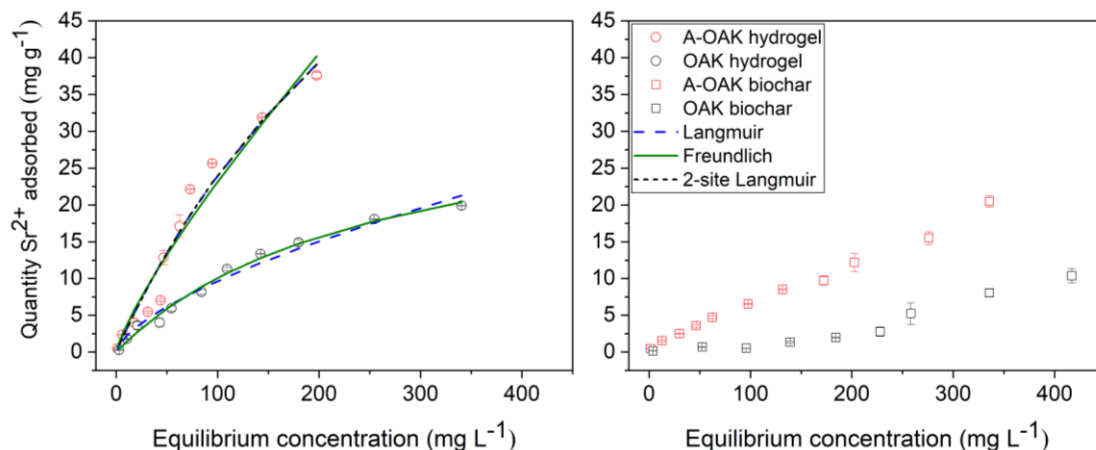


Figure 6.3 Strontium isotherm uptake data for oak wood (OAK) hydrogels (left) and biochars (right). Data are plotted across two identical axis for clarity. Error bars in x and y represent one SD; each data point was taken in triplicate

This trend could almost be described as two distinct uptake data series joined together. This could represent a change in uptake mechanism or possibly be instrumental or experimental error. No indication of error was noted in external standards during ICP-MS measurement of strontium concentration. Any experimental error would likely have been reproduced in other data series to some extent and triplicate data points are in excellent agreement, so it seems most likely this is a concentration dependant uptake effect, suggesting a dual-site adsorption process may be at play in oakwood biochar. A dual-site adsorption would alter the shape of the adsorption series and thus could have contributed to the large uncertainty observed in OAK biochar samples' isotherm fits, which assume either sites with identical energy (Langmuir) or sites with a distribution of energies (Freundlich), neither of which accurately model two sites of discrete energy. The possible cause of this unusual trend is discussed further in Section 6.1.4.3.

6.1.3 Decontamination Factor

A decontamination factor (DF) was calculated at an initial strontium concentration of 5 mg L⁻¹ and results are displayed in Table 6-2. This represents the ratio of strontium removed from solution. The most effective material is the activated rice husk hydrogel. This outperforms all other hydrogels and biochars by quite some margin with a decontamination factor of 6.5. The activated oak wood hydrogel analogue yielded a DF of 3.97. This is on par with both the rice husk and oak wood activated biochars (3.97 and 3.94 respectively). The two unactivated hydrogels have similar DF values, with rice husk (2.01) slightly outperforming oak wood (1.83). Unactivated biochars also perform similarly (1.24 and 1.34). These data also suggest that activation creates the largest increase performance, followed by hydrogel encapsulation, which also results in increased performance, albeit more modestly. What is interesting about these data is that they suggest that the activated rice husk hydrogel outperforms the oak wood analogue by some margin at low strontium concentrations, which is somewhat contrary to the maximal uptake values derived via isotherm fitting, in which the activated oak wood hydrogel composite performed best.

Table 6-2 Decontamination factors of all HNO₃ activated biochars and hydrogels at initial strontium concentration of 5 mgL⁻¹

Sample (OAK)	Decontamination Factor	Sample (RH)	Decontamination Factor
OAK biochar	1.34	RH biochar	1.24
A-OAK biochar	3.94	A-RH biochar	3.97
OAK hydrogel	1.83	RH hydrogel	2.01
A-OAK hydrogel	3.97	A-RH hydrogel	6.50

6.1.4 Extended strontium uptake isotherm data series

6.1.4.1 Isotherm modelling

In light of the enhanced uptake of activated hydrogel composites over biochar controls, activated hydrogels from both: rice husk and oak wood were examined with an extended strontium concentration range. Figure 5-4 displays an extended isotherm concentration range.

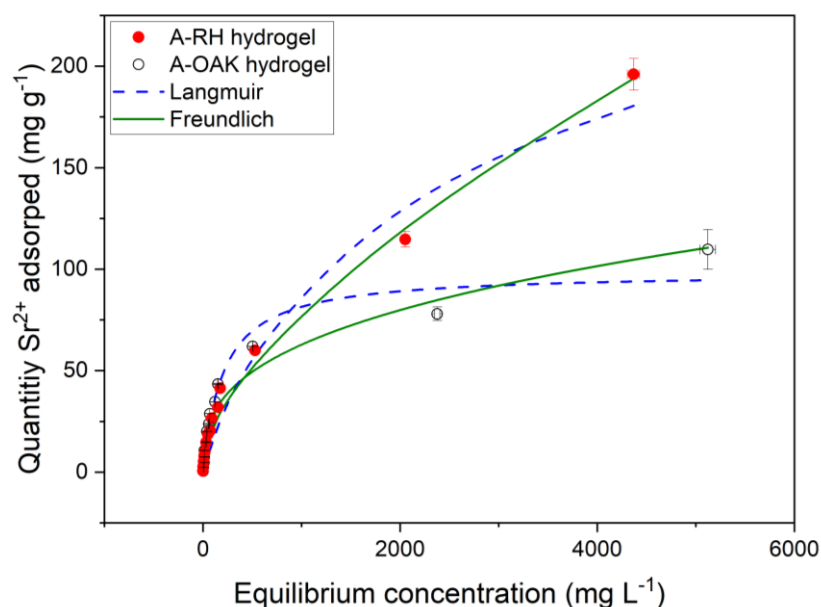


Figure 6-4 Extended strontium uptake isotherms for rice husk and oak wood activated hydrogel composites

This revealed that the rice husk activated hydrogel outperformed the oak wood analogue in maximal uptake capacity by a clear margin. Langmuir modelled maximal uptake capacity was $241 \pm 15 \text{ mg g}^{-1}$ for the rice husk hydrogel and $114 \pm 6.8 \text{ mg g}^{-1}$ for oak wood hydrogel. This oak wood value is in good agreement with the value obtained in in Section 6.1.2, but the rice husk value is greatly increased (from $42.6 \pm 2.1 \text{ mg g}^{-1}$ in Section 6.1.2), demonstrating that foreshortened isotherm data series may underestimate the uptake capacity, in agreement with Nguyen et al. 2017⁴⁴². Isotherm fitting parameters are displayed in Table 5-3. Goodness of fit values suggest these data are best described by the Freundlich isotherm model of a heterogeneous adsorbent with a range of binding sites possessing a distribution of binding energies. This is a logical result since it is well known that biochar – the major constituent of the hydrogel - is amorphous, and given that this is a composite material with alginate binding sites in addition to the activated biochar. The Freundlich isotherm is most often found to describe adsorption in biochars and activated carbons⁵²¹. The

dimensionless Freundlich parameter n indicates favourable adsorption when the value is between 0 and 1, which is found the case for both hydrogels.

Table 6-3 Isotherm modelling parameters using extended data series for activated hydrogel composites derived from both rice husk and oak wood biochars

	Langmuir			Freundlich		
	Q_{MAX} (mg/g)	$K \times 10^{-3}$ (L/mg)	R^2	K_f (mg/g)	n	R^2
A-RH hydrogel	241 ± 15	0.682 ± 0.11	0.9524	2.1 ± 0.31	0.537 ± 0.018	0.9928
A-OK hydrogel	114 ± 6.8	3.49 ± 0.79	0.9441	5.66 ± 0.98	0.349 ± 0.021	0.9729

6.1.4.2 Decontamination Factor

Decontamination factor values at initial strontium concentration of 5 mg L^{-1} are displayed in Table 6-4. DF values of 9.5 (rice husk) and 3.87 (oak wood) were calculated. While the oak wood value is in excellent agreement with the previous analogous result in Table 6-2, the rice husk hydrogel DF has increased by about 1.5 times, a significant increase. No obvious reason presents itself for this increase; possible causes include variability within the feedstock used in the two experiments or could indicate a refinement or improvement in the fabrication process. While every effort was made to standardise the fabrication process such that it resulted in identical treatments, as a novel and experimental process, there are always possible causes of variation which may result in variable performance. Further experimentation and repeat results are thus indicated. Nonetheless, it is a consistent result that DF values are higher for activated rice husk hydrogel than activated oak wood hydrogel under the given regime.

Table 6-4 Decontamination factor at an initial strontium concentration of 5 ppm for the extended activated hydrogel data sets

Sample	Decontamination Factor
A-OAK hydrogel	3.87
A-RH hydrogel	9.50

6.1.4.3 Discussion

HNO₃ activation of biochar consistently increases strontium uptake. This increase is largely due to increases in surface oxygen functionality. Elemental analysis and Infra-red spectroscopic analysis confirm such an increase (Chapter 5). Combining activation with hydrogel encapsulation has a two-fold advantage. It further increases strontium uptake, both in terms of uptake capacity and equilibrium loading at lower concentrations. Hydrogel encapsulation enhances uptake due to the ion-exchange mechanism of calcium with strontium to the alginate phase of the hydrogels. The precise contribution of the alginate phase to strontium uptake was difficult to quantify, since alginate only hydrogels exhibit instability in solution, leading to dissolution of part of the hydrogel. Therefore, baseline alginate only controls were not obtained.

Creating composites results in a more ‘technology ready’ monolithic material which is easy to handle and separate once spent, whereas fine particulate biochar in comparison presents challenges in separation or filtration. The role of the feedstock is a little less clear than activation. Figure 5-4 also displays a curious feature - that relative performance of the two (rice husk and oak wood) activated hydrogels at increasing strontium concentration switches. This is depicted visually in Figure 5-5 and is summarised in brief:

Table 6-5 Summary of relative uptake behaviour - rice husk and oak wood biochar - as a function of initial strontium concentration

Sr²⁺ uptake performance in activated hydrogel – feedstock effect	
RH > OAK Figure 5-5 (bottom left)	At lowest initial concentration (0 – 100 mg L ⁻¹), rice husk performs better than oak wood
OAK > RH Figure 5-5 (bottom left)	At intermediate concentration (approx. 100 – 1000 mg L ⁻¹), oak wood becomes the best performer
RH > OAK Figure 5-5 (top right)	At high concentration (> 1000mg L ⁻¹), rice husk performance diverges from oak wood, significantly outperforming it.

The effect is unlikely to be uncertainty or experimental error due the consistency of the trends and the fact that uncertainty in repeat measurements is much lower than the observed trend. Although visually, the difference at lowest measured concentration (5 - 100 mg L⁻¹) appears to be minimal, but the DF values indicate this could translate to significantly different adsorption behaviour (Table 6-4). Little is known of the relative abundance of distinct oxygen-containing surface functional groups (e.g. carboxyl, hydroxyl etc.) in each biochar. It is possible this 'switching' performance trend is related to relative abundance of different surface groups, with varying affinity for strontium binding. Potentiometric titration techniques could shed some light on this question.

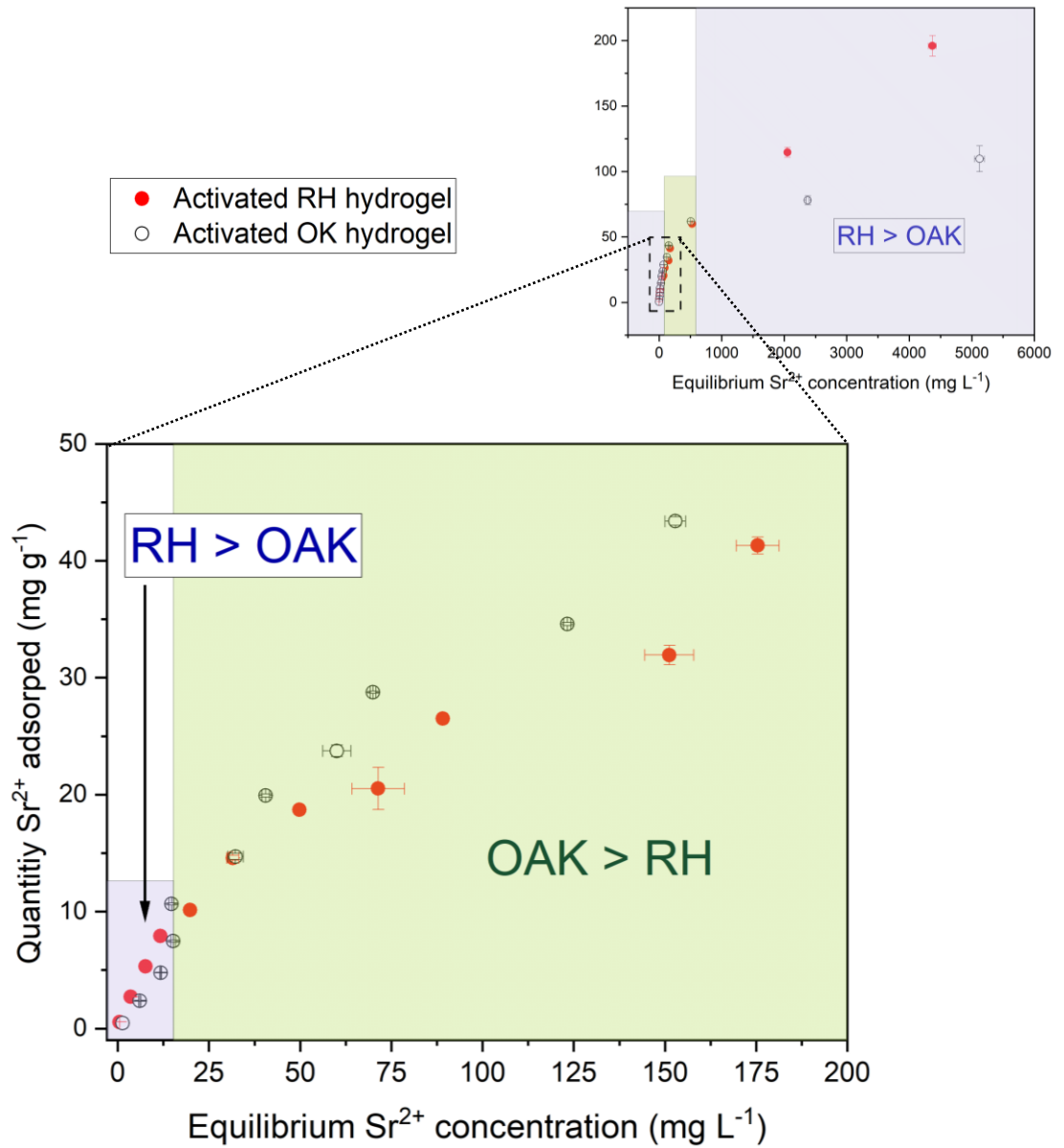


Figure 6-5 Isotherm data series for activated RH and activated OAK hydrogel composites, showing the variation in uptake performance at increasing strontium concentration.

6.2 MnOx activated adsorbents

6.2.1 Isotherm modelling

Oak wood biochar was activated (MnOx biochar) and its strontium uptake behaviour was examined using isotherm series and calculating decontamination factor. An alginate hydrogel composite was also created using the manganese activated biochar (MnOx hydrogel) and similarly examined. Strontium uptake isotherms revealed markedly differing uptake behaviour for the hydrogel composite compared with the biochar. Langmuir isotherm modelling derived a maximum strontium uptake value of $51.2 \pm 1.6 \text{ mg g}^{-1}$ for MnOx hydrogel and $354 \pm 67 \text{ mg g}^{-1}$ for the MnOx biochar. At low initial strontium concentrations, the hydrogel composite outperformed the biochar, as can be seen in Figure 5-6 (right panel). At low initial concentrations, uptake behaviour of the MnOx biochar was somewhat inconsistent and generally quite poor. At much higher initial concentration, MnOx biochar uptake of strontium increases much more rapidly than the MnOx hydrogel and does not approach saturation even at several thousand $\text{mg L}^{-1} \text{ Sr}^{2+}$ (Figure 5-6 left panel). MnOx hydrogel on the other hand, exhibits good uptake at low initial concentration, with a neat, convex isotherm data series which approaches saturation somewhere between 40 - 60 $\text{mg g}^{-1} \text{ Sr}^{2+}$ loading. Both the Langmuir and Freundlich isotherm models were used and parameters are reported in Table 6-6. Goodness of fit values were found to be higher using the Freundlich model for MnOx hydrogel ($R^2 = 0.9978$) than Langmuir ($R^2 = 0.9862$), indicating MnOx hydrogel is a heterogeneous type adsorbent. This is congruent with knowledge of the hydrogel composition, which is a combination of alginate, biochar and MnOx phases.

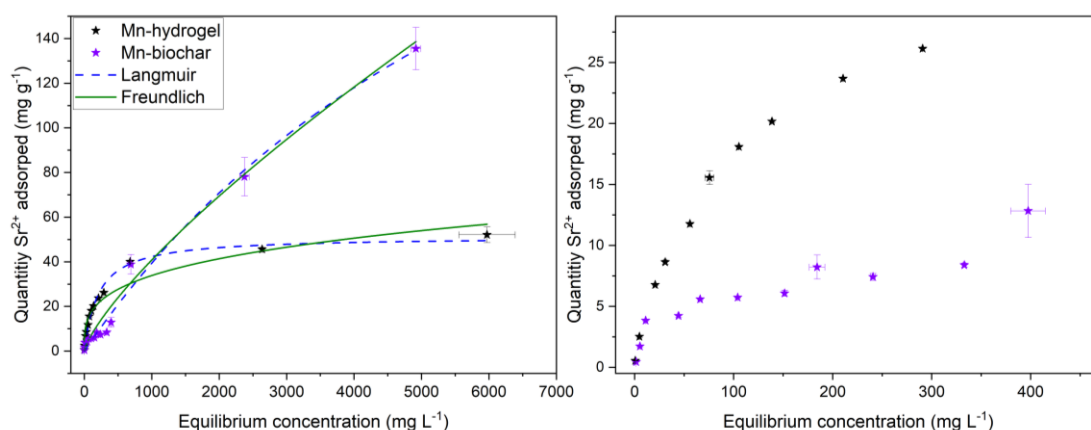


Figure 6-6 Strontium uptake isotherms for Manganese activated biochar and manganese activated hydrogel composites (left) with the initial data points (right) plotted on a smaller scale

Conversely, the Langmuir model best described MnOx biochar ($R^2 = 0.9892$) over the Freundlich model ($R^2 = 0.9356$), suggesting a more homogeneous binding surface in the biochar. Uncertainty in the maximum uptake value for MnOx biochar is comparatively large ($354 \pm 67 \text{ mg g}^{-1}$) which is likely due to a lack of saturation loading, even at extremely high strontium initial concentrations of $1000 - 6000 \text{ mg L}^{-1} \text{ Sr}^{2+}$. At such high concentrations, the non-adsorptive precipitation of strontium onto adsorbent surfaces could become an appreciable factor. Although blank control experiments (strontium solutions without adsorbent) were run without an indication of non-adsorptive precipitation, simply the presence of a solid in the form of the adsorbent could initiate precipitation. As such, blank controls are limited in determining the presence of non-adsorptive precipitation. This of course would not reflect adsorptive behaviour accurately and there is no accurate way to quantify this process and subtract or correct for it in isotherm modelling calculations without a significant amount of additional work. Therefore, extending the isotherm series data range *ad infinitum* in order to reach saturation loading would not add anything valuable to the results presented here. Nor do high concentration solutions reflect “real world” conditions, which is a limitation of the isotherm as an analytical tool for high loading capacity adsorbents. What is clear from these isotherm results is that MnOx biochar possesses *fewer* high affinity strontium binding sites than MnOx hydrogel, as is evidenced by the poorer Sr^{2+} loading by MnOx biochar at low initial concentration seen in Figure 5-6 (right panel). MnOx biochar likely possesses a very large number of lower affinity binding sites since it appears not to reach saturation loading even at very high strontium concentrations.

Table 6-6 Isotherm modelling parameters for manganese adsorbent materials

	Langmuir			Freundlich		
	Q_{MAX} (mg/g)	$K \times 10^{-3}$ (L/mg)	R^2	K_f (mg/g)	n	R^2
MnOx hydrogel	51.2 ± 1.6	4.73 ± 0.45	0.9862	0.20 ± 0.01	0.769 ± 0.01	0.9978
MnOx biochar	354 ± 67	0.13 ± 0.33	0.9892	4.55 ± 0.89	0.290 ± 0.03	0.9356

6.2.2 Decontamination Factor

A decontamination factor (calculated at an initial concentration of 5 mg L^{-1}) provides further evidence for higher affinity sites in MnOx hydrogel. Values of 6.2 for MnOx biochar and 7.6 for MnOx hydrogel (Table 6-7) suggests that at $5 \text{ mg L}^{-1} \text{ Sr}^{2+}$, MnOx hydrogel possesses a greater binding affinity for strontium. This is likely due to the alginate phase present in the hydrogel and which is absent in MnOx biochar.

Table 6-7 Decontamination factors for manganese adsorbents

Sample	Decontamination Factor
MnOx hydrogel	7.6
MnOx biochar	3.2

6.2.3 Discussion – MnOx activated adsorbents

Comparison of DF values of MnOx activated oak wood biochar with control biochar (Table 6-2) revealed an increased uptake of strontium at low concentrations, with a DF value almost as high as HNO_3 activated oak wood biochar. In common with HNO_3 activation, hydrogel encapsulation further increased strontium uptake at low concentration. Manganese oxides have previously been shown to exhibit very high selectivity for strontium. At very high strontium concentration (1000s mg L^{-1}), the MnOx biochar markedly outperforms its hydrogel analogue. Since the hydrogel is 80 % MnOx-biochar by weight (based upon starting material ratios), it should possess a similarly large number of binding sites as the biochar, yet this is not indicated by the near-saturation isotherm observed by the MnOx hydrogel (Figure 5-6). It is possible then that encapsulation of the biochar in the alginate hydrogel may then block access to some of its numerous binding sites. This could occur through pore filling or pore blocking of both biochar and MnOx phases. The trade-off for this partial blocking of the MnOx-biochar bindings sites appears to be a smaller number of higher affinity sites conferred by the alginate component.

6.3 Conclusions

This chapter reports and describes the adsorption behaviour of strontium to biochar, activated biochar as well as hydrogel composites and their activated hydrogel analogues. Activation via nitric acid and via a manganese oxide oxidation protocol was examined in this manner. The uptake behaviour of strontium to rice husk and oakwood biochar achieved modest loadings while their nitric acid activated equivalents showed enhanced loading, demonstrating that nitric acid successfully increased strontium uptake. Fabrication of a biochar-alginate hydrogel composite also enhanced uptake. A combination of hydrogel encapsulation with activation (of the biochar) achieved the highest strontium loadings - $241 \pm 15 \text{ mg g}^{-1}$ for activated rice husk hydrogel and $114 \pm 6.8 \text{ mg g}^{-1}$ for activated oak wood hydrogel. While activation and hydrogel encapsulation have both been previously reported to enhance strontium uptake, the combination of the two steps has not yet been reported. Both hydrogel composites and biochars typically exhibited adsorption behaviour that most closely follows the Freundlich isotherm model, which describes adsorption to a heterogeneous solid with a distribution of binding site energies.

Decontamination factors for the best performing adsorbents (activated hydrogel composites) at an initial strontium concentration of 5 mg g^{-1} was found to be 9.5 and 3.87 for rice husk activated hydrogel and oak wood activated hydrogel respectively. The strontium uptake behaviour of manganese oxide activated biochar and hydrogel composite was also examined. Isotherm modelling indicates that MnOx biochar is capable of a higher overall strontium loading ($354 \pm 67 \text{ mg g}^{-1}$) than MnOx hydrogel ($51.2 \pm 1.6 \text{ mg g}^{-1}$), likely due to some degree of active site blocking which occurs during the hydrogel encapsulation process. However, at strontium concentrations relevant to decontamination (5 mg g^{-1}), the MnOx hydrogel performs better, yielding a DF of 7.6, while MnOx biochar achieves 3.2. The implications of these data are discussed in Chapter 9 jointly with results from Chapter 7.

Chapter 7 X-ray Absorption Spectroscopy: binding mechanism of strontium to biopolymer adsorbents

7.1 Introduction

X-ray absorption spectroscopy was used to examine the binding environment of strontium adsorbed to biopolymer composite hydrogels, biochar and calcium alginate components. HNO₃ activated biochar and analogous hydrogels were also examined. Several strontium standard compounds were also examined. X-ray absorption was captured at the strontium K-edge (16105 eV) at 77 K. The photon backscattering signal was captured over the range 15900 – 16900 eV. k³ weighted EXAFS fitting revealed the presence of a low mass second shell backscattering element beyond the first shell oxygen.

Details of the fitting process are described in Section 4.5 but are also summarised here in brief: Acquired X-ray attenuation data over the range of interest are first examined for quality then merged. This enhances the signal to noise ratio. Data go through a process of background subtraction in order to remove sections of the data that do not pertain to X-ray absorption and back scattering and spectra are normalised and calibrated in X-ray energy by means of a standard. One background subtraction and any data quality issues have been addressed (such as glitches or artefacts), spectra are ready for fitting. Standard compounds are first fit, taking fit parameters from crystallographic data, in order to derive a value for S₀², the amplitude reduction factor. This value should remain stable across all samples in a given experimental set (of the same element) and can thus be used to fit data for which fewer parameters are known, i.e. experimental samples with unknown coordination.

7.1.1 Standards spectral analyses

Pure strontium salts were measured as standard reference compounds and to aid with the fitting of the Fourier transform of the biopolymer samples. Strontium oxalate $\text{Sr}(\text{C}_2\text{O}_4)$, strontium hydroxide $\text{Sr}(\text{OH})_2$, strontium sulphate SrSO_4 and Strontium carbonate SrCO_3 were measured at the strontium K-edge and these

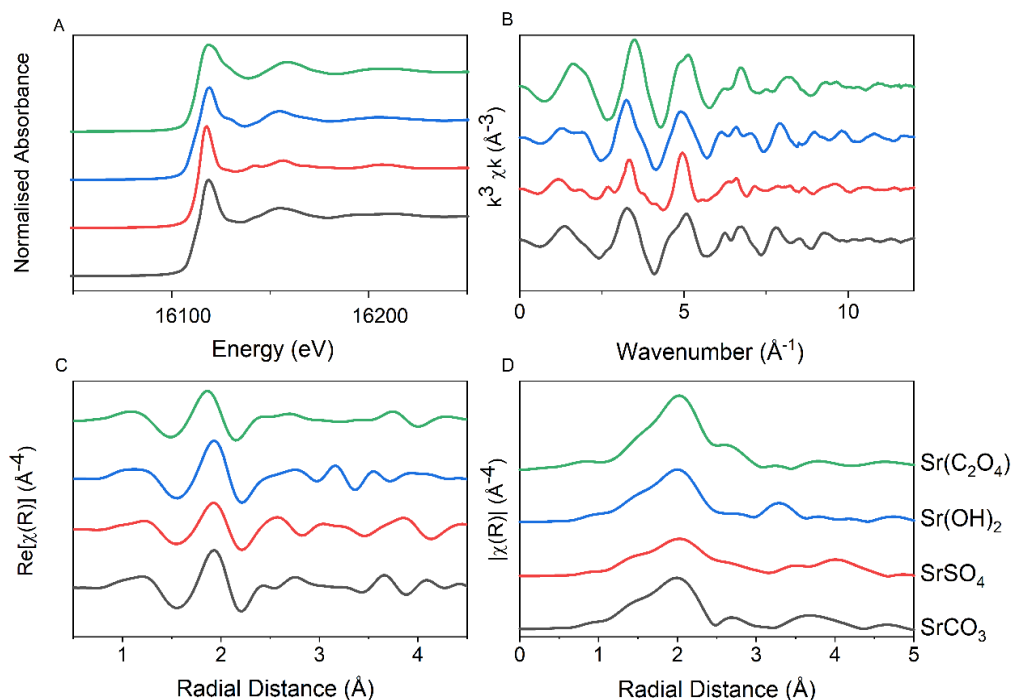


Figure 7.1 Normalised strontium K-edge EXAFS data for four standards: A) K-edge position, B) EXAFS data in k-space, C) the real part of the Fourier transform and D) the magnitude of the Fourier transform. Standards are labelled to the right of D).

data are displayed in . The Fourier transform of these data were fit using reference crystallographic data in order to obtain a value for the amplitude reduction factor for further use in fitting of the biopolymer samples. All standards were satisfactorily fit in this matter. An example fit of strontium oxalate is displayed in with individual backscattering contributions of the nearest neighbour oxygen atoms and second nearest neighbour carbon atoms offset for clarity. Fitting parameters for standards are displayed in Table 7-1.

Measurement of strontium chloride was also attempted but the data obtained was not usable. Pandemic related restrictions to attendance at the experiment meant that “on-the-fly” adjustments to sample preparation, including sample thickness, was not possible. This also meant that data from a number of experimental samples was not usable.

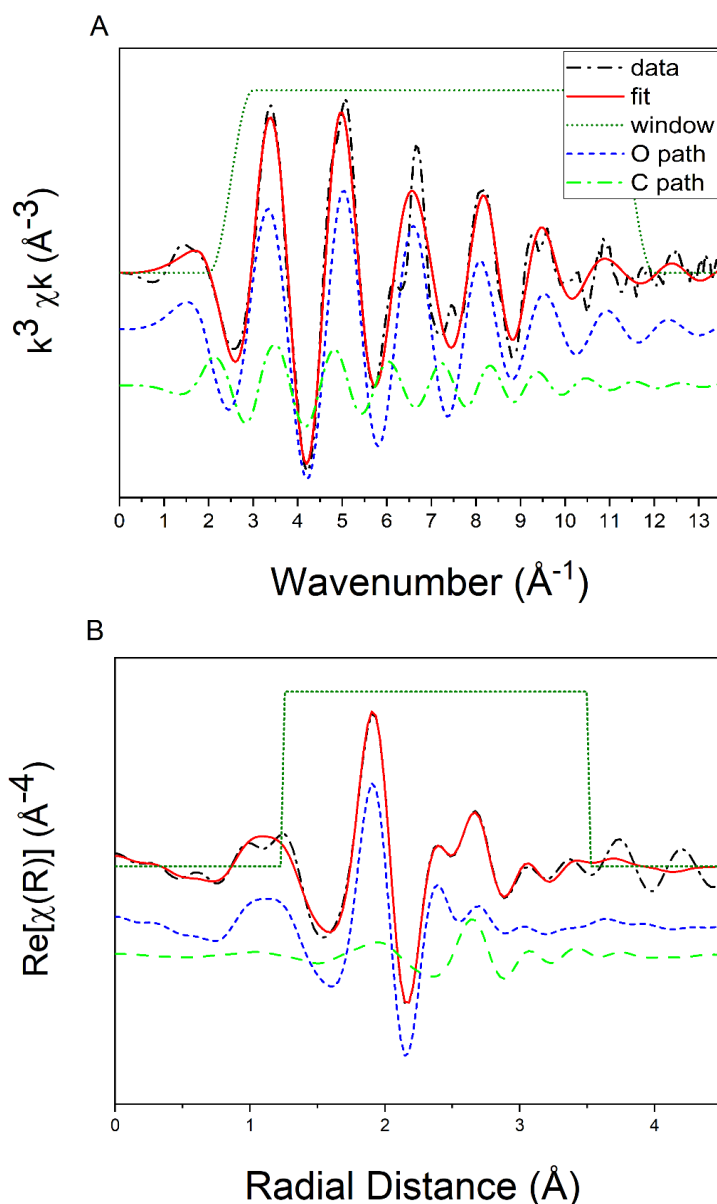


Figure 7.2 EXAFS spectrum for strontium oxalate standard (A) and the real part of the Fourier transform (B). Plots include individual paths for oxygen and carbon shell fits (offset for clarity) as well as overall fit. Fitting range = 2.5-11.5 \AA^{-1} , $dk = 1$, fitting range is 1.25-3.5 \AA .

7.2 Biopolymer composite adsorbents spectral analyses

The binding of strontium adsorbed to several biopolymer adsorbents was probed. Biochar from two biomass feedstocks were selected, rice husk (RH) and oak wood chips (OAK) in order to probe feedstock effects. Binding to both biochar (BC) and a hydrogel composite monolith (HG) was examined. The effect of chemical activation on binding mechanism was also probed with a series of activated analogues (denoted by the prefix A-). Sr K-edge data are

displayed for representative samples of hydrogels, biochar and calcium alginate (ALG) (Figure 6-3). EXAFS spectra in k-space for corresponding samples are shown in Figure 6-4. Fits of the Fourier transformed data are displayed in real space (Figure 6-5 & Figure 6-6) as well as their magnitudes (Figure 6-7 & Figure 6-8) while Table 7-1 lists a comprehensive set of all fitting parameters derived as well as R-factor values which provide a measure of goodness of fit. The effect of initial strontium concentration was also investigated using initial values of 50 ('low') and 250 ('high') mg L⁻¹. Table 7-2 provides a comparison of R-factor values for a range of fit scenarios, including fits which assume the presence of chloride.

7.2.1 Results

Fourier transform data reveal a strong first shell signal in all samples which corresponds to a first shell of oxygen. No spectral differences were observed between measurements taken at room temperature (RT) versus at low temperature (77K), although spectral resolution was improved somewhat at low temperature, therefore low temperature data is displayed herein.

The possible role of strontium chloride in the strontium EXAFS signal was explored by using Sr-Cl and Sr-Sr scattering paths from crystallographic data. Hydrated strontium chloride crystallographic data was also examined using Sr-O and Sr-Cl paths. This was necessary since strontium chloride was used to create the simulant strontium contaminated solution. Fits to the data using Sr-Cl resulted in very poor fits, with ΔE_0 values consistently very high (20-30 eV) and R-factors between 0.3 – 0.5 (Table 7-2). Including a second shell Sr-Sr or Sr-O path did not improve the fits. This suggests that chloride is a the major contributor to the EXAFS first shell backscatterer signal obtained in biochar and hydrogel samples, which are all broadly similar. Sr-O single shell fits produced much improved fits over Sr-Cl fits, with reasonable ΔE_0 and coordination values. However, in all but three cases, all of which were biochar samples, initial fitting of a single Sr-O first shell still yielded R-factors > 0.02 as shown in Table 7-2. This suggests the presence of a second, more distance backscatterer shell beyond the first shell of oxygen. Much of the fitting work focussed on examining and understanding the second shell backscattering signal and in determining the identity of the atoms which yielded this signal

The presence of a second shell appears to be confirmed via numerical fit results in Table 7-1 which improved with the presence of a low mass (Sr-C) back scattering shell between 3.3 – 3.4 Å, with R-factors all < 0.02. The R-factor value is a measure of how well the model fit overlays, or is in accordance with,

the experimental data. Fits were also attempted with a second Sr-O path (R-factors reported in Table 7-2), a binding mechanism suggested by Nie et al. 2017²³⁵. Fitting such a system to these data produced fits with lower R-factors than those fitted with a single (Sr-O) path but higher R-factors than a fit with second shell Sr-C.

Fits using a second shell Sr-Cl signal were also examined (with a first shell Sr-O). Conceptually, placing chloride, as a highly electronegative element in a second shell back scatterer with oxygen, another highly electronegative, as a first shell backscatter doesn't make a great deal of sense. Such an arrangement would surely be energetically unstable and unlikely, despite the electropositivity of charge-dense strontium. More likely, and bearing in mind that EXAFS is an *average* signal, it is conceivable that this Sr-O Sr-Cl fit could describe two distinct binding modes: one being an outer sphere Sr-O binding with absorbent surfaces and a second Sr-Cl binding environment of precipitated strontium chloride salts. In a majority of cases, R-factor values of < 0.02 were obtained with such fits. Coordination numbers for chloride were typically very low ($N < 1$), with uncertainty between 25 – 60 % which is significant.

The fits with lowest R-factor values in all samples are first shell Sr-O, second shell Sr-C fits. This could be indicative of inner sphere complexation of strontium to both rice husk and oak wood biochars, hydrogel composites as well as their activated analogues, and calcium alginate at pH 7. Figure 6-12 and Figure 6-13 provide visual representation of coordination number and interatomic distances as a function of material type, initial strontium concentration and feedstock type for ease of comparison. Given that amorphous samples can be difficult to fit due to a range of possible binding environments, it is not unexpected that these fitting results are not as clear-cut as could be expected from more ordered samples, for example. It is important therefore to treat these results with care in interpretation and this is further discussed in the future works Section 9.1.4 and limitations Section 9.1.5. Nonetheless, the fits which most accurately describe these experimental results do suggest the presence of second shell carbon which in turn indicates stronger inner sphere binding is occurring. Subsequent sections explore this option and develop a conceptual model to explain these data and fits.

7.2.1.1 Calcium alginate EXAFS analysis

Examining the component materials of the hydrogel, it can be seen that calcium alginate possesses the highest second shell Sr-C coordination number of the sample dataset at 4.69 ± 1.37 , consistent with the 'egg-box' theory⁹⁹ of group II

cation binding to alginate (Figure 6-11, right). The fact that the second shell signal is highest in alginate only samples lends credence to the theory of a second shell of carbon, since as a more ordered and well-described polymer, a higher degree of inner sphere binding would be expected here than in biochar. This value for second shell coordination number is consistent at both 'high' and 'low' initial strontium concentrations examined, indicating that the binding environment has not altered significantly with an increase in the number of sites occupied. Thus, in the context of remediation, there are a large number of sites with a high affinity for strontium in calcium alginate hydrogel. This is not surprising given that the alginate only hydrogel is created using the calcium ion as a template around which the monolithic gel forms. Given the electronic and size complementarities between calcium and strontium, this creates binding pockets that are well suited for strong strontium binding. Of course, calcium alginate hydrogel as a standalone material is not well suited for remediation purposes due to its poor mechanical strength and durability. However, it clearly possesses properties that could be highly useful to cation complexation and immobilisation, especially in 'one-use' scenarios that are particularly useful for radionuclide immobilisation for subsequent isolation.

7.2.1.2 Biochar EXAFS analysis

To our knowledge, no published work has yet used EXAFS to examine the binding mechanism of strontium to biochar or any similar type of biopolymer-based adsorbent materials. Both rice husk and oak wood biochars exhibit a similar second shell backscattering signal to both alginate and composite hydrogels, with fitted values for second shell carbon coordination ranging between $N = 3.48 \pm 1.35$ and $N = 2.56 \pm 1.18$. These values are lower than for alginate only and composite hydrogels. Nonetheless, biochars and activated biochar do appear to exhibit inner sphere binding, with no discernible differences based on feedstock, represented visually in Figure 6-12. Nor does activation appear to alter the binding environment in biochar, although a thorough analysis of this variable was not possible. It was unfortunately not possible to complete fitting on all biochar samples prepared due to sample preparation issues. Rice husk biochars seemed to be especially affected by poor transmittance. Only one rice husk biochar yielded sufficient signal for fitting while three oak wood biochars were successfully fit. However, uptake data from Chapter 5 indicate little discernible difference in strontium loadings between the two feedstocks at the two concentrations used for EXAFS measurements. It is possible that the presence of silica which is abundant in rice husks may have attenuated the X-ray signal to a greater extent than that which occurred in oak

wood biochars. Although this was accounted for in sample thickness calculations, it was not possible to precisely measure silica content in the rice husk biochars, and since this experiment was conducted remotely during the 2020 global pandemic, it was not possible to modify samples during the experiment to better account for sample absorption.

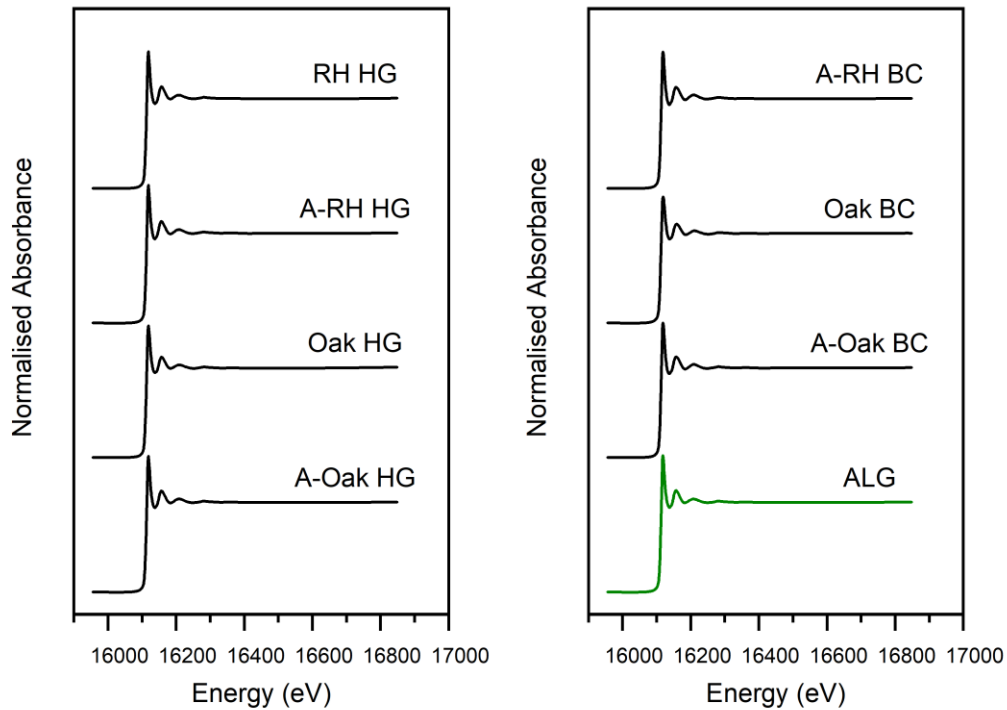


Figure 7-3 Normalised strontium K-edge data of representative samples, showing both activated and unactivated hydrogels (left), and biochar and alginate control samples (right). All samples displayed

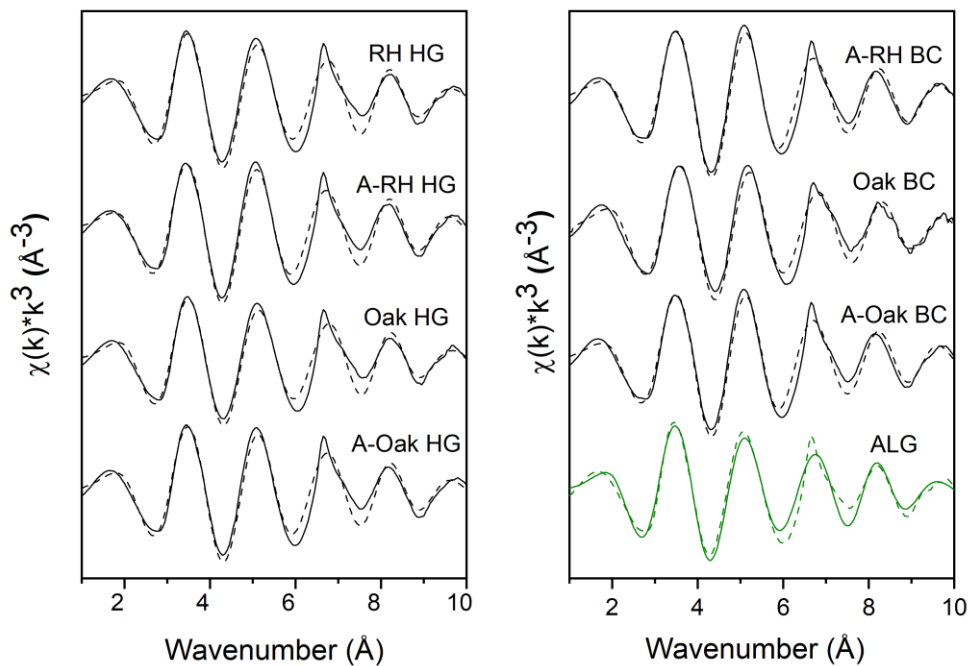


Figure 7-4 Normalised k-space data of representative samples, showing both activated (A-) and unactivated hydrogels (left), and biochar and alginate control samples (right)

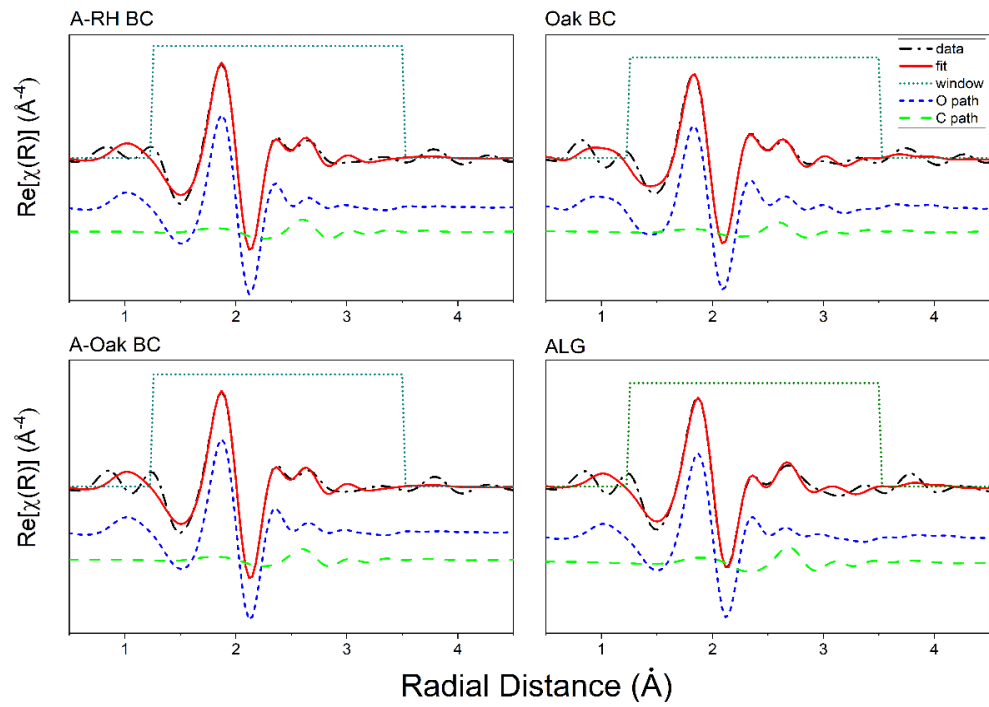


Figure 7-5 The real part of the Fourier transform for three representative biochar adsorbents and calcium alginate, including fits and individual paths (offset for clarity). Data are enumerated in Table 7-1

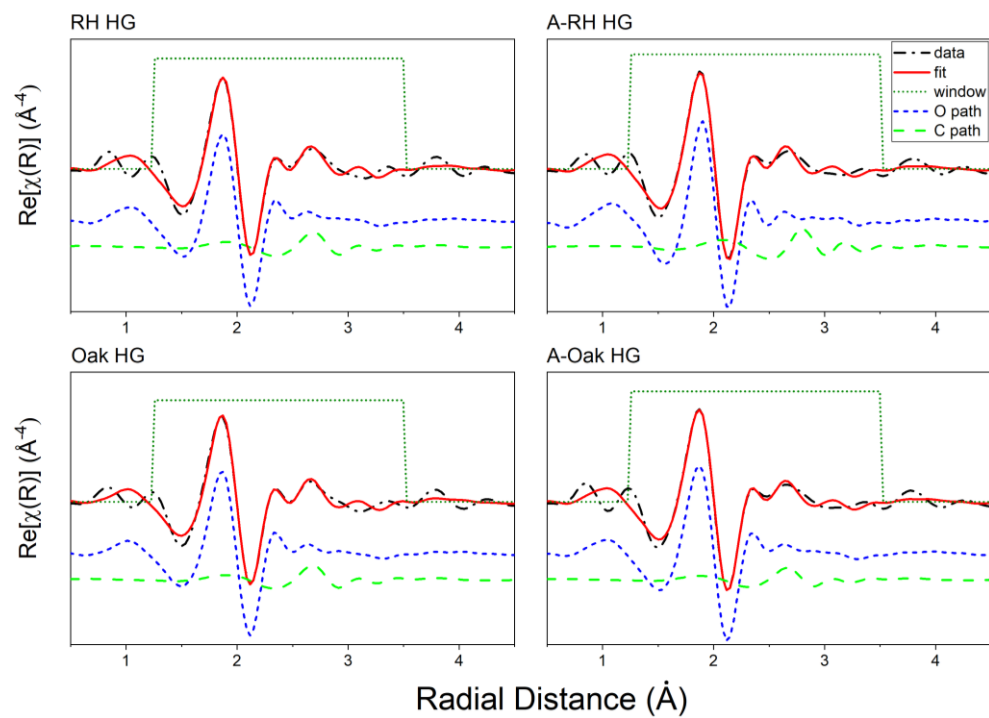


Figure 7-6 The real part of the Fourier transform for four representative hydrogel adsorbents including fits and individual paths (offset for clarity). Data are enumerated in Table 7-1

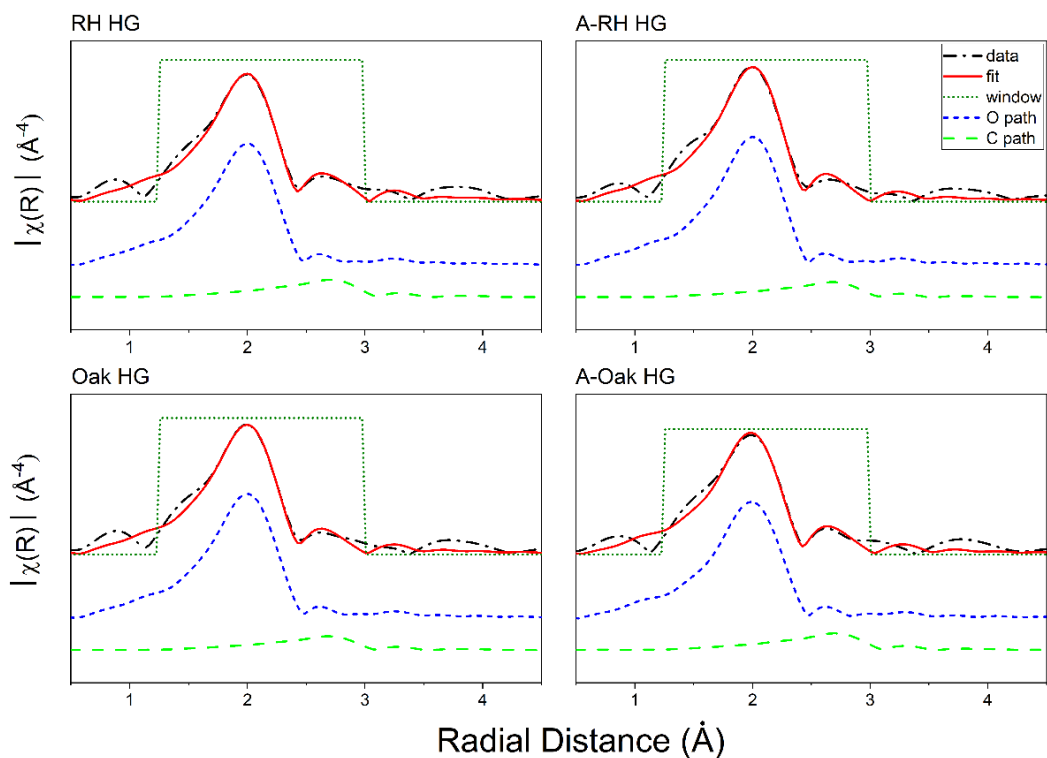


Figure 7-7 Magnitude of the Fourier transform for four representative hydrogel adsorbents including fits and individual paths (offset for clarity)

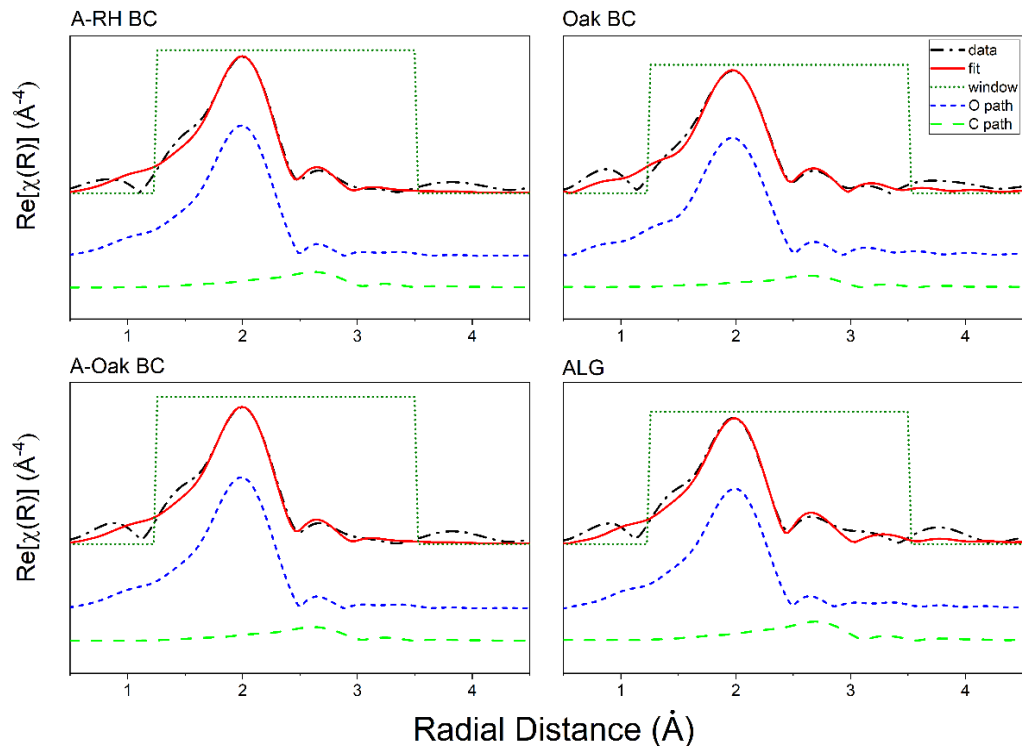


Figure 7-8 Magnitude of the Fourier transform for three representative biochar adsorbents and calcium alginate, including fits and individual paths (offset for clarity)

7.2.1.3 Hydrogel composites EXAFS analysis

Hydrogel composites also display a second shell signal evidenced by the addition of the second shell Sr-C backscattering component improving the fits in all cases. The fitted coordination number for second shell carbon is intermediate between biochar and the alginate only control hydrogel, with values typically around 4-4.5. This trend is displayed visually Figure 6-12. Hydrogel samples on the whole show a higher Sr-C second shell coordination number value over biochar samples which indicates a greater degree of inner sphere binding in hydrogels than biochar. The addition of alginate to biochar in the hydrogel composites appears to increase the degree of inner sphere binding. Interatomic Sr-C (second shell) distances appear slightly shorter in biochar only samples than hydrogels (Figure 6-13 top). Interatomic distances in hydrogels in the second shell more closely resemble those derived in alginate samples. This suggests the binding environment in hydrogels more closely resembles, on average, alginate. The egg-box model of group II binding in alginate could help to explain the slightly lengthened second shell distance, as the binding pockets likely have fixed geometries predetermined by the gelation process. The egg-box model⁹⁹ describes the expected binding mode of the alginate anionic biopolymer around cations such as strontium. This is described in more detail in Section 2.2.3.4 and Figure 2-8. Another contributing factor is in the relative contribution to binding of different oxygen functional groups. This is explored further in Section 7.2.2.

7.2.1.4 HNO₃ Activation

Activation with HNO₃ slightly increases first shell oxygen coordination numbers, while little effect is noticed in the second shell (Figure 6-12 top). Activation is known to increase surface oxygen functionality in biochar which likely explains this trend. Little effect is noticed on interatomic distance due to HNO₃ activation, suggesting activation does not alter interatomic distances in the strontium binding environment (Figure 6-13).

7.2.1.5 Strontium concentration

Binding was examined with two initial strontium concentrations (50 and 250 mg L⁻¹). Figure 6-12 (bottom) shows coordination as a function of both biochar feedstock (showing both hydrogels and biochar samples) and initial strontium concentration. Little effect on either biochar feedstock or initial strontium concentration is noted above uncertainty, suggesting no significant difference in the strontium binding environment across the concentration range.

This indicates that the number of equivalent binding sites are numerous, more numerous than can be saturated by a 250 mg L^{-1} .

Table 7-1 EXAFS fitting parameters for hydrogel beads, biochar and alginate samples. Both Oak wood (Oak) and rice husk (RH) biochar was used. Table continued overleaf (1/3)

Sample	Type	Scatterer shell	Coordination number	R (Å)	ΔE_0 (eV)	$\sigma^2 * 10^{-3}$ (Å ²)	R-factor
Activated Oak hydrogel 250	hydrogel	Sr-O	8.81 ± 0.99	2.57 ± 0.01	3.03 ± 0.95	13.4 ± 1.64	0.0111
		Sr-C	3.42 ± 1.34	3.37 ± 0.04			
Alginate 250	alginate	Sr-O	8.46 ± 1.02	2.57 ± 0.05	3.11 ± 0.96	13.4 ± 1.83	0.01340
		Sr-C	4.69 ± 1.37	3.39 ± 0.01			
Activated Oak biochar 250	biochar	Sr-O	9.05 ± 0.93	2.57 ± 0.01	3.04 ± 0.99	12.9 ± 1.49	0.00974
		Sr-C	2.99 ± 1.38	3.30 ± 0.04			
Activated RH biochar 250	biochar	Sr-O	9.16 ± 0.90	2.57 ± 0.01	3.05 ± 0.95	12.8 ± 1.45	0.009248
		Sr-C	3.48 ± 1.35	3.31 ± 0.04			
Activated RH hydrogel 250	hydrogel	Sr-O	8.91 ± 1.00	2.57 ± 0.01	2.55 ± 0.99	13.0 ± 1.71	0.01201
		Sr-C	3.68 ± 1.39	3.35 ± 0.04			
RH hydrogel 250	hydrogel	Sr-O	8.54 ± 1.03	2.57 ± 0.01	2.99 ± 0.97	13.3 ± 1.81	0.01319
		Sr-C	4.31 ± 1.38	3.38 ± 0.04			

Sample	Type	Scatterer shell	Coordination number	R (Å)	ΔE_0 (eV)	$\sigma^2 * 10^{-3}$ (Å ²)	R-factor
Oak biochar 250	biochar	Sr-O	7.67 ± 0.70	2.57 ± 0.01	4.34 ± 0.88	11.8 ± 1.51	0.01474
		Sr-C	2.62 ± 1.03	3.32 ± 0.04			
Oak Hydrogel 250	hydrogel	Sr-O	7.74 ± 0.91	2.56 ± 0.01	3.25 ± 0.95	12.8 ± 1.83	0.014070
		Sr-C	4.04 ± 1.22	3.38 ± 0.04			
Activated Oak Hydrogel 50	hydrogel	Sr-O	8.23 ± 1.05	2.57 ± 0.01	2.51 ± 1.03	12.8 ± 1.95	0.01600
		Sr-C	4.02 ± 1.38	3.38 ± 0.04			
Alginate 50	alginate	Sr-O	7.96 ± 0.94	2.57 ± 0.01	3.02 ± 0.95	12.4 ± 1.91	0.0160657
		Sr-C	4.55 ± 1.25	3.39 ± 0.04			
Activated Oak biochar 50	biochar	Sr-O	8.36 ± 0.79	2.56 ± 0.01	3.78 ± 0.95	12.6 ± 1.51	0.01125
		Sr-C	2.56 ± 1.18	3.31 ± 0.05			
Activated RH hydrogel 50	hydrogel	Sr-O	8.72 ± 1.13	2.56 ± 0.01	2.69 ± 1.12	13.2 ± 2.10	0.018465
		Sr-C	4.28 ± 1.53	3.36 ± 0.05			
Oak Hydrogel 50	hydrogel	Sr-O	7.85 ± 1.12	2.56 ± 0.01	2.48 ± 1.16	12.9 ± 2.25	0.02007
		Sr-C	4.45 ± 1.48	3.38 ± 0.04			

Sample	Type	Scatterer shell	Coordination number	R (Å)	ΔE_0 (eV)	$\sigma^2 * 10^{-3}$ (Å ²)	R-factor
Sr(C ₂ O ₄)	standard	Sr-O	12.0 ± 0.96	2.59 ± 0.06	0.39 ± 0.75	12.1 ± 1.21	-
		Sr-C	9.48 ± 1.50	3.32 ± 0.14			
Sr(OH) ₂	standard	Sr-O	12.8 ± 1.27	2.62 ± 0.10	1.38 ± 0.71	15.0 ± 1.77	-
		Sr-Sr	2.91 ± 1.18	3.71 ± 0.06			
SrSO ₄	standard	Sr-O	9.07 ± 1.30	2.06 ± 0.11	0.91 ± 1.1	16.2 ± 2.59	-
		Sr-S	5.53 ± 0.77	3.45 ± 0.02			
SrCO ₃	standard	Sr-O	12.84 ± 1.86	2.61 ± 0.03	2.48 ± 1.54	13.6 ± 3.80	-
		Sr-C	8.02 ± 1.12	3.02 ± 0.02			

K range is 2.5-11.5 Å⁻¹, dk = 1, fitting range is 1.25-3.5 Å. σ^2_C values are set equal to σ^2_O . The number of independent data points NIDP is calculated as follows $NIDP = S(2/p)(k_{max} - k_{min})(R_{max} - R_{min})^9$. S_0^2 was set to 1 following standard fitting

Table 7-2 Comparison of R-factor values for a range of fit types. In the majority of cases, a Sr-O Sr-C fit yields the lowest R-factor values, suggesting these fits most accurately follow experimental data. Sr-O Sr-Cl fits also yield low R-factor values in several cases. Thus, coordination number values are also reported for this fit 1/2.

Sample	R-factor Sr-O Sr-C	R-factor Sr-O	R-factor Sr-O Sr-O	R-factor Sr-O Sr-Cl		R-factor Sr-Cl
				R-factor	N Cl	
Activated Oak hydrogel 250	0.01112	0.02082	0.01717	0.01288	0.087 ± 0.041	0.04034
Alginate 250	0.01340	0.03131	0.02459	0.01548	1.0 ± 0.36	0.04403
Activated Oak biochar 250	0.00974	0.01669	0.01455	0.01176	0.50 ± 0.30	0.02173
Activated RH biochar 250	0.00925	0.01779	0.01520	0.01155	0.60 ± 0.30	0.02364
Activated RH hydrogel 250	0.01201	0.02134	0.01784	0.01409	0.090 ± 0.041	0.03000
RH hydrogel 250	0.01319	0.02834	0.02305	0.01466	0.12 ± 0.043	0.04034
Oak biochar 250	0.01474	0.02184	0.01586	0.01552	0.50 ± 0.30	0.03867
Oak Hydrogel 250	0.014070	0.02947	0.02380	0.01544	0.93 ± 0.31	0.04319
Activated Oak Hydrogel 50	0.01600	0.02931	0.02365	0.018055	0.88 ± 0.36	0.04144
Alginate 50	0.016066	0.03323	0.02675	0.016366	1.1 ± 0.32	0.05079
Activated Oak biochar 50	0.01125	0.01616	0.01293	0.013331	0.46 ± 0.27	0.02184
Activated RH hydrogel 50	0.01847	0.03050	0.02384	0.02194	0.8 ± 0.3	0.03826

Sample	R-factor Sr-O Sr-C	R-factor Sr-O	R-factor Sr-O Sr-O	R-factor Sr-O Sr-Cl		R-factor Sr-Cl
				R-factor	N CI	
Oak Hydrogel 50	0.02007	0.03648	0.03071	0.02165	1.01 ± 0.38	0.04832

K range is 2.5-11.5 Å⁻¹, *dk* = 1, fitting range is 1.25-3.5 Å. σ^2_C values are set equal to σ^2_O . The number of independent data points NIDP is calculated as follows $NIDP = S(2/p)(k_{max} - k_{min})(R_{max} - R_{min})^9$. $S\sigma^2$ was set to 1 following standard fitting

7.2.2 Discussion

Evidence of any second shell backscattering at pH 7 is unusual in strontium EXAFS. While samples formed in high pH systems routinely exhibit second and even third shell backscattering signals in a range of studies, circumneutral samples typically reveal little signal beyond the first, dominating oxygen shell. This is interpreted as outer sphere, weak, electrostatic binding of hydrated strontium to adsorbent surfaces. As this behaviour has been observed in a number of EXAFS studies, limited to inorganic phases, it has been argued that strontium *always* forms outer sphere complexation at pH 7. These data appear to challenge this assumption, showing evidence of second shell signals and demonstrating that this class of adsorbent possesses favourable strontium binding properties – inner sphere binding - at circumneutral pH. To our knowledge, no EXAFS studies have been applied to strontium binding in biochar or hydrogel composites. Although it is important to conduct further work to ensure no sample effects or other processes are responsible for the apparent second shell Sr-C signal.

7.2.2.1 Binding mechanism model development in biochar and hydrogel composites

A range of crystallographic data was used to develop a binding model and aid understanding of the likely strontium binding environment in biochar and hydrogels which is indicated by the data. Sr-O first shell bond distances derived in this study (2.56–2.59 Å) fall within the typical range for Sr-O binding derived from both crystallographic^{222,522,523} and spectroscopic^{37,236,239,240} data which typically position oxygen at between 2.5–2.8 Å distant from strontium. Typically, Sr-O distances on the longer end of this range are attributed to water

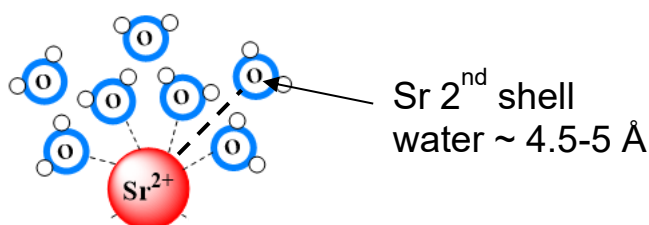


Figure 7-9 Schematic representation of a partial sphere of hydration around a strontium atom, displaying interatomic distance to the second sphere of hydration

molecules^{37,222} while samples in this data set fall towards the shorter end of the length range. As a strongly oxyphilic element, with non-directional valence electrons (s-shell) strontium is almost always found surrounded by between 6 –

12 oxygen atoms⁵²⁴. Therefore the first shell reveals no novel information, nor can the first shell alone reveal whether strontium is bound in inner or outer sphere complexation. More crucial is in examination of second and even third shell signals, which can reveal much more about the nature of the binding environment. Second shell Sr-C distances in both organic and inorganic compounds were used to develop a model of binding within the biopolymers calcium alginate, biochar and in the hydrogel composites. Since EXAFS is only capable of distinguishing approximate atomic mass of a backscatterer, it was necessary to rule out other possible elements as the identity of the second shell backscattering signal. This is particularly so given the known tendency of strontium to retain its hydration shell. Oxygen was ruled out as the second shell back scatterer for the following reasons:

It is unlikely that the second shell signal could be a second sphere of hydration. Evidence suggests that strontium's second shell of hydration sits much more distant from the central strontium atom than the 3.3-3.4 Å observed for the second backscattering shell in measurements^{230,525}. Modelling and experimental data instead suggest the second sphere of hydration for strontium appears at between 4 - 5 Å^{230,525}. This is in part due to hydrogen bonding in water. A 2006 study by Reuter et al²²². into hydrogen bonding in a strontium hydroxide hydrate revealed oxygen-oxygen distances in hydrogen bonded water coordinated around strontium was between 2.67 – 2.87 Å. This is far more distant than the observed second shell distances thus assigning the second shell signal to a second shell of hydration can be ruled out.

Nie et al., in their 2017²³⁵ paper examining adsorption of strontium and selenium to Goethite incorporate a low mass back scatterer into their EXAFS fit at 3.3 ± 0.5 Å. They propose assignment of this signal to a second shell of oxygen ($N = 1.2 \pm 0.3$) which they rationalise as a partial hydration of surface adsorbed strontium. They assign the first shell of oxygen to eight Goethite surface hydroxyl groups ($N = 8.1 \pm 25\%$, $R = 2.57 \pm 0.02$ Å). While their second shell interatomic distance is consistent with this study's second shell observed in biopolymer composites, the coordination number Nie et al. derive is far lower than the majority of samples in this study. Partial hydration consisting of around 1.1 water molecules in addition to around 8.1 surface hydroxyls could indeed be plausible for Goethite. However the high second shell coordination numbers in this study preclude a similar scenario. Furthermore, their stated uncertainty in second shell distance is also much higher at 0.5 Å. This could well be consistent with the known dynamic and disordered nature of strontium's hydration sphere^{230,525,526} however this uncertainty is not consistent with these

data. Nie et al.'s adsorption regime was also conducted in a highly basic solution of pH 10.4. At such high pH, it is likely that spontaneous precipitation of aqueous strontium to carbonate from minor contaminants present during Goethite synthesis, could also be responsible for this small signal as Sr-C³⁷³. In this study, a pH 7 buffer was used in order to prevent precisely such high pH precipitation effects and in order to mimic the environmental conditions that would be expected in the event of accidental release. There is no facile method to distinguish between adsorptive processes and spontaneous precipitation. Indeed precipitation of cations under high pH regimes is likely a major cause of erroneously high uptake capacity data for some cationic metals, notably lead. This is a particular concern for pyro-processed materials such as biochar and some activated carbons, since such thermal treatments tend to produce a basic material that is capable of inducing pH increases in bulk solutions as well as strong local effects which may induce strontium precipitation. Finally, fits to experimental data reported here indicate that fitting a second shell Sr-C path more suitably described the data than a second Sr-O path (Table 7-2).

7.2.2.1.1 Possible role of chloride precursor

Strontium was introduced into the system using a strontium chloride solution. Since strontium is a divalent cation, this meant the chloride concentration present in uptake experiments was double that of strontium – 500 and 100 mg L⁻¹. It is conceivable that chloride may play a role in backscattering signals. Fitting indicates that chloride almost certainly plays no role in first shell backscattering (Table 7-2). Second shell fitting of chloride did yield a number of fits with acceptable (< 0.02) R-factors, although lower still were Sr-C second shell fits. This could indicate some degree of strontium chloride precipitation occurring on the adsorbents. Strontium chloride hexahydrate is a highly soluble salt (53.85 g g⁻¹ at pH 7 and 20 °C)⁵²⁷ which reduces the likelihood of spontaneous precipitation. Further, and as described in Section 4.4, adsorbents were gently rinsed times in ultrapure water in order to remove any salts present on the adsorbent surface. While this doesn't entirely preclude the presence of strontium chloride precipitates on the adsorbent, attempts were made to exclude this possibility in experiment protocol. Future work will focus on specifically excluding this possibility. EXAFS fitting results suggest that second shell Sr-C more accurately reflect experimental data than Sr-Cl signal.

7.2.2.1.2 Possible role of inorganic phases

Given the above points and given the highly carbonaceous nature of biochar, and indeed alginate as a polysaccharide, carbon is the obvious choice for the

identity of the second shell signal. A logical extension of this hypothesis is that the second shell carbon exists in organic forms (i.e. carboxylate, hydroxyl etc.) rather than inorganic form such as carbonate, as these structures are abundant in both biochar and alginate. Although small quantities of carbonate and other mineral phases are found in biochars, substitution of strontium into a carbonate or other inorganic phase is not a known mechanism of uptake and is not expected to play any significant part in uptake at the lower concentrations explored in this study²²⁹. Furthermore, activation with concentrated nitric acid typically removes trace inorganics from the biochar. Given the similarities in the EXAFS signal between unactivated samples, activated samples and alginate samples (which contain no inorganics) it does not seem likely that strontium substitution into inorganics plays any significant role in any samples.

7.2.2.1.3 The role of organic functional groups

Shortest inorganic Sr-C distances tend to fall around 3.0–3.1 Å. Thorpe et al.²³⁹ in a 2012 EXAFS study report 2.98 and 3.04 Å in strontianite and substituted aragonite respectively, while crystallographic data for SrCO₃ shortest Sr-C ranges are 3.0–3.1 Å²²⁹. Organic Sr-C distances typically range between 3.0–3.9 Å depending on the functional group through which binding occurs (). Sr-C distance in strontium diformate, via a bidentate carboxylate type coordination was found to be 3.0–3.1 Å²¹⁸ while strontium oxalate Sr-C distance in a bidentate binding orientation was found to be 3.3 – 3.54^{229,528,529}. A mono dentate type binding mode – such as hydroxyl - was found to give the longest Sr-C distance of between 3.4–3.9 Å^{218,220}. All samples in this study exhibit Sr-C distances which fall intermediate within the range of organic functional groups in , at 3.3–3.4 Å. Fits of standards, strontium oxalate and strontium carbonate correlate well with crystallographic data summarised in . The carbonate standard yielded an Sr-C distance of 3.02 ± 0.02 Å while the oxalate standard yielded 3.32 ± 0.14 Å. Examination of both the structure of the alginate biopolymer and that of biochar and its activated analogue reveal a combination of different binding modes available, including carboxylate, hydroxyl, lactone, and phenolic groups. In alginate only, this is predominantly hydroxyl and carboxylate groups, in accordance with the egg-box model (Figure 6-11). Biochar is well known to possess abundant hydroxyl, phenolic, lactone, ether and carboxylate functionality; activation increases carboxylate and hydroxyl abundance in particular (Figure 5.2). It therefore seems likely, given the amorphous nature of biochar that complexation of strontium is a combination of several modes of binding: carboxylate/oxalate bi-dentate and mono-dentate modes as well as mono-dentate binding via hydroxyls and other oxygen

containing groups. A partial hydration shell likely persists to some extent owing to the charge dense nature of strontium (Figure 6-11). The alginate polysaccharide chain contains only hydroxyl and carboxylate functionality, and the egg-box model Nonetheless, this still represents a strong, inner sphere binding of strontium to biochar and hydrogel composites.

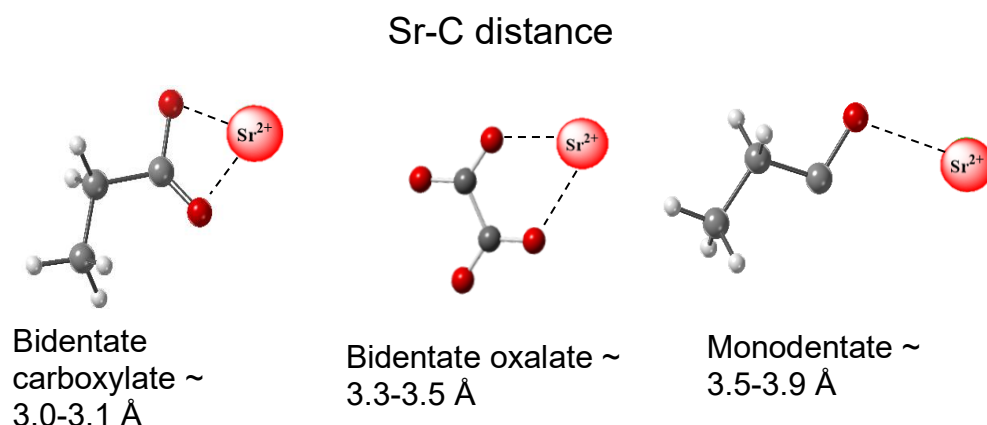


Figure 7.10 Typical Sr-C interatomic distances from crystallographic data for common organic strontium compounds. Carbon is shown in grey and oxygen in dark red. Note: dashed lines represent electrostatic Sr-O attraction not Sr-C distances

The only similar material found in strontium EXAFS literature to the materials in this study, is another bio-derived crystalline calcium oxalate adsorbent²²⁹ which is a common product of many plants and has been found to exist in tree roots. Authors found a binding environment of 7.9 first shell oxygen atoms at 2.56 Å and around 5 second shell carbon atoms at 3.4 Å at pH 6.5. This is in excellent agreement with hydrogel and biochar results.

7.2.2.2 Contribution of component phases

The alginate only control sample appears to exhibit slightly higher second shell coordination numbers consistently. This indicates it has the highest degree of inner sphere strontium binding for all samples tested. As an anionic biopolymer which is known to form hydrogels in the presence of other polyvalent cations, this is no major surprise. Thus, the alginate component of hydrogel composites likely possesses the highest affinity sites for strontium binding. However, as a standalone adsorbent, it exhibits poor mechanical stability. Fortunately, biochar binding sites also possess similar, albeit at a slightly lower degree of inner sphere binding, as evidenced by second shell coordination numbers. Furthermore, no clear differences are observed in binding between 50 and 250 mg L⁻¹ initial strontium concentration samples, indicating that binding site

affinity has not altered with a five-fold increase in strontium ion concentration. A drop in second shell coordination number at higher initial concentration would indicate saturation of higher affinity sites and the gradual occupation of lower affinity sites, yet this is not observed (Figure 6-12). Noting that isotherm data in Chapter 6 consist of data series up to 6000 mg g^{-1} , far higher than concentrations used in EXAFS experiments, this suggests that high affinity, inner sphere type binding sites are not yet saturated at 250 mg L^{-1} , in either hydrogel or biochar, suggesting the adsorbents have high strontium uptake capacities, and crucially, to high affinity sites.

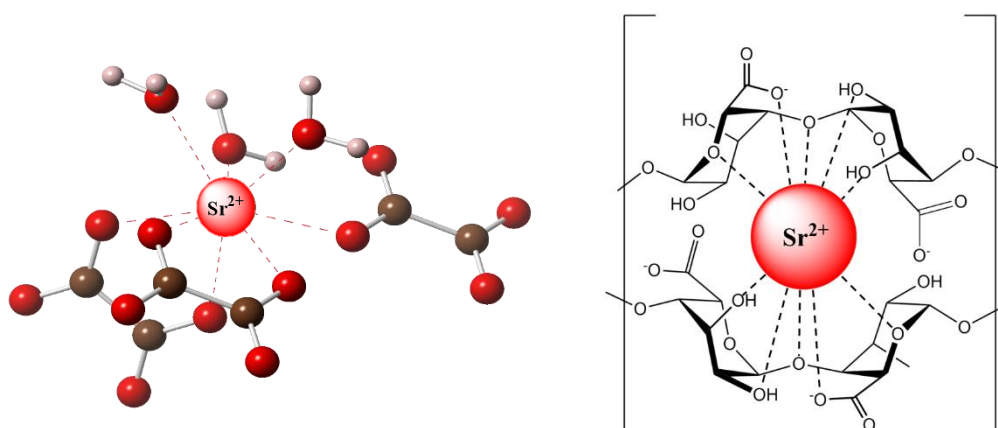


Figure 7-11 A representation of the likely binding environments of strontium in biochar and hydrogel composites, showing (left) a range of possible binding modes in biochar components: bi-dentate, mono-dentate and retention of a partial hydration sphere. (Right), strontium in the “egg-box” binding model of divalent cations to alginate

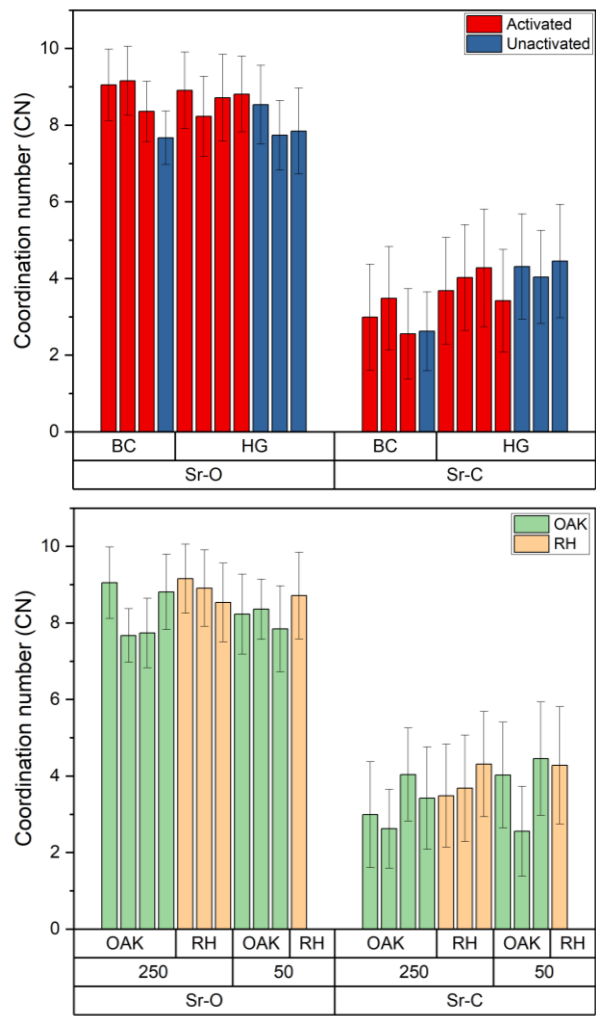


Figure 7-12 Coordination number of absorbing Sr²⁺ atom derived from EXAFS fitting arranged by activation and adsorbent type (top), and biochar feedstock type as well as initial strontium concentration (bottom)

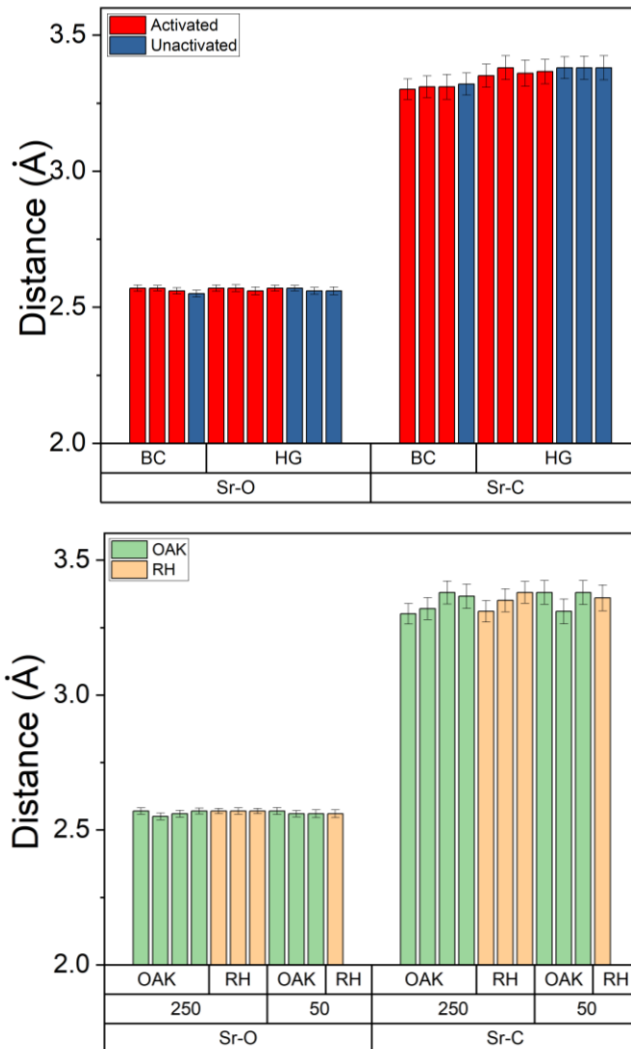


Figure 7-13 Interatomic distances from absorbing Sr²⁺ atom derived from EXAFS fitting organised by adsorbent type and activation (top), initial strontium concentration and biochar feedstock (bottom)

7.3 MnOx activated hydrogel composites

An activated biochar was generated via treatment with potassium permanganate, according to the protocol described by Wang et al. 2015¹⁷⁸. The binding of strontium to the resulting MnOx-biochar and MnOx hydrogel composite was examined using EXAFS (Figure 6-14). Results indicate the presence of both a carbon second shell at $3.34 \pm 0.02 \text{ \AA}$ and a manganese shell at a similar distance ($3.05 \pm 0.02 \text{ \AA}$). By using a simultaneous fitting process, carbon coordination number was fixed at 4.86 ± 1.69 , yielding manganese coordination numbers between 4.6 – 5.77 (Table 7-3). Strontium – carbon distances are consistent with those found in non-MnOx biochar and hydrogels (Section 7.2.1), yielding values in the middle of the range for organic Sr-C distances ($3.0 - 3.15 \text{ \AA}$)⁵³⁰⁻⁵³². The relatively similar Sr-C and Sr-Mn distances suggest two distinct binding environments: one containing carbon and oxygen, and the other manganese and oxygen. The presence of strontium in a single manganese carbonate phase (or similar) is unlikely due to the proximity of manganese to carbon. Such a two-phase model is consistent with understanding of the composite, which consists of a biochar phase (mostly carbon) and a manganese oxide phase. In the case of hydrogels, the additional alginate component is similar to biochar in carbon content. Thus, two distinct binding modes are suggested (Figure 6-15) relating to Sr-C from ‘organic’ phases (biochar and/or alginate) and Sr-Mn from the manganese oxide phase. It should be noted that EXAFS fits did require constraining some parameters and thus detailed interpretation of the data must be cautious. Little difference was observed in fits for different initial strontium concentrations. This suggests that uptake was not preferential to any one phase over the concentration range examined.

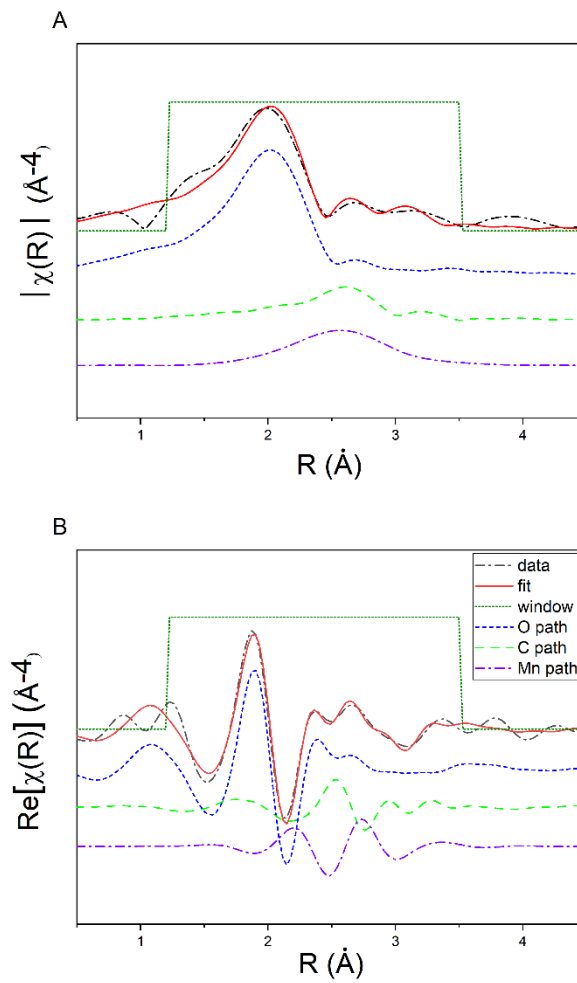


Figure 7-14 Example fit of a MnOx activated hydrogel composites. Magnitude of the Fourier transform (A) and the real part of the Fourier transform (B) including fits and individual paths (offset for clarity)

Table 7-3 Simultaneous EXAFS fitting parameters for MnOx biochar and hydrogel samples at initial strontium concentrations of 50 and 250 mg L⁻¹

Sample	Type	Scatterer shell	Coordination number	R (Å)	ΔE_0 (eV)	$\sigma^2 * 10^{-3}$ (Å ²)
MnOx biochar 250	biochar	Sr-O	9.35 ± 0.85	2.59 ± 0.01		
		Sr-C	4.86 ± 1.69	3.34 ± 0.02		
		Sr-Mn	5.19 ± 1.21	3.05 ± 0.02		
MnOx biochar 50	biochar	Sr-O	9.76 ± 0.85	2.59 ^b	2.77 ± 0.84	14.7 ± 0.96
		Sr-C	4.86 ^a	3.34 ^c		
		Sr-Mn	4.60 ± 0.85	3.05 ^d		
MnOx hydrogel 250	hydrogel	Sr-O	10.3 ± 0.93	2.59 ^b	2.77 ± 0.84	14.7 ± 0.96
		Sr-C	4.86 ^a	3.34 ^c		
		Sr-Mn	5.13 ± 1.16	3.05 ^d		
MnOx hydrogel 50	hydrogel	Sr-O	9.66 ± 1.06	2.59 ^b		
		Sr-C	4.86 ^a	3.34 ^c		
		Sr-Mn	5.77 ± 1.89	3.05 ^d		

K range is 2.5-11.5 Å⁻¹, dk = 1, fitting range is 1.25-3.5 Å. σ^2_C values are set equal to 0.01 Å². σ^2_{Mn} is set to 2 σ^2_O . Simultaneous fit with ^afixed to N_C , ^bfixed to R_O , ^c fixed to R_C , ^dfixed to R_{Mn} of MnOx biochar 250. ΔE_0 was floated once due to the simultaneous fitting. The number of independent data points NIDP is calculated as follows $NIDP = S(2/p)(k_{max} - k_{min})(R_{max} - R_{min})$*

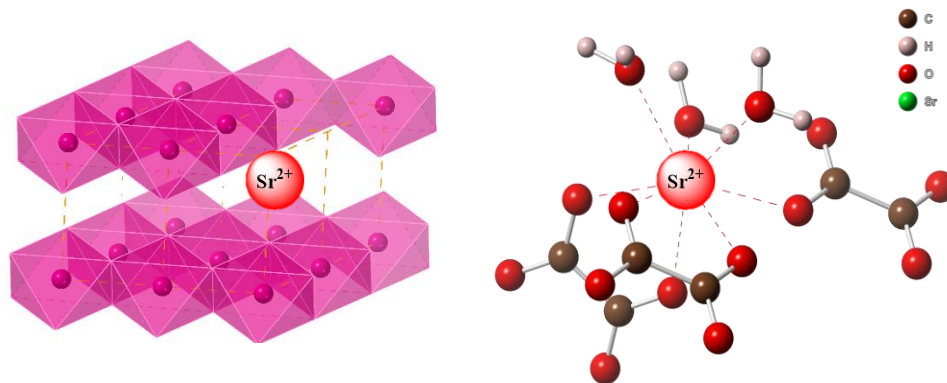


Figure 7-15 Two distinct binding environments are proposed for MnOx biochar and hydrogel composites: an inorganic-type MnOx binding at defect sites (left) and an organic-type binding to alginate or biochar phases within the composite

7.3.1 Manganese oxide identification

The preparation method employed was described in Wang et al. 2015⁵³³ and following McKenzie et al. 1980⁵³⁴. The resulting composite is described therein as a “Birnessite...biochar”. Birnessite is a non-stoichiometric MnO_2 , meaning its oxidation state is nominally Mn^{4+} , but many sites may be occupied by Mn^{3+} or Mn^{2+} . The authors note that this method produced a “poorly crystalline” birnessite within the biochar matrix, but noted higher metal uptake than other, more crystalline preparations. Identifying the precise morphology and oxidation state of the manganese oxide phase used in this study was attempted with similar results. Unfortunately, XRD results proved largely inconclusive, showing only that the mineral present was poorly crystalline in nature. Manganese K-edge XANES was also attempted. Spectra were acquired () however full linear combination fitting failed due to a number of issues mostly relating to difficulties in obtaining high quality data because the experiment was run remotely during the 2020 pandemic. This necessitated all sample preparation in advance of preliminary results and meant that “on-the-fly” modifications to enhance data quality were not possible. Nonetheless, visual comparison of these data with several standard compounds can provide some information. Examination of the edge position and shape suggests that a number of oxidation states are present. Pre-edge features are most consistent with d- MnO_2 (Mn^{4+}), while edge position is intermediate between +2 and +4. Edge shape is similar to that of MnOOH (Mn^{3+}) and Hausmannite ($\text{Mn}^{2+/3+}$). This is consistent with an amorphous, non-stoichiometric birnessite. It is not possible to infer firm conclusions however due to the limitations of the data. Sample self-absorption

and/or sample thickness effects may have contributed to the less than ideal data acquisition.

7.4 Conclusions

Conclusions for this chapter are summarised in Section 9.2 in order to discuss data from Chapter 6 jointly. In brief, EXAFS was used to examine the binding mechanism of strontium to a range of biochar and hydrogel composite adsorbents, both unactivated and activated with nitric acid and a manganese oxide oxidant activation combined dopant. Results indicate a backscattering signal beyond the first shell is present in all samples which fitting indicates is most accurately described by a second shell of carbon atoms, suggestive of an inner sphere type binding between strontium and the adsorbents. This backscattering signal was slightly more prominent in the hydrogel composite adsorbents. Although more work is required to confirm these data, such as exclusion of chloride as a back scatterer, these results suggest that biochar and composite hydrogel adsorbents bind more strongly to strontium at circumneutral pH than most inorganic adsorbents, as reported in literature. More fuller investigation to rule out alternative possible reasons for the back scattering signal beyond the first shell, including chloride, in this work were unfortunately hampered by pandemic related restrictions to synchrotron beamline experiments.

Chapter 8 Pore space analysis of biochar X-ray μ -tomography

8.1 Method Development

Prior to the commencement of this work, only one publication (Jones et al. 2015)⁵³⁵ had presented any quantitative analysis of biochar pore space using XCT, using an X-ray attenuation peak fitting method of the solid vs pore space to derive a pore space volume fraction. This is a markedly different technique for pore space measurement to the more common image analysis based quantification. It is important to note that the intention with this chapter was to analyse pore space using established techniques, and concurrently develop XCT pore space measurement and analysis in order to compare and contrast results. BET gas adsorption analysis in particular is a standard technique for porous carbon materials including biochar. Unfortunately, due to pandemic-related restrictions, and associated limitations to instrumental access, it was not possible to obtain BET gas adsorption results for the entire sample set. As an alternate measure, and since BET analysis is such a standard technique, literature reported values for biochars of the same or similar feedstocks, including activated biochars, have been compiled as a next-best scenario for comparison of XCT results. Literature BET values are collated and reported in Table A-2.

No one established methodology has yet published for XCT image processing for pore space quantification of biochar. In light of this fact, a significant proportion of time was dedicated to the development of an accurate and automated method for pore space analysis of biochar. Although such methods have previously been used to quantify pore spaces of other classes of materials very successfully, and even similar carbon-based materials, phase contrast in

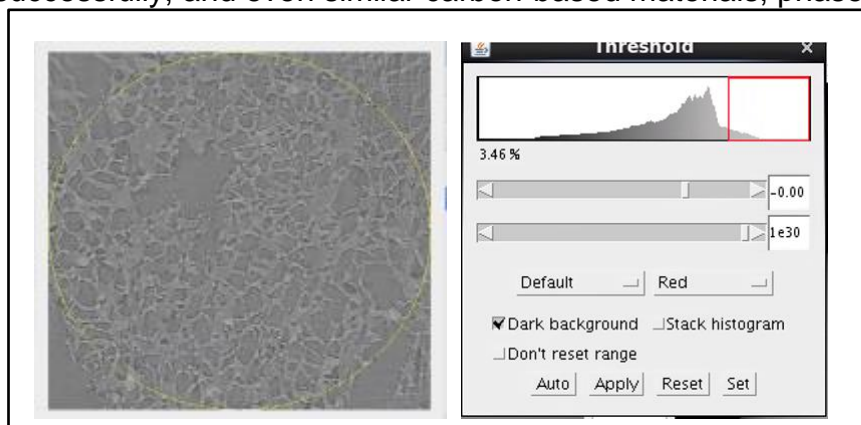


Figure 8-1 A reconstructed tomographic image of biochar pore space without contrast enhancement (left) with its greyscale histogram (right)

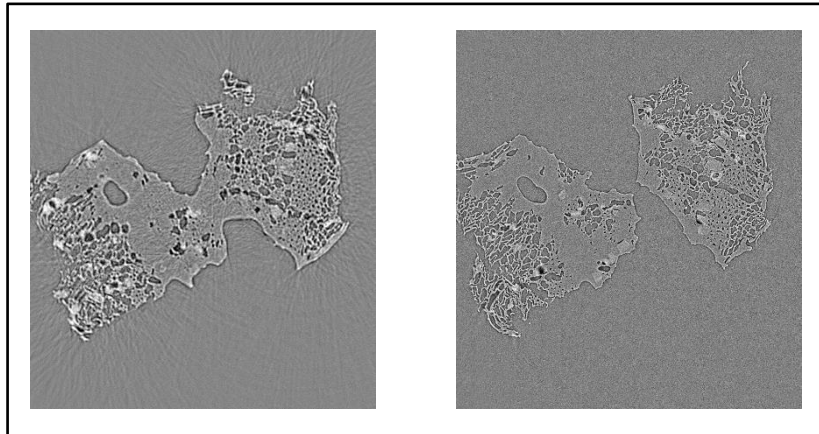


Figure 8-2 The difference in image produced via phase contrast (left) and absorption contrast (right) for an oakwood biochar courtesy of Dr Luke Higgins. Note images are of the same sample but are not identical slice numbers

the reconstructed images (with standard filters applied) of biochar was much too poor to apply any automated pore analysis directly. Figure 7-1 displays such an image with its corresponding greyscale histogram. The histogram plots all pixels in the image according to shade from white to black. As can be observed, the histogram consists of one broad peak, meaning that pixels of pore space and pixels of sample are not well resolved and cannot be trivially classed or separated as such automatically⁵³⁶. This was found to be the case using either phase contrast or absorption contrast modes (Figure 7-2). This is perhaps why Jones et al. opted for their alternative method of X-ray attenuation peak fitting, despite the fact that image analysis has the potential to generate a much wider range of pore space metrics than pore volume alone. Two methods were investigated for image enhancement in order to gain sufficient resolution between pore space and solid sample, each method is summarised in Figure

7-3. Results from both methods were compared in order to ensure that error was not introduced through processing.

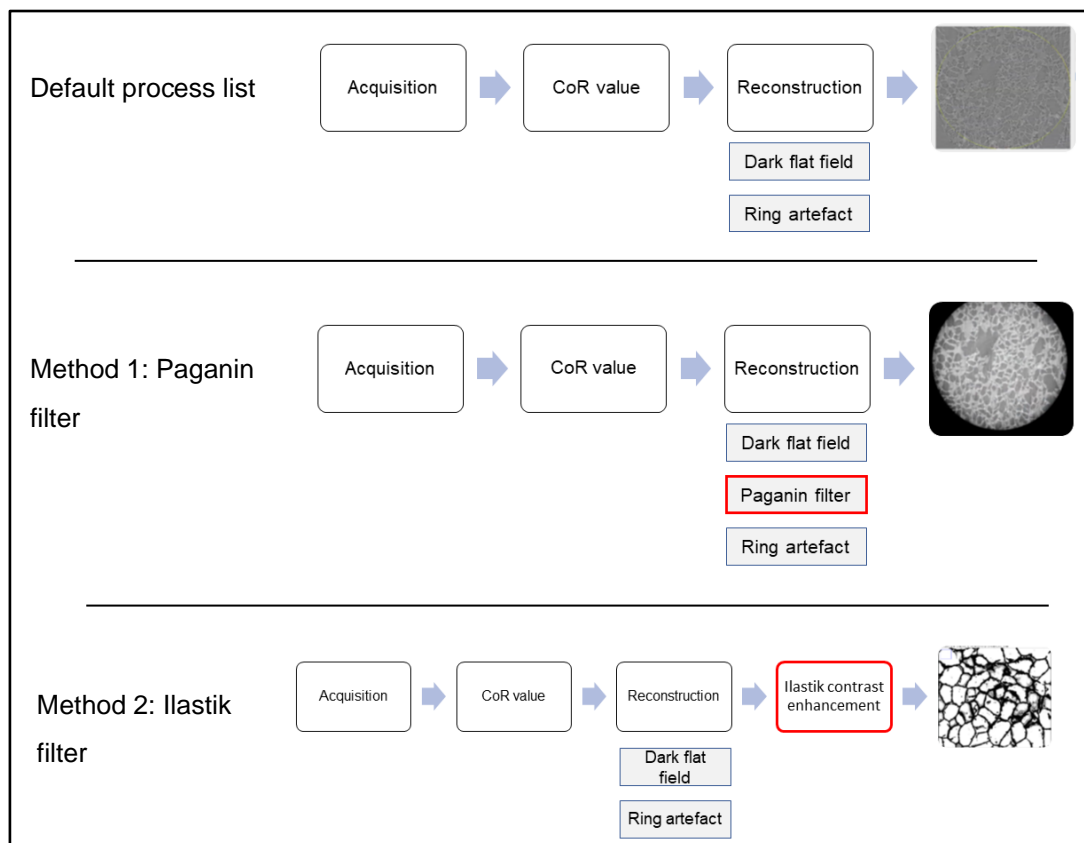


Figure 8-3 Schematic representation of default tomographic reconstruction steps (top) as well as the two modified methods used for contrast enhancement of biochar images

8.1.1 Method 1: Low-pass contrast enhancement and the Savu pipeline

Written in Python, the Savu pipeline was designed specifically for tomographic processing⁵⁰¹. The 'default' Savu pipeline contains in-built corrective filters such as ring artefact removal but also allows the user to 'add on' contrast enhancement via the Paganin filter⁵³⁷. This is a low-pass phase retrieval algorithm able to achieve significant enhancement in image contrast in most tomographic images. This is shown in Figure 7-3 with representative output images from the standard and modified reconstruction process. Central to the filter is the δ/β ratio, the ratio of real to imaginary parts of the estimated complex-valued X-ray index of refraction. It is not possible to derive a value for this ratio experimentally thus the 'best fit' value must be found via trial-and-error. The phase retrieval formula (eqn 18) where φ is phase shift, I_{inc} is incident intensity and I_{Dk} the measured intensity, D_k the propagation distance and F the Fourier transform operator (F^{-1} the inverse equivalent), describes the filter mathematically. Figure 7-4 displays the contrast improvement that the filter achieves (with $\delta/\beta = 120$). Note the greyscale histogram, although not fully resolved into two peaks (corresponding to pore and sample pixels) displays a bi-modal distribution of pixels, much improved as compared with the unfiltered image in Figure 7-1. This improvement was sufficient to proceed with automated thresholding (Section 8.1.3).

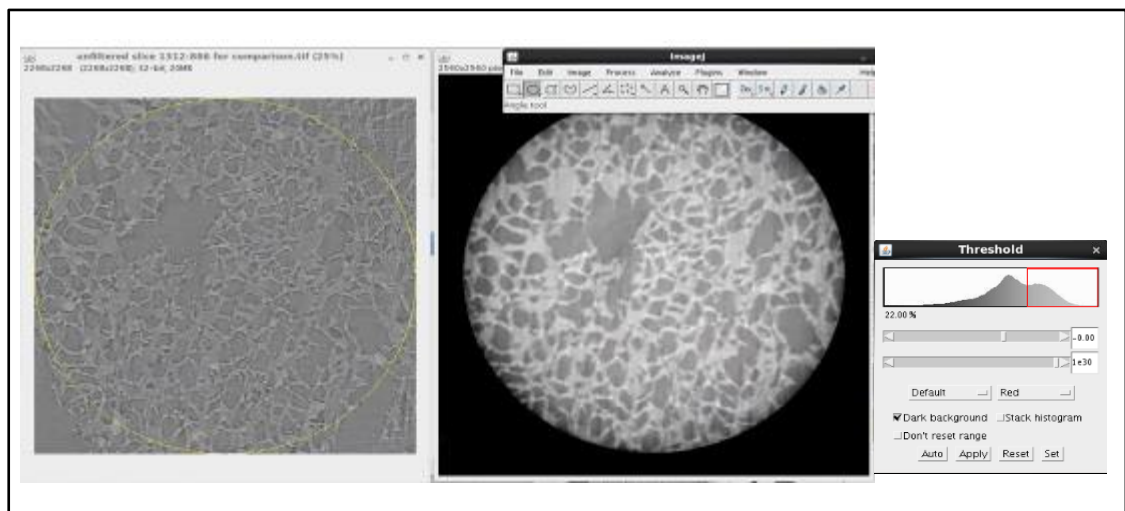


Figure 8-4 The difference in contrast before (left) and after (centre) applying the phase enhancement contrast ($\delta/\beta = 120$). The greyscale histogram (right) is displayed for the enhanced image

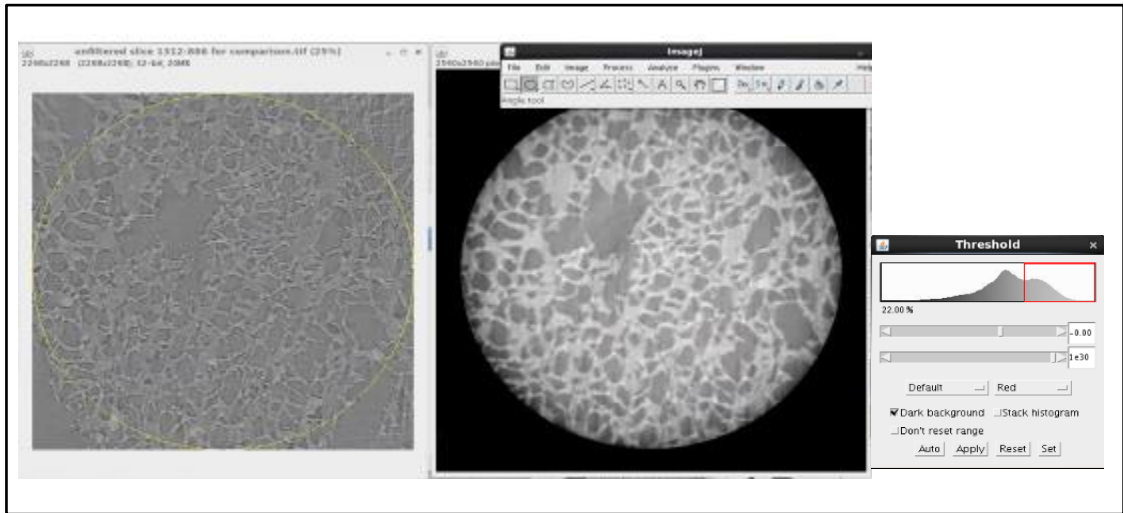


Figure 8.5 The difference in contrast before (left) and after (centre) applying the phase enhancement contrast ($\delta/\beta = 120$). The greyscale histogram (right) is displayed for the enhanced image

It should also be noted that the 'default' filters in the Savu process list were also not necessarily always successful. Sample and experimental differences mean that a degree of 'tuning' must be undertaken to optimise the process. Early processing attempts therefore require a degree of refining or substitution with alternate, more effective filters. shows the effect of two distinct ring artefact removal processes with varying success. Each sample must be checked and tuned in this manner, although consistency across a sample set is typically good.

$$\varphi(x, y) = \frac{1}{2} \frac{\delta_n}{\beta} \ln \left(F^{-1} \left(\frac{F \left(\frac{I_{Dk}}{I_{Inc}} \right) (f)}{1 + \lambda D_k \pi \frac{\delta_n}{\beta} \|f\|^2} \right) (x, y) \right) \quad (18)$$

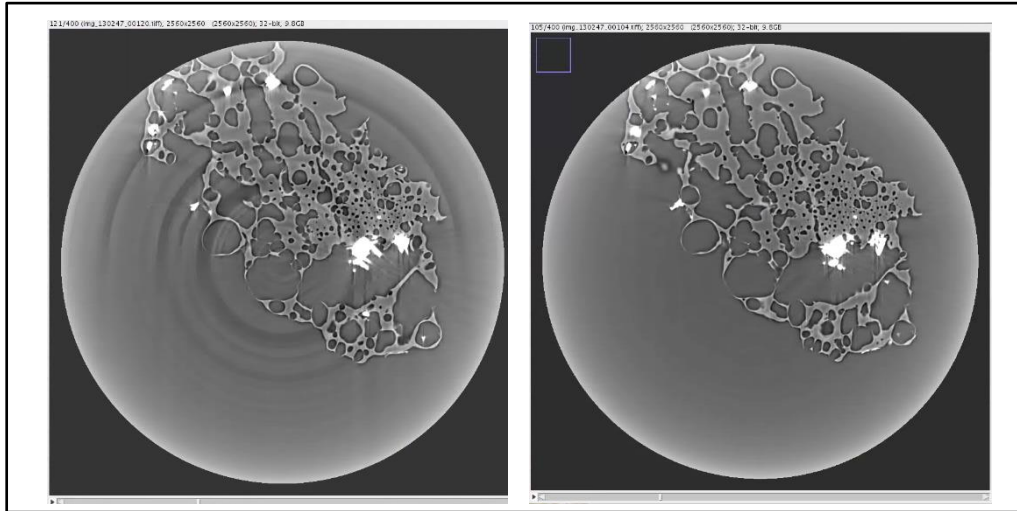


Figure 8.6 Ring artefact removal using two different ring removal processes, the Raven filter (left) and ccpi ring artefact remover (right) in the Savu pipeline

8.1.1.1 Thresholding and quantitative analysis

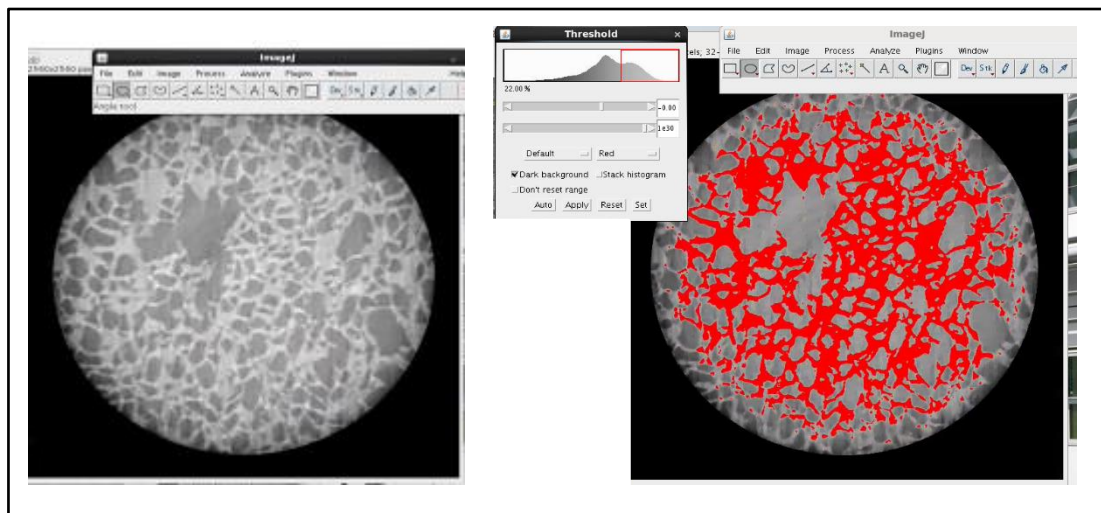


Figure 8-7 An image of biochar processed via the Paganin filter (left) and the same image with a thresholding mask applied (right) with greyscale histogram overlaid

In spite of the Paganin contrast enhancement filter, some radial effects reduced the contrast around the outer rim of the field of view. This prevented accurate thresholding of the full field of view (Figure 7-6), however images were cropped to a central region equal to 0.4 mm^3 which removed the affected region and allowed thresholding. Thresholding is discussed in more detail in Section 8.1.3.

8.1.1.2 Method strengths and limitations

The main drawback of using the Paganin low-pass phase retrieval filter for contrast enhancement is that it tends to slightly increase the area of the solid

sample phase. This is observed as a slight thickening of pore walls and a reduction in pore sizes in filtered images versus unfiltered and results in a loss of some pore features. This effect was especially notable for the smallest of pores and was confirmed in discussion with beamline staff at i-13-2, the data acquisition beamline for this sample set and is due to a smoothing process in the filter. This likely leads to an *underestimation* of overall pore volume and slight underestimation of pore space characteristics. At the time of writing, there is no known method for quantifying this error or correcting for it.

8.1.2 Method 2: Machine learning segmentation

A machine learning tool, Ilastik⁵³⁸ was also used as an alternative method for extracting respective profiles of pore and sample area and volume from tomographic images. Originally developed for cell counting and associated applications in biological sciences, Ilastik has proven successful across a much wider range of domains, including extracting data from tomographic images. A machine learning non-linear algorithm is 'trained' to classify objects in images by the user defining and identifying respective classes, in this case 'pore', 'sample' and in some cases, 'space' denoting free space surrounding sample. No loss of features is noticed using this method. Based upon these user defined classes on a sample sub-set, Ilastik builds and applies a decision surface to the wider sample set. In this manner, it is possible to achieve both binarized images and probability maps with greatly enhanced contrast. The process is summarised in .

8.1.2.1 Thresholding and quantitative analysis

Ilastik's prediction masks are output and undergo thresholding and analysis in ImageJ as above in Section 8.1.1.1. In addition, an uncertainty mask which Ilastik's algorithm generates can also be output and quantified in ImageJ in order to derive a value for uncertainty in the mask creating method. Uncertainty is discussed in more detail in Section 9.2.3.

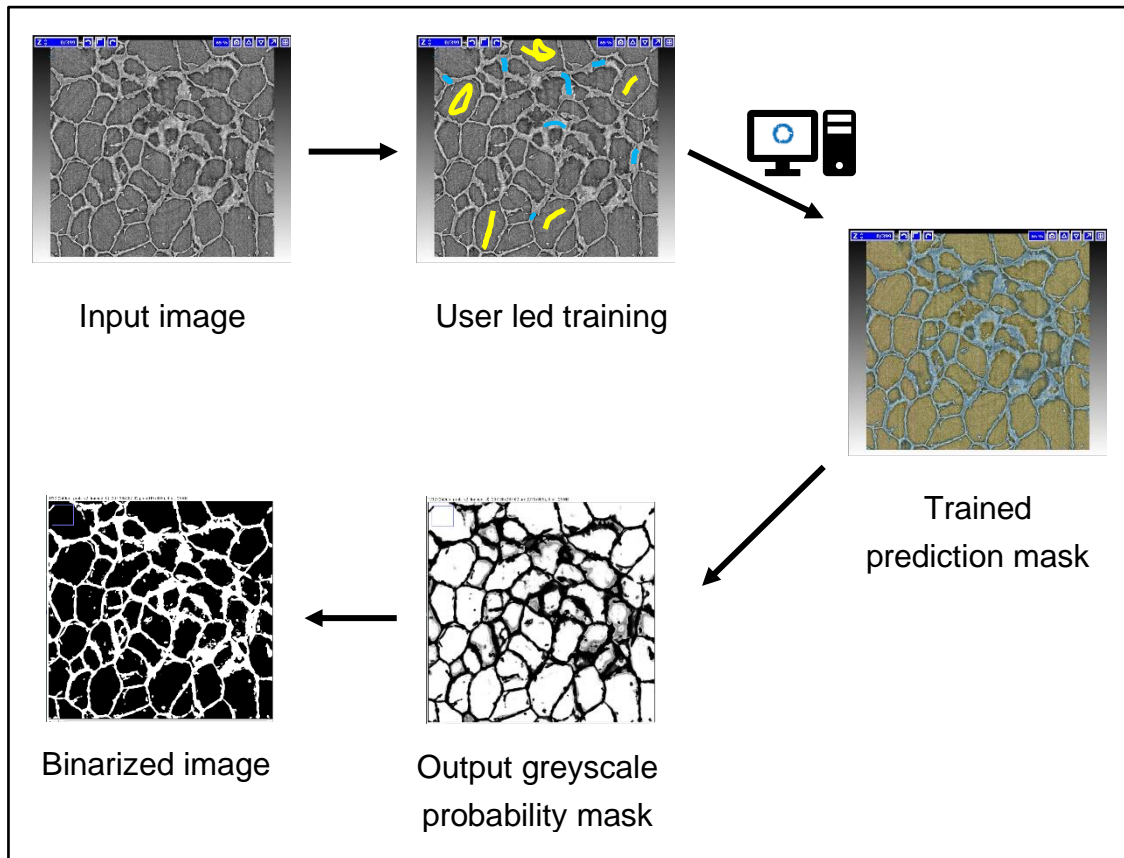


Figure 8.8 Process overview of the Ilastik machine learning object classification method

8.1.2.2 Method strengths and limitations

Ilastik has a degree of built in flexibility by allowing several output forms and also calculated uncertainty in its own results. Output in the form of greyscale probability masks allows for the user to further refine the thresholding, by means of comparison with original images. Uncertainty can be output and quantified separately to derive a value for uncertainty in the image processing. On the other hand, several iterations of training were necessary to achieve the desired accuracy in some cases as the classifier struggled to correctly assign certain shapes or sizes, particularly the rice husk biochar samples since these images contained significant quantities of free space (not sample or pore space). Since the algorithm is optimised for identification of small pores, large blank areas proved problematic, as can be seen by the poorly classified pore space (blue) in . However, since it was possible to extract each of the three layers (red, blue and green) separately, it was possible to obtain pore space metrics using the green layer, details of which are in Section 8.1.3.

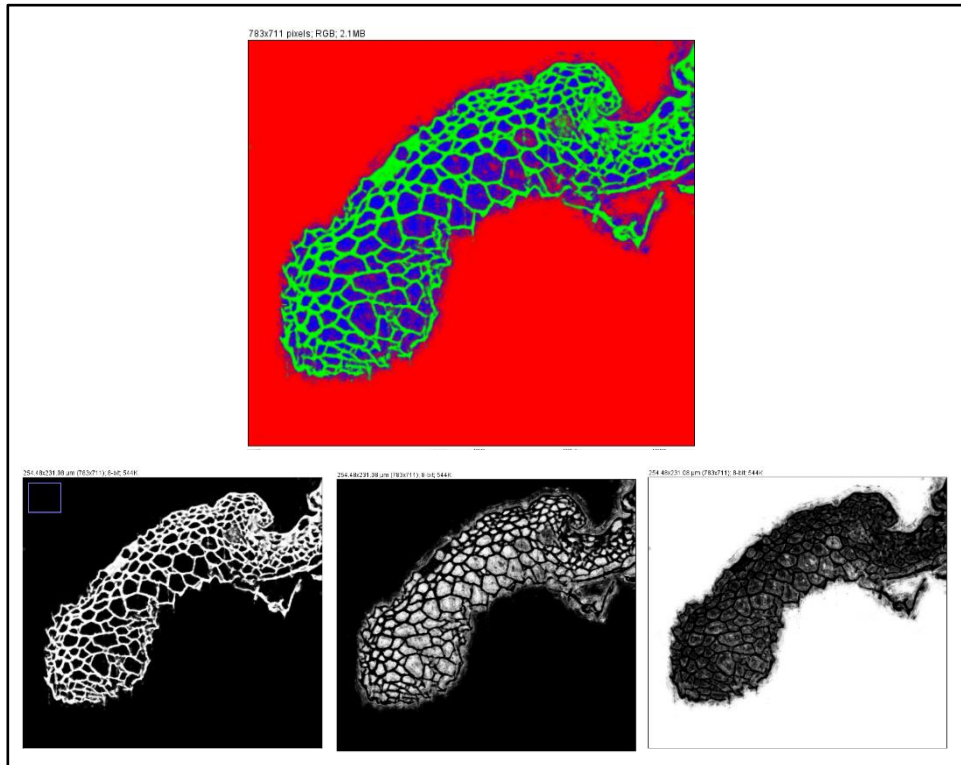


Figure 8.9 Example of three phase training on a rice husk biochar in Ilastik (top) with each of the three green, blue and red layers (left to right) extracted below

8.1.3 Thresholding

Some additional considerations should be mentioned which relate to the thresholding and analysis steps. These apply to both of the contrast enhancement steps outlined above. Thresholding is the process of applying a chosen greyscale threshold value, and excluding all pixels above or below the set value. By this method, it is possible to create a binary image which accurately represents the distribution of two phases in an image. Image binarization is necessary for pixel counting tools which provide pore space metrics. Due to the thin sample thickness of most rice husk samples, applying a standard crop to a central, rectangular volume was not possible. In this case, data were cropped to areas of equal volume to other samples by selecting the most optimal sub-regions.

8.1.3.1 Quantitative analysis

Binarized image sets were analysed using the ImageJ *Analyse Particles* tool, to obtain data for overall pore space fraction, pore Feret diameter (Figure 7-9), circularity (eqn 19) and pore area data were captured. In order to extract pore space data from the rice husk samples, which are surrounded by large areas of free space, a binarized form of the green layer image from was used by deselecting from the analysis all areas above a selected threshold area value, since pores are all at least an order of magnitude smaller than free space area. This allowed for an accurate determination of pore space in such samples, although it did increase the uncertainty in measurements.

Pore circularity is defined by equation 19 where A is area and p is perimeter length:

$$C = \frac{4\pi A}{p^2} \quad (19)$$

8.1.3.2 Automated tortuosity algorithm

The tortuosity of a geometric curve is defined by its geometric length L_G divided by the Euclidian length L_E (the shortest distance between two parallel planes).

$$\tau = \frac{L_G}{L_E} \quad (20)$$

An algorithm based on pixels or voxels (2D or 3D) is used here based on the geodesic reconstruction work of Gommes et al 2009. In the case of a 3D voxel stack, a reference direction is chosen (x, y or z) and the algorithm sweeps through the selected volume, computing the geometric distance L_G of the pores. The number of slices to reach the last slice in the stack is the Euclidian distance L_E .

8.2 Alternative methods

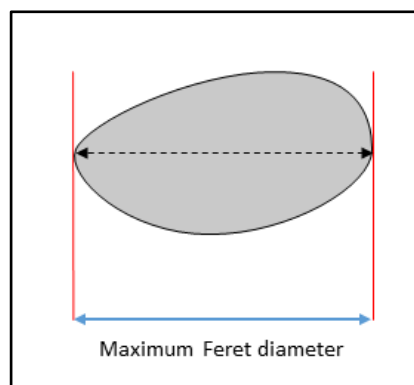


Figure 8-10 The Feret diameter is a measure along the longest axis of a pore or space

Other tools were investigated for image analysis including Avizo and the in-built ImageJ classification tool Weka. Avizo, although a powerful tool for analysis of tomographic data, could not successfully distinguish between pore and sample phases due to the same image contrast issues as previous. Use of the Paganin filtered data sets were successfully examined in Avizo, but the accuracy issues outlined in Section 8.1.1.2. Access to Avizo was highly limited due to licencing restrictions and computational demands. Weka is a similar machine learning tool to Ilastik, but was developed later than Ilastik and still in beta mode at the time of use.

8.3 Results: initial investigation with spent coffee ground biochar

8.3.1 Qualitative data initial set

The effect of activation on the macro pore space of biochar was initially probed by comparing an unactivated spent coffee ground biochar with a ZnCl_2 activated analogue. The raw biomass feedstock was also included for comparison. This initial investigation revealed significant difference in the macro pore structure between all three samples as can be viewed in the cross sectional 2D images in Figure 8.11 (top row), showing representative greyscale images of the internal pore structure. Darker greyscale colours depict pore or void space while solid sample is shown in lighter greyscale tones. By comparison of the control biochar with its biomass precursor, the pyrolysis treatment appears to widen existing pore structures already present in the raw biomass, creating an extensive pore network with relatively thin pore walls. In contrast, the biomass displays smaller, fewer and more dispersed macro pores with far greater volume taken up by solid sample. This is consistent with existing wisdom on the pyrolysis process, in which pore formation proceeds via an extensive mass loss process via thermochemically driven decomposition reactions. This essentially erodes the physical structure, leaving larger pores

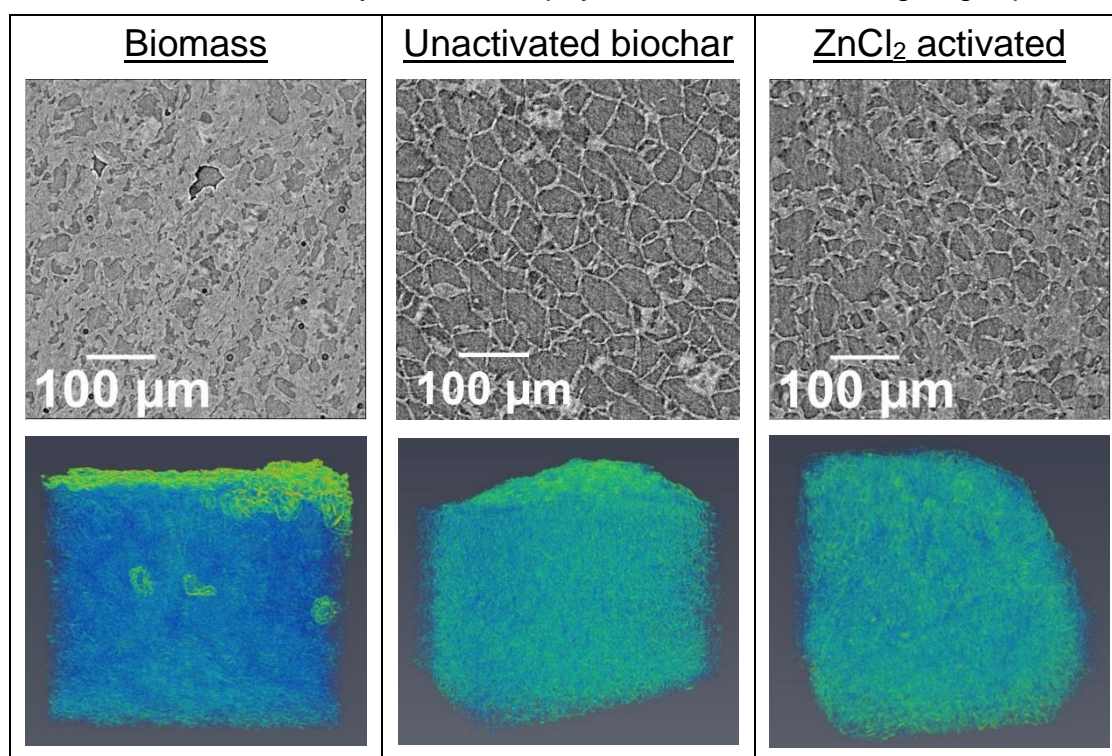


Figure 8.11 Selected 2D (top) and 3D (bottom) reconstructions of initial data set using spent coffee ground biochar. 3D images are shown in a false colour heat map to depict the extensive internal structure. 3D images are not scaled due to angled orientations.

and thinner pore walls. Nonetheless, the majority of the unactivated biochar has a macro pore structure that is recognisable as of biosynthetic origin, due to its repeating nature. This is readily apparent when viewing the 3D sample volume as a series of 2D images.

8.3.2 Activation

The ZnCl_2 activated biochar displays a markedly different macro pore structure to its control biochar. The recognisable biological structure present in the control biochar has to a largely been lost, and instead pore walls appear thicker while pores appear smaller on the whole and less regular in shape. Pore walls appear to be deformed. Typically, the effect of activation on macro pore structure is concluded using surface techniques such as SEM⁵³⁹ which does not reveal any information about internal pore structure, for example interconnectivity or formation of larger cavities. Surface techniques only reveal information about pore mouth appearance and surface morphology. Figure 8.11 (bottom row) displays 3D reconstructions of each sample. Although not as informative as 2D representations, these false colour images can provide more qualitative information on the pore structure. In addition to these differences in general macro pore structure between unactivated and ZnCl_2 activated biochar, the unactivated spent coffee ground biochar revealed larger voids within (Figure 7-11) which indicate a collapse of the internal pore walls into larger cavities during the pyrolysis process. Such voids are absent in the ZnCl_2 activated analogue. The specifics of the activation process are thought to proceed during pyrolysis via zinc ions providing 'activation centres' around which oxygen functional groups can form and are stabilised and protected from decomposition during the high temperature treatment⁷². In contrast, during the thermochemical formation of unactivated biochar, no such stabilising metal centres are present to any significant extent. It is possible that this leads to the thermochemical erosion of the internal pore walls in unactivated biochar, to an extent to which smaller macro pores are collapsed into the larger voids see in Figure 7-11. This feature of pore collapse in unactivated biochar is a possible contributing mechanism to the effect of activation observed for micro and meso porosity. Activation is well known to increase micro and meso pore area and volume⁵⁴⁰. Collapse of macro pores into larger voids in the unactivated biochar provide a smaller internal surface area on which smaller pores may form. Activation appears to protect against this, thus increasing the internal macro pore surface area onto which a greater volume of micro and meso pores may form.

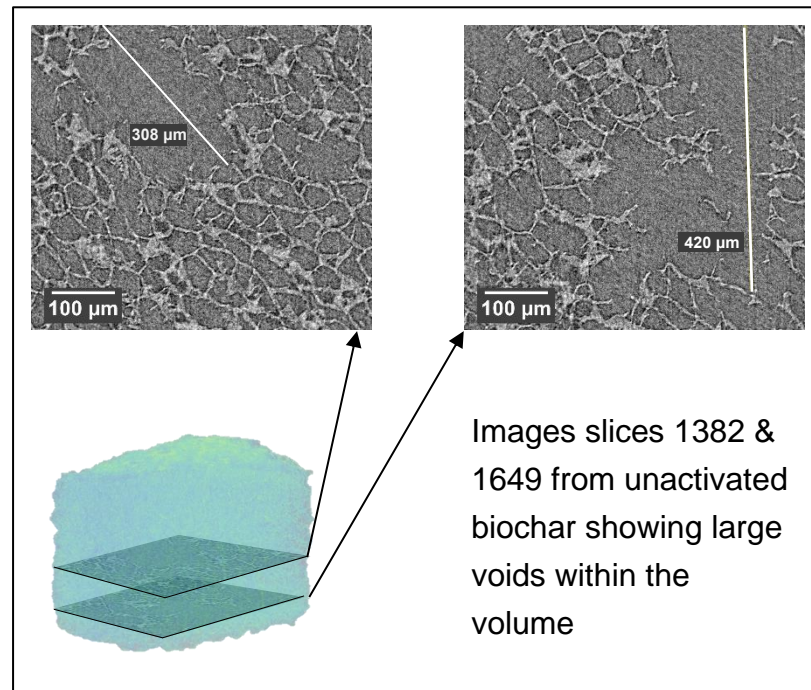


Figure 8-12 Image slices no. 1382 & 1649 of unactivated biochar sample volume showing larger voids present within the internal structure. The widest void diameter (max Feret diameter) are indicated and annotated

8.3.3 Quantitative analysis

Overall macro pore volume was found to be around 30 % higher in unactivated spent coffee ground biochar than ZnCl_2 activated biochar (Figure 7-12). Unactivated biochar was found to have the highest macro pore volume at 71 %, while its ZnCl_2 activated analogue was found to possess 51 % macro porosity. This is consistent with the pore features observed in Section 8.3.1, specifically the slightly larger macro pores as well as larger voids present within the unactivated biochar contributing to a larger macro pore volume than ZnCl_2 activated biochar. Both are significantly more macro porous than their precursor biomass feedstock (spent coffee grounds), which was found to have 12 % macro pore space by volume. Pore circularity and the pore size distribution were compared (). A larger overall pore count (note y-axis inconsistency) and a narrower distribution with a skew towards smaller macro pores is observed in the activated biochar. A higher pore circularity distribution is observed in the activated biochar than unactivated control. Table 7-1 summarises key pore size characteristics of both biochars, which indicate overall that ZnCl_2 activation produces a biochar with smaller macro pores, and a greater number of macro pores per unit volume. The average number of pores per image detected is more than one third greater in activated biochar (140 per image) compared with

the unactivated biochar (90 per image), while average macro pore area for ZnCl₂ activated biochar is 50 % smaller (600 μm²) than for unactivated biochar (1200 μm²). The average maximum Feret diameter of pores is also significantly larger in the unactivated biochar sample. These data suggest a smaller number of larger pores in unactivated biochar as compared with ZnCl₂ activated biochar, which is consistent with a larger overall pore volume as noted in Figure 7-12.

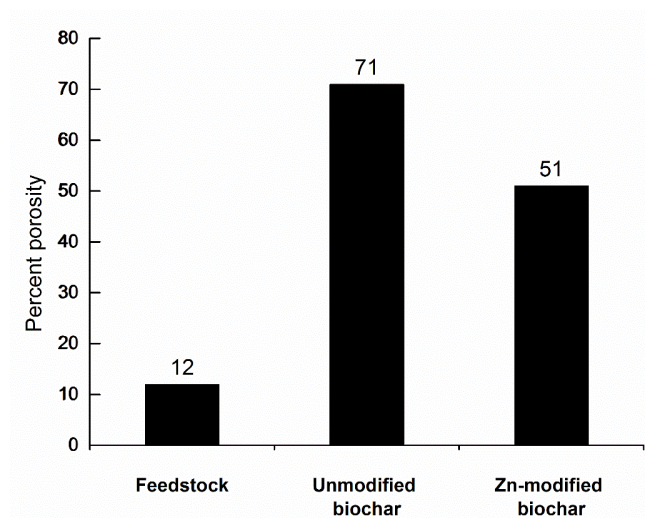


Figure 8-13 Macro pore volume for spent coffee ground as well as a control biochar and ZnCl₂ activated biochar. Measured from a 0.4 mm³ sample volume and a pixel size of 0.325 μm

8.3.4 Discussion

Both qualitative information and quantitative data are self-consistent in describing larger macro pore voids in an unactivated spent coffee ground biochar as compared with its ZnCl₂ activated analogue, which displays smaller macro pores, a greater number of pores and a smaller pore size distribution, at least at these scales. While the effect that common activators such as ZnCl₂ have on the meso and micro pore architecture of biochar is well described and studied, its effect on larger pores is far less studied.

ZnCl₂, as a Lewis acid, interacts with electron lone pairs (non-bonding electrons) e.g. oxygen non-bonding electrons in a cellulose hydroxyl group of precursor biomass. Much in the same way that ZnCl₂ is an effective catalyst for organic synthesis transformations⁵⁴¹, it promotes the thermochemical reactions that occur during pyrolysis of biomass by reducing the activation energy threshold for such processes¹²⁰. It is known to enhance micro and meso porosity of a wide range of biochars (Table A-2).

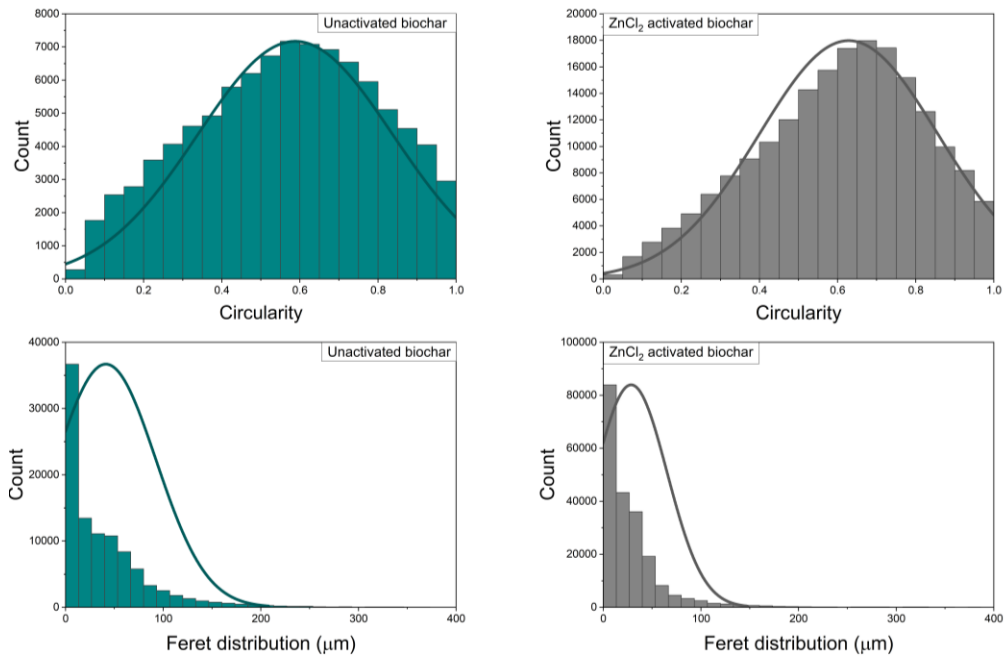


Figure 8.14 Pore circularity (top) and Feret diameter (bottom) distributions for all pores detected for unactivated biochar and ZnCl₂ activated biochar

Table 8-1 Quantitative pore space data for spent coffee ground biochar - control unactivated and ZnCl₂ activated

	% pore volume	Average pore area / μm ²	Largest individual pore area / mm ²	Average number of pores per slice	Feret diameter average / μm
Unactivated biochar	71	1200	0.120	90	41
ZnCl ₂ activated	51	600	0.045	140	29

8.4 Results: expanded Sample Set

8.4.1 Qualitative analysis

Selected 2D tomographic images of the internal macro pore space architecture are displayed in Figure 8.15, showing the respective alterations that activation via common chemical activation agents (HNO_3 , ZnCl_2 and KMnO_4) cause to macro pore morphology. Of three precursor biomass types examined, Oakwood (OAK), spent coffee ground (SCG) and rice husk (RH), the most striking transformations to the macro pore space morphology are those activated with ZnCl_2 . Both OAK and SCG biochars activated with ZnCl_2 are unrecognisable as pertaining to their respective feedstocks, or to their unactivated biochar controls, with extensive modification to the shape and size of pores. A similar effect is also observed in the RH ZnCl_2 activated biochar, although to a lesser extent. Its pores appear widened and more circular, however the distinctive precursor – rice husk - shape and structure of a thickened outer husk layer and a predominance of pores towards the inner husk wall is still recognisable.

HNO_3 activation also appears in general to widen the macro pores or create more extensive macro pore structure. These effects are also clearly modulated by the precursor biomass. HNO_3 activated OAK has clearly exhibits more widened pores than the unactivated OAK biochar, with much thinner more delicate, filigree looking pore walls, a greater occurrence of larger pores and an apparent greater degree of interconnectivity in the macro pore architecture. Pores on the whole appear to have retained some resemblance to the control biochar/precursor in shape although larger pores are more circular. SCG activated with HNO_3 retains the recognisable morphology of its control biochar very well, with perhaps some degree of increased interconnectivity or collapse of pore walls into larger internal voids. The corresponding activated RH sample has again retained the distinctive outer ridge of the husk while the inner section has gained much more extensive macro porosity. Activation via KMnO_4 produced varied results. Its activation effect on OAK macros pore structure is particularly notable. Although the general form of the pore space is retained, pores appear less regular in circularity. Most striking of all is what appear to be some form of pore filling which is apparently present throughout a significant fraction of the volume. This is discussed in more detail in Section 8.5. While little noticeable difference is apparent in images of KMnO_4 activated SCG, the equivalent RH sample appears to show enhanced macro porosity of the inner husk region (the region inside of the ridged, thick outer husk) over the

unactivated RH control biochar. 3D reconstructions of each sample are in displayed in Figure 8.15..

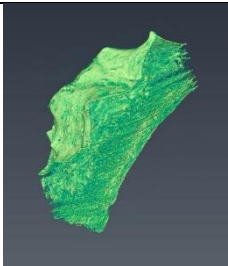
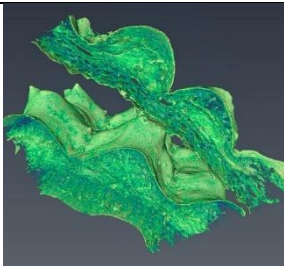
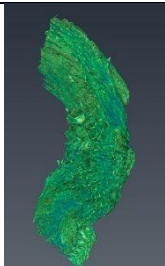
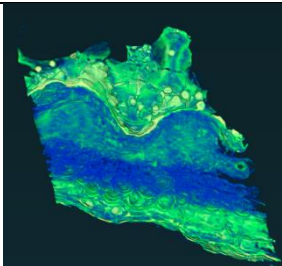
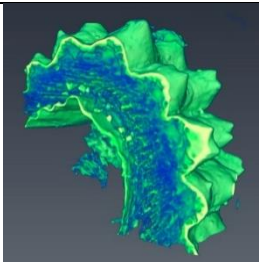
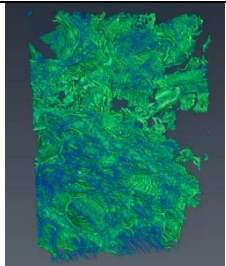
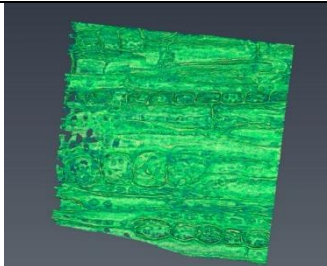
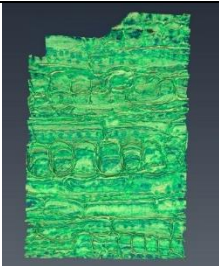
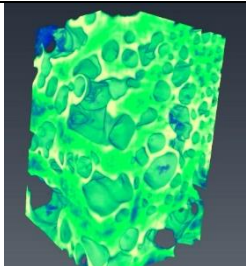

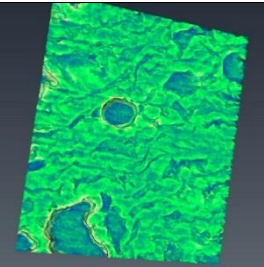
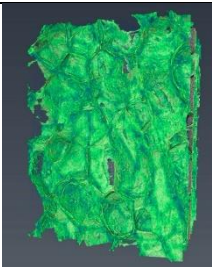
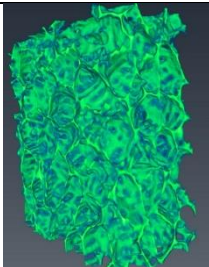
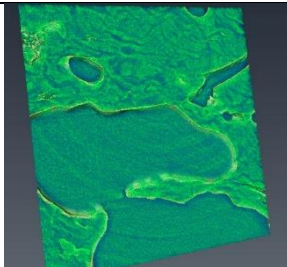
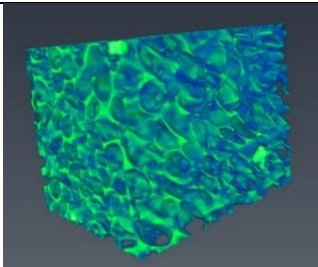
	Feedstock (biomass)	Control biochar	HNO ₃ activated	ZnCl ₂ activated	KMnO ₄ activated
Rice husk (RH)					
Oak wood (OAK)					
Spent coffee (SCG)					

Figure 8.15 3D reconstructions of all samples. Field of view = 0.2 mm³, scale bar not included due to angled orientations

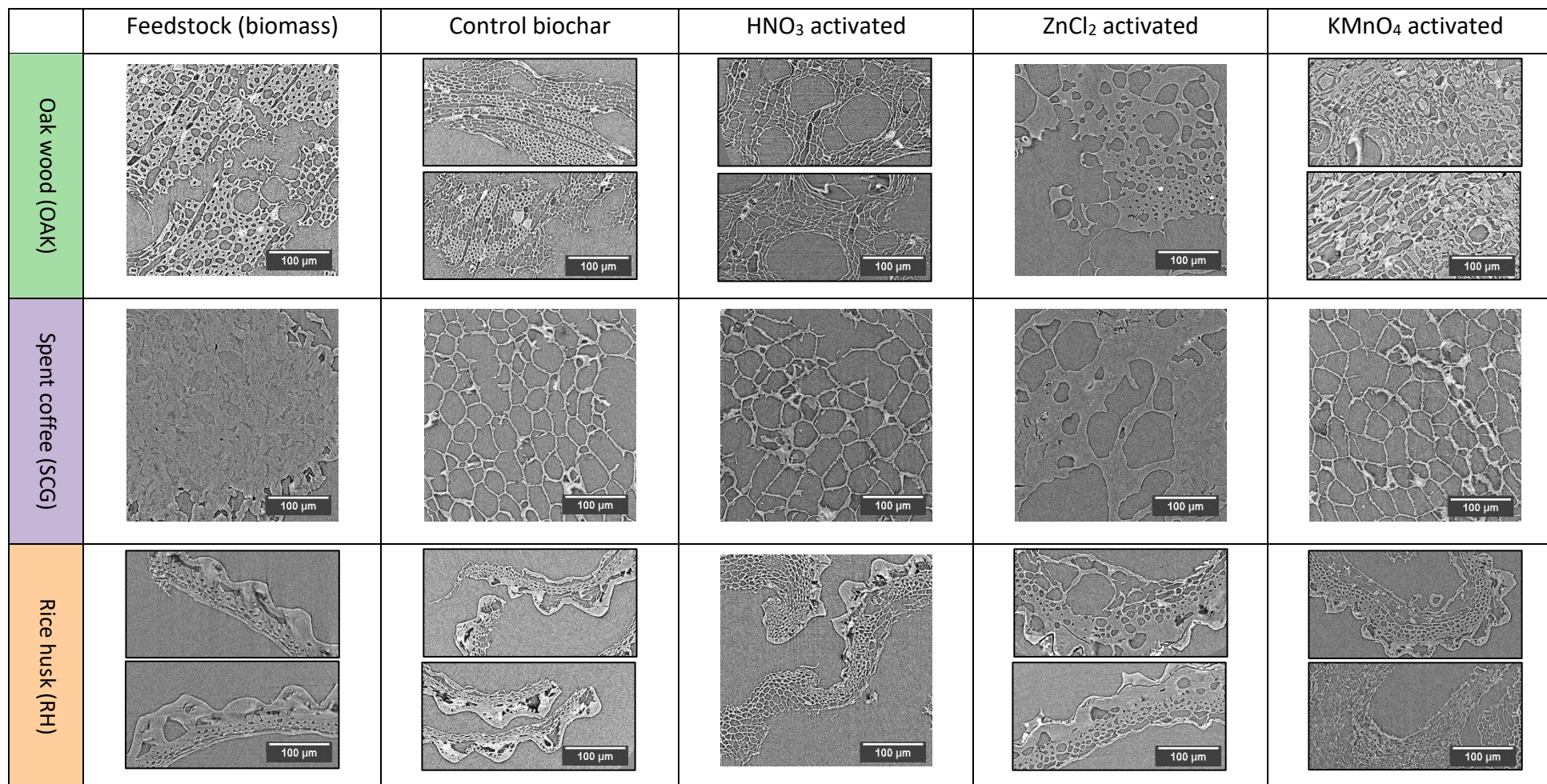


Figure 8.16 Representative 2D tomographic images of the internal macro pore structure for several activated biochars with corresponding unactivated biochar control samples and precursor biomass samples for oak wood, spent coffee grounds and rice husk feedstock precursors

8.4.1.1 Pore space characteristics – Oakwood set

Activation alters the pore architecture of oak wood biochar markedly. Figure 8.15 (top row) displays representative images of the internal pore features of oak wood biomass precursor, a control unactivated biochar and three activated variants. These samples are displayed in more depth in Figure 8.18, with cross-sectional views from each orthogonal plane of orientation. Both the unactivated biochar and HNO_3 activated biochar display significant anisotropy in pore architecture, with a greater number of elongated pores in the XZ and YZ planes. This trend is also continued with OAK- ZnCl_2 which displays similar anisotropy, although pore shapes are slightly less well defined. In contrast, all three planes in OAK- KMnO_4 appear relatively consistent in structure, with only limited evidence of elongated pores in the YZ plane. These much more comprehensively describe the macro pore space. Curiously, KMnO_4 activated OAK displayed not only a modified pore structure, with widened, less circular pores, but also revealed an apparent filling of pores by a phase or phases unknown. This is displayed in Figure 7-15.

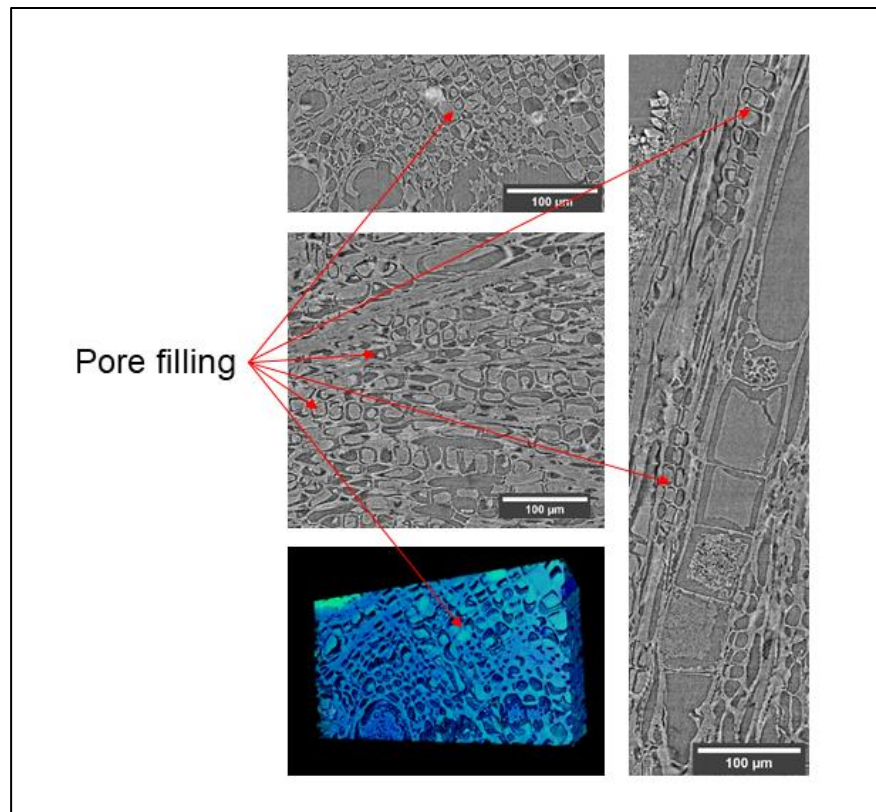


Figure 8-17 Apparent filling of pores in KMnO_4 activated OAK by an unknown phase

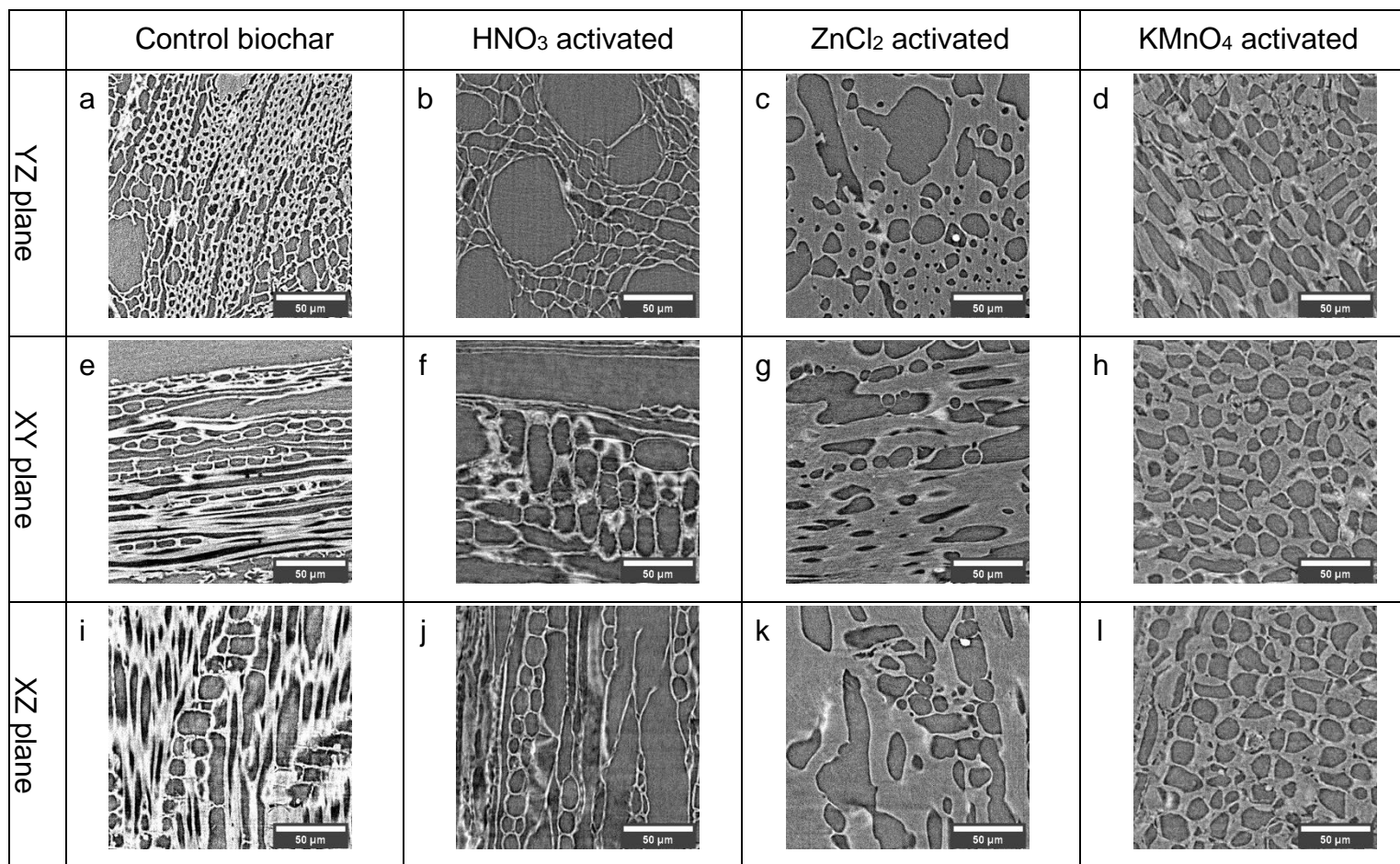


Figure 8.18 Orthogonal views of oak wood biochars: unactivated control biochar (a, e, i), HNO₃ activated (b, f, j), ZnCl₂ activated (c, g, k) and KMnO₄ activated (d, h, l) in the XY, XZ and YZ planes respectively

8.4.1.2 Pore space characteristics – Spent coffee ground set

Orthogonal reconstructions of the macro pore space of spent coffee ground unactivated biochar reveal little obvious anisotropy (Figure 8.19a, e and i). This is also observed in HNO₃ or KMnO₄ activated analogues, which show minimal effect of activation on the macro pore space. There is perhaps a slight pore wall thinning, but this is difficult to gauge from observation alone. In contrast, ZnCl₂ activation has dramatically altered the macro pore structure of the material, rendering it completely unrecognisable as originating from SCG biomass. The material appears to exhibit thicker walls and fewer, larger and less uniform pores. Yet in common with the other SCG samples, it also shows little anisotropic pore features.

8.4.1.3 Pore space characteristics – Rice husk set

All activated rice husk biochars appear to retain the distinctive generalised structure of their precursor biomass. All exhibit a ridged outer section (the tough outer husk section) with increased macro porosity towards the inward section of the husks (most apparent in Figure 8.20 a-d). Images e-h display comparative representations of the YZ plane. A degree of pore space distortion is observed in all three activated biochars, as compared with the unactivated control (image e). Images f-h all show distinctive alteration: HNO₃ activated RH (f) displays some pore wall thinning and extremely irregular pore shapes. ZnCl₂ activated RH (g) shows more circular pores and much thicker internal pore walls. KMnO₄ activated RH (h) displays sections that appear very similar to the control unactivated sample (e), but also contains an internal section which appears to have very thin pore walls and more developed pore space. Images i-l, display each sample in the YZ plane and show very similar pore structure characterised by an undulating, often thick outer surface, and elongated pores within with relatively thick pore walls. KMnO₄ activated RH in addition also exhibits a more filigree inner pore structure, comprising of extremely thin pore walls and more expensive pore space, shown the right hand side of Figure 8.20.

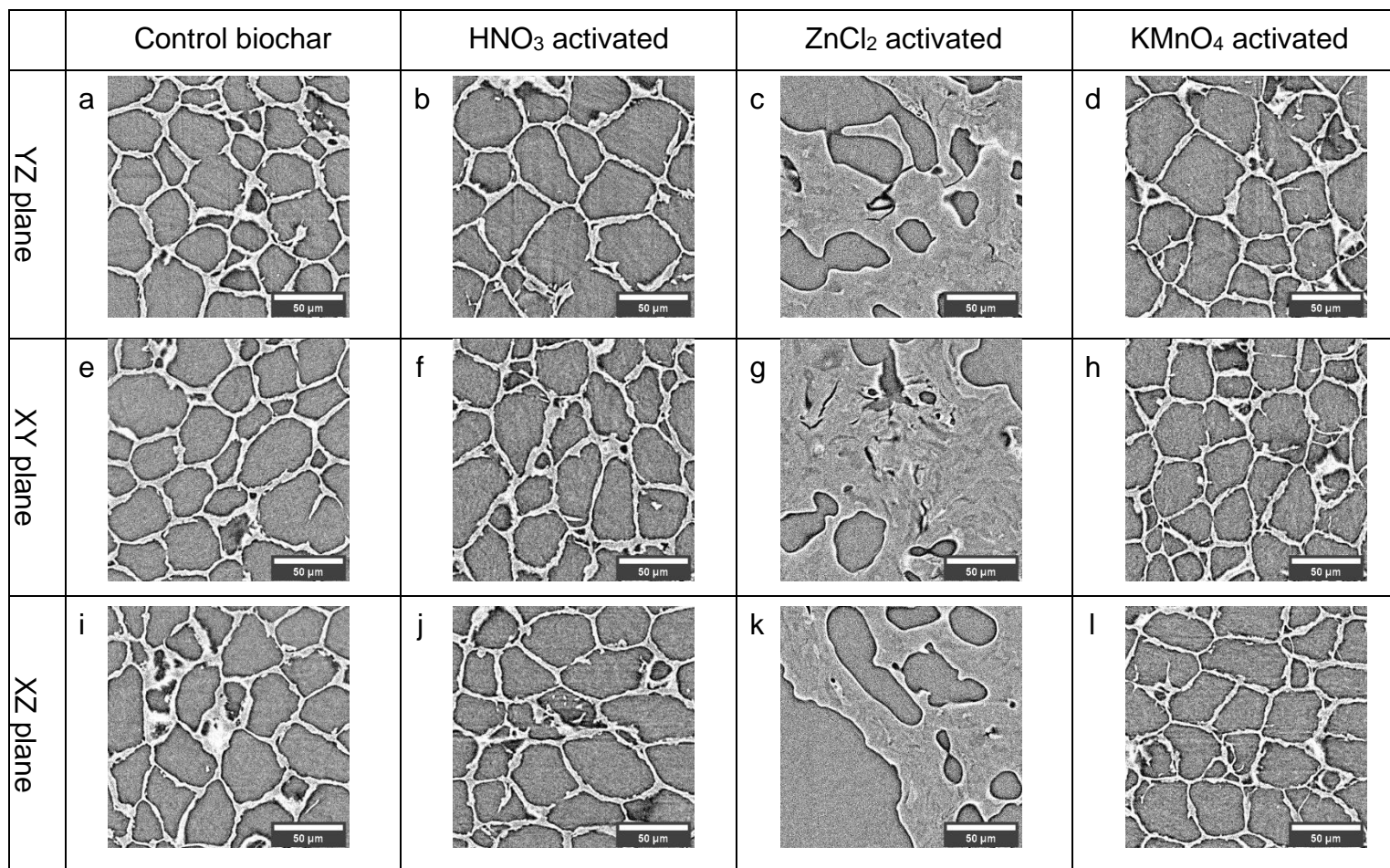


Figure 8.19 Orthogonal views of spent coffee ground biochars: unactivated control biochar (a, e, i), HNO₃ activated (b, f, j), ZnCl₂ activated (c, g, k) and KMnO₄ activated (d, h, l) in the XY, XZ and YZ planes respectively

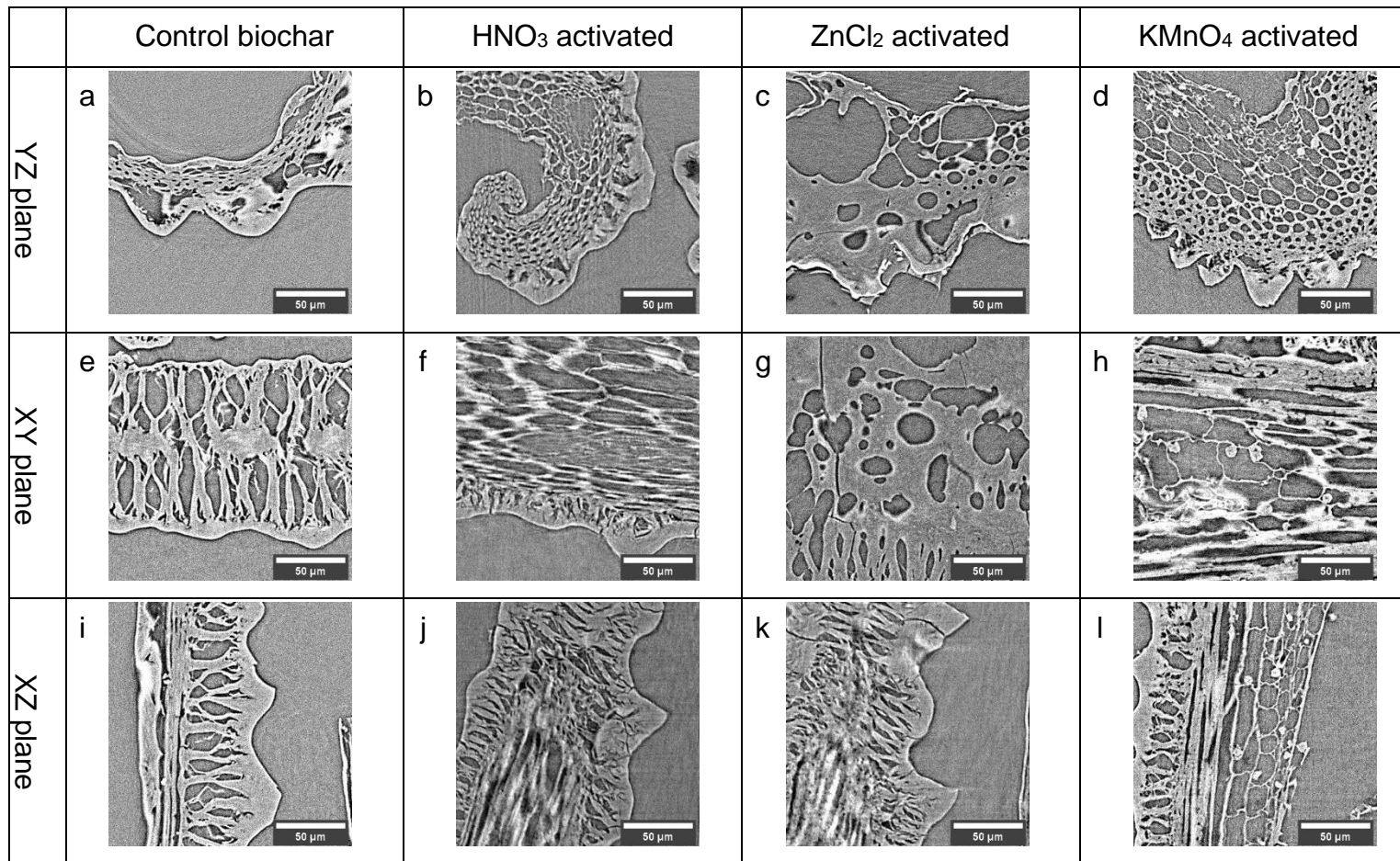


Figure 8.20 Orthogonal views of Rice husk biochars: unactivated control biochar (a, e, i), HNO₃ activated (b, f, j), ZnCl₂ activated (c, g, k) and KMnO₄ activated (d, h, l) in the XY, XZ and YZ planes respectively

8.4.2 Quantitative analysis

Results of the quantitative pore space analysis are presented for each feedstock type, then considered jointly (Section 8.4.2.4). Overall macro pore volume, pore size distribution, pore circularity and related characteristics were determined using the machine learning algorithm Ilastik⁵³⁸, and ImageJ²⁸⁵ inbuilt tools. Tortuosity was investigated using an automated tortuosity calculation method⁵⁴². Results for all three feedstock types are summarised jointly in Section 8.4.2.4. Further discussion of these results are presented in Section 8.5. Precursor biomass feedstocks (Oak, spent coffee grounds and rice husk) overall pore volume values are included in Figure 7-19, Figure 7-21 and Figure 7-22 for confirmation that pyro processing increases macro porosity, but are otherwise excluded from more detailed analysis as they are not the focus of this study.

8.4.2.1 Oak wood

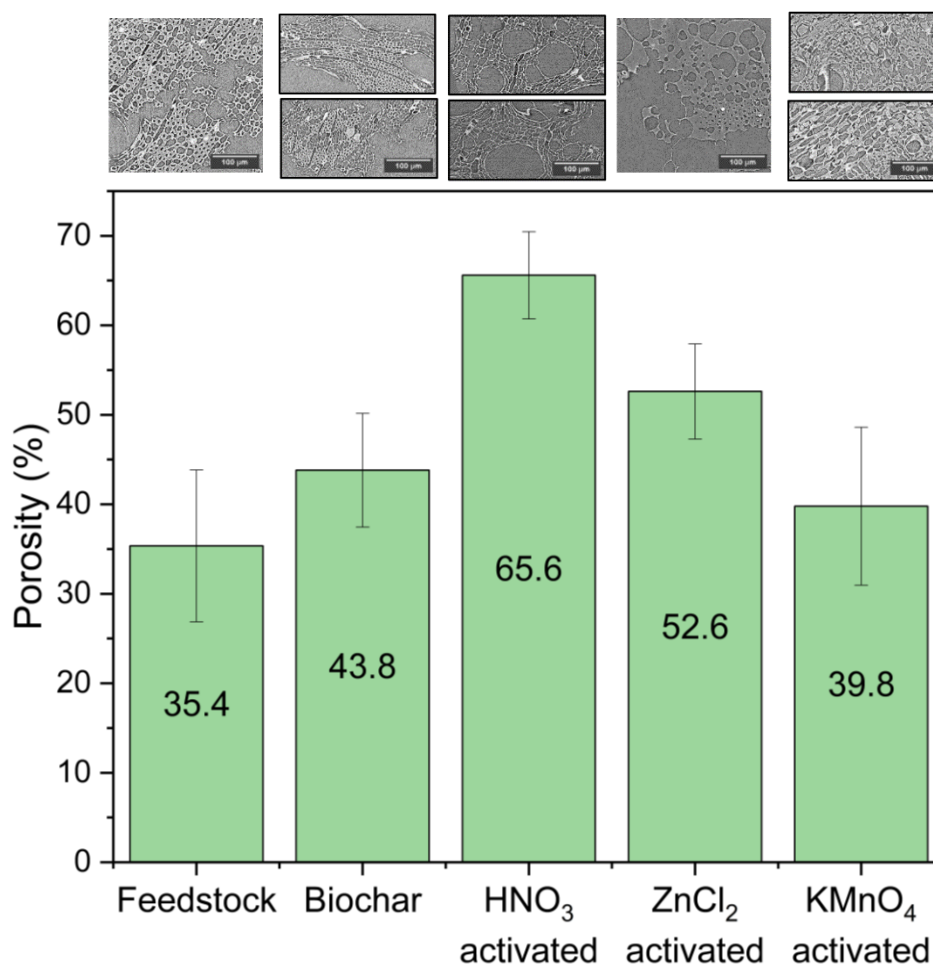


Figure 8-21 Macro pore volume of oak wood biochars and the biomass precursor. Representative XCT images of each material are displayed above for comparative purposes

Overall percent macro pore space in oak wood biochars varied significantly with activation. Figure 7-19 displays these values for the OAK feedstock sub-set, indicating that both HNO₃ and ZnCl₂ activation increases oak wood biochar macro pore volume (65.6 % and 52.6 % respectively) with respect to the unactivated control biochar (43.8 %). In contrast, KMnO₄ activation shows a slight decrease in macro pore volume (39.8 %). Table 8-2 displays further macro pore space data. The unactivated biochar displays the smallest average pore area (263.9 μm²), smallest average Feret diameter (23.7 μm) and largest number of pores per image (471). These data suggest that activation in general creates a material with a fewer number of larger macro pores, as is indicated by increased values for macro pore volume, average pore area, averaged number of pores per slice and Feret diameter in all three activated oak biochars. The presence of larger macro pores is rationally congruent with a higher overall percent macro porosity in HNO₃ and ZnCl₂ activated oak wood biochars. However, the slightly lower overall percent macro porosity of KMnO₄ activated oak wood biochar does not fully follow this trend with its slightly reduced overall macro pore volume. This is discussed in more detail in Section 8.4.2.6.

8.4.2.2 Spent coffee grounds

While spent coffee ground biomass precursor shows very low macro porosity, creating biochars via pyro processing dramatically increases macro porosity () from around 16.7 % to 75.6 %. Consistent with the observed trend in Section 8.4.1.2, activation via HNO₃ and KMnO₄ results in little difference in macro pore volume with respect to the unactivated control. Both HNO₃ activated and KMnO₄ activated show slightly reduced macro pore volume, 73.8 % and 69.5 % respectively. ZnCl₂ activation shows the most dramatic change to macro pore volume, reduced to 41.9 %, almost half that of unactivated biochar control. Comparison of the feedstock, unactivated biochar and ZnCl₂ activated biochar macro pore volumes with those derived in the preliminary data set demonstrate excellent agreement (Section 8.3). Table 8-2 displays further SCG pore space characteristics. These data are, on the whole more self-consistent than oak wood biochars (Figure 7-19) for example, average pore area data shows larger average pore area for all biochars, indicating that the feedstock, SCG has an important role in macro pore architecture, and suggests that SCG macro pore space is less susceptible to modification through activation than oak wood as a feedstock.

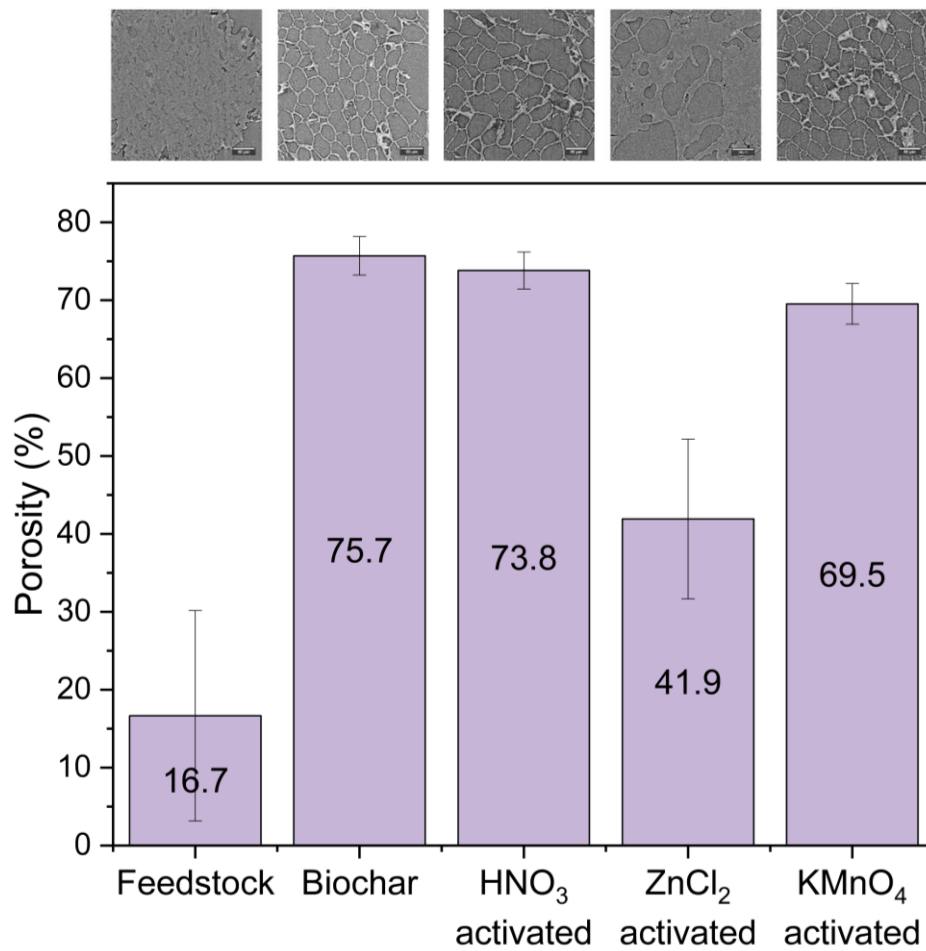


Figure 8.22 Macro pore volume of spent coffee ground biochars and the biomass precursor. Representative XCT images of each material are displayed above for comparative purposes

8.4.2.3 Rice husk

Figure 7-21 shows the macro pore space variation in RH samples, showing overall lower macro pore volume than OAK and SCG materials, even after activation. In contrast to SCG, pyro processing only confers a modest increase in macro pore volume (21.1 %) over the biomass precursor (15.4 %), suggesting pore development during the pyrolysis treatment is far less significant in RH. HNO_3 and KMnO_4 activation is observed to enhance macro porosity to 35.0 % and 40.3% respectively, an increase of 66 % and 91 % to the macro porosity respectively. ZnCl_2 also increases macro porosity to 31.6 %, almost a 50 % increase to macro pore space. Uncertainty in this data set is higher than other feedstocks, due to the thin, lamellar like nature of the rice husks. This made pore space analysis more challenging and also reduced the volume of sample available for analysis.

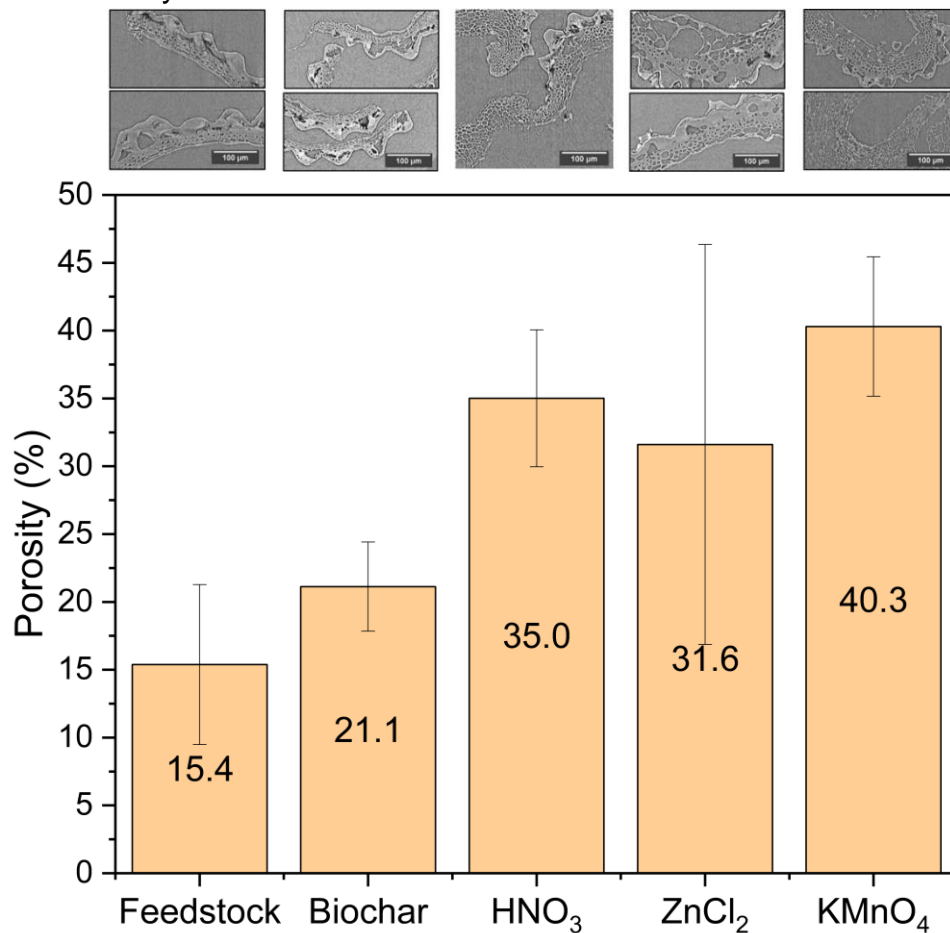


Figure 8-23 Macro pore volume of rice husk biochars and the biomass precursor. Representative XCT images of each material are displayed above for comparative purposes

Figure 7-21 shows that RH biochars on the whole display less variation due to activation than the other two feedstocks. Average Feret diameter values are all

low and fall within a narrow range of 5.2 μm . Average pore circularity values all also lie within a very narrow range with the exception of KMnO_4 activated RH biochar.

8.4.2.4 Combined data set

Figure 7-22 combines Figure 7-19, and Figure 7-21 to display an overall comparison of macro pore space, with respect to both feedstock and activation procedure. The effect of activation on macro pore space appears to interact with feedstock effects in final macro pore characteristics. HNO_3 activation of SCG has little effect or perhaps even causes a slight decrease in macro pore volume. pyro processing produces in SCG an unactivated biochar with a macro pore space that is already remarkably well developed around 76 % pore space. Without formation of larger voids, this leaves little room for activation-induced increases to overall macro porosity. SCG biomass has an extremely low ash content in addition, meaning that HNO_3 assisted removal of inorganic phases during the activation process will be minimal. This suggests that the primary mode of SCG activation via HNO_3 treatment is on surface chemistry modification and micro and meso pore formation, not macro pore space modification. The opposite trend is observed for HNO_3 activation in RH and OAK: it increases macroporosity. RH feedstock has a high silica content, while oakwood contains appreciable quantities of calcium (in the form of calcium oxalate)⁵⁴³, both of which will be rendered soluble in the highly acidic HNO_3 treatment, and thus removed from the biochar to a significant extent. While removal of inorganic species alone is unlikely to account for all of the increased macro porosity in RH and OAK, its dissolution may create access to high energy sites within the biochar structure which can then be more easily attacked and degraded by the HNO_3 acid.

KMnO_4 activation likely results in an activated SCG biochar with a slightly reduced macro pore space due to the combination of i) some MnO_x dopant deposition within the pore space which could slightly reduce overall macroporosity and ii) due to the high initial macro porosity of the unactivated SCG biochar which leaves little room for further increases without degradation of the biochar particle itself. The opposite trend is again observed for RH: an increase macroporosity with application of KMnO_4 activation. While for OAK, KMnO_4 appears to have little overall effect on macro porosity. However, pore space images (Figure 8.18) confirm that significant changes have occurred to the KMnO_4 activated OAK biochar macro pore structure, with some clear pore widening. Any changes to overall macro porosity seems to be counterbalanced with the pore filling noted for KMnO_4 activated biochar (Figure 7-15).

ZnCl₂ activation increases macroporosity in RH and OAK feedstocks, however for SCG feedstock, this nearly halves macro pore volume from 76 % to 42 %, which is relatively consistent with the preliminary results obtained in Section 8.3, despite a difference in pyrolysis temperature. Unlike both HNO₃ and KMnO₄ activation, which are both post-pyrolysis treatments, ZnCl₂ activation is present during pyrolysis, and as such any chemical interaction between the feedstock/biochar and activator chemical is subject to very different regimes of activation energy due to the elevated pyrolysis temperatures involved. It is therefore not unexpected that the most drastic differences are observed in images of ZnCl₂ activated biochars, as compared with their precursor feedstocks and unactivated biochars.

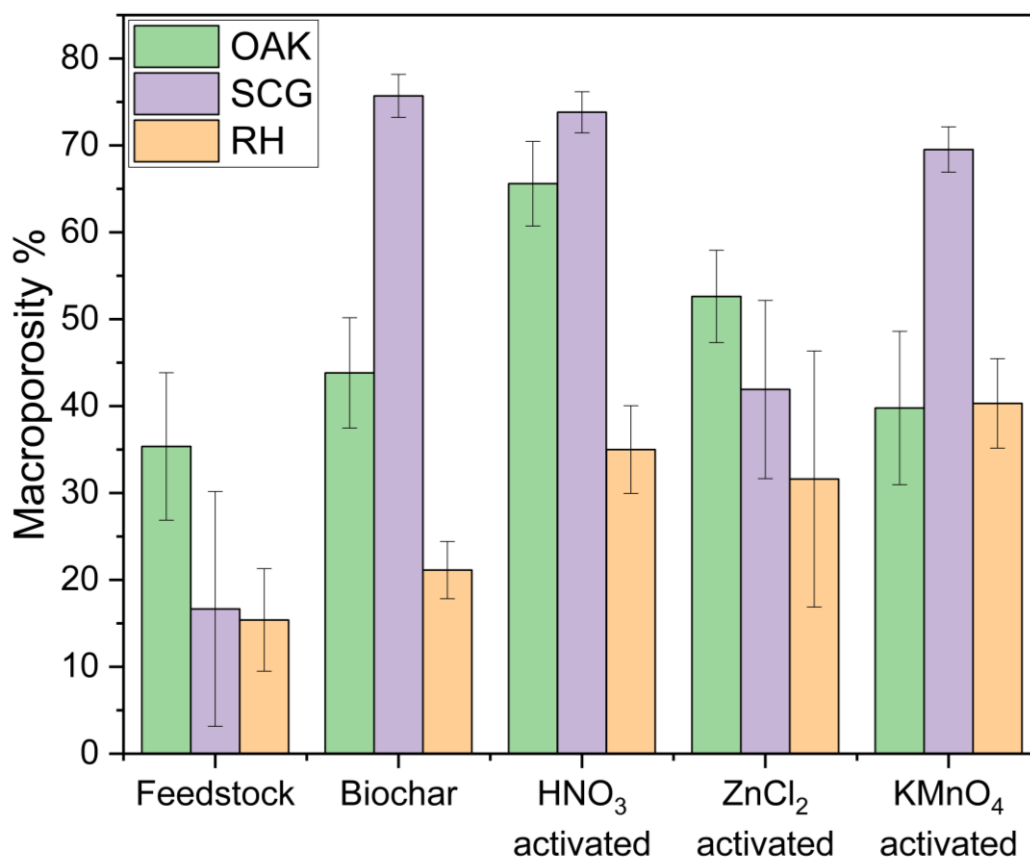


Figure 8-24 Percent macro pore volume for biochars, activated biochars and precursor feedstocks.

Explanations of the interplay between feedstocks and resulting macro porosity requires further investigation, in order to understand the different responses of SCG, RH and OAK feedstocks.

Figure 7-23 displays the maximum Feret diameter distributions for all biochar samples. The maximum Feret diameter is a measure of the longest dimension of a pore and as such can provide pore size distribution data for these samples.

Note that y-scales, showing total pore count with respect to Feret diameter are identical across each feedstock type but vary per feedstock set for ease of viewing. X-axis are all identical.

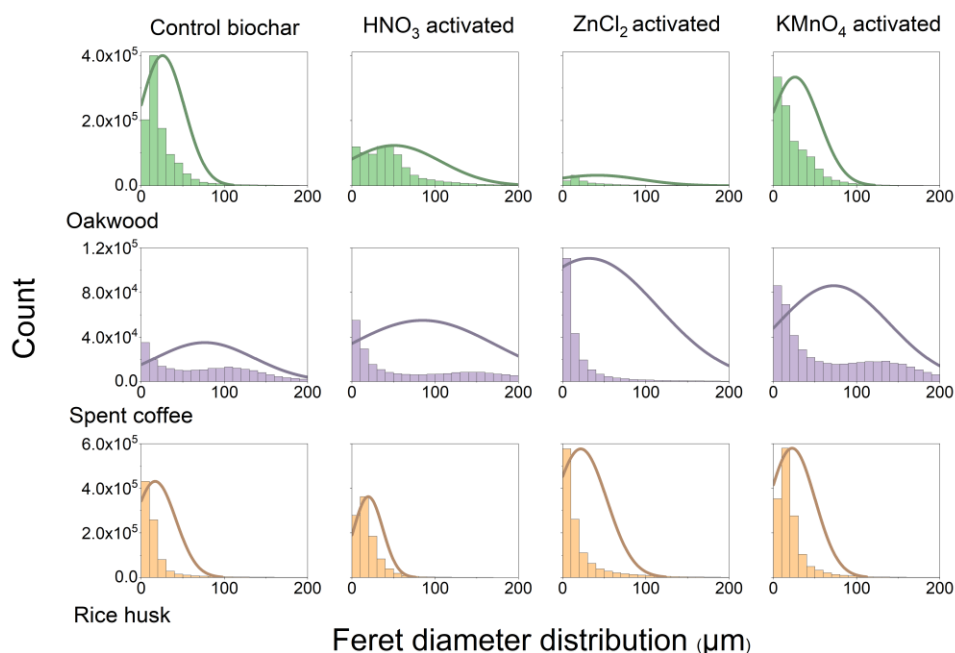


Figure 8-25 Feret diameter distributions for all biochar samples for the range 0 – 200 µm. Axes are common for all

Pore size distributions show clear differences depending on both feedstock and activation. SCG biochars as a set show a far wider macro pore size distribution than OAK or RH biochars in general, with unactivated SCG biochar displaying a very flat distribution between 0.325 – 200 µm. HNO₃ activated SCG follows a similar trend with a slightly higher distribution of smallest macro pores, while the skew to smaller macro pores is much more prominent in both ZnCl₂ and KMnO₄ activated SCG. KMnO₄ activation also appears to increase the distribution of larger (100-200 µm) macro pores. Activation of OAK via HNO₃ and ZnCl₂ has significantly flattened the macro pore distribution in these biochars. Both show a skew towards the smaller macro pores but a smaller number of pores per histogram bin, than the unactivated OAK biochar. KMnO₄ exhibits a relatively unaltered macro pore distribution over this control biochar however, with a similar number of smaller pore sizes. Perhaps the most self-consistent or unaltered by activation, in terms of the macro pore size distribution is the RH set. This is consistent with observed data from both RH qualitative images and pore volume data, which show only mild observable differences with activation and the

smallest variation in macro pore volume across a feedstock set. All four RH biochars display narrow pore size distributions towards the lower macro pore size range. $ZnCl_2$ and $KMnO_4$ activation both increase the contribution of smaller macro pores.

Pore Circularity

Pore circularity is also modified by activation, as shown in Figure 7-24, which displays pore circularity distribution diagrams as calculated via equation 19. Values approaching unity indicate more circular pores, while those approaching 0 indicate poor circularity. The general trend in all samples is fairly wide pore circularity distributions, indicating a range of pore shapes present in all samples. This is not unexpected for amorphous materials such as biochar. The effect of HNO_3 and $KMnO_4$ activation on OAK biochars both follow a similar trend. A noticeable skew in the distribution is visible, with large shoulder appearing at around 0.3 and 0.4 respectively, indicating that these activation protocols result in an increased fraction of less-circular pores and a wider pore circularity distribution. SCG biochars activated with HNO_3 and $KMnO_4$ also show a noticeable albeit smaller skew to lower circularity values. The trend in RH biochars appears to show a *narrower* pore circularity distribution for HNO_3 and

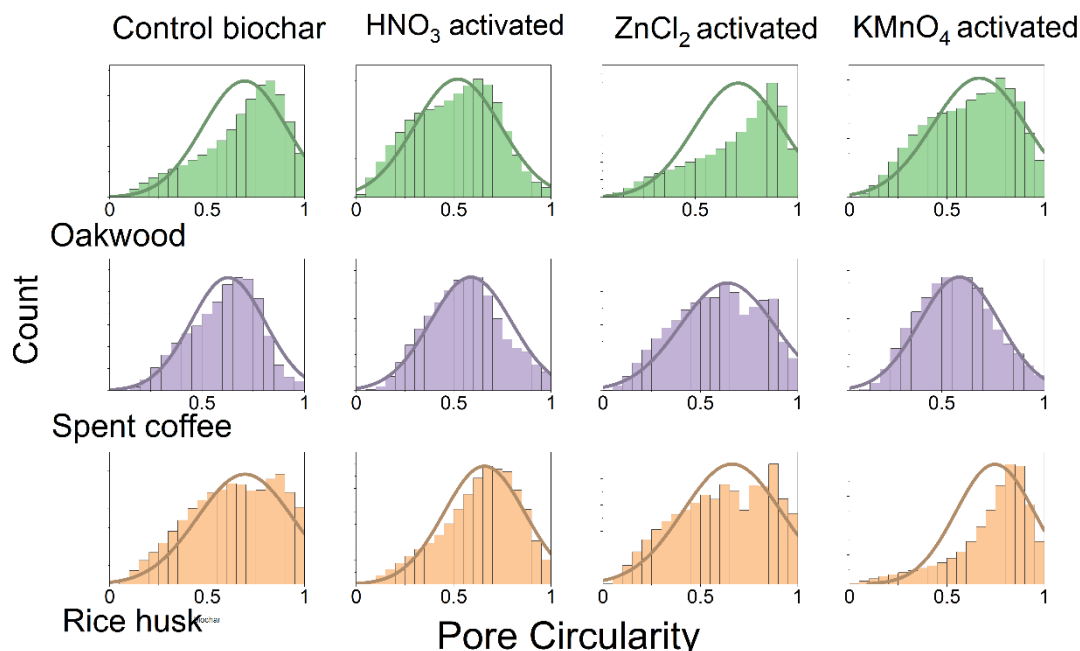


Figure 8-26 Pore circularity distributions for all biochar samples where 1 indicates a perfect circle and approaching 0 indicates low circularity (x-axis). Oak wood biochar (top), spent coffee ground biochar (middle) and rice husk biochar (bottom)

$KMnO_4$ activated samples, without a skew to low circularity. Thus, pores are

typically more circular in these activated biochars. The trend observed in ZnCl₂ activation is a little more complex, which reflects the more comprehensive alterations to the pore architecture observed in Figure 8.15. While in SCG circularity distribution is shifted to slightly higher, more circular values, the trend with RH and OAK appears to be a *wider* pore circularity distribution.

Table 8-2 Macro pore dimension values for oak wood, spent coffee ground and rice husk biochars

	Sample	Average pore area / μm^2	Largest individual pore area / mm^2	Average number of pores per image	Average pore circularity	Feret diameter average / μm
OAK	Control unactivated	264	0.014	471	0.69	23.7
	HNO ₃ activated	1033	0.099	201	0.52	50.9
	ZnCl ₂ activated	1386	0.075	50.3	0.71	41.6
	KMnO ₄ activated	539	0.062	414	0.66	33.2
SCG	Control unactivated	3503	0.019	103	0.63	76.3
	HNO ₃ activated	5187	0.209	113	0.59	84.8
	ZnCl ₂ activated	2068	0.355	138	0.64	31.5
	KMnO ₄ activated	4075	0.081	208	0.59	78.8
RH	Control unactivated	164	0.015	199	0.69	17.4
	HNO ₃ activated	187	0.013	460	0.66	19.6
	ZnCl ₂ activated	383	0.020	273	0.66	21.7
	KMnO ₄ activated	298	0.040	340	0.75	22.6

8.4.2.5 Tortuosity

The tortuosity of the biochar pore space was probed using a geodesic reconstruction (GR) algorithm, which returns a value for pore space tortuosity in each respective direction (x, y, z) through a 3-dimensional sample⁵⁴⁴. This is based upon equation 2 in Section 2.4.1.5. Values equal to unity describe a perfectly straight pore path with no tortuosity. In other words, the path length through the pore is not longer than to the point-to-point (Euclidian) distance e.g. a straight, hollow cylinder. Values for tortuosity > 1 indicate the path length through the pore is greater than the Euclidian distance, indicating increasing tortuosity. Residence time of a fluid in such a tortuous pore structure will be longer. When τ is treated in x, y and z separately, samples with no difference in directional τ would appear on Figure 7-25 as an equilateral triangle, with each apex representing an equal value for τ in each respective (x, y, z) direction. Samples with a large extent of anisotropy in τ appear as irregular triangles, with each directional value of τ unequal. Figure 7-25 displays the results for SCG (top) and OAK (bottom), showing significant anisotropy in directional tortuosity through the pore network. Note that the spider diagrams scale of τ values is larger for the OAK set than SCG in Figure 7-25.

Oak wood

All samples appear to reveal an underlying feedstock effect which governs directional isotropy in τ . This is observed by each OAK sample in Figure 7-25 possessing a similarity in shape on the spider diagram, characterised by a higher τ value in y- and z-directions than in x. The largest deviation from control values is observed in the ZnCl_2 activated sample, where τ values have *increased* significantly. HNO_3 activated biochar also increases τ in y and z. The reason for this is not fully understood, since it would be expected that nitric acid activation would increase macro pore diameter and thus decrease tortuosity. This does however appear to happen in the x-direction (Figure 8.18b), whereby larger voids are clearly present.

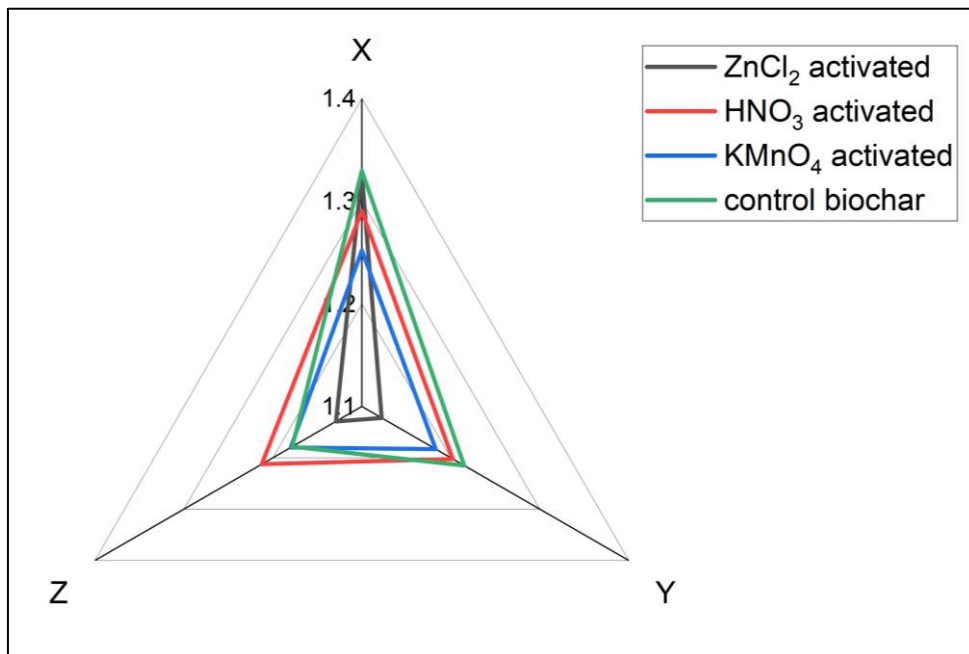
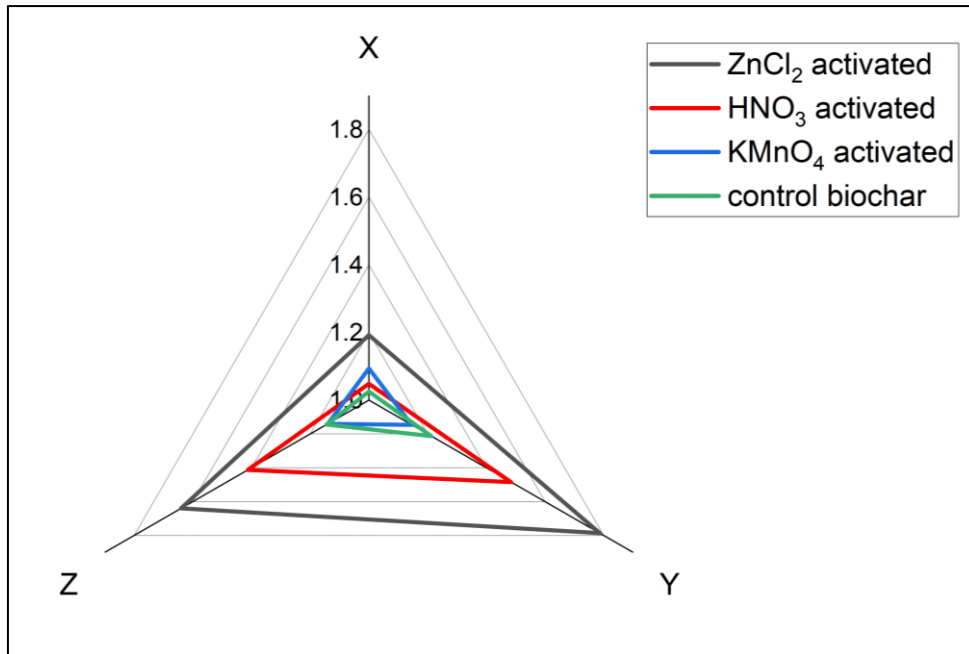


Figure 8-27 Directional tortuosity of oak wood (top) and spent coffee grounds (bottom) biochar pore space and their activated analogues

Spent coffee grounds

All samples show a greater degree of anisotropy of τ in the x-direction, with values of 1.3 ± 0.4 , compared with the y- and z-directions, in which most values fall below 1.2. Since all SCG samples follow this trend, it suggests an underlying anisotropy in τ originating from the feedstock. The differences in τ across this sample set are notable in that they are not apparent from visual inspection of the tomographic images alone. The most isotropic of SCG biochars is KMnO_4 activated biochar, with similar values in all three domains. In common with the OAK, the largest deviation from control is observed in the ZnCl_2 activated sample. However, in this case ZnCl_2 activation appears to have increased anisotropy by *decreasing* tortuosity in the y- and z-directions relative to the control unactivated biochar. A very similar value to control is maintained in the x-direction. Little difference is observed between the control unactivated biochar and HNO_3 activated biochar.

Rice husk

Due to the relatively thin sample thickness of rice husk biochars, tortuosity values for these samples were excluded on the basis of unacceptable error introduced by this feature.

8.4.2.6 Scanning Electron Microscopy Energy Dispersive X-ray spectroscopy (SEM-EDX)

In order to probe the nature of the apparent pore filling substance in the KMnO_4 activated sample, SEM-EDX was used to examine both the form and elemental composition. Several formations similar to those observed via XCT were found as part of surface features. These are displayed in Figure 7-26 and Figure and can be described as series of angular structures, apparently distinct but typically in a close packed, linear formation which most closely resemble inorganic crystal structures. Their sizes conform roughly to those of the macro pore sizes present in the biochar phase and their lamellar-like formation also mirrors that of the macro pore structure of biochar, with larger elongated pores running throughout the biochar structure. EDX confirms that that calcium is a major component of these formations, with evidence that oxygen is also present in similar concentrations. Calcite (CaCO_3) is one of the most common crystalline inorganic phases present in biochar, especially biochars derived from tree feedstocks such as oak wood². Another Common crystalline inorganic in biochar is Whewellite ($\text{Ca}(\text{C}_2\text{O}_4)\text{H}_2\text{O}$) which is derived from abundant calcium oxalate phytoliths within bark and wood⁵⁴³. Since these formations are not observed in the control unactivated oakwood biochar, it is possible that some degree of synergistic interaction is occurring between calcium and manganese during the manganese activation procedure. High levels of CaO (33 %) in oak wood biochars are reported in literature⁵⁴⁶.

There is also evidence in the EDX mapping of a degree of interaction between these calcium phases and manganese, which is otherwise distributed uniformly across the biochar surface, as slightly elevated manganese levels are co-located with the calcium phases. Evidence of interaction between manganese and calcium exists in plant biology^{547,548} where they are known to occupy each other's binding domains or to cooperate in various biological functions such as in the oxygen evolving complex, a sub-section of photosynthesis. Further, Mn^{2+} is known to readily adsorb to calcite⁵⁴⁹, where it can act as a nucleation point for newly formed $\text{Mn}(\text{CO}_3)$ ⁵⁵⁰.

Although this technique cannot provide elemental mapping for the formations observed via XCT which are located within the internal pore structure, the shape and size (on the order of 10s μm) of these calcium-bearing phases closely resemble the unknown pore filling phase observed in Figure 7-15.

Mn-Oak site 1

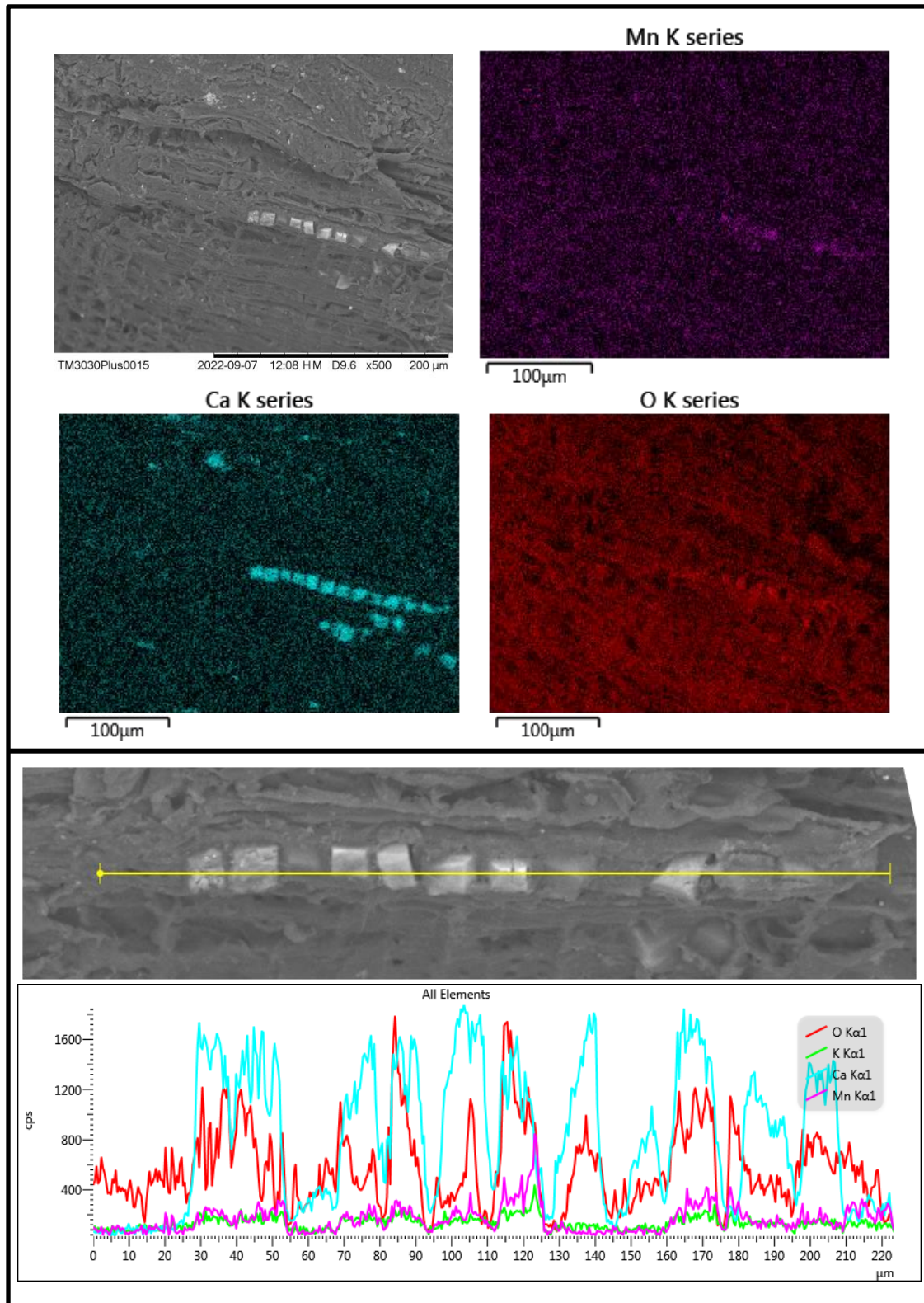


Figure 8-28 SEM-EDX spectroscopy of KMnO_4 activated oak wood biochar site 1. Top panel showing backscattering electron SEM image at 15 keV & x1000 magnification (top left) and 2D elemental maps for calcium, manganese and oxygen. Bottom panel shows a line spectrum through the formation showing elemental composition

Mn-Oak site 2

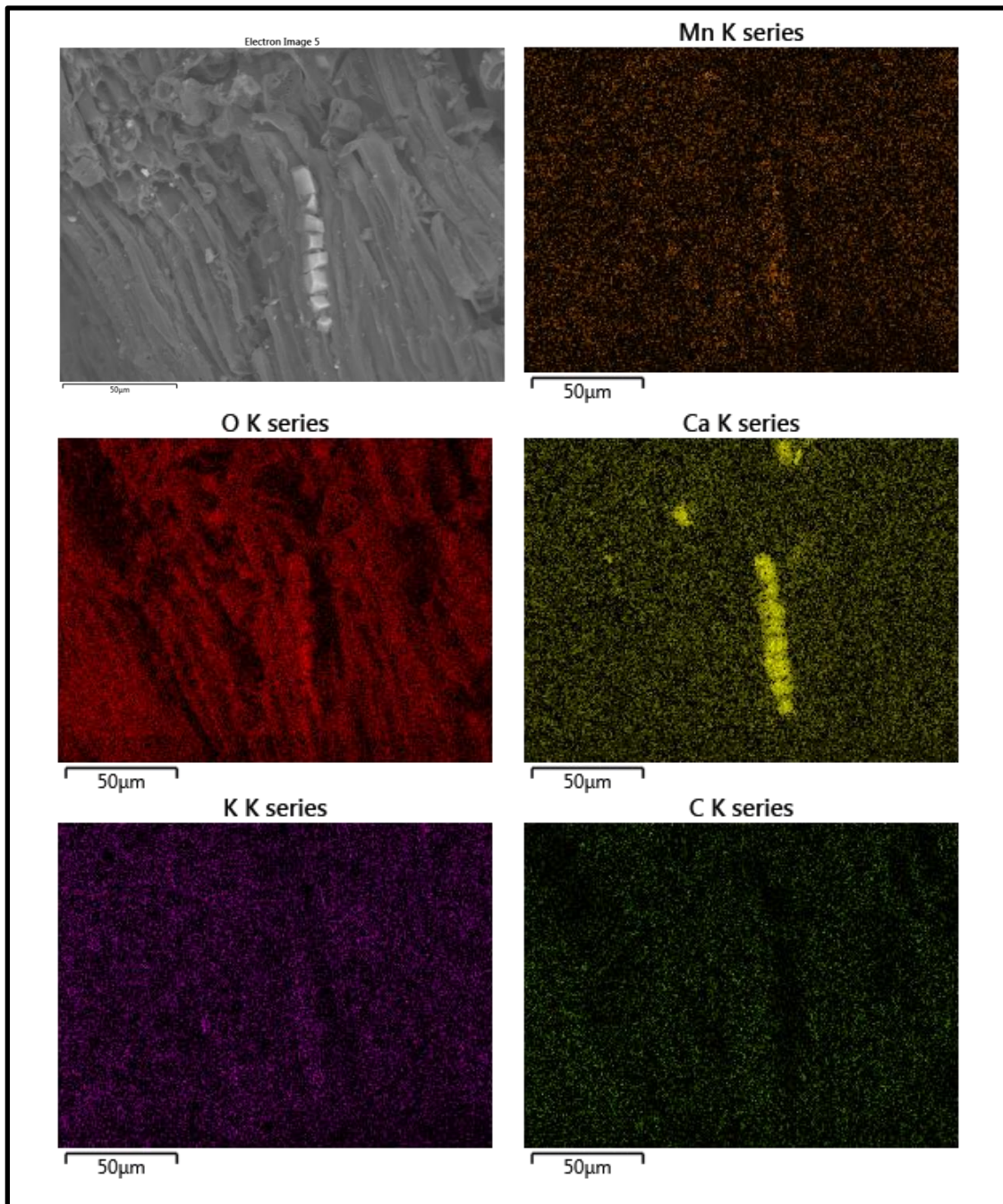


Figure 8-29 SEM-EDX spectroscopy of KMnO_4 activated oak wood biochar site 2, showing backscattering electron (BSE) SEM image at 15 keV & x1000 magnification (top left) and 2D elemental maps for calcium, manganese and oxygen

8.5 Discussion

Biochar pore diameters span some five orders of magnitude²⁹⁵, and fully analysing the porous structure across this wide range of dimensions is challenging requiring a combination of techniques. This is summarised in which displays pore sizes and the working ranges of the most common pore space analysis techniques. Optical techniques cover a wide range of pore sizes but are surface specific and cannot penetrate the internal pore structure to ascertain detail of inner porosity, interconnectivity, internal pore shape or tortuosity. Gas adsorption techniques cover the lower range of pores – meso and micro pores – and have been a crucial tool for pore space analysis of all types of porous media. Their strength is as a comparative tool for various porous media. However, they are underpinned by theoretical assumptions which do not hold well for amorphous and varied materials such as biochar. This then also diminishes the confidence in conducting ‘like-for-like’ comparison of gas adsorption micro pore analysis of biochar with different classes of porous media. Other techniques such as mercury porosimetry are also subject to underpinning theoretical assumptions. X-ray Computed Tomography, as a term that encompasses a cluster of similar techniques including X-ray μ -tomography and X-ray nano tomography (ptychography). XCT is capable of imaging the internal pore structure of materials from meter scale to well into the nano meter range. It is capable of not only imaging and three dimensional reconstructions of the pore architecture in a porous media, but also of quantitation of the entire macro porous range. Parameters such as pore size distribution, pore shape and tortuosity modulate are relevant to performance, across a range of applications, and therefore should be investigated. XCT is an unrivalled pore space measurement tool for the macro pore range and is capable of more in-depth analysis that previously possible. This, when paired with performance data, enhances understanding of the structure-function relationship of macro pore space and will create further opportunity for rational optimisation.

The development of XCT as such a tool has advanced rapidly in the last decade, largely overcoming to key limiting factors of computing power and availability of image analysis tools. This is reflected in the very small number of works that have employed XCT to analyse biochar pore space. Fewer still use thresholding or segmentation to quantify pore spaces. And none yet attempt to examine either the effect of activation on pore space or the tortuosity of the biochar macro pore space. This is in part due to the additional difficulties presented by image contrast in a loss atomic mass material such as biochar,

but now which can be overcome with machine learning and/or automated contrast enhancement filters.

Activation has clear and wide ranging effects on the macro pore space of biochar, as described in three feedstock types: oak wood, spent coffee grounds and rice husks. This is somewhat modulated by biochar precursor type, meaning that each biochar + activator combination produces a distinct pore structure.

Oakwood biochar possesses reasonably high SSA, as well as reasonable macro pore volume, conferring excellent hierarchical porosity prior to any activation. ZnCl_2 has been shown to enhance SSA and micro/meso porosity (Table A-2) while also increasing the macro pore volume (Figure 7-19), while also significantly altering the macro pore structure (Figure 8.18) and increasing tortuosity (Figure 7-25). This yields a highly tortuous, hierarchical biochar which would be most suited to applications where residence time of a target phase in pore structure needs to be lengthened, e.g. if kinetics of catalysis are slow. A different picture emerges for HNO_3 activated OAK. SSA and micro/meso porosity decrease somewhat, while macro pore volume increases by almost one third, and average pore area more than doubles, indicating significant macro pore widening and hinting pore widening is a major factor in lower SSAs^{72,150}. Tortuosity increases to an intermediate value. While increases in SSA is often positively correlated with contaminant uptake, HNO_3 activation (of all biochars) bucks this trend, as it is often successfully used to enhance contaminant uptake capacity of a biochar since oxygen content is known to increase (Table 5-1). Thus, HNO_3 activated biochar, as a moderately tortuous, and still reasonably hierarchical porous material, is well suited to contaminant uptake, especially where uptake kinetics are slow. KMnO_4 activated OAK has unusual macro pore features indicating extensive macro pore filling (Figure 7-15) of CaO and/or CaCO_3 phases (Figure 7-26 and Figure 7-27). MnO_x appears to be evenly distributed across external surfaces, with evidence of some association between Ca^{2+} and Mn^{x+} . Macro pore volume is similar to that of unactivated OAK biochar (Figure 7-19) but there is some evidence of moderate macro pore widening, both visually (Figure 8.18) and via pore analysis (), in agreement with previous wisdom for KMnO_4 -treated micro and meso pores.

Unactivated SCG biochar already possesses a higher macro pore volume than any oakwood or rice husk activated biochars. In addition, unactivated spent coffee ground biochar also displays extremely low SSAs (Table A-2). Thus, SCG biochar is clearly already a highly macro porous material with little micro or

meso porosity without activation. While HNO_3 activation typically increases macro pore volume, the exception to this is the spent coffee ground HNO_3 activated biochar. HNO_3 activation typically induces a slight decrease in SSA. Therefore HNO_3 activation of SCG creates a highly microporous, sparingly micro/meso porous material, with enhanced oxygen surface functionality. ZnCl_2 is known to greatly enhance micro and meso porosity, therefore combining the highly microporous nature of SCG with ZnCl_2 likely creates a hierarchical pore structure. KOH is another such activator that is known to greatly increase micro porosity in SCG^{551,552}, and will likely have a similar outcome, since the macro pore structure of SCG seems stable to all three activators in this study. The effect of KMnO_4 activation is known to vary with wt% ratio biochar to KMnO_4 . An intermediate ratio of 17.4 wt% KMnO_4 was used in this study and similar studies suggest a small decrease in SSA (and micro pore volume) with a slight increase in meso pore width^{77,178}. SCG biochars - activated or not - may lend themselves particularly well to soil amendment applications, where macro pores can confer high water retention capacity and extensive microbial habitats. Another point to note is that it is known that the composition of the aqueous mobile phase passing through the pore space can affect diffusivity²⁸³, with more complex ground waters possessing lower diffusivity coefficients due to dissolved organics, sparingly soluble sediments and dissolved inorganics. In such cases, fouling would be a higher risk and so more macroporous biochars could be a wise choice.

Rice husk unactivated biochar possesses moderate – but not exceptional – micro and meso porosity, with little macro porosity. It could be described as somewhat converse to SCG biochar in this regard, which is much more a macro porous and sparingly micro and meso porous material. Typically, HNO_3 activation slightly decreases SSA and moderately increases macro porosity, creating a material with increased macro pore fraction. ZnCl_2 activation increases macro porosity slightly and significantly increases SSA, creating a more hierarchical, highly microporous material. KMnO_4 , similarly to HNO_3 , slightly increase macro pore volume and decreases SSA. Tortuosity values for RH biochars were subject to unacceptable error due to the thin, lamellar nature of the particles. However, from visual inspection of orthogonal views (Figure 8.20) shows a clear directional anisotropy in pore tortuosity which isn't dissimilar to the structure observed on OAK biochars – one orientation possess clear linear and straight pores while the remaining two orientations suggest higher tortuosity values. Thus, it is theorised that RH biochars will also be more highly tortuous (in at least two of three orientations) than SCG.

Table 8-3 Summary of tuneable hierarchical pore space differences observed using XCT and literature BET micro pore analysis data

	Unactivated	HNO ₃	ZnCl ₂	KMnO ₄
OAK	Somewhat hierarchical	Somewhat hierarchical, medium tortuosity	Hierarchical, high tortuosity	Somewhat hierarchical, pore filling
SCG	Highly macro porous	Highly macro porous	Hierarchical	Highly macro porous, decrease in micro porosity
RH	Micro/meso porous, tortuous	Somewhat hierarchical, tortuous	Hierarchical, highly microporous, tortuous	Somewhat hierarchical, tortuous

Knowledge of macro pore architecture, e.g. pore volume, circularity size distributions and tortuosity is useful for a number of reasons. Transport kinetics of a solution through a porous adsorbent material is dependent on the pore network architecture. Sparingly macro porous materials can also be susceptible to fouling or pore blocking particularly for complex solutions, such as groundwater in remediation applications, or in heterogeneous catalysis.

Fluid dynamics through a porous material is often modelled to gain insight²⁸⁴ due to the complexity of conducting micron or sub-micron scale measurements. However, models more often than not rely of theoretical assumptions and pore geometry simplifications. Perfectly circular pores are one such geometry simplification often assumed. Inner pore diameter is also often assumed to be equal to pore mouth diameter. Both of these assumptions are especially weak for a material such as biochar, which can possess such a wide range of pore geometries.

Differences in directional tortuosity also affect flow kinetics³⁰⁰. It is clear that certain feedstocks - notably from the data presented here oak wood and rice husk - tend to result in biochar particles which favourably cleave in a specific dimension according to the structural properties of the biomass precursor and yielding particles with anisotropic tortuosity. It could be argued that for a bulk quantity of biochar particles, random orientation of particles should likely negate

much of this anisotropy. However, this cannot be assumed, as the biochar particles are likely to pack in certain orientations over others due to their irregular shapes. Therefore, understanding the anisotropy is crucial for accurately predicting bulk properties.

Detailed quantitative pore space data not only provide direct insight into the pore space architecture but can be used for both validating and optimising pore space fluid dynamics modelling. Future models could look to include real three-dimensional data from such pore space reconstructions in order to investigate flow dynamics.

8.6 Conclusions

Concluding remarks and implications of this work are treated in Chapter 9. In brief, X-ray Computed Tomography paired with automated image analysis tools were explored to examine porosity in porous biochars and the effect of chemical activators on the porosity, specifically the macro porosity. Results demonstrate that macro pores in biochar are highly developed and distinct in biochar of different feedstocks. Activation clearly alters the macro pore structure and the alteration is distinct depending on the choice of activator.

Chapter 9 Concluding Remarks

A summary of findings of the work presented in this thesis is divided into two components:

1. Investigation of the chemical features pertinent to the binding of strontium, using uptake experiments and XAS (Chapter 5 and Chapter 7)
2. Investigation of the physical features, specifically macro pore space, of biochar which are pertinent to the binding of radionuclides, using XCT (Chapter 8)

9.1 Binding mechanism of strontium to biopolymer composites

9.1.1 Bulk uptake experiments

Oak wood and rice husk derived biochars were activated using two common activation protocols: HNO_3 and MnOx . HNO_3 activated biochars were encapsulated into alginate hydrogel composite adsorbents. While both activation and hydrogel encapsulation have both been previously reported in separate works, no work to our knowledge has yet to combine these treatment steps. Both of these steps separately enhanced strontium uptake; thus, this work further optimises both processes. Rice husk biochar consistently outperformed oak wood biochar, with a maximal uptake value of 241 mg g^{-1} for HNO_3 activated rice husk hydrogel, and a DF value of 9.5 at 5 mg L^{-1} initial strontium concentration. This is almost an 8-fold increase over control unmodified rice husk biochar. In addition to increasing strontium uptake, encapsulation of activated biochar in alginate hydrogel creates an easy to separate adsorbent material, since it is easy to separate from decontaminated waters.

MnOx activated oak wood hydrogel yielded a maximal uptake value 51 mg g^{-1} and a DF of 7.6, also performing particularly well at lower concentration. At very high strontium concentration, the MnOx biochar outperformed its hydrogel analogue, suggesting that the MnOx biochar possesses a larger number of lower affinity sites.

Higher uptake observed in the hydrogels at lower concentration indicates that the alginate component likely provides some higher affinity binding sites. Its native properties as an anionic biopolymer make it ideal for complexing strongly to group II cations such as calcium, which has a very similar ionic radius and

charge density to strontium. The trade-off for this appears to be some degree of biochar pore blocking by alginate gel.

The role of biochar feedstock in maximal uptake capacity is a little less clear, since uncertainty in the Langmuir modelled maximal uptake capacity is high for all oak wood-derived adsorbents and perhaps warrants further investigation. The speciation and relative abundance of oxygen-containing surface functional groups in particular may aid with understanding the concentration-dependent uptake behaviour of biochars.

9.1.2 X-ray spectroscopic studies

EXAFS was used to examine the binding mechanism of strontium to biopolymer composites. Binding to biochar (rice husk and oak wood), HNO₃ activated biochar, as well as hydrogel analogues were all examined. Evidence of second shell backscattering was found in biochars as well as hydrogels which is most accurately described in fits by a second shell Sr-C. This would indicate inner sphere binding of strontium to the adsorbents at neutral pH, in contrast with almost all other EXAFS studies of strontium binding. Second shell backscattering signal was slightly higher in hydrogels, indicating a higher degree of inner sphere binding relative to biochar. Activation had little effect on binding environment.

EXAFS fitting of MnOx activated biochar and hydrogel revealed evidence of two distinct binding environments, the first consistent with biochar/alginate phase, the second with a MnOx phase. Linear combination fitting of manganese K-edge XANES was not able to resolve the component manganese oxide speciation present, indicating poorly crystalline manganese oxide, and consistent with a non-stoichiometric, amorphous birnessite, with mixed manganese oxidation states present.

9.1.3 Implications and possible application areas

Materials of biosynthetic origin such as biochar and alginate are economic, sustainable and even carbon-negative. They are readily available and can be prepared and deployed rapidly. Both biochar and alginate possess surface functionality suitable for metal complexation and immobilisation and biochar can be functionalised easily. Hydrogel composites of these biopolymers have high uptake capacities of strontium, and spectroscopic studies indicate that binding is strong, inner sphere in nature (although it is important to note that further work is necessary to confirm these results, and to exclude other possible causes of the second shell signal). This makes such biopolymers an attractive

prospect for radionuclide remediation, especially where traditional ion-exchangers may fail, such as in-situ applications.

Owing to the facile synthesis method of ionotropic gelation, it may also be possible to utilise such composites as an injectable permeable reactive barrier which can be formed by the mixing of its two precursor solutions in-situ. Such a method was employed at the US Department of Energy site Hanford, where an injectable hydroxyapatite permeable reactive barrier was successfully created in-situ by the injection of two precursor solutions into sub-surface soils. The PRB successfully immobilised a large quantity of ^{90}Sr which had leaked from storage tanks which had been migrating towards the Columbia river¹⁵. Biochar, as a highly recalcitrant material is also well suited to such an end use.

9.1.4 Future work

As previously mentioned, it is important to repeat EXAFS studies under a range of sample preparation and uptake regimes in order to confirm second shell carbon and exclude other possibilities, such as precipitated chloride. Using a number of distinct precursor strontium salts (nitrate, sulfate etc.) to make simulant solutions for uptake combined with careful EXAFS analysis should achieve this.

Understanding the speciation and abundance of surface groups responsible for the inner sphere complexation of strontium would represent a step forward in understanding. Potentiometric titration coupled with modelling of the complexation process would achieve this.

The issue of selectivity must also be addressed, as a known issue in radionuclide remediation, and particularly for group I and II cations such as strontium. Selectivity experiments to test performance under a range of different ionic regimes would achieve this.

In the MnOx composites, the role the precursor KMnO_4 and its effect on oxidation of the biochar surface is still largely unknown. Therefore it isn't known whether immobilisation can be attributed to MnOx phases or oxidised biochar surface groups.

In the bigger picture, functionalised biopolymers show potential for immobilisation of many radionuclides and this is fortuitous since contamination rarely consists of one element. Further work should focus on a 'universal' radionuclide biopolymer adsorbent which perhaps comprises several functionalisation types, each targeted at a distinct radionuclide.

9.1.5 Limitations

As a bulk technique, EXAFS provides an averaged signal. Biochar is known to be heterogeneous with a likely wide distribution of binding site energies. Thus, it is possible that an appreciable proportion of sites fall at the lower binding energy range of the distribution, potentially not being strongly enough to bind radionuclides. Further work to identify the functional groups responsible in more depth would address this limitation.

Simultaneous EXAFS fitting of MnOx biochar and hydrogels did not result in a fully resolved fit, with certain parameters necessitating constraint. Therefore, such results require repeat measurement to confirm the results. Such work would also address another limitation, namely the lack of precise manganese phase identification. Repeat EXAFS experiments of strontium bound to a range of known manganese oxide phases should provide more information. Work on precise synthesis of manganese oxides is very much an active area of research, especially in biochar composites.

9.2 Physical morphology and pore space analysis of biochar

Biochars from oak wood, spent coffee grounds and rice husk were activated via three common protocols: ZnCl₂, HNO₃ and KMnO₄. Macro pore space was quantitatively analysed. Both feedstock type and activation protocol altered the macro pore space characteristics, opening the possibility of rationally designed pore space. Spent coffee ground biochars yielded very highly macro porous materials, regardless of activation, with relatively low tortuosity and wide macro pore size distributions. Such biochars are likely suited to applications requiring high volume uptake (e.g. water retention) and rapid diffusion kinetics (e.g. for a rapid catalytic reaction or rapid contaminant binding).

Rice husk biochars displayed a somewhat opposite trend of sparingly macro porous but highly micro/meso porous biochars with observably higher tortuosity, narrow macro pore size distributions and greater consistency in pore circularity. The effect of activation increases macro pore space only moderately. Rice husk biochars are hierarchical but with more limited macro porous structures and more extensive micro/meso porous structures.

For oak wood biochar, choice of activator had a clear effect, introducing increased micro/meso porosity for creation of hierarchical, more circular porous structures (ZnCl₂), reduced micro/meso porosity and less circular pores (HNO₃) or micro/meso pore blocking and macro pore widening (KMnO₄). Oak wood biochars therefore are somewhat intermediate between rice husk and spent

coffee biochars, with larger increases to the macro pore volume upon activation as well as reasonable micro/meso pore contributions. ZnCl_2 and HNO_3 increases tortuosity in the macro pore space.

9.2.1 Future work

Conducting laboratory tests to confirm that macro pore space has an effect on mass transport through the pore network would be a next logical step. This would validate some of the more tentative conclusions drawn here. Examining relative contaminant uptake isotherms, flow rate through activated biochars in a column setup would provide useful information about flow rate. Conducting uptake in simulant groundwater or seawaters, rich in DOM and dissolved inorganics would also confirm the reduced fouling effect that others have reported for macro and meso porous adsorbents. Employing a wider range of pore space analysis techniques, particularly BET gas adsorption, would also provide a more complete picture of all pore size ranges. Modelling increasingly plays a role in predicting biochar's bulk behaviour. Utilising the pore space results here in fluid dynamics models through biochar's pore space will show whether it is indeed necessary to account for the differing pore architectures found here.

9.2.2 Implications and possible application areas

Biochars and their composites are versatile porous carbonaceous materials that are increasingly valued for their hierarchical porosity in applications such as catalysis, contaminant immobilisation and energy storage capabilities. Porosity is crucial yet each application has specific requirements for pore architecture. XCT is an ideal tool to examine the effects of tuning on macro pore space, and thus selecting the most appropriate starting feedstock and activation protocol.

Metrics such as pore circularity and pore size distribution are useful for optimising and validating mass transport modelling through the biochar pore space. This is predicted to be a growing area of research and XCT data can both aid model development and help validate such models

9.2.3 Limitations

The limit of resolution of X-ray tomographic techniques is one of the main current limitations. In this study, pixel size = $0.325\ \mu\text{m}$, which is somewhat higher than the threshold diameter value for macro pores

Table 2-2). The limiting factor is detector resolution but technological advances will likely improve this rapidly. Furthermore, the related technique of

ptychography³³⁴ is capable of resolving structures such as pores into the nano meter range. There are three main sources of error in the pore space quantification method.

Error in measurement: These relate X-ray exposure and signal acquisition and include beam artefacts that can appear as a result of several factors. These include beam stability and vibration in the monochromator crystal. Such errors are typically not quantified in literature due to the complexities and unique experimental setup of each synchrotron source, and they are not considered to significantly alter data. Nonetheless, an additional measure was undertaken with these data to minimise radial artefacts - images were cropped to a central region.

Error in reconstruction: Finding the centre of rotation is crucial to accurate image reconstruction. Again, there is typically little possibility for quantification of this source of error. However, this is not thought to be a major source of error provided that care is taken to check and assess the reconstruction.

Error in image processing: Error can result from poor choice of pre-processing filters, which creates inaccurate binarized images for thresholding. Although it is not customary to publish any error estimation in literature, it is possible to estimate error accrued in image segmentation using the Ilastik 'uncertainty' layer. This layer is an expression of uncertainty in the trained prediction algorithm for separation of pore vs sample. These values were also manually verified by thresholding portions of sample at high and low extremes of possible values, similar to that mentioned in Quin et al. 2014³³¹. If anything, this is likely to be an over-estimation of image binarization error.

9.3 Conferences Attended & oral presentations

- Green Carbon Webinar series 2021, remote. Oral presentation
- School Internal Research Exchange 2021, remote. Oral presentation
- Bragg Centre Research Exchange 2019, Leeds. Poster
- Diamond Light Source i13 research seminar, March 2021, remote. Oral presentation
- Asia Oceania Geosciences Society (AOGS) 18th Annual Meeting 2021, remote. Oral presentation
- 19th Radiological Chemistry Conference 15th-20th May 2022, Mariánské Lázně, Czech Republic. Oral presentation
- Student sustainability conference, Leeds 2020, remote. Poster

9.4 Training Courses Attended

- Synchrotron School 2018 at Diamond Light Source, Harwell Science & Innovation campus (4 days)
- XAS workshop at Diamond Light Source, Harwell Science & Innovation campus (1.5 days)

9.5 Awards

- Best oral presentation in Advanced Engineering Materials section, School Internal Research Exchange 2021. £75
- Women of Achievement award 2021 for advancing women in STEM
- Partnership Awards commendation in Equality & Inclusion category (2021 & 2022)
- Supervised Award winning MSc project - Hargreaves Energy & Environment MSc Research Project Prize 2021 & Energy & Environment MSc Prize 2021

9.6 Publications

G. Wadsley, R. J. Wilbraham, A. Fells, S. Foster, C. Bulman, B. C. Hanson, A. Baker. Optimisation of the Hydrophilic Conditioning of Amidoximated Polymers and Evaluation of their Uranium Adsorption. *Nuclear Futures* (2022) ISSN 1745-2058

S. Foster, N. Ramanan, B. Hanson, B. Mishra. Inner sphere binding of strontium to alginate-activated biochar hydrogel composites for sustainable decontamination. *J. Radioanal Nucl Chem* (2022)
<https://doi.org/10.1007/s10967-022-08613-6>

S. Foster, V. Primaj, B. Hanson, B. Mishra. A Critical Review of iron-biopolymer composites for radionuclide remediation. In preparation

S. Foster, F. Brocza, S. Marathe, B. Hanson, B. Mishra. Tuning the multi-scale pore space of biochar – a quantitative X-ray computed tomography study of activation. In preparation

F. Broczaa, S. Foster, C. Peacock, J. Jones. Synthesis and applications of manganese oxide – biochar composites: a systematic review across catalysis, capacitor and sorption applications. Submitted and under review (*Biomass & Bioenergy*). Under Review, expected Autumn 2023.

Appendix

Appendix A.

Table A-1 Selected compositional data for common three feedstock types, expressed in percent dry weight

% composition	Rice husk (RH)	Oak	Spent coffee grounds (SCG)
Lignin	26.3, 26.4, 27.4 ⁵⁵³ ; 23 ⁵⁵⁴ ; 20-25 ⁵⁵⁵ ; 25.2 ⁵⁵⁶	28 ⁵⁵⁷ ; 25, 17-30, 22.2, 29.6, 29.1, 25, 22, 26, 27.6, 27.6 ⁵⁵⁸ , 25.9 ⁵⁵⁶	3 ⁵⁵⁹ ; 24 ⁵⁰⁴ ; 33 ⁵⁶⁰ ; 23 ⁵⁶¹ ; 22.1 ⁵⁵⁶
Cellulose	39.6, 39.0, 39.8 ⁵⁵³ ; 35 ⁵⁵⁴ ; 35-40 ⁵⁵⁵ ; 33.1 ⁵⁵⁶ ;	38, 22-50, 40.5, 41.1, 46.4, 42, 41, 38, 45.7, 42.4 ⁵⁵⁸ ; 38.1 ⁵⁵⁶	31-37 ⁵⁵⁹ ; 12 ⁵⁰⁴ ; 9 ⁵⁶² ; 49.8 ⁵⁵⁶
Hemi- cellulose	17.5, 18.0, 16.7 ⁵⁵³ ; 33 ⁵⁵⁴ ; 15-20 ⁵⁵⁵ ; 19.3 ⁵⁵⁶	29, 17-30, 23.3, 22.2, 18.9, 28, 30, 30, 24.8, 24.8 ⁵⁵⁸ ; 26.1 ⁵⁵⁶	39 ⁵⁰⁴ ; 19-42; 37 ⁵⁶² ; 63 ⁵⁶⁰ ; 9.5 ⁵⁵⁶
Protein	2.9-3.6 ⁵⁶³	-	14-18; 17 ⁵⁰⁴ ; 14 ⁵⁶²
Lipids	8-12 ⁵⁶³	-	11-17 ⁵⁵⁹ ; 2 ⁵⁰⁴

Table A-2 Selected literature values for BET surface area of activated biochars versus unactivated control biochars

Biochar precursor type	BET surface area (m ² /g)				Reference
	Unactivated biochar	ZnCl ₂ activated biochar	HNO ₃ activated biochar	KMnO ₄ activated biochar	
Grape stalk	83.7	1411.8			539
Sewage sludge	0.7	490			75
Rice husk	334	1840			130
Rice husk	50				417
Rice husk	90				564
Rice husk	243				518
Spent coffee grounds	1.93	763.7			128
Spent coffee grounds	2.8				205
Spent coffee grounds	1.62				565
Spent coffee grounds	11				209
Oakwood chips	21.4	458.3			566
Oakwood chips	216	633			567
Oakwood sawdust	550	1380			131
Oak tree	288				518
Red cedar wood chips	433		317		150
Tea leaves	1398		524		568
Sunflower seed husks	438		614		569
Weeds	40.5		17.7		113
Rice husk	71.4		87.2	87.8	175
Oak wood	470			576	546
Rice husk	128			93.8	77
Rice husk	223.9			138	570
Corn straw	61			24	159
Rape straw	111			19	177

--	--	--	--

--	--	--	--

Appendix B.

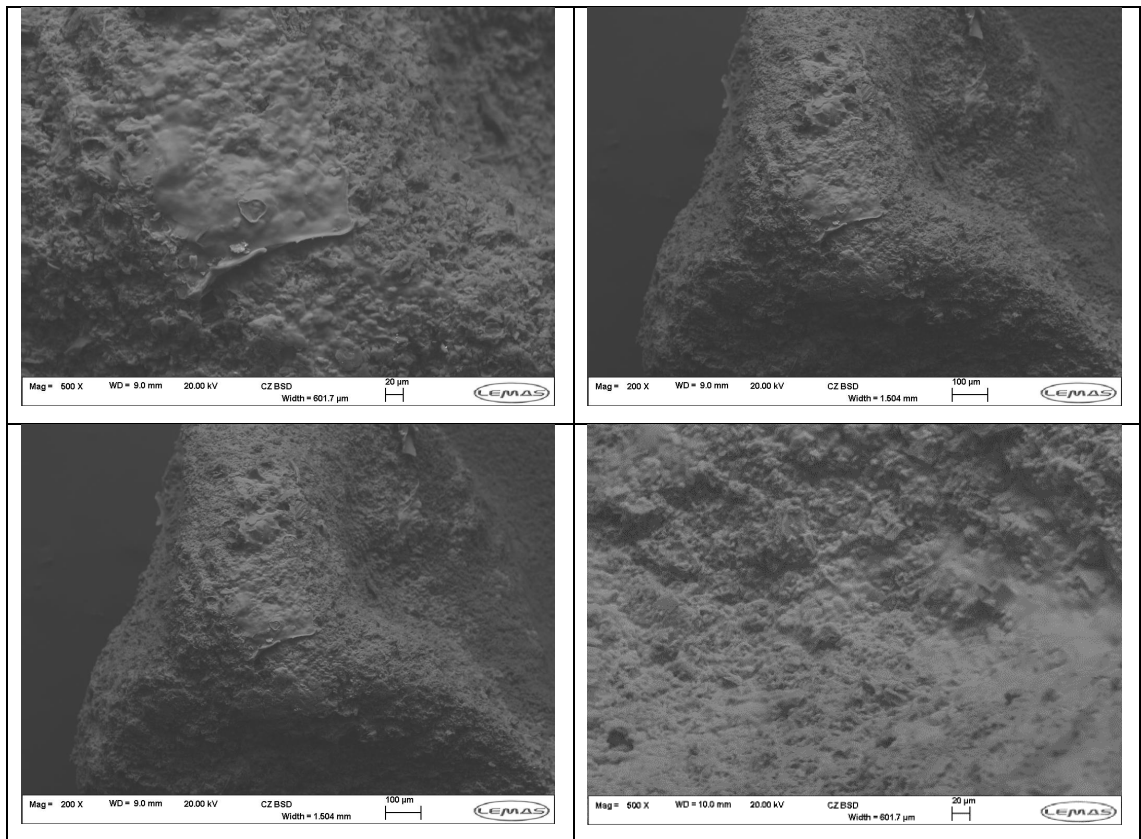


Figure B.1 Evidence of formation of a film or coating on Oak wood hydrogel

Appendix C.

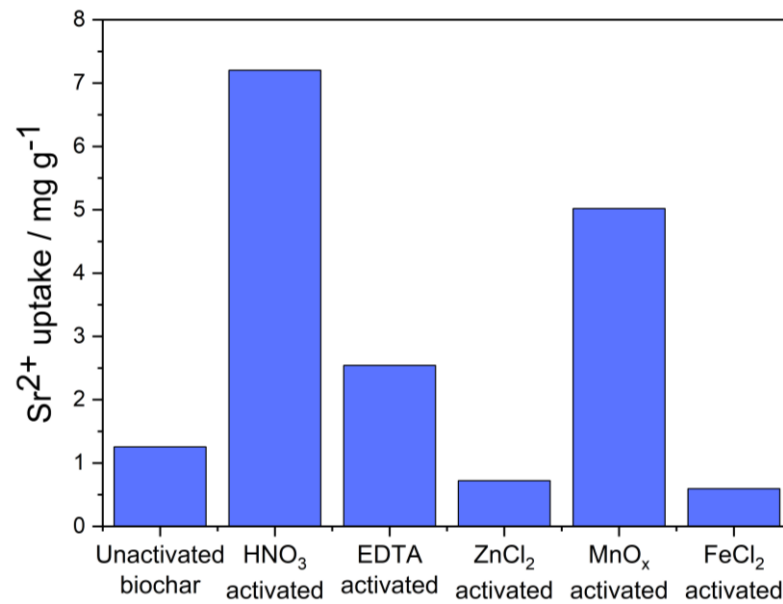


Figure C-1 Relative strontium uptake for a range of activated biochars (Initial strontium concentration was 10 mg L⁻¹, mass adsorbent used was 0.4 g in 50 mL of solution, contact time 1 hr

Table C-1 Kinetic modelling parameters for biochar and HNO₃ activated biochar

	Pseudo first order			Pseudo second order		
	k_1 (1/min)	q_e (mg/g)	R^2	k_2 (g/mg/min)	q_e (mg/g)	R^2
Control biochar	-3.07×10^{-3}	0.46	0.4345	1.93×10^{-2}	1.16	0.9500
HNO ₃ activated biochar	-1.06×10^{-2}	1.19	0.8316	2.29×10^{-2}	7.31	0.9999

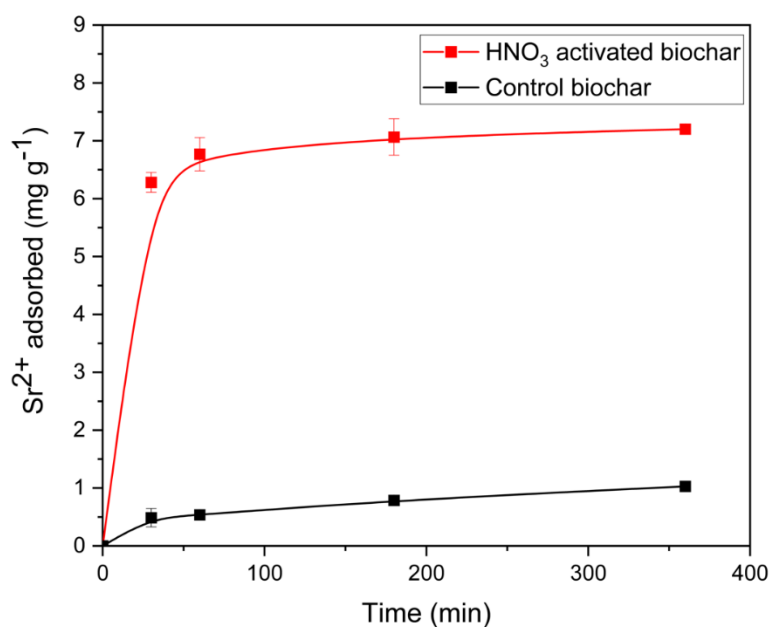


Figure C-2 The effect of contact time on strontium adsorption to unactivated and nitric acid activated biochar

Calibration – ICP-MS

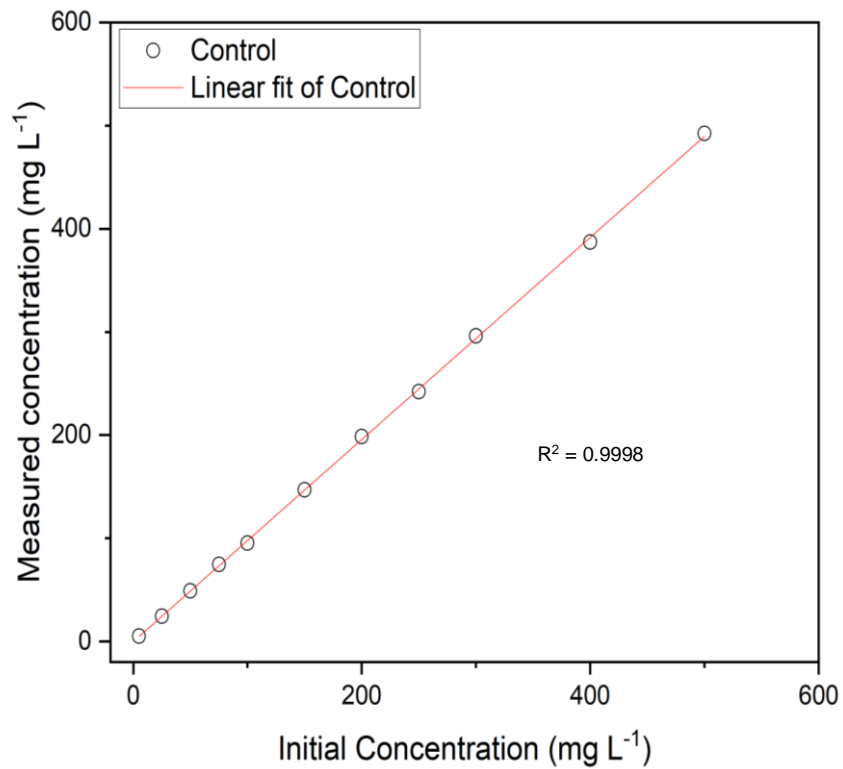
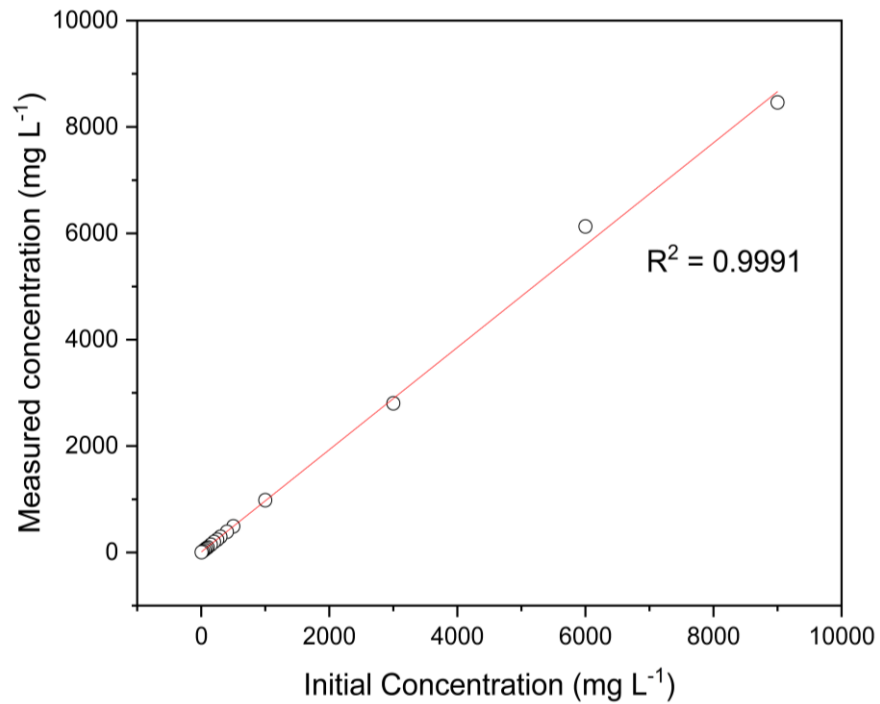


Figure C-3 ICP-MS control samples. The measured strontium concentration in a series of blanks (no adsorbent added) plotted against expected strontium concentration. Full concentration range (top) and low concentration points (bottom)

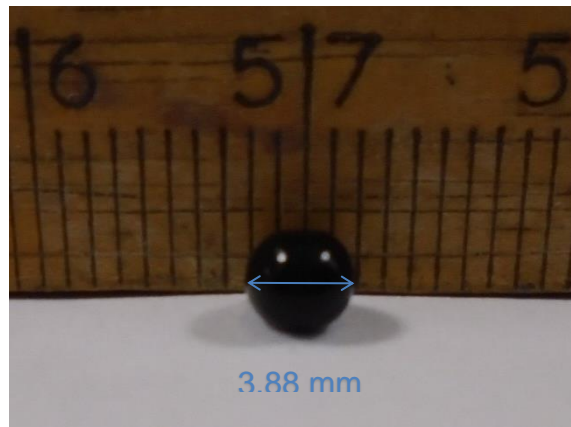
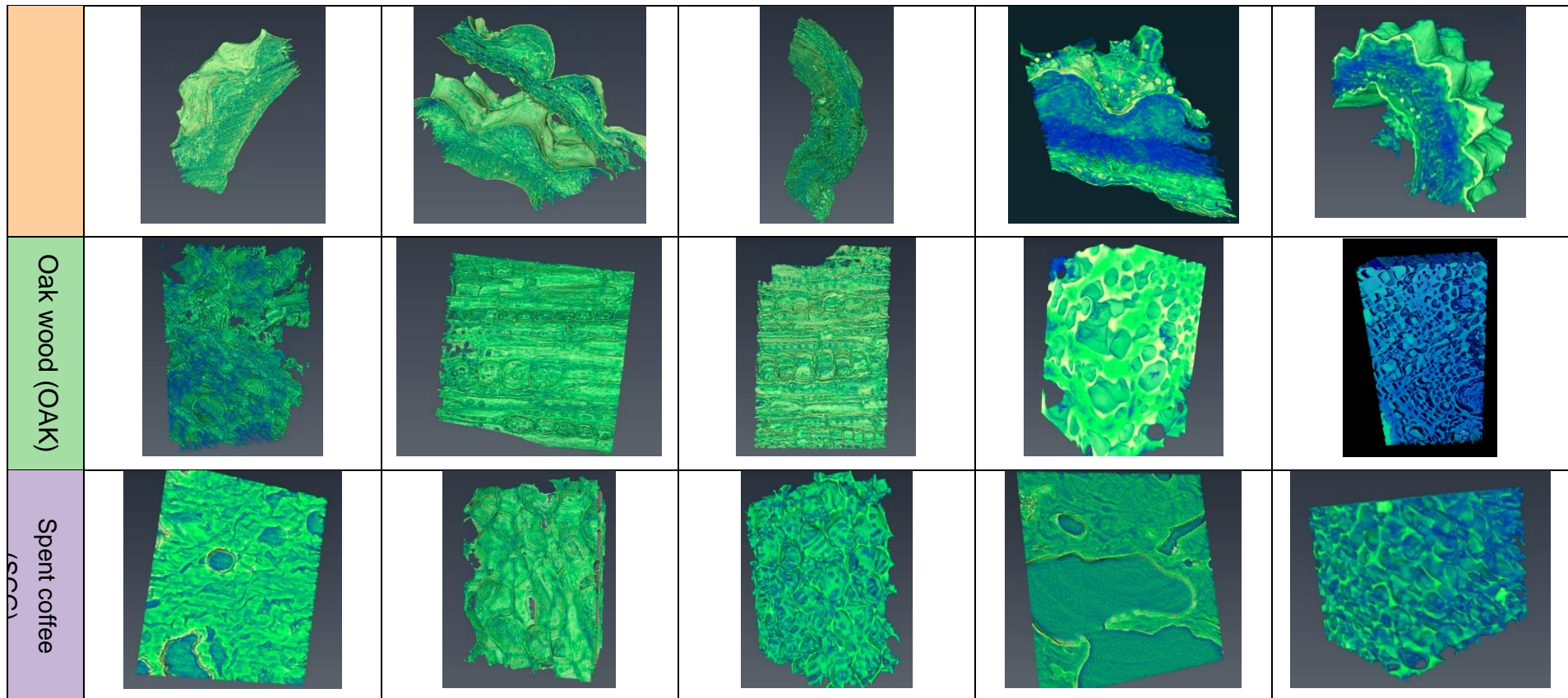


Figure C-4 Scaled image of biochar-alginate hydrogel bead

Appendix E.

Figure E-1 3D reconstructions of all samples.



Savu

A typical Savu process list comprises several modules such as a dataset loader, process modules, reconstruction and saver modules. An example of a process list used is listed below.

1) NxtomoLoader

- 1) preview : []
- 2) image_key_path : entry1/tomo_entry/instrument/detector/image_key
- 3) name : tomo
- 4) 3d_to_4d : False
- 5) flat : [None, None, 1]
- 6) data_path : entry1/tomo_entry/data/data
- 7) dark : [None, None, 1]
- 8) angles : None
- 9) ignore_flats : None

2) DarkFlatFieldCorrection

- 1) in_datasets : []
- 2) upper_bound : None
- 3) out_datasets : []
- 4) lower_bound : None
- 5) pattern : PROJECTION
- 6) warn_proportion : 0.05

3) PaganinFilter

- 1) Ratio : 250.0
- 2) in_datasets : []
- 3) Distance : 1.0
- 4) Padtopbottom : 10
- 5) out_datasets : []
- 6) Padmethod : edge
- 7) Energy : 53.0
- 8) increment : 1.0
- 9) Resolution : 1.28
- 10) Padleftright : 10

4) CcpiRingArtefactFilter

- 1) num_series : 1
- 2) param_r : 0.005
- 3) in_datasets : []
- 4) out_datasets : []
- 5) param_n : 0

5) AstraReconGpu

- 1) init_vol : None
- 2) preview : []

- 3) log : False
 - 4) algorithm : FBP_CUDA
 - 5) n_iterations : 1
 - 6) res_norm : False
 - 7) centre_of_rotation : 1367.2
 - 8) FBP_filter : ram-lak
 - 9) in_datasets : []
 - 10) ratio : 0.95
 - 11) out_datasets : []
 - 12) centre_pad : False
 - 13) outer_pad : False
 - 14) log_func : np.nan_to_num(-np.log(sino))
 - 15) force_zero : [None, None]
-

6) TiffSaver

- 1) in_datasets : []
 - 2) prefix : None
 - 3) pattern : VOLUME_XZ
-

Bibliography

1. Kemp, R. & O'Riordan, T. Planning for radioactive waste disposal. *Land use policy* **5**, 37–44 (1988).
2. International Atomic Energy Agency. *Management of large volumes of waste arising in a nuclear or radiological emergency*. https://www-pub.iaea.org/MTCD/Publications/PDF/TE-1826_web.pdf (2017).
3. Lee, W. E., Ojovan, M. I. & Jantzen, C. M. *Radioactive waste management and contaminated site clean-up*. (Woodhead Publishing, 2013).
4. Dyer, A. *et al.* The use of columns of the zeolite clinoptilolite in the remediation of aqueous nuclear waste streams. *J. Radioanal. Nucl. Chem* **318**, 2473–2491. (2018)
5. International Atomic Energy Agency. *The Fukushima Daiichi Accident: Post-accident Recovery*. vol. 5 <http://www.iaea.org/books> (2015).
6. Department of Energy and Climate Change. *Implementing Geological Disposal: A Framework for the long-term management of higher activity radioactive waste*. (2014).
7. Ojovan, M. I. W. & Lee, W. E. Treatment of Radioactive Wastes. in *An Introduction to Nuclear Waste Immobilisation* 171–203 (2014).
8. Ojovan, M. I. *Handbook of Advanced Radioactive Waste Conditioning Technologies. Series in Energy: Number 12* (2011)
9. Awual, M. R. *et al.* A Reliable Hybrid Adsorbent for Efficient Radioactive Cesium Accumulation from Contaminated Wastewater. *Sci. Rep.* **6**, 2–11 (2016).
10. Nuclear Decommissioning Authority & Department of Business Energy and Industrial Strategy. *Radioactive Wastes in the UK: UK Radioactive Waste Inventory Report*. (2017)
11. Cohen, J. E. & Small, C. Hypsographic demography: The distribution of human population by altitude. *Proc. Natl. Acad. Sci.* **95**, 14009 LP – 14014 (1998).
12. Li, P. *et al.* Highly efficient elimination of uranium from wastewater with facilely synthesized Mg-Fe layered double hydroxides: Optimum preparation conditions and adsorption kinetics. *Ann. Nucl. Energy* **140**, 107140 (2020).
13. Salbu, B., Lind, O. C. & Skipperud, L. Radionuclide speciation and its relevance in environmental impact assessments. *J. Environ. Radioact.* **74**, 233–242 (2004).
14. TEPCO. Fukushima Daiichi Nuclear Power Station Leakage from the Contaminated Water Storage Facility RO Concentrated Water Reservoir (Final Report). (2014).
15. Vermeul, V. R. *et al.* An Injectable Apatite Permeable Reactive Barrier for In Situ ⁹⁰Sr Immobilization. *Groundw. Monit. Remediat.* **34**, 28–41 (2014).

16. Wilkinson, P., Meldrum, P., Kuras, O. & Oxby, L. A Trial of 4D Cross Borehole Electrical Resistivity Tomography (ERT) for Detecting and Monitoring Subsurface Leakage and Contaminant Transport. in *WM 2014 Conference* (2014).
17. Hakem, N. L., Al Mahamid, I., Apps, J. A. & Moridis, G. J. Sorption of cesium and strontium on Hanford soil. *J. Radioanal. Nucl. Chem.* **246**, 275–278 (2000).
18. Riley, R. G., Zachara, J. M. & Wobber, F. J. Chemical contaminants on DOE lands and selection of contaminant mixtures for subsurface science research. *US DOE Off. Energy Res. Subsurf. Res. Program, Washingt. DC 77* (1992).
19. Agency(IAEA), I. A. E. *REFERENCE DATA SERIES No. 1 2020 Edition*. IAEA-RDS-1/41. 978-92-0-130321-9 (2021).
20. Kelly, M. & Thorne, M. *Radionuclides handbook*. The Environment Agency (2003) 1844321762
21. Campbell, K. M. Radionuclides in Surface Water and Groundwater. Ch9. *Handbook of Water Purity and Quality* 1st Ed (2009).
22. Liu, B., Peng, T., Sun, H. & Yue, H. Release behavior of uranium in uranium mill tailings under environmental conditions. *J. Environ. Radioact.* **171**, 160–168 (2017).
23. *Uranium mining in Virginia: Scientific, technical, environmental, human health and safety, and regulatory aspects of uranium mining and processing in Virginia*. National Academies Press (2012)
24. Fathi, R. A., Matti, L. Y., Al-Salih, H. S. & Godbold, D. Environmental pollution by depleted uranium in Iraq with special reference to Mosul and possible effects on cancer and birth defect rates. *Med. Confl. Surviv.* **29**, 7–25 (2013).
25. Brugge, D. & Buchner, V. Health effects of uranium: new research findings. *Rev Environ Health*, 231–249 (2011).
26. Ahmed, R. S. & Mohammed, R. S. Assessment of uranium concentration in blood of Iraqi females diagnosed with breast cancer. *Radiat. Environ. Biophys.* **60**, 193–201 (2021).
27. Sahoo, S. K. *et al.* Strontium-90 activity concentration in soil samples from the exclusion zone of the Fukushima daiichi nuclear power plant. *Sci. Rep.* **6**, 10 (2016).
28. Musilli, S. *et al.* DNA damage induced by Strontium-90 exposure at low concentrations in mesenchymal stromal cells: The functional consequences. *Sci. Rep.* **7**, 1–15 (2017).
29. Mirkhani, R., Roozitalab, M. H., Khaleghpanah, N. & Majadabadi, A. Sorption behavior of cesium and strontium in selected soils of semiarid and arid regions of Iran. *J. Radioanal. Nucl. Chem.* **293**, 587–594 (2016).
30. Povinec, P. P. *et al.* Cesium, iodine and tritium in NW Pacific waters-a comparison of the Fukushima impact with global fallout. *Biogeosciences* **10**, 5481–5496 (2013).

31. Tazoe, H. *et al.* Observation of dispersion in the Japanese coastal area of released ^{90}Sr , ^{134}Cs , and ^{137}Cs from the Fukushima Daiichi nuclear power plant to the sea in 2013. *Int. J. Environ. Res. Public Health* **16**, (2019).
32. Hijikata, T., Koyama, T., Aikyo, Y., Shimura, S. & Kawanishi, M. Strontium adsorption characteristics of natural Zeolites for permeable reactive barrier in Fukushima Daiichi nuclear power station. *J. Nucl. Sci. Technol.* **58**, 1079–1098 (2021).
33. Nuclear Energy Agency. Chernobyl: Assessment of Radiological and Health Impacts. *Organisation for Economic Co-operation and Development* 1–29 (2002).
34. WILKEN, R.-D. & OIEHL, R. Strontium-90 in Environmental Samples from Northern Germany before and after the Chernobyl Accident. *Radiochim. Acta* **41**, 157–162 (1987).
35. Labunska, I. *et al.* Current radiological situation in areas of Ukraine contaminated by the Chornobyl accident: Part 2. Strontium-90 transfer to culinary grains and forest woods from soils of Ivankiv district. *Environ. Int.* **146**, 106282 (2021).
36. McKinley, J. P., Zachara, J. M., Smith, S. C. & Liu, C. Cation exchange reactions controlling desorption of $^{90}\text{Sr}^{2+}$ from coarse-grained contaminated sediments at the Hanford site, Washington. *Geochim. Cosmochim. Acta* **71**, 305–325 (2007).
37. Sahai, N., Carroll, S. A., Roberts, S. & O'Day, P. A. X-ray absorption spectroscopy of strontium(II) coordination. II. Sorption and precipitation at kaolinite, amorphous silica, and goethite surfaces. *J. Colloid Interface Sci.* **222**, 198–212 (2000).
38. Liu, W. & Tsai, S. Environmental Science Processes & Impacts An EXAFS study for characterizing the time- dependent adsorption of cesium on bentonite. *Environ. Sci. Processes Impacts* 930–937 (2019)
39. Lestaevel, P. *et al.* Caesium 137: Properties and biological effects resulting of an internal contamination. *Med. Nucl. Imag. Fonct. Metab.* **34**, 108–118 (2010).
40. Chino, M., Nakayama, H. & Nagai, H. Preliminary Estimation of Release Amounts of I and Cs Accidentally Discharged from the Fukushima Daiichi Nuclear Power Plant into the Atmosphere. *Journal of Nuclear Science and Technology*,48:7,1129-1134 (2012).
41. *Report of the Japanese Government to the IAEA Ministerial Conference on Nuclear Safety - The Accident at TEPCO's Fukushima Nuclear Power Stations.* (2011).
42. Jørgensen, S. E. Adsorption and Ion Exchange. in *Developments in Environmental Modelling* 14 65–81 (1989).
43. Payne, T. E. *et al.* Guidelines for thermodynamic sorption modelling in the context of radioactive waste disposal. *Environ. Model. Softw.* **42**, 143–156 (2013).
44. Marinin, D. V. & Brown, G. N. Studies of sorbent/ion-exchange materials

- for the removal of radioactive strontium from liquid radioactive waste and high hardness groundwaters. *Waste Manag.* **20**, 545–553 (2000).
45. Goldberg, S., Criscenti, L. J., Turner, D. R., Davis, J. A. & Cantrell, K. J. Adsorption–Desorption Processes in Subsurface Reactive Transport Modeling. *Vadose Zone Journal*, **6**: 407–435 (2007)
 46. Stumm, W. The Inner-Sphere Surface Complex. *Advances in Chemistry* **244** 1–32 (1995)
 47. Yin, L. *et al.* Rationally designed core-shell and yolk-shell magnetic titanate nanosheets for efficient U(VI) adsorption performance. *Environ. Pollut.* **238**, 725–738 (2018).
 48. International Atomic Energy Agency. *Application of Ion Exchange Processes for the Treatment of Radioactive Waste and Management of Spent Ion Exchangers*. 0074–1914; no. 408 (2002)
 49. Vandebossche, M., Jimenez, M., Casetta, M. & Traisnel, M. Remediation of Heavy Metals by Biomolecules : A Review. *Critical Reviews in Environmental Science and Technology*, 1644-1704 **3389**, (2015).
 50. Abdel-Karim, A. A. M., Zaki, A. A., Elwan, W., El-Naggar, M. R. & Gouda, M. M. Experimental and modeling investigations of cesium and strontium adsorption onto clay of radioactive waste disposal. *Appl. Clay Sci.* **132–133**, 391–401 (2016).
 51. Vellingiri, K., Kim, K. H., Pournara, A. & Deep, A. Towards high-efficiency sorptive capture of radionuclides in solution and gas. *Prog. Mater. Sci.* **94**, 1–67 (2018).
 52. Renault, F. *et al.* Chitosan flocculation of cardboard-mill secondary biological wastewater. *Chem. Eng. J.* **155**, 775–783 (2009).
 53. Sodha, V. *et al.* Comprehensive Review on Zeolite-Based Nanocomposites for Treatment of Effluents from Wastewater. *Nanomaterials* **12**, (2022).
 54. Tokyo Electric Power Company. *Overview of the Multi-nuclide Removal Equipment (ALPS) at Fukushima Daiichi Nuclear Power Station*. <https://www7.tepco.co.jp/> (2013).
 55. Gupta, D. K., Voronina, A. V., Semenishchev, V. S. & Chatterjee, S. Green Sorbents for Radioactive Pollutant Removal from Natural Water. *Green Adsorbents for Pollutant Removal. Environmental Chemistry for a Sustainable World*, vol 19. 377–396 (2018)
 56. Ching, S. H., Bansal, N. & Bhandari, B. Alginate gel particles—A review of production techniques and physical properties. *Crit. Rev. Food Sci. Nutr.* **57**, 1133–1152 (2017).
 57. Jang, J. *et al.* Science of the Total Environment Rice straw-based biochar beads for the removal of radioactive strontium from aqueous solution. *Sci. Total Environ.* **615**, 698–707 (2018).
 58. Crini, G. Recent developments in polysaccharide-based materials used as adsorbents in wastewater treatment. *Prog. Polym. Sci.* **30**, 38–70

- (2005).
59. Herdzik, L. F. I., Polkowska, K. H. & Oszczak, M. A. Novel procedure for removal of the radioactive metals from aqueous wastes by the magnetic calcium alginate. *Int. J. Environ. Sci. Technol.* **15**, 2657–2668 (2018).
 60. Liu, M. *et al.* Programmed gradient descent biosorption of strontium ions by *Saccaromyces cerevisiae* and ashing analysis: A decrement solution for nuclide and heavy metal disposal. *J. Hazard. Mater.* **314**, 295–303 (2016).
 61. Mendonça, F. G. de, Cunha, I. T. da, Soares, R. R., Tristão, J. C. & Lago, R. M. Tuning the surface properties of biochar by thermal treatment. *Bioresour. Technol.* **246**, 28–33 (2017).
 62. Rodriguez-Narvaez, O. M., Peralta-Hernandez, J. M., Goonetilleke, A. & Bandala, E. R. Biochar-supported nanomaterials for environmental applications. *J. Ind. Eng. Chem.* **78**, 21–33 (2019).
 63. Godlewska, P., Schmidt, H. P., Ok, Y. S. & Oleszczuk, P. Biochar for composting improvement and contaminants reduction. A review. *Bioresour. Technol.* **246**, 193–202 (2017).
 64. Ahmad, M. *et al.* Biochar as a sorbent for contaminant management in soil and water: A review. *Chemosphere* **99**, 19–23 (2014).
 65. Mandal, S. *et al.* Mechanistic insights of 2,4-D sorption onto biochar: Influence of feedstock materials and biochar properties. *Bioresour. Technol.* **246**, 160–167 (2017).
 66. Namaalwa, J., Sankhayan, P. & Hofstad, O. A dynamic bio-economic model for analyzing deforestation and degradation: An application to woodlands in Uganda. *For. Policy Econ.* **9**, 479–495 (2007).
 67. Yoon, K. *et al.* Fabrication of engineered biochar from paper mill sludge and its application into removal of arsenic and cadmium in acidic water. *Bioresour. Technol.* **246**, 69–75 (2017).
 68. Rajapaksha, A. U. *et al.* Engineered/designer biochar for contaminant removal/immobilization from soil and water: Potential and implication of biochar modification. *Chemosphere* **148**, 276–291 (2016).
 69. Sizmur, T., Fresno, T., Akgül, G., Frost, H. & Moreno-Jiménez, E. Biochar modification to enhance sorption of inorganics from water. *Bioresour. Technol.* **246**, 34–47 (2017).
 70. Sajjadi, B., Chen, W. & Egiebor, N. O. A comprehensive review on physical activation of biochar for energy and environmental applications. *Reviews in Chemical Engineerin.* **35**(6), 735-776. (2018).
 71. Lee, H. W. *et al.* Review of the use of activated biochar for energy and environmental applications. **26**, 1–10 (2018).
 72. Sajjadi, B., Chen, W. Y. & Egiebor, N. O. Chemical activation of biochar for energy and environmental applications: a comprehensive review. *Rev. Chem. Eng.* **35**, 735–776 (2019).
 73. Liatsou, I. Triggering selective uranium separation from aqueous solutions by using salophen-modified biochar fibers. *J. Radioanal. Nucl. Chem.* **5**,

- (2018).
74. Mishra, S., Dwivedi, J. & Sankararamkrishnan, N. Studies on salophen anchored micro / meso porous activated carbon fibres for the removal and recovery of uranium. *RSC Advances*, 33023–33036 (2015)
 75. Nguyen, N. *et al.* Preparation of Zn-Doped Biochar from Sewage Sludge for Chromium Ion Removal. *J Nanosci Nanotechnol.* 18(8):5520-5527 (2018)
 76. Wang, S. *et al.* Bioresource Technology Manganese oxide-modified biochars : Preparation , characterization , and sorption of arsenate and lead. *Bioresour. Technol.* **181**, 13–17 (2015).
 77. Wu, Z., Chen, X., Yuan, B. & Fu, M. A facile foaming-polymerization strategy to prepare 3D MnO₂ modified biochar-based porous hydrogels for efficient removal of Cd(II) and Pb(II). *Chemosphere*, **239**, (2020).
 78. You, S. *et al.* A critical review on sustainable biochar system through gasification: Energy and environmental applications. *Bioresour. Technol.* **246**, 242–253 (2017).
 79. Liu, W., Jiang, H. & Yu, H. Development of Biochar-Based Functional Materials : Toward a Sustainable Platform Carbon Material. *Chem Rev.* **22** 115 (2015)
 80. Dai, L. *et al.* Post-engineering of biochar via thermal air treatment for highly efficient promotion of uranium(VI) adsorption. *Bioresour. Technol.* **298**, 122576 (2020).
 81. Ashry, A., Bailey, E. H., Chenery, S. R. N. & Young, S. D. Kinetic study of time-dependent fixation of UVI on biochar. *J. Hazard. Mater.* **320**, 55–66 (2016).
 82. Mishra, V. & Sureshkumar, M. K. Study on Sorption Characteristics of Uranium onto Biochar Derived from Eucalyptus Wood. *Water Air Soil Pollut.* **228**, 309 (2017)
 83. Alam, S. *et al.* Mechanisms of the Removal of U (VI) from Aqueous Solution Using Biochar : A Combined Spectroscopic and Modeling Approach. *Environ. Sci. Technol.* **52**, 13057–13067 (2018).
 84. Hadjittofi, L. & Pashalidis, I. Uranium sorption from aqueous solutions by activated biochar fibres investigated by FTIR spectroscopy and batch experiments. *J Radioanal Nucl Chem* **304**, 897–904 (2015)
 85. Jin, J. *et al.* HNO₃ modified biochars for uranium(VI) removal from aqueous solution. *Bioresour. Technol.* **256**, 247–253 (2018).
 86. Dong, L. *et al.* Effect of various environmental factors on the adsorption of U(VI) onto biochar derived from rice straw. *J. Radioanal. Nucl. Chem.* **314**, 377–386 (2017).
 87. Yamauchi, S., Yamagishi, T., Kirikoshi, K. & Yatagai, M. Cesium adsorption from aqueous solutions onto Japanese oak charcoal I: effects of the presence of group 1 and 2 metal ions. *J. Wood Sci.* **60**, 473–479 (2014).

88. Kimura, K. *et al.* Removal of Radioactive Cesium (^{134}Cs plus ^{137}Cs) from Low-Level Contaminated Water by Charcoal and Broiler Litter Biochar. *Food Sci. Technol. Res.* **20**, 1183–1189 (2014).
89. Hamilton, T. F. *et al.* A preliminary assessment on the use of biochar as a soil additive for reducing soil-to-plant uptake of cesium isotopes in radioactively contaminated environments. *J. Radioanal. Nucl. Chem.* **307**, 2015–2020 (2016).
90. Yakout, S. M. & Elsherif, E. Biosorption behavior of Sr^{2+} using straw-derived biochar: equilibrium and isotherm study. *Desalin. Water Treat.* **57**, 7262–7269 (2016).
91. Zhang, D. *et al.* Application of a rice husk-derived biochar in soil immobilization of iodide (I^-) and iodate (IO_3^-). *J Soils Sediments* **18**, 1540–1547 (2018)
92. Chen, T., Zhang, N., Xu, Z., Hu, X. & Ding, Z. Integrated comparisons of thorium(IV) adsorption onto alkali-treated duckweed biomass and duckweed-derived hydrothermal and pyrolytic biochar. *Environ. Sci. Pollut. Res.* **26**, 2523–2530 (2019)
93. Zhu, Y., Zheng, C., Wu, S., Song, Y. & Hu, B. Interaction of Eu(III) on magnetic biochar investigated by batch, spectroscopic and modeling techniques. *J. Radioanal. Nucl. Chem.* **316**, 1337–1346 (2018).
94. Dan, M., Viglas, E. & Dan, M. Sorption behaviour of pertechnetate on oxidized and reduced surface of activated carbon. *J Radioanal Nucl Chem* **314** 2219–2227 (2017)
95. Tsechansky, L. & Graber, E. R. Letter to the Editor Methodological limitations to determining acidic groups at biochar surfaces via the Boehm titration. *Carbon N. Y.* **66**, 730–733 (2013).
96. Fidel, R. B., Laird, D. A. & Thompson, M. L. Evaluation of Modified Boehm Titration Methods for Use with Biochars. *J Environ Qual.* (6):1771-8 (2013)
97. Li, X. *et al.* Macroscopic and molecular investigations of immobilization mechanism of uranium on biochar: EXAFS spectroscopy and static batch. *J. Mol. Liq.* **269**, 64–71 (2018).
98. Watkins, E. & Kieduszynski, I. Structural Components of Alginic Acid. *Biopolymers* **12**, 1865–1878 (1973).
99. Cao, L., Lu, W., Mata, A., Nishinari, K. & Fang, Y. Egg-box model-based gelation of alginate and pectin: A review. *Carbohydr. Polym.* **242**, 116389 (2020).
100. Gok, C., Gerstmann, U. & Aytas, S. Biosorption of radiostrontium by alginate beads: Application of isotherm models and thermodynamic studies. *J. Radioanal. Nucl. Chem.* **295**, 777–788 (2013).
101. Vandenbossche, M., Jimenez, M., Casetta, M. & Traisnel, M. Remediation of heavy metals by biomolecules: A review. *Crit. Rev. Environ. Sci. Technol.* **45**, 1644–1704 (2015).
102. Yan Ning & Chen Xi. Don't waste seafood waste Turning cast-off shells

- into nitrogen-rich chemicals would benefit economies and the environment, say Ning Yan and Xi Chen. *Nature* **524**, 155–157 (2015).
103. Wang, J., Zhuang, S. & Liu, Y. Metal hexacyanoferrates-based adsorbents for cesium removal. *Coord. Chem. Rev.* **374**, 430–438 (2018).
 104. Zhou, Y. *et al.* Biochar-supported zerovalent iron for removal of various contaminants from aqueous solutions. *Bioresour. Technol.* **152**, 538–542 (2014).
 105. Jin, J., Huang, X., Zhou, L., Peng, J. & Wang, Y. In situ preparation of magnetic chitosan resins functionalized with triethylene-tetramine for the adsorption of uranyl(II) ions. *J. Radioanal. Nucl. Chem.* **303**, 797–806 (2015).
 106. Ma, X., Liu, X., Anderson, D. P. & Chang, P. R. Modification of porous starch for the adsorption of heavy metal ions from aqueous solution. *Food Chem.* **181**, 133–139 (2015).
 107. Zhuang, S. & Wang, J. Removal of cesium ions using nickel hexacyanoferrates-loaded bacterial cellulose membrane as an effective adsorbent. *J. Mol. Liq.* **294**, 111682 (2019).
 108. Kim, Y., Kim, Y. K., Kim, S., Harbottle, D. & Lee, J. W. Nanostructured potassium copper hexacyanoferrate-cellulose hydrogel for selective and rapid cesium adsorption. *Chem. Eng. J.* **313**, 1042–1050 (2017).
 109. Zong, Y. *et al.* Preparation of a novel microsphere adsorbent of prussian blue capsulated in carboxymethyl cellulose sodium for Cs(I) removal from contaminated water. *J. Radioanal. Nucl. Chem.* **311**, 1577–1591 (2017).
 110. Eun, S. *et al.* Prussian blue-embedded carboxymethyl cellulose nanofibril membranes for removing radioactive cesium from aqueous solution. *Carbohydr. Polym.* **235**, 115984 (2020).
 111. Popescu, I. C. *et al.* Removal of uranium (VI) from aqueous systems by nanoscale zero-valent iron particles suspended in carboxy-methyl cellulose. *J. Nucl. Mater.* **443**, 250–255 (2013).
 112. Hollabaugh, C. B., Burt, L. H. & Walsh, A. P. Carboxymethylcellulose-Uses and Applications. *Ind. Eng. Chem.* **37**, 10, 943–947 (1945).
 113. Akkaya, G., Güzel, F. & Say, H. Optimal oxidation with nitric acid of biochar derived from pyrolysis of weeds and its application in removal of hazardous dye methylene blue from aqueous solution. *Journal of Cleaner Production*, **144**, 260–265 (2017).
 114. Chakraborty, R., Vilya, K., Pradhan, M. & Nayak, A. K. An overview on engineering the surface area and porosity of biochar. *J. Mater. Chem. A* **10**, 6965–7005 (2022).
 115. Lou, K., Rajapaksha, A. U., Ok, Y. S. & Chang, S. X. Pyrolysis temperature and steam activation effects on sorption of phosphate on pine sawdust biochars in aqueous solutions. *Chem. Speciat. Bioavailab.* **28**, 42–50 (2016).
 116. Leng, L. *et al.* An overview on engineering the surface area and porosity of biochar. *Sci. Total Environ.* **763**, 144204 (2021).

117. Caccin, M., Giacobbo, F., Da Ros, M., Besozzi, L. & Mariani, M. Adsorption of uranium, cesium and strontium onto coconut shell activated carbon. *J. Radioanal. Nucl. Chem.* **297**, 9–18 (2013).
118. Chen, Y., Zhang, X., Chen, W., Yang, H. & Chen, H. The structure evolution of biochar from biomass pyrolysis and its correlation with gas pollutant adsorption performance. *Bioresour. Technol.* **246**, 101–109 (2017).
119. Kaçan, E. & Kütahyalı, C. Adsorption of strontium from aqueous solution using activated carbon produced from textile sewage sludges. *J. Anal. Appl. Pyrolysis* **97**, 149–157 (2012).
120. Sajjadi, B., Chen, W. Y. & Egiebor, N. O. Chemical activation of biochar for energy and environmental applications: a comprehensive review. *Rev. Chem. Eng.* (2018) doi:10.1515/revce-2017-0113.
121. Ma, P., Yao, S., Wang, Z., Qi, F. & Liu, X. Preparation of nitrogen-doped hierarchical porous carbon aerogels from agricultural wastes for efficient pollution adsorption. *Sep. Purif. Technol.* **311**, 123250 (2023).
122. Post, J. E. Manganese Oxide Minerals: Crystal Structures and Economic and Environmental Significant. *Proc. Matl. Acad. Sci.* **96**, 3447–3454 (1999).
123. Wang, Z., Giammar, D. E., States, U., Louis, S. & States, U. Metal Contaminant Oxidation Mediated by Manganese Redox Cycling in Subsurface Environment. *Advances in the Environmental Biogeochemistry of Manganese Oxides* Ch2 29-50 (2015).
124. Dong, Y. *et al.* Synthesis of mesoporous carbon fibers with a high adsorption capacity for bulky dye molecules. *J. Mater. Chem. A* **1**, 7391–7398 (2013).
125. Pang, H. *et al.* Adsorptive and reductive removal of U(VI) by Dictyophora indusiata-derived biochar supported sulfide NZVI from wastewater. *Chem. Eng. J.* **366**, 368–377 (2019).
126. Fu, F., Dionysiou, D. D. & Liu, H. The use of zero-valent iron for groundwater remediation and wastewater treatment: A review. *J. Hazard. Mater.* **267**, 194–205 (2014).
127. Namane, A., Mekarzia, A., Benrachedi, K., Belhaneche-Bensemra, N. & Hellal, A. Determination of the adsorption capacity of activated carbon made from coffee grounds by chemical activation with ZnCl₂ and H₃PO₄. *J. Hazard. Mater.* **119**, 189–194 (2005).
128. Bekirogullari, M. Hydrogen production from sodium borohydride by ZnCl₂ treated defatted spent coffee ground catalyst. *Int. J. Hydrogen Energy* **45**, 9733–9743 (2020).
129. Boonamnuayvitaya, V., Sae-ung, S. & Tanthapanichakoon, W. Preparation of activated carbons from coffee residue for the adsorption of formaldehyde. *Separation and Purification Technology* **42**, 159–168 (2005).
130. Irfan, M. *et al.* Evaluation of enhancement factor for removal of heavy metal ions from water through adsorption by non-activated and activated

- carbon prepared from rice husk. *Pakistan J. Sci. Ind. Res. Ser. A Phys. Sci.* **64**, 206–213 (2021).
131. Nirmaladevi, S. & Palanisamy, P. N. Adsorptive behavior of biochar and zinc chloride activated hydrochar prepared from acacia leucophloea wood sawdust: Kinetic equilibrium and thermodynamic studies. *Desalin. Water Treat.* **209**, 170–181 (2021).
 132. Xia, D. *et al.* ZnCl₂-activated biochar from biogas residue facilitates aqueous As(III) removal. *Appl. Surf. Sci.* **377**, 361–369 (2016).
 133. Dan, M. *et al.* Preparation and characterization of adsorbent based on carbon for pertechnetate adsorption. *J Radioanal Nucl Chem* **303**, 277–286 (2015)
 134. Wang, B., Ran, M., Fang, G., Wu, T. & Ni, Y. Biochars from lignin-rich residue of furfural manufacturing process for heavy metal ions remediation. *Materials (Basel)*. **13**, (2020).
 135. Ho, S. H. *et al.* High-efficiency removal of lead from wastewater by biochar derived from anaerobic digestion sludge. *Bioresour. Technol.* **246**, 142–149 (2017).
 136. Ma, Y., Wang, Q., Wang, X., Sun, X. & Wang, X. A comprehensive study on activated carbon prepared from spent shiitake substrate via pyrolysis with ZnCl₂. *J. Porous Mater.* **22**, 157–169 (2015).
 137. Kütahyalı, C. & Eral, M. Sorption studies of uranium and thorium on activated carbon prepared from olive stones : Kinetic and thermodynamic aspects. *J. Nucl. Mater.* **396**, 251–256 (2010).
 138. Ozdemir, I., Şahin, M., Orhan, R. & Erdem, M. Preparation and characterization of activated carbon from grape stalk by zinc chloride activation. *Fuel Process. Technol.* **125**, 200–206 (2014).
 139. Angin, D., Altintig, E. & Köse, T. E. Influence of process parameters on the surface and chemical properties of activated carbon obtained from biochar by chemical activation. *Bioresour. Technol.* **148**, 542–549 (2013).
 140. Tian, W., Gao, Q., Tan, Y. & Li, Z. Unusual interconnected graphitized carbon nanosheets as the electrode of high-rate ionic liquid-based supercapacitor. *Carbon N. Y.* **119**, 287–295 (2017).
 141. Ahmadpour, A. & Do, D. D. The preparation of active carbons from coal by chemical and physical activation. *Carbon N. Y.* **34**, 471–479 (1996).
 142. Wang, S. *et al.* Carboxymethyl cellulose stabilized ZnO / biochar nanocomposites : Enhanced adsorption and inhibited photocatalytic degradation of methylene blue. *Chemosphere* **197**, 20–25 (2018).
 143. Härmas, M. *et al.* Microporous–mesoporous carbons for energy storage synthesized by activation of carbonaceous material by zinc chloride, potassium hydroxide or mixture of them. *J. Power Sources* **326**, 624–634 (2016).
 144. Mikhalovsky, S. V, Sandeman, S. R., Howell, C. A., Phillips, G. J. & Nikolaev, V. G. Biomedical Applications of Carbon Adsorbents. *Novel Carbon Adsorbents* (2012).

145. Cheng, B. H., Zeng, R. J. & Jiang, H. Recent developments of post-modification of biochar for electrochemical energy storage. *Bioresour. Technol.* **246**, 224–233 (2017).
146. Franz, J. E., Herber, J. F. & Knowles, W. S. Mechanism of the Nitric Acid Oxidation of Olefins. *J. Org. Chem.* **30**, 1488–1491 (1965).
147. Li, B. & Li, K. Effect of nitric acid pre-oxidation concentration on pore structure and nitrogen/oxygen active decoration sites of ethylenediamine - modified biochar for mercury(II) adsorption and the possible mechanism. *Chemosphere* **220**, 28–39 (2019).
148. Salame, I. I. & Bandosz, T. J. Surface Chemistry of Activated Carbons : Combining the Results of Temperature-Programmed Desorption , *Boehm , and Potentiometric Titrations.* **258**, 252–258 (2001).
149. Hadjittofi, L., Prodromou, M. & Pashalidis, I. Activated biochar derived from cactus fibres - Preparation, characterization and application on Cu(II) removal from aqueous solutions. *Bioresour. Technol.* **159**, 460–464 (2014).
150. Jiang, J. *et al.* Highly ordered macroporous woody biochar with ultra-high carbon content as supercapacitor electrodes. *Electrochim. Acta* **113**, 481–489 (2013).
151. Hubetska, T. S., Kobylinska, N. G. & García, J. R. Sunflower biomass power plant by-products: Properties and its potential for water purification of organic pollutants. *J. Anal. Appl. Pyrolysis* **157**, 105237 (2021).
152. Yakout, S. M. & Elsherif, E. Batch kinetics, isotherm and thermodynamic studies of adsorption of strontium from aqueous solutions onto low cost rice-straw based carbons. *Carbon - Sci. Technol.* **3**, 144–153 (2010).
153. Shawabkeh, R. A., Rockstraw, D. A. & Bhada, R. K. Copper and strontium adsorption by a novel carbon material manufactured from pecan shells. *Carbon N. Y.* **40**, 781–786 (2002).
154. Martell, a. E. The chelate effect. In *werner centennial* vol. 62 19–272 (american chemical society, 1967).
155. Joseph, S. *et al.* The Electrochemical Properties of Biochars and How They Affect Soil Redox Properties and Processes. *Agronomy* **5**, 322–340 (2015).
156. Yuan, Y. *et al.* Applications of biochar in redox-mediated reactions. *Bioresour. Technol.* **246**, 271–281 (2017).
157. Hadjittofi, L. & Pashalidis, I. Uranium sorption from aqueous solutions by activated biochar fibres investigated by FTIR spectroscopy and batch experiments. *J. Radioanal. Nucl. Chem.* **304**, 897–904 (2015).
158. Jin, J. *et al.* HNO₃ modified biochars for uranium (VI) removal from aqueous solution. *Bioresour. Technol.* **256**, 247–253 (2018).
159. Song, Z. *et al.* Synthesis and characterization of a novel MnO_x-loaded biochar and its adsorption properties for Cu²⁺ in aqueous solution. *Chem. Eng. J.* **242**, 36–42 (2014).
160. Qiao, L. & Swihart, M. T. Solution-phase synthesis of transition metal

- oxide nanocrystals: Morphologies, formulae, and mechanisms. *Adv. Colloid Interface Sci.* **244**, 199–266 (2017).
161. Post, J. E. Manganese oxide minerals: Crystal structures and economic and environmental significance. *Proc. Natl. Acad. Sci.* **96**, 3447–3454 (1999).
 162. Marshall, K. C. Chapter 5 Biogeochemistry of Manganese Minerals. *Biogeochem. Cycl. Miner. Elem. Volume 3*, 253–292 (1979).
 163. Trakal, L. *et al.* AMOchar: Amorphous manganese oxide coating of biochar improves its efficiency at removing metal(loid)s from aqueous solutions. *Sci. Total Environ.* **625**, 71–78 (2018).
 164. Wang, S., Gao, B., Li, Y., Wan, Y. & Creamer, A. E. Sorption of arsenate onto magnetic iron-manganese (Fe-Mn) biochar composites. *RSC Adv.* **5**, 67971–67978 (2015).
 165. Wang, L. *et al.* Mechanisms and reutilization of modified biochar used for removal of heavy metals from wastewater: A review. *Sci. Total Environ.* **668**, 1298–1309 (2019).
 166. Sun, C. *et al.* Enhanced adsorption for Pb(II) and Cd(II) of magnetic rice husk biochar by KMnO₄ modification. *Environ. Sci. Pollut. Res.* **26**, 8902–8913 (2019).
 167. Baccar, R., Bouzid, J., Feki, M. & Montiel, A. Preparation of activated carbon from Tunisian olive-waste cakes and its application for adsorption of heavy metal ions. *J. Hazard. Mater.* **162**, 1522–1529 (2009).
 168. Egorin, A. *et al.* Investigation of Sr uptake by birnessite-type sorbents from seawater. *J. Radioanal. Nucl. Chem.* **317**, 243–251 (2018).
 169. Ghaeni, N., Taleshi, M. S. & Elmi, F. Removal and recovery of strontium (Sr (II)) from seawater by Fe₃O₄/MnO₂/fulvic acid nanocomposite. *Mar. Chem.* **213**, 33–39 (2019).
 170. Ivanets, A. I. *et al.* Sorption behavior of structure Sr onto manganese oxides with tunnel. **0123456789**, 673–683 (2018).
 171. Greenwood, N. N. & Earnshaw, A. Chemical reactivity and trends. in *Chemistry of the Elements* (Elsevier, 1997).
 172. Faheem *et al.* Preparation of MnOx-loaded biochar for Pb²⁺ removal: Adsorption performance and possible mechanism. *J. Taiwan Inst. Chem. Eng.* **66**, 313–320 (2016).
 173. Wang, M. C., Sheng, G. D. & Qiu, Y. P. A novel manganese-oxide/biochar composite for efficient removal of lead(II) from aqueous solutions. *Int. J. Environ. Sci. Technol.* **12**, 1719–1726 (2015).
 174. Della Puppa, L., Komárek, M., Bordas, F., Bollinger, J.-C. & Joussein, E. Adsorption of copper, cadmium, lead and zinc onto a synthetic manganese oxide. *J. Colloid Interface Sci.* **399**, 99–106 (2013).
 175. Yakout, S. M. Monitoring the changes of chemical properties of rice straw-derived biochars modified by different oxidizing agents and their adsorptive performance for organics. *Bioremediat. J.* **19**, 171–182 (2015).
 176. Ivanets, A. I. *et al.* Sorption behavior of ⁸⁵Sr onto manganese oxides with

- tunnel structure. *J. Radioanal. Nucl. Chem.* **316**, 673–683 (2018).
177. Li, B. *et al.* Adsorption of Cd (II) from aqueous solutions by rape straw biochar derived from different modification processes. *Chemosphere* **175**, 332–340 (2017).
 178. Wang, S. *et al.* Manganese oxide-modified biochars: Preparation, characterization, and sorption of arsenate and lead. *Bioresour. Technol.* **181**, 13–17 (2015).
 179. Kamran, U. & Park, S. MnO₂-decorated biochar composites of coconut shell and rice husk : An efficient lithium ions adsorption-desorption performance in aqueous media. *Chemosphere* **260**, 127500 (2020).
 180. Allahbakhsh, A. & Bahramian, A. R. Self-assembled and pyrolyzed carbon aerogels: an overview of their preparation mechanisms, properties and applications. *Nanoscale* 14139–14158 (2015)
 181. Wu, D., Fu, R., Zhang, S. & Dresselhaus, M. S. Preparation of low-density carbon aerogels by ambient pressure drying. *Carbon* **42**, 2033–2039 (2004).
 182. Smirnova, I. & Gurikov, P. Aerogels in Chemical Engineering : Strategies Toward Tailor-Made Aerogels. *Annual Review of Chemical and Biomolecular Engineering.* **8**:307-334 (2017).
 183. Saranya, R., Kumar, M., Tamilarasan, R., Fauzi, A. & Arthanareeswaran, G. Functionalised activated carbon modified polyphenylsulfone composite membranes for adsorption enhanced phenol filtration. *J. Chem. Technol. Biotechnol.*, **91** 748-761 (2015)
 184. Park, B. *et al.* Dual-functional micro-adsorbents: Application for simultaneous adsorption of cesium and strontium. *Chemosphere* **263**, 128266 (2021).
 185. Liang, L. *et al.* Stereoscopic porous gellan gum-based microspheres as high performance adsorbents for U(VI) removal. *J. Radioanal. Nucl. Chem.* **319**, 213–225 (2019).
 186. Chen, Y. W. & Wang, J. L. Removal of cesium from radioactive wastewater using magnetic chitosan beads cross-linked with glutaraldehyde. *Nucl. Sci. Tech.* **27**, 1–6 (2016).
 187. Elwakeel, K. Z. & Atia, A. A. Uptake of U(VI) from aqueous media by magnetic Schiff's base chitosan composite. *J. Clean. Prod.* **70**, 292–302 (2014).
 188. Plazinski, W. & Drach, M. Calcium- α - L - Guluronate Complexes : Ca²⁺ Binding Modes from DFT- *MD Simulations.* (2013).
 189. Gurikov, P., Raman, S. P., Weinrich, D., Fricke, M. & Smirnova, I. A novel approach to alginate aerogels : carbon dioxide induced gelation. *RSC Advances.* 7812–7818 (2015)
 190. Gurikov, P. & Smirnova, I. gels Non-Conventional Methods for Gelation of Alginate. *Gels* **4**(1) (2018)
 191. Hajizadeh, A. & Reza, A. Effect of initial sol concentration on the microstructure and morphology of carbon aerogels. *J. Sol-Gel Science*

- and Technology* **1** 220–226 (2015)
192. Subrahmanyam, R., Gurikov, P., Meissner, I. & Smirnova, I. Preparation of Biopolymer Aerogels Using Green Solvents. *J Vis Exp* **2**, 3–7 (2016).
 193. Lazzari, K. & Perondi, D. Cellulose / biochar aerogels with excellent mechanical and thermal insulation properties. *Cellulose* **3**, 9071–9083 (2019).
 194. Horvat, G., Pantić, M., Knez, Ž. & Novak, Z. A Brief Evaluation of Pore Structure Determination for Bioaerogels. *Gels* **8**, 1–18 (2022).
 195. Jang, J. *et al.* Rice straw-based biochar beads for the removal of radioactive strontium from aqueous solution. *Sci. Total Environ.* **615**, 698–707 (2018).
 196. Zhu, W. *et al.* Environment-friendly bio-materials based on cotton-carbon aerogel for strontium removal from aqueous solution. *J Radioanal Nucl Chem* **8**, 553–560 (2018).
 197. Mihara, Y. *et al.* Adsorption kinetic model of alginate gel beads synthesized micro particle-prussian blue to remove cesium ions from water. *J. Water Process Eng.* **10**, 9–19 (2016).
 198. Jang, J. & Lee, D. S. Enhanced adsorption of cesium on PVA-alginate encapsulated Prussian blue-graphene oxide hydrogel beads in a fixed-bed column system. *Bioresour. Technol.* **218**, 294–300 (2016).
 199. Vipin, A. K., Ling, S. & Fugetsu, B. Sodium cobalt hexacyanoferrate encapsulated in alginate vesicle with CNT for both cesium and strontium removal. *Carbohydr. Polym.* **111**, 477–484 (2014).
 200. Fuks, L., Herdzik-Koniecko, I., Polkowska-Motrenko, H. & Oszczak, A. Novel procedure for removal of the radioactive metals from aqueous wastes by the magnetic calcium alginate. *Int. J. Environ. Sci. Technol.* **15**, 2657–2668 (2018).
 201. Cho, E., Kim, J., Park, C. W., Lee, K. W. & Lee, T. S. Chemically bound Prussian blue in sodium alginate hydrogel for enhanced removal of Cs ions. *J. Hazard. Mater.* **360**, 243–249 (2018).
 202. Chen, C. C. & Hayes, K. F. X-ray absorption spectroscopy investigation of aqueous Co(II) and Sr(II) sorption at clay-water interfaces. *Geochim. Cosmochim. Acta* **63**, 3205–3215 (1999).
 203. Shannon, B. Y. R. D. *et al.* Revised Effective Ionic Radii and Systematic Studies of Interatomic Distances in Halides and Chalcogenides. *Acta Cryst.* **A32**, 751–766 (1976).
 204. Pourret, O. & Houben, D. Characterization of metal binding sites onto biochar using rare earth elements as a fingerprint. *Heliyon* **4** (2018).
 205. Shin, J. *et al.* Changes in adsorption mechanisms of radioactive barium, cobalt, and strontium ions using spent coffee waste biochars via alkaline chemical activation: Enrichment effects of O-containing functional groups. *Environ. Res.* **199**, (2021).
 206. Rae, I. B., Pap, S., Svobodova, D. & Gibb, S. W. Comparison of sustainable biosorbents and ion-exchange resins to remove Sr²⁺ from

- simulant nuclear wastewater: Batch, dynamic and mechanism studies. *Sci. Total Environ.* **650**, 2411–2422 (2019).
207. Guo, Y. *et al.* Strontium Ion Removal From Artificial Seawater Using a Combination of Adsorption With Biochar and Precipitation by Blowing CO₂ Nanobubble With Neutralization. *Front. Bioeng. Biotechnol.* **10**, 1–13 (2022).
 208. Yakout, S. M. & Elsherif, E. Investigation of strontium (II) sorption kinetic and thermodynamic onto straw-derived biochar. *Part. Sci. Technol.* **33**, 579–586 (2015).
 209. Shin, J. *et al.* Effects of physicochemical properties of biochar derived from spent coffee grounds and commercial activated carbon on adsorption behavior and mechanisms of strontium ions (Sr²⁺). *Environ. Sci. Pollut. Res.* **28**, 40623–40632 (2021).
 210. Sumalatha, B. *et al.* A Sustainable Green Approach for Efficient Capture of Strontium from Simulated Radioactive Wastewater Using Modified Biochar. *Int. J. Environ. Res.* **16**, 1–13 (2022).
 211. Jang, J. *et al.* Rice straw-based biochar beads for the removal of radioactive strontium from aqueous solution. *Sci. Total Environ.* **615**, 698–707 (2018).
 212. Choe, S. R. *et al.* Fabrication of alginate/humic acid/Fe-aminoclay hydrogel composed of a grafted-network for the efficient removal of strontium ions from aqueous solution. *Environ. Technol. Innov.* **9**, 285–293 (2018).
 213. Zhang, X., Wang, L., Weng, L. & Deng, B. Strontium ion substituted alginate-based hydrogel fibers and its coordination binding model. *J. Appl. Polym. Sci.* **137**, 1–9 (2020).
 214. Tokunaga, K., Kozai, N. & Takahashi, Y. A new technique for removing strontium from seawater by coprecipitation with barite. *J. Hazard. Mater.* **359**, 307–315 (2018).
 215. O'Day, P. A., Newville, M., Neuhoﬀ, P. S., Sahai, N. & Carroll, S. A. X-Ray Absorption Spectroscopy of Strontium(II) Coordination I. Static and Thermal Disorder in Crystalline, Hydrated, and Precipitated Solids and in Aqueous Solution. *J. Colloid Interface Sci.* **197**, 184–197 (2000).
 216. Parkman, R. H., Charnock, J. M., Livens, F. R. & Vaughan, D. J. A study of the interaction of strontium ions in aqueous solution with the surfaces of calcite and kaolinite. *Geochim. Cosmochim. Acta* **62**, 1481–1492 (1998).
 217. Boda, A. *et al.* From microhydration to bulk hydration of Sr²⁺ + metal ion : DFT , MP2 and molecular dynamics study. *J. Mol. Liq.* **172**, 110–118 (2012).
 218. Stahl, K., Shim, I. & Christgau, S. Structures of strontium diformate and strontium fumarate . A synchrotron powder diffraction study research papers. *Acta Crystallogr. Sect. B Struct. Sci.* 481–487 (2009)
 219. Jarosch, D. & Heger, G. Neutron diffraction investigation of strontianite , SrCO₃. *Bull. Minéralogie* **111**, 139–142 (1988).

220. Vanhoyland, G., Bael, M. K. Van, Mullens, J. & Poucke, L. C. Van. Structure determination of anhydrous acid strontium oxalate by conventional X-ray powder diffraction. *Powder Diffr.* **16**, 224–226 (2007).
221. Um, W. & Papelis, C. Sorption mechanisms of Sr and Pb on zeolitized tuffs from the Nevada test site as a. *J. Am. Chem. Soc.* **60**, 309–319 (2003).
222. Reuter, H., Kamaha, S. & Zerzouf, O. Hydrogen bonds in the crystal structure of strontium hydroxide octahydrate $\text{Sr}(\text{OH})_2 \cdot 8\text{H}_2\text{O}$. *Zeitschrift fur Naturforsch. - Sect. B J. Chem. Sci.* **62**, 215–219 (2007).
223. Wallace, S. H., Shaw, S., Morris, K., Small, J. S. & Burke, I. T. Alteration of sediments by hyperalkaline k-rich cement leachate: Implications for strontium adsorption and incorporation. *Environ. Sci. Technol.* **47**, 3694–3700 (2013).
224. Collins, B. C. R., Sherman, D. M. & Ragnarsdóttir, K. V. The Adsorption Mechanism of Sr^{2+} on the Surface of Goethite. *Radiochimica Acta* **206**, 201–206 (1998).
225. Fuller, A. J., Shaw, S., Peacock, C. L., Trivedi, D. & Burke, I. T. EXAFS Study of Sr sorption to Illite, Goethite, Chlorite, and Mixed Sediment under Hyperalkaline Conditions. *Langmuir* **32**, 2937–2946 (2016).
226. Bots, P. *et al.* Emerging investigator series: A holistic approach to multicomponent EXAFS: Sr and Cs complexation in clayey soils. *Environ. Sci. Process. Impacts* **23**, 1101–1115 (2021).
227. Sun, Y. *et al.* Mutual effect of Cs(i) and Sr(ii) sorption on nano-talc investigated by EXAFS, modeling and theoretical calculations. *Environ. Sci. Nano* **6**, 672–683 (2019).
228. Collins, C. R., Sherman, D. M. & Vala Ragnarsdóttir, K. The Adsorption Mechanism of Sr^{2+} on the Surface of Goethite. *Radiochim. Acta* **81**, 201–206 (1998).
229. Singer, D. M., Johnson, S. B., Catalano, J. G., Farges, F. & Brown, G. E. Sequestration of Sr(II) by calcium oxalate-A batch uptake study and EXAFS analysis of model compounds and reaction products. *Geochim. Cosmochim. Acta* **72**, 5055–5069 (2008).
230. D'Angelo, P., Migliorati, V., Sessa, F., Mancini, G. & Persson, I. XANES reveals the flexible nature of hydrated strontium in aqueous solution. *J. Phys. Chem. B* **120**, 4114–4124 (2016).
231. Chen, C.-C. & Hayes, K. F. X-ray absorption spectroscopy investigation of aqueous Co (II) and Sr (II) sorption at clay – water interfaces. *J. Colloid Interface Sci.* **63**, 3205–3215 (1999).
232. Yamaguchi, A., Tanaka, M., Kurihara, Y. & Takahashi, Y. Local structure of strontium adsorbed on 2:1 clay minerals and its comparison with cesium by XAFS in terms of migration of their radioisotopes in the environment. *J. Radioanal. Nucl. Chem.* **317**, 545–551 (2018).
233. Ooyong, W. U. M. & Apelis, C. H. P. Sorption mechanisms of Sr and Pb on zeolitized tuffs from the Nevada test site as a function of pH and ionic

- strength. *J. Am. Mineralogist* **88**, 2028–2039 (2003).
234. Carroll, S. A., Roberts, S. K., Criscenti, L. J. & O'Day, P. A. Surface complexation model for strontium sorption to amorphous silica and goethite. *Geochem. Trans.* **9**, 1–26 (2008).
 235. Nie, Z. *et al.* Adsorption of Selenium and Strontium on Goethite: EXAFS Study and Surface Complexation Modeling of the Ternary Systems. *Environ. Sci. Technol.* **51**, 3751–3758 (2017).
 236. Axe, L., Bunker, G. B., Anderson, P. R. & Tyson, T. A. An XAFS Analysis of Strontium at the Hydrous Ferric Oxide Surface. *Journal of Colloid and Interface Science* **52**, 44–52 (1998).
 237. Bunker, G. Application of the ratio method of EXAFS analysis to disordered systems. *Nucl. Instruments Methods Phys. Res.* **207**, 437–444 (1983).
 238. Wallace, S. H. *et al.* Effect of groundwater pH and ionic strength on strontium sorption in aquifer sediments: Implications for ⁹⁰Sr mobility at contaminated nuclear sites. *Appl. Geochemistry* **27**, 1482–1491 (2012).
 239. Thorpe, C. L. *et al.* Strontium sorption and precipitation behaviour during bioreduction in nitrate impacted sediments. *Chem. Geol.* **306–307**, 114–122 (2012).
 240. Cleary, A. *et al.* Bioremediation of strontium and technetium contaminated groundwater using glycerol phosphate. *Chem. Geol.* **509**, 213–222 (2019).
 241. Bots, P. Emerging investigator series: a holistic approach to multicomponent EXAFS: Sr and Cs complexation in clayey soils. *Environ. Sci. Process. Impacts* **23**, (2021).
 242. Dyer, A. *et al.* The use of columns of the zeolite clinoptilolite in the remediation of aqueous nuclear waste streams. *J. Radioanal. Nucl. Chem.* **318**, 2473–2491 (2018).
 243. Dietz, M. L. & Jensen, M. P. EXAFS investigations of strontium complexation by a polymer-supported crown ether. *Talanta* **62**, 109–113 (2004).
 244. Wieland, E., Tits, J., Kunz, D. & Dähn, R. Strontium uptake by cementitious materials. *Environ. Sci. Technol.* **42**, 403–409 (2008).
 245. Sahai, N., Carroll, S. A., Roberts, S. & O'Day, P. A. X-ray absorption spectroscopy of strontium(II) coordination. II. Sorption and precipitation at kaolinite, amorphous silica, and goethite surfaces. *J. Colloid Interface Sci.* **222**, 198–212 (2000).
 246. Li, M., Liu, H., Chen, T., Dong, C. & Sun, Y. Science of the Total Environment Synthesis of magnetic biochar composites for enhanced uranium (VI) adsorption. *Sci. Total Environ.* **651**, 1020–1028 (2019).
 247. Hu, Q., Zhu, Y., Hu, B., Lu, S. & Sheng, G. Mechanistic insights into sequestration of U(VI) toward magnetic biochar: Batch, XPS and EXAFS techniques. *J. Environ. Sci. (China)* **70**, 217–225 (2018).
 248. Vorhauer-Huget, N., Altaf, H., Dürr, R., Tsotsas, E. & Vidaković-Koch, T.

- Computational optimization of porous structures for electrochemical processes. *Processes* **8**, (2020).
249. McGlashan, M. L. & Paul, M. A. Manual of Symbols and Terminology for Physicochemical Quantities and Units. *Pure Appl. Chem.* **51**, 1–41 (1973).
 250. Bates, R. G., Macaskill, J. B. & Bates, R. G. International Union of Pure and Applied Chemistry Standard Potential of the Silver-Silver Chloride Electrode. *Pure Appl. Chem.* **50**, 1701–1706 (1978).
 251. Zdravkov, B. D., Čermák, J. J., Šefara, M. & Janků, J. Pore classification in the characterization of porous materials: A perspective. *Cent. Eur. J. Chem.* **5**, 385–395 (2007).
 252. Mays, T. J. *A new classification of pore sizes. Studies in Surface Science and Catalysis* 160 (2007).
 253. Ouali, F. F. *et al.* Wetting considerations in capillary rise and imbibition in closed square tubes and open rectangular cross-section channels. *Microfluid. Nanofluidics* **15**, 309–326 (2013).
 254. Estela, M. C. C. B., Juliana, S., Matos, T. T. S. & Mayara, R. F. Effect of surface and porosity of biochar on water holding capacity aiming indirectly at preservation of the Amazon biome. *Sci Rep* 1–9 (2018)
 255. Hyväluoma, J. *et al.* Quantitative characterization of pore structure of several biochars with 3D imaging. *Environ. Sci. Pollut. Res.* **25**, 25648–25658 (2018).
 256. Jeong, G. Y. *et al.* Metal-organic framework patterns and membranes with heterogeneous pores for flow-assisted switchable separations. *Nat. Commun.* **9**, 1–9 (2018).
 257. Ma, X. *et al.* Adsorption performance and kinetic study of hierarchical porous Fe-based MOFs for toluene removal. *Sci. Total Environ.* **793**, 148622 (2021).
 258. Yin, L. *et al.* Rationally designed core-shell and yolk-shell magnetic titanate nanosheets for efficient U(VI) adsorption performance. *Environ. Pollut.* **238**, 725–738 (2018).
 259. Hartmann, M., Thommes, M. & Schwieger, W. Hierarchically-Ordered Zeolites: A Critical Assessment. *Adv. Mater. Interfaces* **8**, (2021).
 260. Li, J., Zan, Y., Zhang, Z., Dou, M. & Wang, F. Prussian blue nanocubes decorated on nitrogen-doped hierarchically porous carbon network for efficient sorption of radioactive cesium. *J. Hazard. Mater.* **385**, 121568 (2020).
 261. Cheng, P. *et al.* Hierarchically porous carbon by activation of shiitake mushroom for capacitive energy storage. *Carbon N. Y.* **93**, 315–324 (2015).
 262. Luan, Y., Xue, Y. W. & Shi, Z. G. Synthesis of hierarchically macro/meso/microporous carbon spheres and its application in fast rechargeable electric double layer capacitor. *Mater. Lett.* **88**, 30–32 (2012).

263. Liu, H. *et al.* 3D hierarchical porous-structured biochar aerogel for rapid and efficient phenicol antibiotics removal from water. *Chem. Eng. J.* **368**, 639–648 (2019).
264. Yang, F. *et al.* Porous biochar composite assembled with ternary needle-like iron-manganese-sulphur hybrids for high-efficiency lead removal. *Bioresour. Technol.* **272**, 415–420 (2019).
265. Li, J., Zan, Y., Zhang, Z., Dou, M. & Wang, F. Prussian blue nanocubes decorated on nitrogen-doped hierarchically porous carbon network for efficient sorption of radioactive cesium. *J. Hazard. Mater.* **385**, 121568 (2020).
266. Wu, X., Zhu, Y., Huang, Q. & Huang, Z. Facile synthesis of magnetic hierarchical porous carbon and the adsorption properties. *Mater. Charact.* **193**, 112273 (2022).
267. Lehmann, J. *et al.* Biochar effects on soil biota - A review. *Soil Biol. Biochem.* **43**, 1812–1836 (2011).
268. Gul, S., Whalen, J. K., Thomas, B. W., Sachdeva, V. & Deng, H. Physico-chemical properties and microbial responses in biochar-amended soils: Mechanisms and future directions. *Agric. Ecosyst. Environ.* **206**, 46–59 (2015).
269. Ivanets, A. I., Kuznetsova, T. F. & Prozorovich, V. G. Sol – Gel Synthesis and Adsorption Properties of Mesoporous Manganese Oxide. *Russ. J. Phys. Chem* **89**, 481–486 (2015).
270. Lee, S. *et al.* Development of Meso- and Macro-Pore Carbonization Technology from Biochar in Treating the Stumps of Representative Trees in Taiwan. *Sustainability* **14**, (2022).
271. Eftekhari, A. & Fan, Z. Ordered mesoporous carbon and its applications for electrochemical energy storage and conversion. *Mater. Chem. Front.* **1**, 1001–1027 (2017).
272. Eftekhari, A. Ordered mesoporous materials for lithium-ion batteries. *Microporous Mesoporous Mater.* **243**, 355–369 (2017).
273. Li, W., Liu, J. & Zhao, D. Mesoporous materials for energy conversion and storage devices. *Nat. Rev. Mater.* **1**, 16023 (2016).
274. Katiyar, A., Yadav, S., Smirniotis, P. G. & Pinto, N. G. Synthesis of ordered large pore SBA-15 spherical particles for adsorption of biomolecules. *J. Chromatogr. A* **1122**, 13–20 (2006).
275. Nagy, B., Villar-Rodil, S., Tascón, J. M. D., Bakos, I. & László, K. Nitrogen doped mesoporous carbon aerogels and implications for electrocatalytic oxygen reduction reactions. *Microporous Mesoporous Mater.* **230**, 135–144 (2016).
276. Dong, Y. *et al.* Synthesis of mesoporous carbon fibers with a high adsorption capacity for bulky dye molecules. *J. Mater. Chem. A* **1**, 7391–7398 (2013).
277. Mishra, S., Dwivedi, J. & Sankararamkrishnan, N. Studies on salophen anchored micro / meso porous activated carbon fibres for the removal and

- recovery of uranium. *RSC Adv.* **42** 33023–33036 (2015)
278. Dolatyari, L., Reza, M. & Rostamnia, S. Removal of uranium (VI) ions from aqueous solutions using Schiff base functionalized SBA-15 mesoporous silica materials. *J. Environ. Manage.* **169**, 8–17 (2016).
 279. Shi, J., Wang, J., Wang, W., Teng, W. & Zhang, W. xian. Stabilization of nanoscale zero-valent iron in water with mesoporous carbon (nZVI@MC). *J. Environ. Sci. (China)* **81**, 28–33 (2019).
 280. Carrott, R. Pore size control in activated carbons obtained by pyrolysis under different conditions of chemically impregnated cork. *J. of Analytical and Applied Pyrolysis* **75**, 120–127 (2006).
 281. Clennell, M. Ben. Tortuosity: a guide through the maze. *Geol. Soc. London, Spec. Publ.* **122**, 299 LP – 344 (1997).
 282. Gao, X., Diniz da Costa, J. C. & Bhatia, S. K. Understanding the diffusional tortuosity of porous materials: An effective medium theory perspective. *Chem. Eng. Sci.* **110**, 55–71 (2014).
 283. Hung, H. W. & Lin, T. F. Adsorption of MTBE from contaminated water by carbonaceous resins and mordenite zeolite. *J. Hazard. Mater.* **135**, 210–217 (2006).
 284. Tiab, D. & Donaldson, E. C. Chapter 3 - Porosity and Permeability. *Petrophysics (Fourth Ed.)* 67–186 (2016).
 285. Schneider, C. A., Rasband, W. S. & Eliceiri, K. W. NIH Image to ImageJ: 25 years of image analysis. *Nat. Methods* **9**, 671–675 (2012).
 286. Schwieger, W. *et al.* Hierarchy concepts: Classification and preparation strategies for zeolite containing materials with hierarchical porosity. *Chem. Soc. Rev.* **45**, 3353–3376 (2016).
 287. Kerstens, D. *et al.* State of the Art and Perspectives of Hierarchical Zeolites: Practical Overview of Synthesis Methods and Use in Catalysis. *Adv. Mater.* **32**, 1–47 (2020).
 288. Mikhaylin, S. & Bazinet, L. Fouling on ion-exchange membranes: Classification, characterization and strategies of prevention and control. *Adv. Colloid Interface Sci.* **229**, 34–56 (2016).
 289. Bennett, T. D., Coudert, F. X., James, S. L. & Cooper, A. I. The changing state of porous materials. *Nat. Mater.* **20**, 1179–1187 (2021).
 290. Abednatanzi, S. *et al.* Mixed-metal metal-organic frameworks. *Chem. Soc. Rev.* **48**, 2535–2565 (2019).
 291. Neverov, V. D., Lukyanov, A. E., Krasavin, A. V, Vagov, A. & Croitoru, M. D. Correlated disorder as a way towards robust superconductivity. *Commun. Phys.* **5**, 177 (2022).
 292. Simonov, A. & Goodwin, A. L. Designing disorder into crystalline materials. *Nat. Rev. Chem.* **4**, 657–673 (2020).
 293. Li, Z. *et al.* Engineered disorder in CO₂ photocatalysis. *Nat. Commun.* **13**, 7205 (2022).
 294. Chaney, D. *et al.* Tuneable correlated disorder in alloys. *Phys. Rev.*

- Mater.* **5**, 35004 (2021).
295. Brewer, C. E. *et al.* New approaches to measuring biochar density and porosity. *Biomass and Bioenergy* **66**, 176–185 (2014).
 296. Thomas, B. & Alexander, L. K. Enhanced synergetic effect of Cr(VI) ion removal and anionic dye degradation with superparamagnetic cobalt ferrite meso–macroporous nanospheres. *Appl. Nanosci.* **8**, 125–135 (2018).
 297. Li, M., Li, X., Jiang, G. & He, G. Hierarchically macro-mesoporous ZrO₂-TiO₂ composites with enhanced photocatalytic activity. *Ceram. Int.* **41**, 5749–5757 (2015).
 298. Qiu, Z. *et al.* Biochar-based carbons with hierarchical micro-meso-macro porosity for high rate and long cycle life supercapacitors. *J. Power Sources* **376**, 82–90 (2018).
 299. Feng, H. *et al.* Hierarchical structured carbon derived from bagasse wastes: A simple and efficient synthesis route and its improved electrochemical properties for high-performance supercapacitors. *J. Power Sources* **302**, 164–173 (2016).
 300. Caguiat, J. N., Arpino, G., Krigstin, S. G., Kirk, D. W. & Jia, C. Q. Dependence of supercapacitor performance on macro-structure of monolithic biochar electrodes. *Biomass and Bioenergy* **118**, 126–132 (2018).
 301. Liu, H. *et al.* Nitrogen-rich hierarchical porous polyphosphazene for rapid and efficient adsorption of anionic contaminants: Kinetics, isotherm, thermodynamics and mechanism. *Appl. Surf. Sci.* **616**, 156538 (2023).
 302. Wang, Y. *et al.* Biofouling-resistant polyamidoxime-based natural hierarchical porous bamboo strips prepared by in-situ polymerization for uranium extraction from seawater. *J. Environ. Chem. Eng.* **11**, 109277 (2023).
 303. Jiang, Y., Tan, P., Liu, X.-Q. & Sun, L.-B. Process-Oriented Smart Adsorbents: Tailoring the Properties Dynamically as Demanded by Adsorption/Desorption. *Acc. Chem. Res.* **55**, 75–86 (2022).
 304. Hou, Z. *et al.* Hierarchically porous carbon derived from pore remodeling of waste polymeric membranes for high-efficiency adsorption applications. *Resour. Conserv. Recycl.* **190**, 106845 (2023).
 305. Liu, H. *et al.* A sustainable one-step strategy for highly graphitized capacitive carbons with hierarchical micro-meso-macro porosity. *Nanoscale Adv.* **4**, 1394–1407 (2022).
 306. Edeh, I. G. & Mašek, O. The role of biochar particle size and hydrophobicity in improving soil hydraulic properties. *Eur. J. Soil Sci.* **73**, 1–14 (2022).
 307. Mašek, O. *et al.* Consistency of biochar properties over time and production scales: A characterisation of standard materials. *J. Anal. Appl. Pyrolysis* **132**, 200–210 (2018).
 308. Liao, W. & Thomas, S. C. Biochar Particle Size and Post-Pyrolysis

- Mechanical Processing Affect Soil pH, Water Retention Capacity, and Plant Performance. *Soil Systems* vol. 3 (2019).
309. de Jesus Duarte, S., Glaser, B. & Pellegrino Cerri, C. E. Effect of Biochar Particle Size on Physical, Hydrological and Chemical Properties of Loamy and Sandy Tropical Soils. *Agronomy* vol. 9 (2019).
 310. Liu, Z., Dugan, B., Masiello, C. A. & Gonnermann, H. M. Biochar particle size, shape, and porosity act together to influence soil water properties. *Plos one* **12** (2017).
 311. Bello, A. *et al.* Biochar reduces nutrient loss and improves microbial biomass of composted cattle manure and maize straw. *Biotechnol. Appl. Biochem.* **67**, 799–811 (2020).
 312. Rosales, E., Mejjide, J., Pazos, M. & Sanromán, M. A. Challenges and recent advances in biochar as low-cost biosorbent: From batch assays to continuous-flow systems. *Bioresour. Technol.* **246**, 176–192 (2017).
 313. Kolliopoulos, P. & Kumar, S. Capillary flow of liquids in open microchannels: overview and recent advances. *npj Microgravity* **7**, 35–37 (2021).
 314. Cai, J. *et al.* Lucas-Washburn Equation-Based Modeling of Capillary-Driven Flow in Porous Systems. *Langmuir* **37**, 1623–1636 (2021).
 315. Palakurthi, N. K., Konangi, S., Ghia, U. & Comer, K. Micro-scale simulation of unidirectional capillary transport of wetting liquid through 3D fibrous porous media: Estimation of effective pore radii. *Int. J. Multiph. Flow* **77**, 48–57 (2015).
 316. Gang, D., Uddin Ahmad, Z., Lian, Q., Yao, L. & Zappi, M. E. A review of adsorptive remediation of environmental pollutants from aqueous phase by ordered mesoporous carbon. *Chem. Eng. J.* **403**, 126286 (2021).
 317. Sekhon, S. S., Kaur, P. & Park, J. S. From coconut shell biomass to oxygen reduction reaction catalyst: Tuning porosity and nitrogen doping. *Renew. Sustain. Energy Rev.* **147**, 111173 (2021).
 318. Zhang, J., Zhang, X., Tian, Y., Zhong, T. & Liu, F. Novel and wet-resilient cellulose nanofiber cryogels with tunable porosity and improved mechanical strength for methyl orange dyes removal. *J. Hazard. Mater.* **416**, 125897 (2021).
 319. Wang, Q. *et al.* Honeycomb-like carbon with tunable pore size from bio-oil for supercapacitor. *Microporous Mesoporous Mater.* **309**, 110551 (2020).
 320. Huang, J. F. *et al.* Floatable, macroporous structured alginate sphere supporting iron nanoparticles used for emergent Cr(VI) spill treatment. *Carbohydr. Polym.* **146**, 115–122 (2016).
 321. Brunauer, S., Emmett, P. H. & Teller, E. Adsorption of Gases in Multimolecular Layers. *J. Am. Chem. Soc.* **60**, 309–319 (1938).
 322. Donato, I. D. & Lazzara, G. Porosity determination with helium pycnometry as a method to characterize waterlogged woods and the efficacy of the conservation treatments. *Archaeometry* **54**, 906–915 (2012).

323. Blankenship, L. S., Jagiello, J. & Mokaya, R. Confirmation of pore formation mechanisms in biochars and activated carbons by dual isotherm analysis. *Mater. Adv.* 3961–3971 (2022)
324. Pizzanelli, S. *et al.* The Effect of Activation on the Structure of Biochars Prepared from Wood and from *Posidonia Oceanica*: A Spectroscopic Study. *Physchem* **2**, 286–304 (2022).
325. Giesche, H. Mercury porosimetry: A general (practical) overview. *Part. Part. Syst. Charact.* **23**, 9–19 (2006).
326. Hu, X., Mangano, E., Friedrich, D., Ahn, H. & Brandani, S. Diffusion mechanism of CO₂ in 13X zeolite beads. *Adsorption* **20**, 121–135 (2014).
327. Illingworth, J., Williams, P. T. & Rand, B. Characterisation of biochar porosity from pyrolysis of biomass flax fibre. *J. Energy Inst.* **86**, 63–70 (2013).
328. Wu, X., Zhu, Y., Pei, B., Cai, P. & Huang, Z. Effect of FeCl₂ on the pore structure of porous carbon obtained from phenol formaldehyde resin and ethylene glycol. *Mater. Lett.* **215**, 50–52 (2018).
329. Jones, K., Ramakrishnan, G., Uchimiya, M. & Orlov, A. New applications of X-ray tomography in pyrolysis of biomass: Biochar imaging. *Energy and Fuels* **29**, 1628–1634 (2015).
330. Jeffery, S. *et al.* Biochar application does not improve the soil hydrological function of a sandy soil. *Geoderma* **251–252**, 47–54 (2015).
331. Quin, P. R. *et al.* Oil mallee biochar improves soil structural properties — A study with X-ray micro-CT. *Agric. Ecosyst. Environ.* **191**, 142–149 (2014).
332. Basyigit, C., Akkurt, I., Kilincarslan, S. & Akkurt, A. Investigation of photon attenuation coefficients for marble. *J. Radiol. Prot.* **25**, 189–192 (2005).
333. Barr, M. R. *et al.* Towards a mechanistic understanding of particle shrinkage during biomass pyrolysis via synchrotron X-ray microtomography and in-situ radiography. *Sci. Rep.* **11**, 1–13 (2021).
334. Zhu, K., Song, G., Ren, X. & Chen, C. Solvent-free engineering of Fe₀/Fe₃C nanoparticles encased in nitrogen-doped carbon nanoshell materials for highly efficient removal of uranyl ions from acidic solution. *J. Colloid Interface Sci.* **575**, 16–23 (2020).
335. Jang, S., Kang, S., Haldorai, Y. & Giribabu, K. Synergistically strengthened 3D micro-scavenger cage adsorbent for selective removal of radioactive cesium. *Nat. Publ. Gr.* 1–12 (2016)
336. Zhang, Q. *et al.* Synthesis of nanoscale zero-valent iron loaded chitosan for synergistically enhanced removal of U(VI) based on adsorption and reduction. *J. Colloid Interface Sci.* **552**, 735–743 (2019).
337. Dickinson, M. & Scott, T. B. The application of zero-valent iron nanoparticles for the remediation of a uranium-contaminated waste effluent. *J. Hazard. Mater.* **178**, 171–179 (2010).
338. Yu, S. *et al.* Efficient removal of uranium(VI) by layered double hydroxides supported nanoscale zero-valent iron: A combined experimental and

- spectroscopic studies. *Chem. Eng. J.* **365**, 51–59 (2019).
339. Cantrell, K. J., Kaplan, D. I. & Wietsma, T. W. Zero-valent iron for the in situ remediation of selected metals in groundwater. *J. Hazard. Mater.* **42**, 201–212 (1995).
 340. Ma, Y. *et al.* Factors influencing the reduction of U(VI) by magnetite. *Chemosphere* **254**, (2020).
 341. Kikuchi, S., Kashiwabara, T. & Shibuya, T. Molecular-scale insights into differences in the adsorption of cesium and selenium on biogenic and abiogenic ferrihydrite. *Geochim. Cosmochim. Acta* **251**, 1–14 (2019).
 342. Tang, C. *et al.* Rapid removal of selenate in a zero-valent iron/Fe₃O₄/Fe²⁺ synergetic system. *Appl. Catal. B Environ.* **184**, 320–327 (2016).
 343. Coutelot, F., Thomas, R. J. & Seaman, J. C. Using porous iron composite (PIC) material to immobilize rhenium as an analogue for technetium. *Environ. Int.* **128**, 379–389 (2019).
 344. Boglaienko, D., Emerson, H. P., Katsenovich, Y. P. & Levitskaia, T. G. Comparative analysis of ZVI materials for reductive separation of ⁹⁹Tc(VII) from aqueous waste streams. *J. Hazard. Mater.* **380**, 120836 (2019).
 345. Emerson, H. P. *et al.* Impact of zero valent iron aging on reductive removal of technetium-99. *J. Environ. Chem. Eng.* **8**, 103767 (2020).
 346. Liu, C. H., Shih, Y. J., Huang, Y. H. & Huang, C. P. Kinetic and thermodynamic studies for adsorptive removal of Sr²⁺ using waste iron oxide. *J. Taiwan Inst. Chem. Eng.* **45**, 914–920 (2014).
 347. Balek, V., Málek, Z., Šubrt, J. & Ždimera, A. Characterization of iron(III) oxide and oxide-hydroxide as Sr-sorbent. *J. Radioanal. Nucl. Chem.* **212**, 321–331 (1996).
 348. Wang, Z., Wu, Z., Wang, M., An, X. & Li, H. Continuous separation and recovery of caesium by electromagnetic coupling regeneration process with an electroactive magnetic Fe₃O₄@cupric hexacyanoferrate. *J. Appl. Electrochem.* **48**, 49–60 (2018).
 349. Devi, P. & Saroha, A. K. Simultaneous adsorption and dechlorination of pentachlorophenol from effluent by Ni-ZVI magnetic biochar composites synthesized from paper mill sludge. *Chem. Eng. J.* **271**, 195–203 (2015).
 350. Li, Z. *et al.* Biochar-supported nanoscale zero-valent iron as an efficient catalyst for organic degradation in groundwater. *J. Hazard. Mater.* **383**, 121240 (2020).
 351. Su, Y. fan, Cheng, Y. ling & Shih, Y. hsin. Removal of trichloroethylene by zerovalent iron/activated carbon derived from agricultural wastes. *J. Environ. Manage.* **129**, 361–366 (2013).
 352. Chanthapon, N., Sarkar, S., Kidkhunthod, P. & Padungthon, S. Lead removal by a reusable gel cation exchange resin containing nano-scale zero valent iron. *Chem. Eng. J.* **331**, 545–555 (2018).
 353. Bae, S., Gim, S., Kim, H. & Hanna, K. Effect of NaBH₄ on properties of

- nanoscale zero-valent iron and its catalytic activity for reduction of p-nitrophenol. *Appl. Catal. B Environ.* **182**, 541–549 (2016).
354. Zhu, K. & Chen, C. *Application of nZVI and its composites into the treatment of toxic/radioactive metal ions. Interface Science and Technology* vol. 29 (2019).
 355. Ling, L., Huang, X. Y. & Zhang, W. X. Enrichment of Precious Metals from Wastewater with Core–Shell Nanoparticles of Iron. *Adv. Mater.* **30**, 1–6 (2018).
 356. Pang, H. *et al.* Adsorptive and reductive removal of U(VI) by Dictyophora indusiata-derived biochar supported sulfide NZVI from wastewater. *Chem. Eng. J.* **366**, 368–377 (2019).
 357. Lawrinenko, M., Laird, D. A. & Van Leeuwen, J. H. Sustainable Pyrolytic Production of Zerovalent Iron. *ACS Sustain. Chem. Eng.* **5**, 767–773 (2017).
 358. Li, Z. J. *et al.* Efficient removal of uranium from aqueous solution by zero-valent iron nanoparticle and its graphene composite. *J. Hazard. Mater.* **290**, 26–33 (2015).
 359. Chen, A., Shang, C., Shao, J., Zhang, J. & Huang, H. The application of iron-based technologies in uranium remediation: A review. *Sci. Total Environ.* **575**, 1291–1306 (2017).
 360. Dong, H. & Lo, I. M. C. Influence of humic acid on the colloidal stability of surface-modified nano zero-valent iron. *Water Res.* **47**, 419–427 (2013).
 361. Wang, P., Tang, L., Wei, X., Zeng, G. & Zhou, Y. Applied Surface Science Synthesis and application of iron and zinc doped biochar for removal of p-nitrophenol in wastewater and assessment of the influence of co-existed Pb (II). *Appl. Surf. Sci.* **392**, 391–401 (2017).
 362. Shi, M. *et al.* Recent progress in understanding the mechanism of heavy metals retention by iron (oxyhydr)oxides. *Sci. Total Environ.* **752**, 141930 (2021).
 363. Jung, K. W., Choi, B. H., Jeong, T. U. & Ahn, K. H. Facile synthesis of magnetic biochar/Fe₃O₄ nanocomposites using electro-magnetization technique and its application on the removal of acid orange 7 from aqueous media. *Bioresour. Technol.* **220**, 672–676 (2016).
 364. Zhu, K. *et al.* In situ carbothermal reduction synthesis of Fe nanocrystals embedded into N-doped carbon nanospheres for highly efficient U(VI) adsorption and reduction. *Chem. Eng. J.* **331**, 395–405 (2018).
 365. Shang, H., Wang, Q., Ok, Y. S., Zhang, S. & Zhu, X. Magnetic biochar production alters the molecular characteristics and biological response of pyrolysis volatile-derived water-soluble organic matter. *Sci. Total Environ.* **778**, 146142 (2021).
 366. Massart, R. Preparation of aqueous magnetic liquids in alkaline and acidic media. *IEEE Trans. Magn.* **17**, 1247–1248 (1981).
 367. Roth, H. C., Schwaminger, S. P., Schindler, M., Wagner, F. E. & Berensmeier, S. Influencing factors in the CO-precipitation process of

- superparamagnetic iron oxide nano particles: A model based study. *J. Magn. Mater.* **377**, 81–89 (2015).
368. Zemska, L., Egorin, A., Tokar, E., Ivanov, V. & Bratskaya, S. New chitosan/iron oxide composites: Fabrication and application for removal of Sr²⁺ radionuclide from aqueous solutions. *Biomimetics* **3**, 1–10 (2018).
369. Asai, M. *et al.* Effects of the variation of metal substitution and electrolyte on the electrochemical reaction of metal hexacyanoferrates. *RSC Adv.* **8**, 37356–37364 (2018).
370. Chem, J. M. Large Cs adsorption capability of nanostructured Prussian Blue particles with high accessible surface areas. 18261–18267 (2012)
371. Bok-Badura, J., Jakóbk-Kolon, A., Kazek-Kesik, A. & Karoń, K. Hybrid pectin-based sorbents for cesium ion removal. *Materials (Basel)*. **13**, (2020).
372. Alby, D., Charnay, C., Heran, M., Prelot, B. & Zajac, J. Recent developments in nanostructured inorganic materials for sorption of cesium and strontium: Synthesis and shaping, sorption capacity, mechanisms, and selectivity—A review. *J. Hazard. Mater.* **344**, 511–530 (2018).
373. Liu, S. *et al.* Mineral-ions modified biochars enhance the stability of soil aggregate and soil carbon sequestration in a coastal wetland soil. *Catena* **193**, 104618 (2020).
374. Li, Z. *et al.* Biochar-supported nanoscale zero-valent iron as an efficient catalyst for organic degradation in groundwater. *J. Hazard. Mater.* **383**, 121240 (2020).
375. Zhang, H., Xue, G., Chen, H. & Li, X. Magnetic biochar catalyst derived from biological sludge and ferric sludge using hydrothermal carbonization: Preparation, characterization and its circulation in Fenton process for dyeing wastewater treatment. *Chemosphere* **191**, 64–71 (2018).
376. Baig, S. A., Zhu, J., Muhammad, N., Sheng, T. & Xu, X. Effect of synthesis methods on magnetic Kans grass biochar for enhanced As(III, V) adsorption from aqueous solutions. *Biomass and Bioenergy* **71**, 299–310 (2014).
377. Hoch, L. B. *et al.* Carbothermal synthesis of carbon-supported nanoscale zero-valent iron particles for the remediation of hexavalent chromium. *Environ. Sci. Technol.* **42**, 2600–2605 (2008).
378. Tao, Q. *et al.* Copper hexacyanoferrate nanoparticle-decorated biochar produced from pomelo peel for cesium removal from aqueous solution. *J. Radioanal. Nucl. Chem.* **322**, 791–799 (2019).
379. Kong, L. *et al.* Simultaneous reduction and adsorption for immobilization of uranium from aqueous solution by nano-flake Fe-SC. *J. Hazard. Mater.* **320**, 435–441 (2016).
380. Lu, J. *et al.* Iron-montmorillonite treated corn straw biochar: Interfacial chemical behavior and stability. *Sci. Total Environ.* **708**, 134773 (2020).
381. Hu, B. *et al.* Decontamination of U(VI) from nZVI/CNF composites investigated by batch, spectroscopic and modeling techniques. *J. Mol.*

- Liq.* **237**, 1–9 (2017).
382. Fu, F., Dionysiou, D. D. & Liu, H. The use of zero-valent iron for groundwater remediation and wastewater treatment: A review. *J. Hazard. Mater.* **267**, 194–205 (2014).
 383. Klüpfel, L., Keiluweit, M., Kleber, M. & Sander, M. Redox properties of plant biomass-derived black carbon (biochar). *Environ. Sci. Technol.* **48**, 5601–5611 (2014).
 384. Kappler, A. *et al.* Biochar as an Electron Shuttle between Bacteria and Fe(III) Minerals. *Environ. Sci. Technol. Lett.* **1**, 339–344 (2014).
 385. Chen, Z. *et al.* Preparation of nano-Fe₀ modified coal fly-ash composite and its application for U(VI) sequestration. *J. Mol. Liq.* **266**, 824–833 (2018).
 386. Liu, D., Liu, Z., Wang, C. & Lai, Y. Removal of uranium (VI) from aqueous solution using nanoscale zero-valent iron supported on activated charcoal. *J. Radioanal. Nucl. Chem.* **310**, 1131–1137 (2016).
 387. Lv, Z. *et al.* Nanoscale zero-valent iron/magnetite carbon composites for highly efficient immobilization of U(VI). *J. Environ. Sci. (China)* **76**, 377–387 (2019).
 388. Abasolo, W. P., Yoshida, M., Yamamoto, H. & Okuyama, T. Silica in Several Rattan Species. **55**, 595–600 (2001).
 389. Chongtham, N., Bisht, M. S., Santosh, O., Bajwa, H. K. & Indira, A. Mineral elements in Bamboo shoots and Potential role in Food Fortification. *J. Food Compos. Anal.* **95**, 103662 (2021).
 390. Silviana, S. & Bayu, W. J. Silicon Conversion from Bamboo Leaf Silica by Magnesiothermic Reduction for Development of Li-ion Battery Anode. *MATEC Web Conf.* **156**, 0–3 (2018).
 391. PrévotEAU, A., Ronsse, F., Cid, I., Boeckx, P. & Rabaey, K. The electron donating capacity of biochar is dramatically underestimated. *Sci. Rep.* **6**, 1–11 (2016).
 392. Zhang, H. *et al.* Carbothermal reduction for preparing nZVI / BC to extract uranium : Insight into the iron species dependent uranium adsorption behavior. *J. Clean. Prod.* **239**, 117873 (2019).
 393. Hu, X. *et al.* Effects of biomass pre-pyrolysis and pyrolysis temperature on magnetic biochar properties. *J. Anal. Appl. Pyrolysis* **127**, 196–202 (2017).
 394. Vincent, C. *et al.* Chitin-Prussian blue sponges for Cs(I) recovery: From synthesis to application in the treatment of accidental dumping of metal-bearing solutions. *J. Hazard. Mater.* **287**, 171–179 (2015).
 395. Mergen, Ö. B., Arda, E. & Evingür, G. A. Electrical, optical and mechanical properties of chitosan biocomposites. *J. Compos. Mater.* **54**, 1497–1510 (2019).
 396. Zhou, L., Shang, C., Liu, Z., Huang, G. & Adesina, A. A. Selective adsorption of uranium(VI) from aqueous solutions using the ion-imprinted magnetic chitosan resins. *J. Colloid Interface Sci.* **366**, 165–172 (2012).

397. Liang, L. *et al.* Stereoscopic porous gellan gum-based microspheres as high performance adsorbents for U(VI) removal. *J. Radioanal. Nucl. Chem.* **319**, 213–225 (2019).
398. Hamza, M. F. *et al.* Functionalization of magnetic chitosan particles for the sorption of U(VI), Cu(II) and Zn(II)-hydrazide derivative of glycine-grafted chitosan. *Materials (Basel)*. **10**, (2017).
399. Shehzad, H. *et al.* Effective adsorption of U(VI) from aqueous solution using magnetic chitosan nanoparticles grafted with maleic anhydride: equilibrium, kinetic and thermodynamic studies. *J. Radioanal. Nucl. Chem.* **315**, 195–206 (2018).
400. Vipin, A. K., Ling, S. & Fugetsu, B. Sodium cobalt hexacyanoferrate encapsulated in alginate vesicle with CNT for both cesium and strontium removal. *Carbohydr. Polym.* **111**, 477–484 (2014).
401. Yang, H. M., Park, C. W. & Lee, K. W. Enhanced surface decontamination of radioactive Cs by self-generated, strippable hydrogels based on reversible cross-linking. *J. Hazard. Mater.* **362**, 72–81 (2019).
402. Fuks, L. Improvement of the novel method for decontamination of the radioactive aqueous solutions. *Environ. Technol. Innov.* **12**, 286–292 (2018).
403. Liao, H. *et al.* Nano-zero-valent Fe/Ni particles loaded on collagen fibers immobilized by bayberry tannin as an effective reductant for uranyl in aqueous solutions. *Appl. Surf. Sci.* **507**, 145075 (2020).
404. Hu, Q., Zhu, Y., Hu, B., Lu, S. & Sheng, G. ScienceDirect Mechanistic insights into sequestration of U (VI) toward magnetic biochar : Batch , XPS and EXAFS techniques. *J. Environ. Sci.* **70**, 217–225 (2018).
405. Pang, H. *et al.* Precursor impact and mechanism analysis of uranium elimination by biochar supported sulfurized nanoscale zero-valent iron. *J. Environ. Chem. Eng.* **10**, 107288 (2022).
406. Yuan, Y. *et al.* Applications of biochar in redox-mediated reactions. *Bioresour. Technol.* **246**, 271–281 (2017).
407. Yenier, Z. *et al.* Manufacturing and mechanical, thermal and electrical characterization of graphene loaded chitosan composites. *Compos. Part B Eng.* **98**, 281–287 (2016).
408. Zhang, Q. *et al.* Active biochar support nano zero-valent iron for efficient removal of U(VI) from sewage water. *J. Alloys Compd.* **852**, 156993 (2021).
409. Hritcu, D., Humelnicu, D., Dodi, G. & Popa, M. I. Magnetic chitosan composite particles: Evaluation of thorium and uranyl ion adsorption from aqueous solutions. *Carbohydr. Polym.* **87**, 1185–1191 (2012).
410. Chen, Y. & Wang, J. Removal of radionuclide Sr²⁺ ions from aqueous solution using synthesized magnetic chitosan beads. *Nucl. Eng. Des.* **242**, 445–451 (2012).
411. Li, M., Liu, H., Chen, T., Dong, C. & Sun, Y. Synthesis of magnetic biochar composites for enhanced uranium (VI) adsorption. *Sci. Total*

- Environ.* **651**, 1020–1028 (2019).
412. Wang, B. *et al.* Efficient removal of U(VI) from aqueous solutions using the magnetic biochar derived from the biomass of a bloom-forming cyanobacterium (*Microcystis aeruginosa*). *Chemosphere* **254**, 126898 (2020).
413. Hu, X., Ding, Z., Zimmerman, A. R., Wang, S. & Gao, B. Batch and column sorption of arsenic onto iron-impregnated biochar synthesized through hydrolysis. *Water Res.* **68**, 206–216 (2015).
414. Frišták, V., Micháleková, B. & Eva, R. Sorption separation of Eu and As from single - component systems by Fe - modified biochar : kinetic and equilibrium study. *J. Iranian Chemical Society* 521–530 (2017)
415. Rawal, A. *et al.* Mineral – Biochar Composites: Molecular Structure and Porosity. *Environmental Science and Technology* **50** 14 (2016)
416. Wang, S., Guo, W., Gao, F., Wang, Y. & Gao, Y. Lead and uranium sorptive removal from aqueous solution using magnetic and nonmagnetic fast pyrolysis rice husk biochars. *RSC Adv.* **8**, 13205–13217 (2018).
417. Philippou, K., Anastopoulos, I., Dosche, C. & Pashalidis, I. Synthesis and characterization of a novel Fe₃O₄-loaded oxidized biochar from pine needles and its application for uranium removal. Kinetic, thermodynamic, and mechanistic analysis. *J. Environ. Manage.* **252**, 109677 (2019).
418. Ahmed, W. *et al.* Utilization of *Citrullus lanatus* L. seeds to synthesize a novel MnFe₂O₄-biochar adsorbent for the removal of U(VI) from wastewater: Insights and comparison between modified and raw biochar. *Sci. Total Environ.* **771**, 144955 (2021).
419. Hamza, M. F. *et al.* Uranium(VI) and zirconium(IV) sorption on magnetic chitosan derivatives – effect of different functional groups on separation properties. *J. Chem. Technol. Biotechnol.* **94**, 3866–3882 (2019).
420. Hamza, M. F., Roux, J. C. & Guibal, E. Uranium and europium sorption on amidoxime-functionalized magnetic chitosan micro-particles. *Chem. Eng. J.* **344**, 124–137 (2018).
421. Wang, J. S., Peng, R. T., Yang, J. H., Liu, Y. C. & Hu, X. J. Preparation of ethylenediamine-modified magnetic chitosan complex for adsorption of uranyl ions. *Carbohydr. Polym.* **84**, 1169–1175 (2011).
422. Hamza, M. F., Wei, Y., Benettayeb, A., Wang, X. & Guibal, E. Efficient removal of uranium, cadmium and mercury from aqueous solutions using grafted hydrazide-micro-magnetite chitosan derivative. *J. Mater. Sci.* **55**, 4193–4212 (2020).
423. Huang, Y. *et al.* Highly selective uranium adsorption on 2-phosphonobutane-1,2,4-tricarboxylic acid-decorated chitosan-coated magnetic silica nanoparticles. *Chem. Eng. J.* **388**, 124349 (2020).
424. Singhal, P., Jha, S. K., Pandey, S. P. & Neogy, S. Rapid extraction of uranium from sea water using Fe₃O₄ and humic acid coated Fe₃O₄ nanoparticles. *J. Hazard. Mater.* **335**, 152–161 (2017).

425. Chen, Z. *et al.* Synthesis of magnetic Fe₃O₄/CFA composites for the efficient removal of U(VI) from wastewater. *Chem. Eng. J.* **320**, 448–457 (2017).
426. Yuvaraja, G. *et al.* Removal of U(VI) from aqueous and polluted water solutions using magnetic *Arachis hypogaea* leaves powder impregnated into chitosan macromolecule. *Int. J. Biol. Macromol.* **148**, 887–897 (2020).
427. Galhoum, A. A., Mahfouz, M. G., Gomaa, N. M., Vincent, T. & Guibal, E. Chemical modifications of chitosan nano-based magnetic particles for enhanced uranyl sorption. *Hydrometallurgy* **168**, 127–134 (2017).
428. Liu, C. H., Shih, Y. J., Huang, Y. H. & Huang, C. P. Kinetic and thermodynamic studies for adsorptive removal of Sr²⁺ using waste iron oxide. *J. Taiwan Inst. Chem. Eng.* **45**, 914–920 (2014).
429. Balek, V., Malek, Z., Subrt, J. & Zdimera, A. Characterisation of iron(III) oxide and oxide-hydroxide as Sr-sorbent. *J. Nucl. Chem. Lett.* **212**, 321–331 (1996).
430. Ji, Y. Q. *et al.* Biosorption of strontium ions by magnetically modified yeast cells. *Sep. Sci. Technol.* **45**, 1499–1504 (2010).
431. Egorin, A. *et al.* Composite magnetic sorbents based on iron oxides in different polymer matrices: Comparison and application for removal of strontium. *Biomimetics* **5**, (2020).
432. Yin, Y., Wang, J., Yang, X. & Li, W. Removal of Strontium Ions by Immobilized *Saccharomyces Cerevisiae* in Magnetic Chitosan Microspheres. *Nucl. Eng. Technol.* **49**, 172–177 (2017).
433. Lu, Y., Yu, J. & Cheng, S. Magnetic composite of Fe₃O₄ and activated carbon as a adsorbent for separation of trace Sr(II) from radioactive wastewater. *J. Radioanal. Nucl. Chem.* **303**, 2371–2377 (2015).
434. Hong, H. J. *et al.* Highly stable and magnetically separable alginate/Fe₃O₄ composite for the removal of strontium (Sr) from seawater. *Chemosphere* **165**, 231–238 (2016).
435. Cheng, Z. *et al.* Preparation of magnetic Fe₃O₄ particles modified sawdust as the adsorbent to remove strontium ions. *Chem. Eng. J.* **209**, 451–457 (2012).
436. Xie, Y. *et al.* Emerging natural and tailored materials for uranium-contaminated water treatment and environmental remediation. *Prog. Mater. Sci.* **103**, 180–234 (2019).
437. Oszczak, A. & Fuks, L. Sorption of Sr-85 and Am-241 from liquid radioactive wastes by alginate beads. *Nukleonika* **60**, 927–931 (2015).
438. Ali, M. M. S., Sami, N. M. & El-Sayed, A. A. Removal of Cs⁺, Sr²⁺ and Co²⁺ by activated charcoal modified with Prussian blue nanoparticle (PBNP) from aqueous media: kinetics and equilibrium studies. *J. Radioanal. Nucl. Chem.* **324**, 189–201 (2020).
439. Choe, S. R. *et al.* Fabrication of alginate/humic acid/Fe-aminoclay hydrogel composed of a grafted-network for the efficient removal of strontium ions from aqueous solution. *Environ. Technol. Innov.* **9**, 285–

293 (2018).

440. Alby, D. *et al.* Microwave-assisted hydrothermal synthesis of manganate nanoflowers for selective retention of strontium. *J. Hazard. Mater.* **368**, 661–669 (2019).
441. Nguyen, H., You, S. & Hosseini-bandegharaei, A. Mistakes and inconsistencies regarding adsorption of contaminants from aqueous solutions : A critical review. *Water Res.* **120**, 88–116 (2017).
442. Xia, T., Yin, L., Xie, Y. & Ji, Y. Efficiently remove of Cs(I) by metals hexacyanoferrate modified magnetic Fe₃O₄-chitosan nanoparticles. *Chem. Phys. Lett.* **746**, (2020).
443. Tsai, C. J., Chang, Y. R., Chen, M. L., Lo, Y. K. & Lee, D. J. Stable poly(vinyl alcohol) and alginate cross-linked granules with immobilized ferric hexacyanoferrate for cesium removal from waters. *J. Taiwan Inst. Chem. Eng.* **95**, 1–10 (2019).
444. Vanderheyden, S. R. H., Yperman, J., Carleer, R. & Schreurs, S. Enhanced cesium removal from real matrices by nickel-hexacyanoferrate modified activated carbons. *Chemosphere* **202**, 569–575 (2018).
445. Parajuli, D. *et al.* Comparative study of the factors associated with the application of metal hexacyanoferrates for environmental Cs decontamination. *Chem. Eng. J.* **283**, 1322–1328 (2016).
446. Vincent, T., Vincent, C. & Guibal, E. Immobilization of metal hexacyanoferrate ion-exchangers for the synthesis of metal ion sorbents - A mini-review. *Molecules* **20**, 20582–20613 (2015).
447. Vipin, A. K., Hu, B. & Fugetsu, B. Prussian blue caged in alginate/calcium beads as adsorbents for removal of cesium ions from contaminated water. *J. Hazard. Mater.* **258–259**, 93–101 (2013).
448. Basu, H., Saha, S., Pimple, M. V. & Singhal, R. K. Graphene-prussian blue nanocomposite impregnated in alginate for efficient removal of cesium from aquatic environment. *J. Environ. Chem. Eng.* **6**, 4399–4407 (2018).
449. Mihara, Y. *et al.* Journal of Water Process Engineering Adsorption kinetic model of alginate gel beads synthesized micro particle-prussian blue to remove cesium ions from water. *J. Water Process Eng.* **10**, 9–19 (2016).
450. Lalmunsiama, Lalhriatpuia, C., Tiwari, D. & Lee, S. M. Immobilized nickel hexacyanoferrate on activated carbons for efficient attenuation of radio toxic Cs(I) from aqueous solutions. *Appl. Surf. Sci.* **321**, 275–282 (2014).
451. Adibmehr, M. & Faghihian, H. Magnetized Activated Carbon Prepared by Oak Shell Biowaste and Modified with Nickel Hexacyanoferrate for Selective Removal of Cesium. *J. Inorg. Organomet. Polym. Mater.* **29**, 1941–1955 (2019).
452. Chemical modification of biochar pore structure for enhanced adsorption. doi:10.1515/revce-2017-0113.
453. Park, J. H. *et al.* Sequential removal of radioactive Cs by electrochemical

- adsorption and desorption reaction using core-shell structured carbon nanofiber–Prussian blue composites. *Chem. Eng. J.* **399**, 125817 (2020).
454. Yamashita, A., Sasaki, T. & Tanaka, S. Electrochemical synthesis and immobilization of a beadwork-like Prussian Blue on carbon fiber and the removal of cesium. *J. Environ. Chem. Eng.* **5**, 2912–2920 (2017).
 455. Fujisaki, T., Kashima, K., Hagiri, M. & Imai, M. Isothermal Adsorption Behavior of Cesium Ions in a Novel Chitosan-Prussian Blue-Based Membrane. *Chem. Eng. Technol.* **42**, 910–917 (2019).
 456. Zemskova, L., Egorin, A., Tokar, E. & Ivanov, V. Chitosan-based biosorbents: immobilization of metal hexacyanoferrates and application for removal of cesium radionuclide from aqueous solutions. *J. Sol-Gel Sci. Technol.* **92**, 459–466 (2019).
 457. Li, T., He, F. & Dai, Y. D. Prussian blue analog caged in chitosan surface-decorated carbon nanotubes for removal cesium and strontium. *J. Radioanal. Nucl. Chem.* **310**, 1139–1145 (2016).
 458. Xia, T., Wu, H., Yin, L. & Ji, Y. Selective removal of cesium by ammonium molybdophosphate-magnetic Fe₃O₄-chitosan composites. *J. Mater. Res.* **36**, 2926–2935 (2021).
 459. Rethinasabapathy, M. *et al.* Highly stable Prussian blue nanoparticles containing graphene oxide–chitosan matrix for selective radioactive cesium removal. *Mater. Lett.* **241**, 194–197 (2019).
 460. Wang, K. *et al.* Hybrid porous magnetic bentonite-chitosan beads for selective removal of radioactive cesium in water. *J. Hazard. Mater.* **362**, 160–169 (2019).
 461. Çetin, B., Özcan, M. & Karakelle, B. Synthesis of modified nanocomposite material and its use on removal of cesium from aqueous media. *Turkish J. Chem.* **46**, 46–58 (2022).
 462. El-Din, A. M. S., Monir, T. & Sayed, M. A. Nano-sized Prussian blue immobilized costless agro-industrial waste for the removal of cesium-137 ions. *Environ. Sci. Pollut. Res.* **26**, 25550–25563 (2019).
 463. Kim, H. *et al.* Prussian blue immobilized cellulosic filter for the removal of aqueous cesium. *Sci. Total Environ.* **670**, 779–788 (2019).
 464. Kadam, A. A., Jang, J. & Lee, D. S. Facile synthesis of pectin-stabilized magnetic graphene oxide Prussian blue nanocomposites for selective cesium removal from aqueous solution. *Bioresour. Technol.* **216**, 391–398 (2016).
 465. Chang, S. *et al.* In situ green production of Prussian blue/natural porous framework nanocomposites for radioactive Cs⁺ removal. *J. Radioanal. Nucl. Chem.* **316**, 209–219 (2018).
 466. Lai, Y. C. *et al.* Poly(vinyl alcohol) and alginate cross-linked matrix with immobilized Prussian blue and ion exchange resin for cesium removal from waters. *Bioresour. Technol.* **214**, 192–198 (2016).
 467. Crane, R. A., Dickinson, M. & Scott, T. B. Nanoscale zero-valent iron particles for the remediation of plutonium and uranium contaminated

- solutions. *Chem. Eng. J.* **262**, 319–325 (2015).
468. Zhu, Y., Zheng, C., Wu, S., Song, Y. & Hu, B. Interaction of Eu (III) on magnetic biochar investigated by batch, spectroscopic and modeling techniques. *J. Radioanal. Nucl. Chem.* **316**, 1337–1346 (2018).
 469. Zhu, Y., Hu, J. & Wang, J. Removal of Co²⁺ from radioactive wastewater by polyvinyl alcohol (PVA)/chitosan magnetic composite. *Prog. Nucl. Energy* **71**, 172–178 (2014).
 470. Monier, M., Ayad, D. M., Wei, Y. & Sarhan, A. A. Adsorption of Cu(II), Co(II), and Ni(II) ions by modified magnetic chitosan chelating resin. *J. Hazard. Mater.* **177**, 962–970 (2010).
 471. Chen, Y. & Wang, J. The characteristics and mechanism of Co(II) removal from aqueous solution by a novel xanthate-modified magnetic chitosan. *Nucl. Eng. Des.* **242**, 452–457 (2012).
 472. Bolster, C. H. & Hornberger, G. M. On the Use of Linearized Langmuir Equations. *Soil Sci. Soc. Am. J.* **72**, 1848 (2008).
 473. Langmuir, I. The Adsorption of Gases on Plane surfaces of Glass Mica and Platinum. *J. Am. Chem. Soc.* **40**, 1361–1403 (1918).
 474. Freundlich, H. Über die Adsorption in Lösungen. *Zeitschrift für Phys. Chemie* **57U**, 385–470 (1907).
 475. Sayers, D. E., Stern, E. A. & Lytle, F. W. New technique for investigating noncrystalline structures: Fourier analysis of the extended x-ray-absorption fine structure. *Phys. Rev. Lett.* **27**, 1204–1207 (1971).
 476. Lytle, F. W., Sayers, D. E. & Stern, E. A. Extended x-ray-absorption fine-structure technique. II. Experimental practice and selected results. *Phys. Rev. B* **11**, 4825–4835 (1975).
 477. Newville, M., Livijn, P., Yacoby, Y., Rehr, J. J. & Stern, E. A. Near-edge x-ray-absorption fine structure of Pb: A comparison of theory and experiment. *Phys. Rev. B* **47**, 14126–14131 (1993).
 478. Newville, M. Fundamentals of XAFS. Univ Chicago, (2004).
 479. Maire, E. & Withers, P. J. Quantitative X-ray tomography. *Int. Mater. Rev.* **59**, 1–43 (2014).
 480. Cheng, C., Ching, Y., Ko, P. & Hwu, Y. Correction of center of rotation and projection angle in synchrotron X-ray computed tomography. *Sci. Rep.* 1–9 (2018)
 481. Park, H. S., Chung, Y. E. & Seo, J. K. Computed tomographic beam-hardening artefacts: Mathematical characterization and analysis. *Philos. Trans. R. Soc. A Math. Phys. Eng. Sci.* **373**, 1–11 (2015).
 482. Ketcham, R. A. & Carlson, W. D. Acquisition , optimization and interpretation of X-ray computed tomographic imagery : applications to the geosciences. **27**, 381–400 (2001).
 483. Barnes, J. E. Characteristics and control of contrast in CT. *Radiographics* **12**, 825–837 (1992).
 484. Fitzgerald, P. F. *et al.* CT image contrast of high-Z elements: Phantom

- imaging studies and clinical implications. *Radiology* **278**, 723–733 (2016).
485. Taud, H., Martinez-Angeles, R., Parrot, J. F. & Hernandez-Escobedo, L. Porosity estimation method by X-ray computed tomography. *J. Pet. Sci. Eng.* **47**, 209–217 (2005).
486. Vo, N. T., Drakopoulos, M., Atwood, R. C. & Reinhard, C. Reliable method for calculating the center of rotation in parallel-beam tomography. *Opt. Express* **22**, 19078 (2014).
487. van Aarle, W. *et al.* Fast and flexible X-ray tomography using the ASTRA toolbox. *Opt. Express* **24**, 25129 (2016).
488. van Aarle, W. *et al.* The ASTRA Toolbox: A platform for advanced algorithm development in electron tomography. *Ultramicroscopy* **157**, 35–47 (2015).
489. Wang Min, Cen, Y.-W., Hu, X.-F., Xiao-Liu, Y. & Pei-Ping, Z. Error mechanism of light source for synchrotron radiation computed tomography technique. *Acta Phys. Sin.* **57**, 9–25 (2008).
490. Langmuir, I. Adsorption of Gases on Glass, Mica and Platinum. *J. Am. Chem.* **345**, (1918).
491. Klosowski, P., Koennecke, M., Tischler, J. Z. & Osborn, R. NeXus: A common format for the exchange of neutron and synchrotron data. *Phys. B Condens. Matter* **241–243**, 151–153 (1997).
492. Basham, M. *et al.* Data Analysis Workbench (DAWN). *J. Synchrotron Radiat.* **22**, 853–858 (2015).
493. Atwood, R. C., Bodey, A. J., Price, S. W. T., Basham, M. & Drakopoulos, M. A high-throughput system for high-quality tomographic reconstruction of large datasets at diamond light source. *Philos. Trans. R. Soc. A Math. Phys. Eng. Sci.* **373**, (2015).
494. Ding, D. *et al.* Adsorption of cesium from aqueous solution using agricultural residue - Walnut shell: Equilibrium, kinetic and thermodynamic modeling studies. *Water Res.* **47**, 2563–2571 (2013).
495. Antsyshkina, A. S., Sadikov, G. G., Sergienko, V. S. & Poznyak, A. L. Crystal Structure of SrFe(EDTA)Cl 5H₂O. *Crystallogr. Rep* **49**, 722–727 (2004).
496. Varga, Z., Lanza, G., Minichino, C. & Hargittai, M. Temperature Gas-Phase Electron Diffraction and Quantum-Chemical. *J Struct Chem* 8345–8357 (2006)
497. Kerridge, A. & Kaltsoyannis, N. Quantum chemical studies of the hydration of Sr²⁺ in vacuum and aqueous solution. *Chem. - A Eur. J.* **17**, 5060–5067 (2011).
498. Makkos, E., Kerridge, A. & Kaltsoyannis, N. The importance of second shell effects in the simulation of hydrated Sr²⁺ hydroxide complexes. *Dalton Trans* **44** 11572–11581 (2015)
499. Price, D. J., Powell, A. K. & Wood, P. T. Hydrothermal crystallisation and X-ray structure of anhydrous strontium oxalate. *Polyhedron* **18**, 2499–2503 (1999).

500. Christensen, A. N. & Hazell, R. G. Thermal Analysis and Crystal Structure of Tetragonal Strontium Oxalate Dihydrate and of Triclinic Strontium Oxalate Hydrate. *Acta Chem. Scand.* **52**, 508–512 (1998).
501. Kriegel, R., Feltz, A., Walz, L., Simon, A. & Mattausch, H.-J. Über die Verbindung Sr₇Mn₄O₁₅ und Beziehungen zur Struktur von Sr₂MnO₄ und α-SrMnO₃. *Zeitschrift für Anorg. und Allg. Chemie* **617**, 99–104 (1992).
502. Rossell, H. J. *et al.* Structural and Solid-State Examination of Ca₄Mn₃O₁₀ and Sr₄Mn₃O₁₀. *Aust. J. Chem.* **49**, 205–217 (1996).
503. Craddock, S. & Senn, M. S. On the “alpha-phase” of Ca_{2-x}Sr_xMnO₄ and extending the chemistry of Sr_{7-y}Ca_yMn₄O₁₅ to y>1. *J. Solid State Chem.* **248**, 157–163 (2017).
504. Wang, S. *et al.* Manganese oxide-modified biochars: Preparation, characterization, and sorption of arsenate and lead. *Bioresour. Technol.* **181**, 13–17 (2015).
505. McKenzie, R. M. The Adsorption of Lead and Other Heavy Metals on Oxides of Manganese and Iron. *Soil Research* **18**, 61–73 (1980).
506. Jones, K., Ramakrishnan, G., Uchimiya, M. & Orlov, A. New Applications of X - ray Tomography in Pyrolysis of Biomass: Biochar Imaging. *Energy and Fuels* **29**, 1628–1634 (2015).
507. Bartoš, M., Suchý, T. & Foltán, R. Note on the use of different approaches to determine the pore sizes of tissue engineering scaffolds: What do we measure? *Biomed. Eng. Online* **17**, 1–15 (2018).
508. Paganin, D., Mayo, S. C., Gureyev, T. E., Miller, P. R. & Wilkins, S. W. Simultaneous phase and amplitude extraction from a single defocused image of a homogeneous object. *J. Microsc.* **206**, 33–40 (2002).
509. Berg, S. *et al.* Ilastik: Interactive Machine Learning for (Bio)Image Analysis. *Nat. Methods* **16**, 1226–1232 (2019).
510. Mehmet, Ş., Orhan, R. & Erdem, M. Preparation and characterization of activated carbon from grape stalk by zinc chloride activation. *Fuel Processing Technology* **125**, 200–206 (2014).
511. McMurry, J. *Organic chemistry (2nd ed.)*. 97 (1988).
512. Roque, W. L. & Costa, R. R. A. A plugin for computing the pore/grain network tortuosity of a porous medium from 2D/3D MicroCT image. *Appl. Comput. Geosci.* **5**, 100019 (2020).
513. Nakata, P. A. Advances in our understanding of calcium oxalate crystal formation and function in plants. *Plant Sci.* **164**, 901–909 (2003).
514. Roque, W. L. & Costa, R. R. A. A plugin for computing the pore/grain network tortuosity of a porous medium from 2D/3D MicroCT image. *Appl. Comput. Geosci.* **5**, 100019 (2020).
515. ULERY, A. L., GRAHAM, R. C. & AMRHEIN, C. Wood-ash composition and soil pH following intense burning. *Soil Sci.* **156**, (1993).
516. Jin, X. *et al.* Catalytic conversion of toluene by biochar modified with KMnO₄. *Fuel* **332**, 126237 (2023).

517. Rorsman, P. & Hellman, B. The interaction between manganese and calcium fluxes in pancreatic β -cells. *Biochem. J.* **210**, 307–314 (1983).
518. Maas, E. V., Moore, D. P. & Mason, B. J. Influence of calcium and magnesium on manganese absorption. *Plant Physiol.* **44**, 796–800 (1969).
519. Mucci, A. Manganese uptake during calcite precipitation from seawater: Conditions leading to the formation of a pseudokutnahorite. *Geochim. Cosmochim. Acta* **52**, 1859–1868 (1988).
520. Franklin, M. L. & Morse, J. W. The interaction of manganese(II) with the surface of calcite in dilute solutions and seawater. *Mar. Chem.* **12**, 241–254 (1983).
521. Li, G. *et al.* Preparation and characterization of the hydrogen storage activated carbon from coffee shell by microwave irradiation and KOH activation. *Int. Biodeterior. Biodegrad.* **113**, 386–390 (2016).
522. Laksaci, H., Khelifi, A., Trari, M. & Addoun, A. Synthesis and characterization of microporous activated carbon from coffee grounds using potassium hydroxides. *J. Clean. Prod.* **147**, 254–262 (2017).
523. Pfeiffer, F. X-ray ptychography. *Nat. Photonics* **12**, 9–17 (2018).
524. Baetge, S. & Kaltschmitt, M. Rice straw and rice husks as energy sources — comparison of direct combustion and biogas production. 719–737 (2018).
525. Johar, N., Ahmad, I. & Dufresne, A. Extraction, preparation and characterization of cellulose fibres and nanocrystals from rice husk. *Ind. Crops Prod.* **37**, 93–99 (2012).
526. Gao, Y. *et al.* A full utilization of rice husk to evaluate phytochemical bioactivities and prepare cellulose nanocrystals. *Sci. Rep.* **8**, 1–8 (2018).
527. TNO Biobased and Circular Technologies. Phyllis2. <https://phyllis.nl/>.
528. Grønli, M. G., Várhegyi, G. & Di Blasi, C. Thermogravimetric analysis and devolatilization kinetics of wood. *Ind. Eng. Chem. Res.* **41**, 4201–4208 (2002).
529. Le Floch, A., Jourdes, M. & Teissedre, P. L. Polysaccharides and lignin from oak wood used in cooperage: Composition, interest, assays: A review. *Carbohydr. Res.* **417**, 94–102 (2015).
530. Farah, A. Coffee Constituents. *Coffee Emerg. Heal. Eff. Dis. Prev.* 21–58 (2012)
531. Ballesteros, L. F., Teixeira, J. A. & Mussatto, S. I. Chemical, Functional, and Structural Properties of Spent Coffee Grounds and Coffee Silverskin. *Food Bioprocess Technol.* **7**, 3493–3503 (2014).
532. Pil, J., Seok, H., Seok, Y., Chae, H. & Joon, S. Fast pyrolysis of coffee grounds : Characteristics of product yields and biocrude oil quality. *Energy* **47**, 17–24 (2012).
533. Tronto, J. Characterization of biochars from different sources and evaluation. 395–403 (2017) doi:10.5935/1806-6690.20170046.

534. Mussatto, S. I., Machado, E. M. S., Martins, S. & Teixeira, J. A. Production, Composition, and Application of Coffee and Its Industrial Residues. *Food Bioprocess Technol.* **4**, 661–672 (2011).
535. Aderolu, A. Z., Iyayi, E. A. & Onilude, A. A. Changes in Nutritional Value of Rice Husk during *Tricho-derma viride* Degradation. *Bulg. J. Agric. Sci.* **13**, 583–589 (2007).
536. Li, M., Liu, H., Chen, T., Dong, C. & Sun, Y. Synthesis of magnetic biochar composites for enhanced uranium(VI) adsorption. *Sci. Total Environ.* **651**, 1020–1028 (2019).
537. Jindo, K., Mizumoto, H., Sawada, Y., Sanchez-Monedero, M. A. & Sonoki, T. Physical and chemical characterization of biochars derived from different agricultural residues. *Biogeosciences* **11**, 6613–6621 (2014).
538. Aly, Z. & Luca, V. Uranium extraction from aqueous solution using dried and pyrolyzed tea and coffee wastes. *J. Radioanal. Nucl. Chem.* **295**, 889–900 (2013).
539. Erdem, A. & Dogru, M. Process intensification: Activated carbon production from biochar produced by gasification highly porous carbon substances with low production costs. *Johnson Matthey Technol. Rev.* **65**, 352–365 (2021).
540. Siggins, A., Abram, F. & Healy, M. G. Pyrolysed waste materials show potential for remediation of trichloroethylene-contaminated water. *J. Hazard. Mater.* **390**, 121909 (2020).
541. Gokce, Y. & Aktas, Z. Nitric acid modification of activated carbon produced from waste tea and adsorption of methylene blue and phenol. *Appl. Surf. Sci.* **313**, 352–359 (2014).
542. Hubetska, T. S., Kobylinska, N. G. & García, J. R. Sunflower biomass power plant by-products: Properties and its potential for water purification of organic pollutants. *J. Anal. Appl. Pyrolysis* **157**, 105237 (2021).
543. Kamran, U. & Park, S. MnO₂-decorated biochar composites of coconut shell and rice husk : An efficient lithium ions adsorption-desorption performance in aqueous media. *Chemosphere* **260**, 127500 (2020).